Springer Series in Materials Science

Volume 125

For further volumes:
http://www.springer.com/series/856

The Springer Series in Materials Science covers the complete spectrum of materials physics, including fundamental principles, physical properties, materials theory and design. Recognizing the increasing importance of materials science in future device technologies, the book titles in this series reflect the state-of-the-art in understanding and controlling the structure and properties of all important classes of materials.

Ajay Kumar Saxena

High-Temperature Superconductors

Second Edition

Springer

Ajay Kumar Saxena
Department of Physics
Awadhesh Pratap Singh University
Rewa
Madhya Pradesh 486003
India

ISSN 0933-033X
ISBN 978-3-642-28480-9 ISBN 978-3-642-28481-6 (eBook)
DOI 10.1007/978-3-642-28481-6
Springer Heidelberg New York Dordrecht London

Library of Congress Control Number: 2012941132

© Springer-Verlag Berlin Heidelberg 2010, 2012
This work is subject to copyright. All rights are reserved by the Publisher, whether the whole or part of the material is concerned, specifically the rights of translation, reprinting, reuse of illustrations, recitation, broadcasting, reproduction on microfilms or in any other physical way, and transmission or information storage and retrieval, electronic adaptation, computer software, or by similar or dissimilar methodology now known or hereafter developed. Exempted from this legal reservation are brief excerpts in connection with reviews or scholarly analysis or material supplied specifically for the purpose of being entered and executed on a computer system, for exclusive use by the purchaser of the work. Duplication of this publication or parts thereof is permitted only under the provisions of the Copyright Law of the Publisher's location, in its current version, and permission for use must always be obtained from Springer. Permissions for use may be obtained through RightsLink at the Copyright Clearance Center. Violations are liable to prosecution under the respective Copyright Law.
The use of general descriptive names, registered names, trademarks, service marks, etc. in this publication does not imply, even in the absence of a specific statement, that such names are exempt from the relevant protective laws and regulations and therefore free for general use.
While the advice and information in this book are believed to be true and accurate at the date of publication, neither the authors nor the editors nor the publisher can accept any legal responsibility for any errors or omissions that may be made. The publisher makes no warranty, express or implied, with respect to the material contained herein.

Printed on acid-free paper

Springer is part of Springer Science+Business Media (www.springer.com)

This book is dedicated to my Family: Alka,
Ankur and Akshat for their patience,
support and understanding

Preface to the Second Edition

I am thankful to the readers for the interest and appreciation offered for this book. The book has been revised and more new additions have been made. These include film/substrate lattice matching and buffer layer considerations in HTSC films, "brick-wall" microstructure in epitaxial YBCO films, abstracts of author's papers, Hubbard model and band structure, electronic structure of CuO_2 layer, phase-diagram (T_c vs hole concentration), Is the coupling s-wave or d-wave in HTSCs?, scenario of theories, arguments against applicability of BCS theory to HTSCs, identification of non-phonon mechanism and lastly, three appendices.

I am thankful to the scientists and researchers whose papers have been consulted for the new additions. I am grateful to Dr. Claus Ascheron (Heidelberg) for enabling the chance to make new additions.

Thanks are also due to Gowrishankar Chakkravarthy (SPS, India) and Adelheid Duhm for their efforts in handling vexatious details faced in bringing out this edition.

Last but not the least, I am thankful to my colleagues and my family members for boosting my morale.

Rewa (M.P.), India, July 2012 Ajay Kumar Saxena

Preface to the First Edition

The aim of this book is to acquaint the reader with the phenomenon of superconductivity and the high temperature superconductors discovered in 1986 by Bednorz and Muller. Just after this discovery, a lot of research work was carried out by scientists worldwide for more than about 10 years.

This book describes the superconductivity phenomenon (Chap. 1), the structure of high Tc superconductors (Chap. 2), the critical currents (Chap. 3), synthesis of high Tc superconductors (Chap. 4), the superconductivity in cuprates (Chap. 5), proximity effect and SQUID devices, their design criteria and noise aspects (Chap. 6), theories (Chap. 7) and applications (Chap. 8).

The author is grateful to Professor O. N. Srivastava, Banaras Hindu University, Varanasi for valuable guidance and discussions during the Ph.D. tenure of the author and is also thankful to Prof. R. S. Tiwari, Dr. K. Ramakrishna, Dr. Balak Das, Dr. K. K. Verma, Dr. G. D. Varma and Dr. H. K. Singh, who worked along with the author during research at B.H.U., leading to his Ph.D.

The author is thankful to Prof. D. P. Tiwari (Head, Physics Department, A.P.S. University, Rewa), Dr. A. P. Mishra and Dr. S. L. Agrawal, Physics Department, A.P.S. University, for boosting his morale. The author is thankful to scientists and researchers whose work/papers have been consulted for preparing the manuscript. Further, he expresses his thanks to Mr. Dharmendra Saxena for preparing typescript.

Thanks are also due to Dr. Priti Nanda (Springer India), Adelheid Duhm and Dr. Habil Claus E. Ascheron (Springer Physics, Executive Editor) for bringing out the book in a short time. Suggestions from readers for future improvements would be highly welcome.

Last but not the least, I wish to thank my wife Alka and sons Ankur and Akshat for exerting endurance during the completion of the task.

Rewa (M.P.), India, June 2009 Ajay Kumar Saxena

Contents

Chapter 1
The Phenomenon: Occurrence and Characteristics

1.1 Marching Towards Absolute Zero

The phenomenon of superconductivity has been observed only at low temperatures. Therefore, we shall first consider the efforts made and the achievements on the way to absolute zero temperature.

A very common way of liquefying gases is to compress them. This causes the gas molecules to come closer, and the role of cohesive forces increases. This makes gas–liquid transition to become possible: However, at temperatures higher than the critical point, it is not possible to turn the gas into a liquid, however, large the pressure applied. So, it is necessary to cool the gas first before compressing it. In 1877, French scientist Caillettet succeeded in liquefying oxygen at a temperature 90.2 K. Six years later, N_2 was liquefied at 77.4 K. The hydrogen was found to be liquefied at a temperature of 20.4 K. This was made possible by sir James Dewar in 1898, who invented a vacuum vessel, which is used even nowadays to store liquid hydrogen. Helium was discovered in 1869 in the spectrum of solar corona. For a long time, it could not be detected on earth. It was only in 1895 that Sir William Ramsay found it among gases released when certain minerals were heated. At the end of nineteenth century, it became known that the boiling point of helium was even lower than that of hydrogen. In the late 1890s, Dutch scientist K. Onnes began his experiments aimed at liquefying helium. It was ultimately found that the transition temperature is 4.2 K and liquefaction was achieved in 1908.

Liquid helium is often called a quantum fluid. It is a striking demonstration of the fact that quantum behaviour may be manifested by macroscopic bodies as well. Liquid He remains a liquid even at absolute zero (even though at $0\,^{\circ}$K, there would be no thermal motion at all). This is because of very low density of liquid helium; it is eight times lighter than water. Therefore, light and inert helium atoms are widely separated. Near absolute zero, the laws of quantum physics prevent it from becoming a solid, that is, the usual classical concept that: atoms are completely at rest at absolute zero is incorrect.

A. K. Saxena, *High-Temperature Superconductors,* Springer Series in Materials Science 125, DOI: 10.1007/978-3-642-28481-6_1,

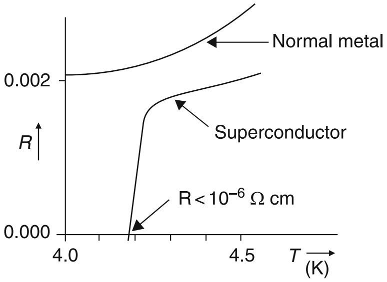

Fig. 1.1 Temperature dependence of resistance of a normal metal and a superconductor

Having attained recorded low temperatures and having obtained liquid helium, K. Onnes turned to undertake a systematic study of the properties of matter at low temperatures.

1.2 Discovery of Superconductivity

The attainment of liquid helium temperatures opened a new regime of low temperatures and it was discovered by K. Onnes in 1911, while investigating the electrical properties of frozen mercury when the electrical resistance of mercury completely disappeared on approaching 4.2 K. In his own words,

> The experiment left no doubt that as far as the accuracy of measurement went, the resistance disappeared. At the same time, however, some thing unexpected occurred. The disappearance did not take place gradually, but abruptly. From 1/500, the resistance at 4.2 K drops to a millionth part. At the lowest temperature, 1.5 K, it could be established that the resistance had become less than a thousand–millionth part of that at normal temperature. Thus, the mercury at 4.2 K has entered a new state, which, owing to its particular electrical properties, can be called the state of superconductivity.

The phenomenon of superconductivity is manifested in the electrical resistance vanishing at a finite temperature called the critical temperature and denoted T_c (Fig. 1.1). The latest data show that the resistivity of a superconductor is below $10^{-27}\,\Omega$-cm. This can be compared with the resistivity of copper (an excellent conductor), which is $10^{-9}\,\Omega$-cm. So, there is no doubt that we are dealing with ideal conductivity (total vanishing of electrical resistance).

K. Onnes discovery was followed by a large number of experimental studies. New superconducting materials were further discovered and their physical properties were studied.

1.3 Occurrence of Superconductivity

Superconductivity has been found to be exhibited by many elements: alloys, binary and ternary compounds, organic superconductors and lately discovered (1986) high T_c superconductors.

1.3.1 Elemental Superconductivity

Superconductivity in elements is displayed by non-transition metals, e.g. Be ($T_c =$ 0.03 K), Al (1.19 K), Pb (7.0 K), Sn (3 K). Examples of superconducting transition metals are Nb (9.2 K), Mo (0.92 K), Zn (0.9 K). Semiconductor elements, which display superconductivity are Si (8.3 K at 165 kbar pressure), Ge, Se and Te. Semimetal Bismuth also shows superconductivity depending on its crystal structure (Different modifications show different transition temperatures and one modification does not show superconductivity down to 10^{-2} K). Ferromagnetic materials (Fe, Co, Ni) do not display superconductivity.

1.3.2 Alloys

A large number of alloys display superconductivity with a relatively high transition temperature, e.g. Nb–Ti is important in cryogenic applications and $Nb_3Al_{0.75}Ge_{0.25}$ has a T_c of 20.7 K.

1.3.3 Binary Compounds (A-15 Materials)

Some binary compounds also show superconductivity. These are the so called A-15 compounds discovered by G.E. Hardy and J. Hulme in 1954.

Until the discovery of the high T_c superconductors (i.e. prior to 1986), most of the highest T_c superconducting materials all had the crystal structure illustrated in Fig. 1.2. The stoichiometry (the relative composition of constituent atoms mandated by the ideal crystal structure) of the material of this class is A_3B, where A is one of the transition metals (such as Nb, V, Ta or Zr) and the B atom comes from the IIIA or IVA column of the periodic table and is a metal or semiconductor, such as Sn, Al, Ga, Ge, In or Si.

The A elements are situated at the corners of a cube and the B elements form three orthogonal chains the T_cs of a few A-15 compounds are

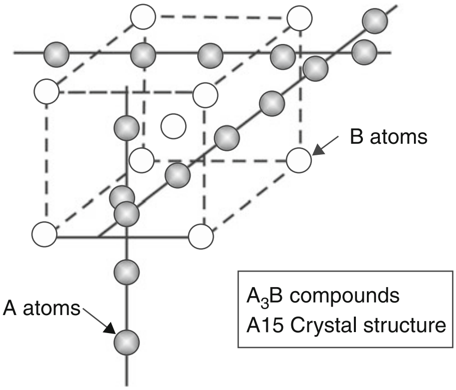

Fig. 1.2 Structure of A 15 materials

$$\begin{aligned}&V_3Ga(16.5K),\ Nb_3Ge(23.2\,K),\\&V_3Si(17\,K),\ Nb_3Al(17.5\,K),\\&Nb_3Sn(18\,K).\end{aligned}$$

The niobium compounds have typically the highest transition temperature with that of Nb_3Ge (23.2 K) being the highest one. The T_c is quite sensitive to the stoichiometry and the maximum T_c corresponds to the ratio being just 3:1 of the ordered material.

1.3.4 Heavy Fermion Superconductors

These are contemporary of organic superconductors and were discovered in 1979 by Steglich et al. [1]. These are characterised by low value of T_c, for example: $CeCu_2Si$ (0.5 K), UBe_{13} (0.85 K) and UPt_3 (0.5 K). Their names reflect their important feature: the effective mass is several hundred times greater than that of a free electron. The superconducting state displays some anomalous properties. In conventional superconductors, the electronic heat capacity decreases exponentially with temperature, whereas in heavy fermions superconductors, a power law decrease is observed.

1.3.5 Organic Superconductors

These are an unusual class of superconductors, which are insulators in normal state (with very low conductivity).

The first organic superconductor was discovered by Jerome et al. in 1980 [2] with T_c of only 1 K. However, in 1990, an organic superconductor with a T_c of 12 K was synthesised. At present, there are two known classes of organic superconductors. One of them is described by the chemical formula $(TMTSF)_2X$. The TMTSF (*Tetra*

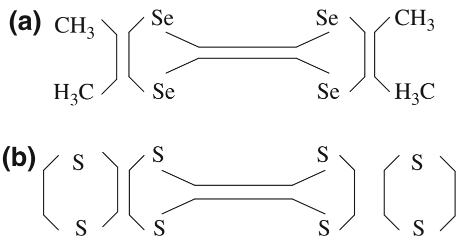

Fig. 1.3 **a** The TMTSF molecule **b** The BEDT-TTF molecule

methyltetra selena ful valene) structure is shown in Fig. 1.3a, where X is a monovalent inorganic anion. Typical anions are PF_6^-, AsF_6^- and NbF_6^-.

The other class is formed by materials with the composition $(BEDT\text{-}TTF)_2X$. The *bis-ethylene dithio tetra thia ful valene* (BEDT-TTF) molecule is shown is Fig. 1.3b, where X is again a monovalent anion.

The crystal $(BEDT\text{-}TTF)_2I_3$ has $T_c = 8.1\,K$.

1.3.5.1 High Temperature Superconductors

These oxide superconductors are defect perovskite like cuprate materials, which were discovered lately in 1986 by Bednorz and Müller (They were awarded the Nobel prize for their remarkable discovery) [3]. This discovery waited for nearly 70 years after the discovery of superconductivity. These materials have T_cs as high as 90–125 K (prior to this, T_c achieved was below 23.2 K, corresponding to that of Nb_3Ge). Bednorz and Muller discovered high temperature superconductivity ($T_c \sim 35\,K$) in defect perovskite like oxide material $La_{2-x}Ba_xCuO_4$. These materials are layered structures in which sheets of copper and oxygen atoms alternate with sheets of rare-earth (and oxygen) atoms. Soon after, Paul Chu and his coworkers [4] discovered the so called 123 oxides of the general formula $LnBa_2Cu_3O_{7-\delta}$ (Ln = Y, Nd, Sm, Eu, Gd, Dy, Ho, Er, Tm or Yb) with T_c values in the 90 K region. The discovery of materials with superconductivity above the liquid-N_2 temperature raised much hope and prompted intensive search for new classes of oxides with still higher T_cs. Two series of compounds belonging to the Bi–Sr–Ca–Cu–O and Tl–Ba–Ca–Cu–O systems have been found to exhibit superconductivity between 60 and 125 K [5, 6].

It is noteworthy that all the high T_c cuprates possess "defect perovskite layers" and all except 123 compounds contain rock salt type oxide layers. The crystal structure of perovskite and rock salt type layers are shown in Fig. 1.4.

The structure in bulk corresponds to K_2NiF_4 structure, depicted in Fig. 1.5 (La_2CuO_4). In this Ba/Sr is substituted on Lanthanum sites. The perovskite layers consist of corner sharing CuO_6 octahedra.

Some important superconductors, their T_cs and year of discovery are given in Table 1.1.

In the La based, Y-based, Bi-based, Tl-based and Hg-based cuprate families, the carriers of superconducting current are electron-vacancies or holes (pairs).

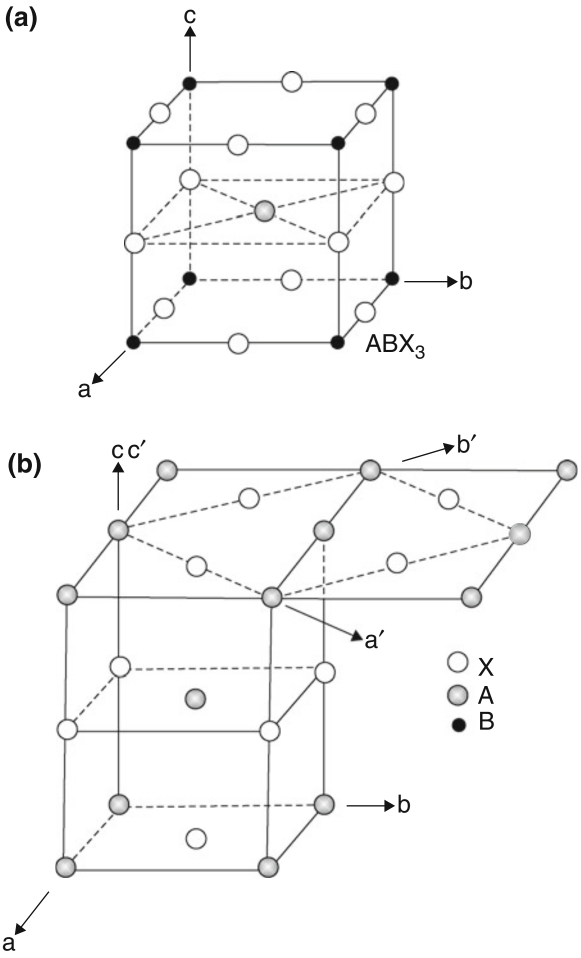

Fig. 1.4 Crystal structure of **a** perovskite and **b** rock salt. The conventional unit cell is face centered and is defined by axes a', b' and c'

By contrast, in the HTSC discovered in 1989 ($Nd_{2-x}Ce_xCuO_4$), the carriers are electron-pairs as verified by Hall-coefficient measurement.

1.3.6 C_{60}*-Based Superconductors*

The C_{60} molecule (termed as *Buckminster fullerene*) consisting of a geodesic sphere of 60 carbon atoms was discovered by Richard Smalley (USA) and Harry Kroto (England) and their discovery appeared in “Nature” (14 Nov. 1985). By doping C_{60}

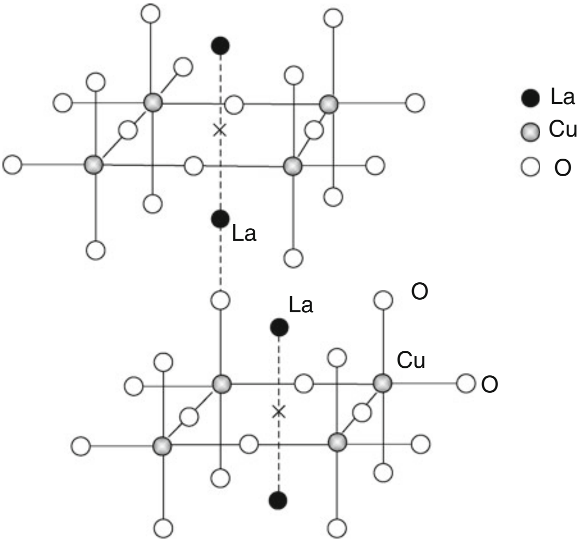

Fig. 1.5 K_2NiF_4 structure (La_2CuO_4)

with potassium atoms, Hebard et al. [7] obtained superconductivity at 18 K in K_xC_{60}. Rb-doped C_{60} produced superconductor with a $T_c \sim 28$ K. In 1991, S.P. Kelty et al. reported superconductivity at ∼30 K in Cs doped C_{60}, however, the superconducting phase was less stable than K- and Rb-doped superconductors.

Figure 1.6 shows various superconductors discovered, their T_cs versus year of discovery. It is to be conjectured here that attainment of liquefaction of gases like O_2 (at 90.2 K), N_2 (at 77.4 K), H_2 (at 20.4 K) and then He (at 4.2 K) were important milestones in the area of cryogenics (low temperature physics). The discovery of high T_c materials with superconductivity well above boiling point of liquid nitrogen (LN_2) was, therefore, a notable discovery from the viewpoint of technological applications. Further, availability of these materials raised the hopes for reducing the cost of cryogenics involved in operating at LN_2 temperatures compared to that operating at liquid-He temperatures. (LN_2 costs only 20 Rupees per litre, whereas liquid-He costs about 1,000 times higher). As a consequence, thermal insulation required for cryostats was also reduced.

1.4 The Superconducting State

The fact that apparently there is no scattering of electrons by the atoms of the crystal lattice leads to the conclusion that the wave function describing the electrons in the superconducting state must be different substantially from those in the normal state. Since (in superconducting state) lattice periodicity has no influence on the

Table 1.1 Some important superconductors

Material	Highest T_c(K)	Year of discovery	Discovered by
Hg	4.1	1911	K. Onnes
Pb	7.2	1913	–
Nb	9.2	1930	–
Nb_3Sn	18.1	1954	–
NbTi	9.5	1961	–
TiO, NbO	1	1964	–
$SrTiO_{3-x}$	0.7	1964	–
A_3WO_3	6	1965	–
A_3MoO_3	4	1969	–
A_3ReO_3	4	1969	–
V_3Ga	14.5	1966	–
$PbMo_5S_6$	15.0	1972	–
Nb_3Ge	23.3	1973	J. R. Gevaler
$Ba(Pb, Bi)O_3$	13	1975	–
$(La, Ba)_2CuO_4$	35	1986	J. G. Bednorz and K. A. Muller
$YBa_2Cu_3O_7$	90	1987	M. K. Wu and C. W. Chu
Bi–Sr–Cu–O	22	1987	Michel et al.
Bi–Sr–Ca–Cu–O	100	1987	Maeda and Tarascan
Tb–Ba–Ca–Cu–O	122	1988	Sheng and Hermann
Hg–Ba–Ca–Cu–O	130	1992	Putilin and A. Schilling
$Ln_{2-x}Ce_xCuO_{4+y}$ (Lx = Pr, Nd, Sm)	25	1989	Tokura, Takagi and Uchida

electrons, therefore, the wave function is not localised but has infinite extent. In view of the uncertainty relation, this implies a precisely definite momentum. Ground state (superconducting state) is described by

$$\psi_G = \psi(r_1,\ r_2)\,\psi(r_3,\ r_4)\ldots\ldots.\psi\left(r_{n_{s-1}},\ r_{n_s}\right)$$

where n_s = number of super electrons (there are $n_s/2$ pairs), i.e. the wave function is product of the pair wave functions. All the pairs have the same wave function given by

$$\psi(r', r'') = \sqrt{n_s}\,e^{iS(\vec{r})},$$

where the phase function $S(\vec{r})$ characterises the coherent state.

As the temperature is lowered, the electrons having energy close to Fermi energy get a chance to interact with ion-lattice via phonons due to reduced scattering at low temperatures. As a result, Cooper pairs get formed, the length scales over which their motion is correlated is the *coherence-length*:

$$\xi(T) = \frac{0.74\,\xi_0}{\sqrt{(1-T)}};\quad \xi_0 = \frac{\hbar v_F}{\pi\Delta_0},$$

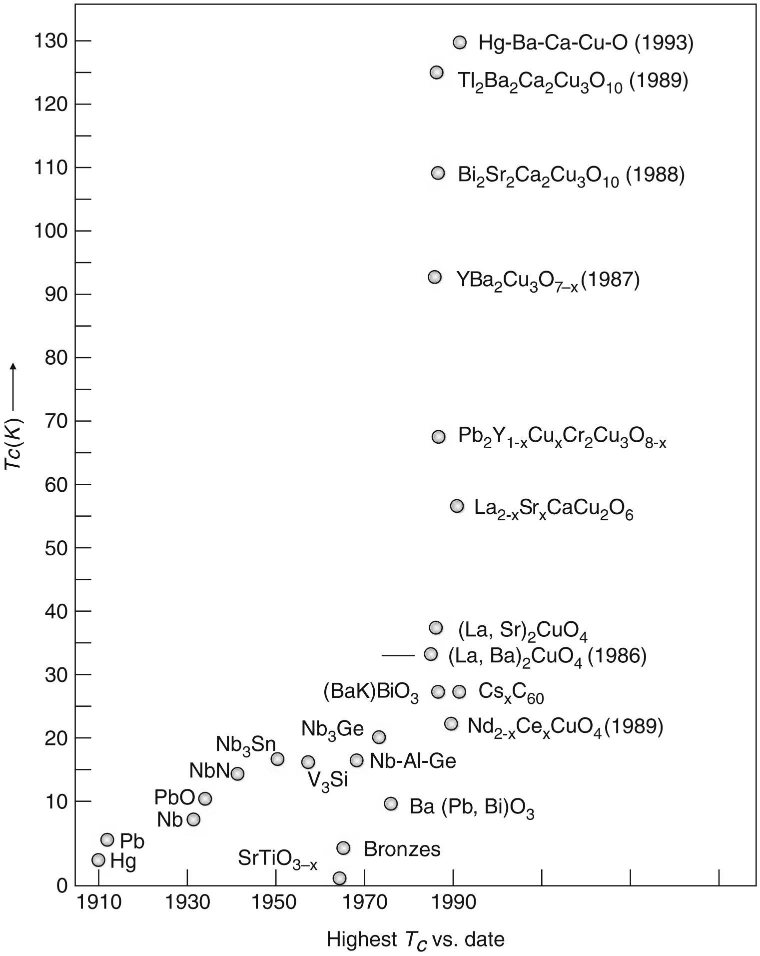

Fig. 1.6 Critical temperature versus year of discovery

where, v_F is the fermi velocity and Δ_0 is the energy gap (at 0°K), which is the gap between superconducting pairs and normal electrons. *The paired electrons move without resistance, whereas single electrons do not*:

Before pairing, electrons are separate entities (Fermions) having random momenta (due to scattering). When pairs form, two electrons of a pair have zero net momentum and opposite spins, so that in current carrying state they do not under go incoherent scattering, i.e. a pair is like a singlet and all pairs acquire same momentum in the same direction. Same momenta implies the same value of phase gradient for all pairs (momentum $\vec{P} = \hbar \nabla S = 2mev$). Therefore, there will be no change in current flow. Their motions are correlated (*Phase coherence*). The only scattering event, which will reduce the current will be when a pair is imparted with an energy greater than the binding energy of the pair (i.e. $\geq \Delta_0$).

For $I < I_c$, there is no way to impart this energy. The long range coulomb repulsion between two electrons of a pair has been largely suppressed by screening due to strong correlation effects of the other electrons.

1.5 Phase Coherence

The superconducting ground state is represented by many electron wave function

$$\psi_G\left(\vec{r}_1, \vec{r}_2, \ldots \vec{r}_{n_s}\right) = \phi\left(\vec{r}_1, \vec{r}_2\right)\phi\left(\vec{r}_3, \vec{r}_4\right)\cdots\phi\left(\vec{r}_{n_{s-1}}, \vec{r}_{n_s}\right),$$

where total number of pairs equals $n_s/2$. $\vec{r}_n$ is the position coordinate of nth electron and the ϕ's are the same for all pairs. The local super fluid density is given by

$$n_s(\vec{r}) = \left|\psi_G(\vec{r})\right|^2 \tag{1.1}$$

and the super-current density is expressed by

$$\vec{J}(\vec{r}) = -i\frac{e\hbar}{2m_e}\left[\psi_G^*\nabla\psi_G - \psi_G\nabla\psi_G^*\right] - \frac{e^2}{m_e}\vec{A}\left(\vec{r}\right)\psi_G^*\nabla\psi_G \tag{1.2}$$

$\vec{A}\left(\vec{r}\right)$ is the vector potential $\left(\vec{B} = \nabla \times \vec{A}\right)$.

For steady state conditions, ψ_G or ψ can be written

$$\begin{aligned}\psi\left(\vec{r}\right) &= \psi_0 e^{iS(\vec{r})}\\ &= (n_s)^{1/2} e^{iS(\vec{r})}\end{aligned} \tag{1.3}$$

where the phase $S(\vec{r})$ is a real function of position $\vec{r}$. Then, (1.2) becomes

$$\vec{J}_s = \frac{n_s}{2}\frac{e}{m_e}(\hbar\nabla S - 2e\vec{A}) \tag{1.4}$$

$$(\because \psi^*\psi = 1)$$

(assuming that condensate in superconductor can be represented by a macroscopic wave function in the form of (1.3)).

We anticipate that the condensate is made up of pairs of electrons of number density $n_s/2$, mass 2 m_e (and charge $2e$).

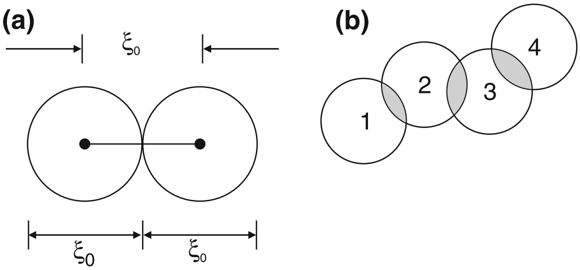

Fig. 1.7 **a** The pairs centre of mass phases are locked over a distance ξ **b** establishment of long range phase order

Equations (1.3) and (1.4) imply we cannot describe a super-current in a homogeneous material, unless $\psi(\overrightarrow{r})$ is complex. The physical situation depends on the variation of the phase and not simply on the magnitude of ψ.

From (1.4),

$$m^{*}\overrightarrow{v}_{s}(\overrightarrow{r}) = \hbar\nabla S(\overrightarrow{r}) - e^{*}\overrightarrow{A}(\overrightarrow{r}). \tag{1.5}$$

In the absence of a magnetic field, the phase function $S(\vec{r})$ plays the part of a velocity potential for the super fluid velocity $\vec{v}_s$. Therefore, if S did not vary in space, there would be no super-current. The phase function $S(\vec{r})$ characterises the electron ordering, represents the same phase of all pairs (phase coherence).

In the absence of $\vec{A}$, the local value of S varies with position at a rate proportional to v_s, i.e. $\nabla S \propto \vec{v}_s$ along the direction of flow.

1.6 Coherence Length

The maximum distance between electrons of a cooper-pair in real space upto which their motion is correlated (by taking advantage of the attractive interaction) is known as the *Coherence length* (ξ_0).

The pairs control the local phase order within a superconductor. All pairs lying in a sphere of diameter ξ_0 have the same centre-of-mass-momentum and the same centre-of-mass-phases.

In Fig. 1.7b, circles represent spheres of diameters ξ. Starting from sphere 1, we note that in the region of overlap with sphere 2, the phases must be same. Thus, if sphere 2 locks phases within it, phase-locking is continued from the basic length to the entire superconductor (by overlapping spheres of diameter ξ_0), establishing a long range phase order (Coherence).

The phase continuation (i.e. coherence) is forced by virtue of condensation energy associated with the overlap regions between two spheres.

1.6.1 Pippard's Equation and Coherence Length

If one looks at the expression of penetration depth as given by

$$\lambda = \sqrt{\frac{m}{\mu_0 n_\mathrm{s} e^2}} \quad \text{(see article 1.14)}$$

then impurities in a material should not change appreciably the penetration depth. Pippard did an experiment by measuring the microwave surface impedance of Sn diluted with small amounts of indium at about 3 cm wavelength and estimated the penetration depths from the surface impedance values. According to London's theory, there should not be an appreciable change in the penetration depth of Sn, but Pippard observed that penetration depth changes roughly by a factor of 2 at low temperatures, and this led to the non-local modification of the London theory and the concept of (electromagnetic) coherence length ξ, which depends on the mean free path.

We have,

$$\vec{H} = -\frac{m}{\mu_0 n_\mathrm{s} e^2} \operatorname{curl} \vec{j}_\mathrm{s}\,. \tag{1.6}$$

$$\text{Therefore } \vec{A} = -\frac{m}{\mu_0 n_\mathrm{s} e^2}\, \vec{j}_\mathrm{s} \quad (\because \vec{H} = \nabla \times \vec{A}) \tag{1.7}$$

Pippard postulated that current density at any point in the superconductor depends on the vector potential $\vec{A}$ not at that point, but integrated over a domain of radius ξ known as (Pippard's) coherence length. ξ must depend on the mean free path of the electrons to account for the variation of penetration depth with impurity content. The current-density is given by the generalised expression (Fig. 1.8)

$$\vec{j}_\mathrm{s}(\vec{r}) = \int K(r, r')\, \vec{A}(r')\mathrm{d}r' \tag{1.8}$$

The width of the Kernel function $K(\vec{r} - \vec{r}')$ defines the Pippard's coherence length (ξ). Pippard suggested the form of the kernel as

$$K(r, r') = \exp\left[-\frac{(r - r')}{\xi}\right] \tag{1.9}$$

$$\text{with } \frac{1}{\xi} = \frac{1}{\xi_0} = +\frac{1}{\alpha \wedge}. \tag{1.10}$$

Here, ξ is electromagnetic coherence length, which is of the order of 10^{-4} cm, α is an empirical constant (of the order of unity) and $\wedge$ is mean free path (ξ_0 is known as intrinsic coherence length).

The appearance of the electron mean free path shows that the coherence length is reduced by the presence of impurities and the ratio

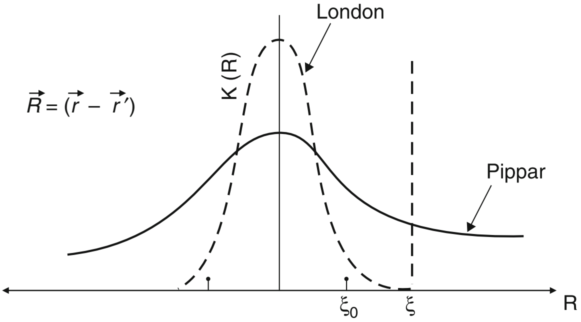

Fig. 1.8 Kernel function $K(R)$ versus R (representation of Coherence length)

$$k = \frac{\lambda}{\xi} \quad \text{(where } l \text{ is penetration depth)}$$

is a number known as *Ginzberg Landau parameter*. It is controlled by alloying or doping a superconductor.

1.6.2 The Size of an Electron Pair

The spatial spread of electrons in a Cooper pair is, (using uncertainty relation)

$$\delta r = \frac{\hbar v_F}{\Delta}$$

where v_F is Fermi velocity.

The coherence length (size of the Cooper pair) is described by

$$\xi_0 = \frac{\delta r}{\pi} \equiv \frac{\hbar v_\mathrm{F}}{\pi \Delta}. \tag{1.11}$$

It characterises the scale of spatial correlation in a superconductor. Substituting for v_F and Δ, we find

$$\xi_0 \cong 10^{-4}\,\text{cm}.$$

Period of a crystal lattice is $\sim 10^{-8}$ cm. Thus, $\xi_0 \cong 10^4 \times$ lattice spacing. This indicates a long range correlation in a superconductor, which is unique in the inorganic world.

1.6.3 Analogy Between Long Range Spatial Order in a Solid and Phase-Order in a Superconductor

In a solid, the typical range of inter-atomic forces are $\sim$ inter-atomic spacing. Once a part of the crystal forms the continued propagation, the order is established in a stepwise manner with the arrangement of the occupied sites legislating the arrangement of subsequent level through the short range interactions ($\sim$ inter-atomic spacing).

In case of a superconductor, we are dealing with an interaction whose "range" is associated with the retarded nature of the phonon-exchange interaction.

Since the important lattice frequencies are of the order of the Debye frequency (ω_{D}), an electron with velocity (v_{F}) can come from a distance ($v_{\mathrm{F}}/\omega_{\mathrm{D}}$) to feel the lattice disturbance produced by another electron. Thus, in a superconductor, the phonon exchange interaction may "extend" on the order of $\frac{v_{\mathrm{F}}}{\omega_{\mathrm{D}}} \approx 10^{-5}$ cm. The attractive nature of interaction leads to the formation of pairs, which are spread out over a coherence length ξ (which is $\sim 10^{-4}$cm). The center of mass coordinates of some 10^6 pairs lie in a sphere of diameter ξ. For the attractive electron–phonon attraction to be taken advantage of, by each of the pairs, the space–time correlation are to be such that all have the same center-of-mass momentum. More generally, in presence of electromagnetic fields, we may extend this to the statement that the pairs must have the same center-of-mass phase. To the extent that they do not, the condensation energy is lost (This is how a short range force produces a long range order).

Therefore, just as atoms of a solid control the local spatial order around them, pairs (in a superconductor) control the local phase-order (within a coherence length).

1.7 Critical Magnetic Field

It was discovered by K. Onnes that application of magnetic fields destroy superconductivity. The minimum magnetic field necessary to vanish superconductivity is called the critical magnetic field. It is found to be dependent on temperature and is given by

$$H_{\mathrm{c}}(T) = H_{\mathrm{c}}(0)\left[1 - \left(\frac{T}{T_{\mathrm{c}}}\right)^2\right]. \tag{1.12}$$

This is known as *Tuyn*'s *law* $H_{\mathrm{c}}(0)$ is the critical field at absolute zero. $H_{\mathrm{c}}(0)$ and T_{c} are constants and characteristic of the material (Fig. 1.9).

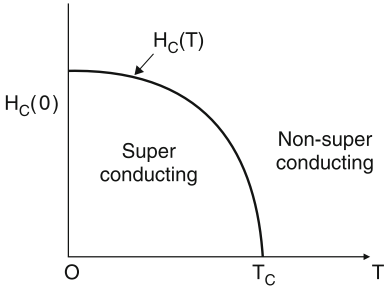

Fig. 1.9 Critical magnetic field as function of temperature

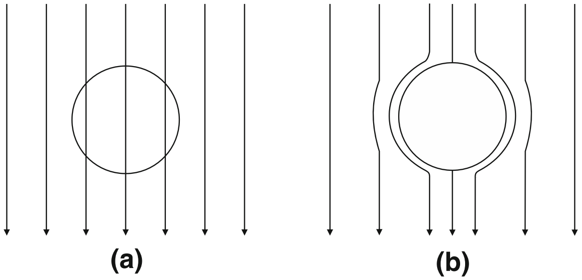

Fig. 1.10 The Meissner effect **a** For $T > T_c$ or $H > H_c$, normal conductor **b** $T < T_c$ and $H < H_c$, material is superconductor

1.8 Meissner Effect

In metals, other than ferromagnetic, the magnetic fields created by the elementary atomic currents are oriented chaotically in the metal and cancel out, therefore, magnetic induction $B = 0$ in the absence of an external field. In presence of an external field H, there appears a finite induction $\vec{B} = \mu \vec{H}$, where μ is the permeability

$\mu > 1$ (for paramagnetics),
$\mu < 1$ (for diamagnetics),
$\mu = 0$ (for superconductors),

i.e. in the superconducting state, a superconductor exhibits perfect diamagnetism. Meissner effect is the phenomenon, which relates diamagnetism with superconductors. This as follows:

Meissner and Ochsenfeld discovered in 1933 that below the critical temperature ($T < T_c$), if a superconductor is placed in a magnetic field, the magnetic field is expelled from the interior of a superconductor. This is known as *Meissner effect* (Fig. 1.10). Further, if $H > H_c$ (or $T > T_c$), the flux penetrates the superconductor, because then the material is non-superconducting and behaves like a normal conductor.

The point noteworthy here is that not only a magnetic field is excluded (for $T < T_c$) as the superconductor is placed in a magnetic field, but also a field present in an originally normal sample is expelled. This reversible nature of the Meissner effect is related thermodynamically to the free-energy difference between the normal and superconducting states in zero field, the so called *condensation energy* of the superconducting state, i.e.

$$f_n(T) - f_s(T) = \frac{H_c^2(T)}{8\pi} \quad \text{(c.g.s.unit)}, \tag{1.13}$$

where f_n and f_s are the Helmholtz free energies/volume in the respective phases in zero field.

1.9 Comparison Between a Superconductor and a Very Good (or Ideal) Conductor

The electron–lattice interaction is the basic mechanism of electrical resistance in an ordinary metal. Metals, such as Au, Ag and Cu are excellent conductors but do not display superconductivity, because very good conductivity indicates that electrical resistance is very low. Therefore, the interaction between electrons and lattice is very weak, which at low temperatures does not create sufficient inter-electron attraction to overcome the coulomb repulsion. Therefore, there is no transition to superconducting state.

A perfect conductor does not exhibit Meissner effect, i.e. no flux expulsion on cooling:

In fact, the magnetic behaviour of an ideal conductor depends on whether the sample is first cooled to below T_c before applying the field (1) or the field is applied and then cooled (2).

For a superconductor, the final states are identical, regardless of whether B_{ext} is switched on before, or after cooling.

For any closed path enclosing an area "a" in a material, it must be true that

$$IR = V = \iint \text{curl}\,\vec{E} \cdot \text{d}\,\vec{a} = -\frac{\partial \vec{B}}{\partial T} \cdot \vec{A} \tag{1.14}$$

(using Maxwell's equation) vanishing resistance implies magnetic flux $\vec{B} \cdot \vec{A}$ through the loop may not alter, that is, magnetic field inside must be maintained (what was initially there) both after cooling and after switching off the external field B_{ext}.

On switching off B_{ext} in the cooled state, this requirement is satisfied (in both A and B, Fig. 1.11), because the process of switching off B_{ext} induces persistent currents inside the material surface, which maintain the value of magnetic field in the interior. Now, in sense of (1.14), an ideal conductor (for $B_{\text{ext}} = 0$ and $T < T_c$) may adopt

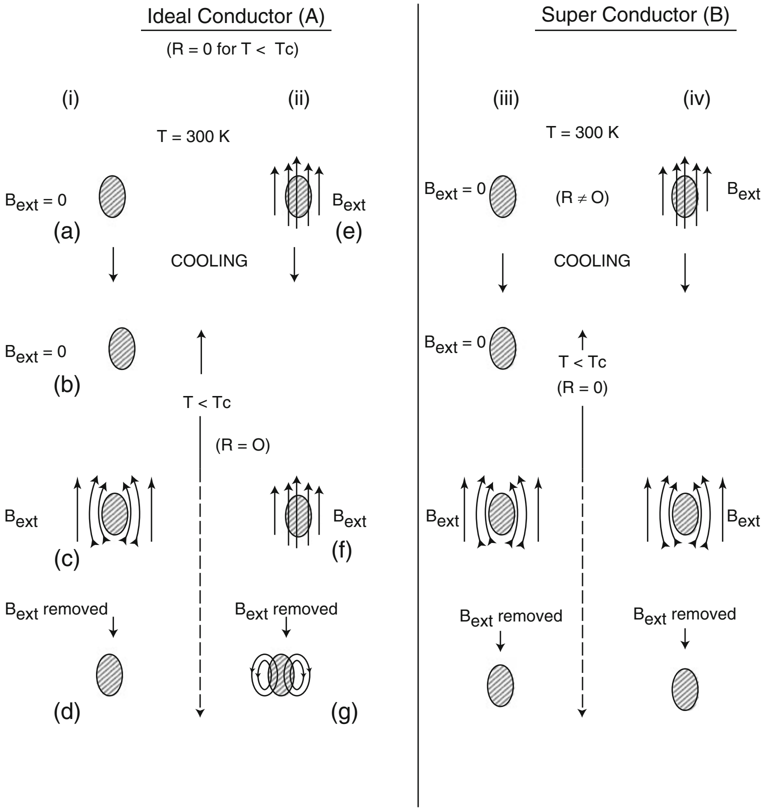

Fig. 1.11 Comparison of magnetic behaviours of an ideal conductor and a superconductor. Both have $R = 0$ for $T < T_c$

two different states ((c) or (f)) depending on the order of events leading to this state. Thus, we have two different states (d) and (g) for an ideal conductor. However, if a superconductor was merely such an “ideal conductor”, the superconducting state would not be a state in the thermodynamic sense. In fact, in the superconductor, not only $\frac{\partial \vec{B}}{\partial T} = 0$, but also $\vec{B} = 0$ independent of the path by which the state (c) or (f) is reached.

This Meissner effect, which represents the property of ideal diamagnetism (for a superconductor) follows independent of vanishing of electrical resistance. However, an ideal conductor does not show ideal diamagnetism (as evident from state (g)), i.e. external field is not expelled, if cooling is done after the application of external field.

Table 1.2 Values of isotope effect coefficient for some elements

Element	β
Sn	0.46
Mg	0.5
Ru	0(±0.05)
Zr	0(±0.05)
Mo	0.33
Os	0.21

1.10 Isotope Effect

Historically, the isotope effect has been instrumental in understanding the mechanism responsible for Cooper-pair formation in conventional superconductors. It has been observed experimentally that the superconducting transition temperature T_c varies with the isotopic mass M of the material as

$$T_c \propto M^{-\beta} \tag{1.15}$$

$$\text{Or } -\frac{d(\ell n T_c)}{d(\ell n M)} \equiv \beta \tag{1.16}$$

where β is called the isotope effect coefficient and is given by (BCS theory) as

$$\beta = 0.5[1 - 0.01\{N(0)V\}^{-2}] \tag{1.17}$$

where $N(0)$ is the density of single particle states for one spin at the Fermi level and V is the potential between the electrons. β has the value 0.4–0.5 for many superconductors, however, there are some notable exceptions (see Table 1.2).

Isotope effect was first discovered in mercury. It has been found that in mercury T_c varies from 4.185 K to 4.146 K, as isotopic mass varies from 1.995 amu to 203.4 amu. Since, Debye temperature θ_D is proportional to the velocity of sound, which varies as $M^{-1/2}$, therefore, T_c can be related to θ_D as

$$T_c \propto \theta_D \quad \text{or} \quad T_c/\theta_D = \text{a constant}. \tag{1.18}$$

Since Debye temperature depends on lattice vibrations, the above relation implies that lattice vibrations play an important role in superconductivity, as also suggested by Frohlich prior to the BCS theory.

The departure in values of β from 0.5 could be explained by Eliasberg theory, taking into consideration the competition between (1) electron-phonon interaction and (2) the Coulomb-repulsion.

1.11 Isotope Effect in HTSCs

Many experimental data indicate that the new high T_c oxides display many features of the BCS theory, such as carrier pairing and the presence of an energy gap. The pairing is caused by some intermediate field (may be other excitations like plasmons, excitons or magnons).

It still remains to figure out, which of these excitations are responsible for inter-electron attraction. Higher T_cs of cuprates does not imply presence of non-phonon mechanisms. The interest in investigating pairing mechanism in the cuprates has included much discussion on the relevance of the electron–phonon coupling mechanism (which is responsible for superconductivity in conventional superconductors). There have been several experimental indications of the isotope shift of T_c, due to presumably strong electron–phonon interactions. The indications are in the vibrational behaviour: Experiments performed on high T_c oxides with oxygen isotopic substitution yielded a very small shift of T_c. Similar results were obtained by Cu and Ba isotopic substitution.

1.11.1 *Optical Behaviour Study*

1. In 1987, it was identified infra-red active modes in LSCO (i.e.La–Sr–Cu–O) at 240 and 495 cm^{-1}. These arise from coupling of optic phonons to the electronic system.
2. It has been inferred from a number of studies that observation of Raman active and infra-red active modes with strong temperature dependent frequencies and line widths are due to electron–phonon coupling (Anharmonicity may be another possibility).
3. In 1988, Zeyner and Zwicknage provided a theoretical analysis of the temperature dependence of Raman- and infra-red active modes in YBCO system, which indicates that this material is in the strong electron-phonon coupling limit.

1.11.2 *Elastic and Ultrasonic Studies*

These show, however, anomalies in their temperature dependence often closely correlated with T_c, which reflect strong electron–phonon coupling.

The character and strength of the electron–phonon interaction are of central interest, both for understanding the unusual physical properties of the cuprates as well as for describing the electronic system itself.

The electron–phonon interaction has been discussed widely as a possible pairing mechanism and, also as an impossible pairing mechanism for producing $T_c \sim 100\,\mathrm{K}$.

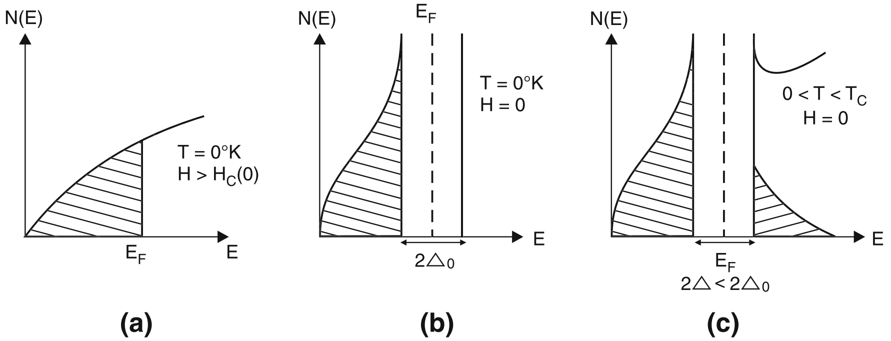

Fig. 1.12 Density and occupancy of states: **a** in absence of superconductivity, **b** in superconducting ground state, **c** superconducting state at finite temperature

The isotope-shift of T_c initially expected to be the crucial experiment, has not been as conclusive as was naively expected at first.

The smaller and negative values of the β could be explained with the help of Eliasberg theory, only if $T_c \sim 1\,\mathrm{K}$ or less. In case of early results on cuprates, the oxygen isotope effect (with $T_c \sim 100\,\mathrm{K}$) showed $\beta_{ox} \sim 0$ (implying a result inconsistent with the electron phonon model), and therefore, the electron–phonon model was abandoned, favouring an electronic model. Many electronic models have been proposed but none yet completely expected. However, a smaller value of β_{ox} can be accounted for by considering (at the cost of some accuracy) a joint phonon, but largely electronic mechanism.

Recently "strange isotope-effect" has been observed, which has added to the confusion, a rapid variation in the β_{ox} value is found (even >0.5) with doping variation (so as to change T_c), e.g. rapid increase in β for $Y_{1-x}Pr_xBa_2Cu_3O_7$.

1.12 The Energy Gap

The behaviour of the specific heat in the superconducting state is a strong indication of the existence of an energy gap in the excitation spectrum of the electrons in the conduction band. Figure 1.12b illustrates this by comparing the difference between the occupancy of states in a normal metal (Fig. 1.12a) and a superconductor. Figure 1.12b illustrates the superconducting ground state for absolute zero temperature. This shows a zero density of states for energy within $\pm\Delta(0)$ or $2\Delta_0$. At $T = 0$, no electrons are excited to higher states. Figure 1.12c shows effect of a finite temperature T ($<T_c$).

The superconducting energy gap $\Delta(T)$ is now smaller than Δ_0. A fraction of electron number is now in states above $E_F(0) + \Delta(T)$, leaving behind some unoccupied states below $E_F(0) - \Delta(T)$. The quantity $2\Delta(0)$ is the pair binding energy. It is to

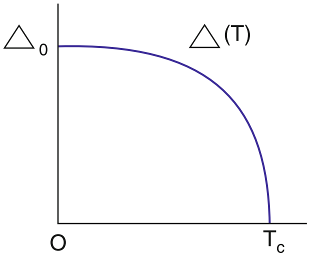

Fig. 1.13 Energy gap versus temperature

Table 1.3 Energy gap ($2\Delta_0$) (at 0° K) for some elements

Element	$2\Delta_0$(meV)	T_c(K)	$(2\Delta_0)/(k_B T_c)$
Nb	3.05	9.50	3.8
Ta	1.40	4.48	3.6
Al	0.34	1.20	3.3
Sn	1.15	3.72	3.5
Pb	2.90	7.19	4.3
Hg	1.65	4.15	4.6

Note Once set in a drift motion, a Cooper pair may be scattered only if the collision mechanism imparts an energy to the pair which is at least equal to $2\Delta_0$. But at low temperatures, this amount of energy cannot be supplied by the phonons because in superconducting state ($T < T_c$) only very low energy phonons are excited. Thus, the Cooper pair continues its drift motion indefinitely

be noted here that the energy interval 2Δ (i.e. discreteness in energy for a superconductor) is in macroscopic electron system, unlike energy gap in a semiconductor or an insulator.

The energy gap is a function of temperature and the temperature dependence is as shown in Fig. 1.13. With increasing temperature, the gap decreases and finally vanishes at $T = T_c$. In the BCS theory, it is shown that

$$\Delta(T)_{T \to T_c} = aT_c(1 - (T/T_c))^{1/2}, \tag{1.19}$$

where, in the weak coupling approximation $a = a_{BCS} = 3.06$. At temperatures below T_c, the presence of quasi-particles (normal electrons) being less than the total number of electrons.

The value of the energy gap at 0°K (i.e. $2\Delta_0$) of some of the elements is shown in Table 1.3. The ratio $2\Delta_0$ to $k_B T_c$, according to BCS theory is 3.52, which is the same for all superconductors. The ratios given in the last column of the table show good agreement with the theory. In high temperature superconductors (HTSCs), because of the layered structure, the carrier motion is quasi-two-dimensional, which favours better pairing, therefore, even carriers far from E_F bind, leading to a large value of Δ. The ratio $\Delta(0)/E_F$ indicates the fraction of carriers paired and is much larger in HTSCs than in conventional superconductors.

1.13 Thermodynamics of Superconductors

The transition to the superconducting state is a function of temperature and applied magnetic field. In pure samples, the transition is reversible and can be described by equilibrium thermodynamics. The conditions for equilibrium are found by minimising the magnetic Gibbs free energy at constant T and H.

The change from the normal to the superconducting state occurs since the Gibbs free energy in the superconducting state (G_s) is lower than its value G_N in the normal state.

$$\text{Now,}\quad G\,(T,\,H) = U - TS + U_\mathrm{M}, \tag{1.20}$$

where U, T, S and U_M are internal energy, temperature entropy and the magnetic energy, respectively.

For a superconductor placed in a magnetic field H_a, the magnetic energy

$$U_\mathrm{M} = \int\limits_0^{H_\mathrm{a}} \mu_0 H \mathrm{d}M = \int\limits_0^{H_\mathrm{a}} \mu_0 H \chi \mathrm{d}M = -\frac{1}{2}\mu_0 \chi H_\mathrm{a}^2 \tag{1.21}$$

(if susceptibility χ is independent of H).

Thus,

$$G(T,\,H_\mathrm{a}) = U - TS - \frac{1}{2}\mu_0 \chi H_\mathrm{a}^2, \tag{1.22}$$

$$\begin{aligned} \mathrm{d}G &= \mathrm{d}U - \mathrm{d}\,(TS) - \mu_0\,\mathrm{d}\,(HM)\ \ (\because\ U_\mathrm{M} \equiv \mu_0\,HM) \\ \text{or}\quad \mathrm{d}G &= \mathrm{d}U - T\mathrm{d}S - S\mathrm{d}T - \mu_0 H\mathrm{d}M - \mu_0 M\mathrm{d}H. \end{aligned} \tag{1.23}$$

From second law of thermodynamics,

$$\begin{aligned} \mathrm{d}U &= T\mathrm{d}S + \mu_0 H\mathrm{d}M \\ \therefore \mathrm{d}G &= -S\mathrm{d}T - \mu_0 M\mathrm{d}H. \end{aligned} \tag{1.24}$$

This equation can be integrated for an isothermal magnetisation

$$G\,(T,\ H_\mathrm{a}) - G\,(T,\ 0) = -\,(1/2)\,\mu_0\,\chi\,H_\mathrm{a}^2$$

(for a metal in the superconducting rate, $\chi = -1$)

$$\therefore G_\mathrm{s}\,(T,\,H_\mathrm{a}) - G_\mathrm{s}\,(T,0) = (1/2)\,\mu_0\,H_\mathrm{a}^2. \tag{1.25}$$

In the normal state, $\chi = 10^{-6}$ (emu) (i.e. for $T > T_\mathrm{c}$) magnetisation is taken to be zero so,

$$G_\mathrm{N}\,(T,\ H_\mathrm{a}) = G_\mathrm{N}\,(T,0)\,.$$

Fig. 1.14 Free energies G_S and G_N versus applied magnetic field

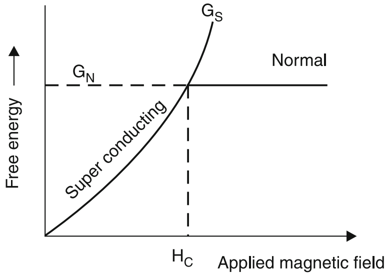

At $H_a = H_c$, the normal and superconducting phases are in equilibrium at the same temperature and field

$$\begin{aligned}\therefore G_s(T,\ H_c) &= G_N(T,\ H_c) = G_N(T, 0)\\ &= G_s(T,\ 0) + 1/2\mu_0\, H_c^2(T)\,.\\ G_N(T,\ 0) - G_s(T, 0) &= 1/2\mu_0\, H_c^2(T)\,.\end{aligned} \tag{1.26}$$

For $H_a > H_c$, we have $G_s > G_N$, whereas for $H_a < H_c$, $G_s < G_N$ and therefore, the superconducting state is stable.

The above equation provides a direct measure of the condensation energy of the superconducting state, i.e. the reduction in the free energy in forming the new phases is $1/2\mu_0 H_c^2(T)$ per unit volume.

The Gibbs free energies G_S and G_N from (1.25) and (1.26) are plotted in Fig. 1.14.

Equation (1.24) can now be used to determine the entropy as

$$S = -\left(\frac{\partial G}{\partial T}\right)_H \tag{1.27}$$

using (1.26) and (1.27), we have

$$\begin{aligned}S_N &= S_s - \frac{1}{2}\mu_0 \frac{d}{dT}(H_c^2)\\ S_N &= S_s - \mu_0\left(H_c \frac{dH_c}{dT}\right).\end{aligned} \tag{1.28}$$

Experimentally, it is observed that dH_c/dT is always negative. Therefore, entropy in the superconducting state is lower than that in the normal state, i.e. the superconducting state is more ordered than the normal state.

Further, specific heat

$$C_v^e = T\left(\frac{\partial S}{\partial T}\right) H_c. \tag{1.29}$$

Using (1.28) and (1.29), we obtain

$$\begin{aligned} C_{\mathrm{N}} - C_{\mathrm{s}} &= -\mu_0 T \frac{\mathrm{d}}{\mathrm{d}T}\left[H_{\mathrm{c}}\frac{\mathrm{d}H_{\mathrm{c}}}{\mathrm{d}T}\right] \\ \text{or}\quad C_{\mathrm{eN}} - C_{\mathrm{es}} &= -\mu_0 T\left[\left(\frac{\mathrm{d}H_{\mathrm{c}}}{\mathrm{d}T}\right)^2 + H_{\mathrm{c}}\frac{\mathrm{d}^2 H_{\mathrm{c}}}{\mathrm{d}T^2}\right] \\ \text{or}\quad C_{\mathrm{es}} - C_{\mathrm{eN}} &= \mu_0 T\left[\left(\frac{\mathrm{d}H_{\mathrm{c}}}{\mathrm{d}T}\right)^2 + H_{\mathrm{c}}\frac{\mathrm{d}^2 H_{\mathrm{c}}}{\mathrm{d}T^2}\right]. \end{aligned} \tag{1.30}$$

Evaluated at T_{c}, this equation yields

$$\frac{\Delta C}{\gamma T_{\mathrm{c}}} = \frac{\mu_0}{\gamma}\left(\frac{\mathrm{d}H_{\mathrm{c}}}{\mathrm{d}T}\right)^2_{T=T_{\mathrm{c}}}. \tag{1.31}$$

The electron contribution to specific heat shows two features related to opening of energy gap, when the temperature is lowered through T_{c}. With respect to the normal state specific heat

$$C_{\mathrm{eN}} = \gamma T \tag{1.32}$$

$$\text{with } \gamma = 2\pi^2 k_{\mathrm{B}}^2 N(0)/3. \tag{1.33}$$

C_{es} at T_{c} shows the jump given by

$$(C_{\mathrm{es}} - C_{\mathrm{eN}})/T_{\mathrm{c}} = 1.43, \tag{1.34}$$

followed by an exponential decrease roughly proportional to $\exp\left[-\frac{\Delta_0}{k_{\mathrm{B}}T}\right]$. The phonon specific heat does not change in the superconducting state (Fig. 1.15).

It is to be noted here that, although H_{c} vanishes at $T = T_{\mathrm{c}}$, $(\mathrm{d}H_{\mathrm{c}}/\mathrm{d}T)$ does not, as a result the specific heat must exhibit a discontinuity at this temperature.

1.13.1 Latent Heat of Superconducting Transitions

Since $\mathrm{d}Q = T\mathrm{d}S$ for a reversible flow of heat, we find from (1.28) that the latent heat of transition from the superconducting to the normal state is

$$L = -T\mu_0 H_{\mathrm{c}}\frac{\mathrm{d}H_{\mathrm{c}}}{\mathrm{d}T}. \tag{1.35}$$

This is analogous to the Clausius–Clapeyron relation ($L = T\Delta V\mathrm{d}P/\mathrm{d}T$) that describes the dependence of the latent heat of a first-order transition on change of pressure with temperature and of change of volume with phase.

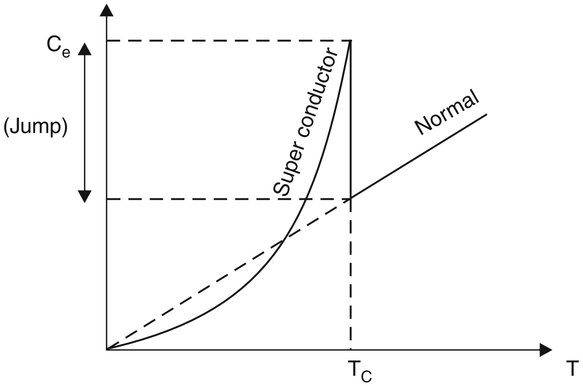

Fig. 1.15 The temperature dependence of electronic specific heat of a conductor in the normal and superconducting states

Fig. 1.16 Latent heat of a superconductor

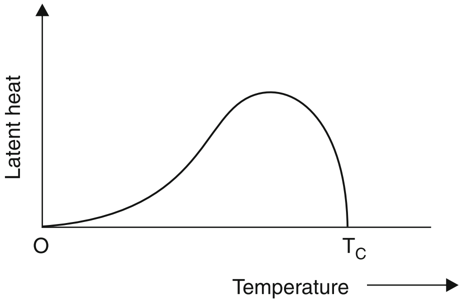

The latent heat of transition for a superconductor is plotted in Fig. 1.16.

It seems to vanish at $T = 0$, because of Nernst theorem, and also at T_c, since H_c vanishes there.

The fact that L and $S_N - S_s$ is zero at T_c is typical of a phase transition that involves a change of order rather than a change of state. Such transitions are known as transitions of the second-order (it is to be noted that dH_c/dT is equal to zero only at $T = 0$ and $T - T_c$. Thus, although $S_s < S_N$. There is no discontinuity in S and hence, no latent heat for transition at $T = T_c$).

In contrast, for $T < T_c$, the transition to normal state induced by a field involves a finite entropy change and correspondingly, a latent heat (i.e. a change of state). This is consequently a first-order transition.

1.13.2 Heat Capacity of Superconductors

The specific heat, C_{v} in a normal conductor at low temperatures consists of two contributions

$$C_{\mathrm{v}} = \gamma T + \alpha T^3, \tag{1.36}$$

where α and γ are constants.

For an insulator $\gamma = 0$, a pure T^3 behaviour. For metals, $\gamma \neq 0$; the linear term is a contribution from conduction electrons. The T^3 term (in both the cases) is due to lattice vibrations.

In usual superconductors, the transition has practically no effect on the lattice. From the theory of normal metals, it is known that at low temperatures $C_l^{\mathrm{n}} \sim T^3$. The same dependence characterises C_l^{s} in the superconducting state. Whereas, the electronic contribution changes drastically and is given by an exponential decay (of $C_{\mathrm{el}}^{\mathrm{s}}$) as $T \to 0$. This behaviour is explained as follows:

Because of the energy gap, the number of quasi-particles (excited across the gap) varies roughly by a Boltzmann factor $\exp\left(-\Delta/k_{\mathrm{B}}T\right)$.

At finite temperature, the quasi-particles behave just like ordinary electrons and are given by

$$n = \left[\exp\left(\frac{\in}{T}\right) + 1\right]^{-1}, \tag{1.37}$$

$$\text{where } \in = \sqrt{\in'^2 + \Delta^2(T)} \tag{1.38}$$

$$\text{and } \Delta(T)\big|_{T \to T_{\mathrm{c}}} = a' T_{\mathrm{c}} \left(1 - \frac{T}{T_{\mathrm{c}}}\right)^{\frac{1}{2}}. \tag{1.39}$$

$\in'$ is the normal metal electron energy given by

$$\in' = \left(\frac{p^2}{2m^*} - E_{\mathrm{F}}\right) \tag{1.40}$$

and in weak coupling approximation $a' = 3.06$ (BCS limit).

Because of the appearance of $\Delta(T)$ term in $\in$, the number of excitations n of a given energy is less than the corresponding number of electrons in a normal metal (at $T < T_{\mathrm{c}}$). (It is to be noted here that for $T \geq T_{\mathrm{c}}$, $\Delta = 0$, the excitations vanish and the function given by (1.37) becomes the usual expression for electrons in a normal metal). Thus, superconductor is described by a two fluid model, which has normal electrons and a "superconducting" component.

For $T \ll T_{\mathrm{c}}$, the heat capacity is given by

$$\frac{C_{\mathrm{el}}^{\mathrm{s}}(T)}{C_{\mathrm{el}}^{\mathrm{n}}(T_{\mathrm{c}})} = \left[\frac{3\sqrt{2}}{\pi^{3/2}} \frac{\Delta(0)}{T_{\mathrm{c}}}\right] \left(\frac{\Delta(0)}{T}\right)^{3/2} \mathrm{e}^{-\frac{\Delta(0)}{T}}. \tag{1.41}$$

Therefore, presence of energy gap leads to electronic heat capacity behaving radically different from normal metal result ($C_{\mathrm{el}}^{\mathrm{n}} \sim T$).

In weak coupling (i.e. BCS) case

$$\frac{\Delta(0)}{T_{\mathrm{c}}} = 1.76. \tag{1.42}$$

At $T = T_{\mathrm{c}}$, there is a jump in the heat capacity. When the temperature is reduced, the specific heat jumps to a higher value at $T = T_{\mathrm{c}}$ and then falls much more rapidly as $\mathrm{e}^{-\Delta(0)/T}$ for $T < T_{\mathrm{c}}$.

$$\frac{C_{\mathrm{el}}^{\mathrm{s}}}{\alpha T_{\mathrm{c}}} = a \exp\left(-\frac{bT_{\mathrm{c}}}{T}\right), \tag{1.43}$$

where αT_{c} is the "low temperature" electronic specific heat of normal state, a and b are constants, independent of temperature ($a \approx 9$, $b \approx 1.5$). The size of the discontinuity in specific heat at $T = T_{\mathrm{c}}$ is 2.5 in units of αT_{c}.

1.13.3 Strong Coupling Case

In BCS theory

$$2\Delta = 3.52\, T_{\mathrm{c}}, \tag{1.44}$$

$$\frac{C_{\mathrm{s}} - C_{\mathrm{n}}}{C_{\mathrm{n}}} = 1.43. \tag{1.45}$$

These formulae are of a universal character.

The universality is due to the fact that the BCS theory was developed in the weak coupling approximation, i.e. electron–phonon interaction was assumed to be weak (and coupling constant $\lambda < 1$). However, there were some pronounced deviations from this universality, e.g. for Pb–Bi alloy, $2\Delta = 5T_{\mathrm{c}}$. The experimentally observed deviations are caused by the fact that electron–phonon coupling is not weak. Thus, the effect of strong coupling must be taken into account. The foundation of the theory of strong coupling is formed by an equation derived by Eliasberg in 1960. This equation contains a very important term

$$g(\Omega) = \alpha^2(\Omega)\; F(\Omega),$$

where $F(\Omega)$ equals density of states of lattice vibrations and $\alpha^2(\Omega)$ describes interaction between electrons and the lattice. Thus, it describes both the state of the phonon system and the electron–phonon interaction.

Geilikman and Kresin in 1966 obtained the following formula for the energy gap

$$\frac{2\Delta(0)}{T_\mathrm{c}} = 3.52\left[1+\alpha\left(\frac{T_\mathrm{c}}{\bar{\Omega}}\right)^2 \ell n\left(\frac{\bar{\Omega}}{T_\mathrm{c}}\right)\right], \tag{1.46}$$

where $\alpha = 5.3$ and $\bar{\Omega}$ is the characteristic frequency of lattice vibrations. The second term in brackets is the correction due to strong coupling. The temperature dependence of energy gap changes from

$$\begin{aligned} \frac{\Delta(T)}{T_\mathrm{c}} &= a\left[1-\left(\frac{T}{T_\mathrm{c}}\right)\right]^{\frac{1}{2}}, \quad (a_\mathrm{BCS} = 3.06), \\ \frac{\Delta(T)}{T_\mathrm{c}} &= 3.06\left[1+8.8\frac{T_\mathrm{c}}{\bar{\Omega}^2}^2 \ell n\left(\frac{\bar{\Omega}}{T_\mathrm{c}}\right)\right]. \end{aligned} \tag{1.47}$$

(Note: factor 2 is inclusive in $\Delta(T)$).

1.14 London Equations and Penetration Depth

The two basic electrodynamics properties, viz. perfect conductivity and perfect diamagnetism, were well described in 1935 by F. London and H. London, who proposed two equations (known as London equations) to govern the microscopic electric and magnetic fields.

It was shown by London brothers that the magnetic flux lines are not completely expelled from a superconductor rather they remain confined in a thin surface layer called the *penetration depth*. They postulated a two fluid model for electrons with super-fluid and normal densities n_s and n_n (and velocities v_s and v_n, respectively). If n_o denotes number of electrons per unit volume, then

$$n_0 = n_\mathrm{s} + n_\mathrm{s}. \tag{1.48}$$

The equation of motion for super fluid electrons is

$$m\frac{\mathrm{d}\vec{v}_\mathrm{s}}{\mathrm{d}t} = -e\vec{E}. \tag{1.49}$$

The current density of the super fluid electrons is

$$\vec{J}_\mathrm{s} = -en_\mathrm{s}v_\mathrm{s}. \tag{1.50}$$

Equation (1.49) and (1.50) yield

$$\frac{\mathrm{d}\vec{j}_{\mathrm{s}}}{\mathrm{d}t} = \frac{n_{\mathrm{s}}e^2}{m}\vec{E}\,. \tag{1.51}$$

This is called the *first London equation*. Taking curl of this equation,

$$\nabla \times \frac{\mathrm{d}\vec{j}_{\mathrm{s}}}{\mathrm{d}t} = \left(\frac{n_{\mathrm{s}}e^2}{m}\right) \operatorname{curl} \vec{E}$$

$$\text{or} \quad \nabla \times \frac{\mathrm{d}\vec{j}_{\mathrm{s}}}{\mathrm{d}t} = -\frac{n_{\mathrm{s}}e^2}{m}\left(\frac{\partial B}{\partial t}\right)$$

using Maxwell's equation.

Integrating the above expression with respect to time and choosing the constant of integration to be zero (for consistency with Meissner effect), we have

$$\nabla \times \vec{j}_{\mathrm{s}} = -\left(\frac{n_{\mathrm{s}}e^2}{m}\right)\vec{B}\,. \tag{1.52}$$

This is called the *second London equation*. We may derive the Meissner effect from the second London equation by using Maxwell's equation

$$\nabla \times \vec{B} = \mu_0 \vec{j}_{\mathrm{s}}. \tag{1.53}$$

Taking the curl of this equation

$$\nabla(\nabla \cdot \vec{B}) - \nabla^2 \vec{B} = \mu_0 \nabla \times \vec{j}_{\mathrm{s}}. \tag{1.54}$$

Since $\nabla \cdot \vec{B} = 0$, therefore

$$\nabla^2 \vec{B} = \frac{1}{\lambda^2}\vec{B} \quad \text{(using (1.52))}\,, \tag{1.55}$$

$$\text{where } \lambda = \left(\frac{m}{\mu_0 n_{\mathrm{s}} e^2}\right)^{\frac{1}{2}} \text{ is called London penetration depth.} \tag{1.56}$$

The solution of the (1.55) for $\vec{B} = \vec{B}(x)$ is of the form

$$\vec{B}(x) = B_0 \mathrm{e}^{-\frac{x}{\lambda}} \quad \text{(see Fig. 1.17)} \tag{1.57}$$

Thus, $\vec{B}$ does not penetrate very deeply into a superconductor, rather penetrates only a distance λ within the surface (it implies the *Meissner effect*)

From (1.51) and (1.52) we have two equations

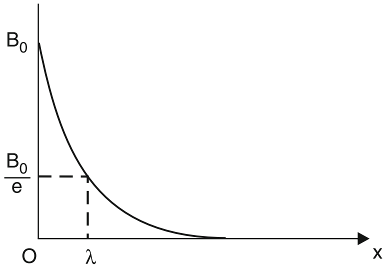

Fig. 1.17 Decay of the magnetic field penetrating in a superconducting half space (existing for $x \geq 0$)

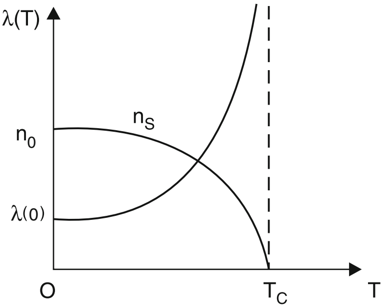

Fig. 1.18 Variation of penetration depth and n_s with temperature

$$\vec{E} = \frac{\partial}{\partial t}(\wedge\, \vec{j_s}) \tag{1.58}$$

$$\text{and} \quad \vec{B} = -\text{curl}\,(\wedge\, \vec{j_s}), \tag{1.59}$$

which govern the microscopic electric and magnetic fields, where

$$\wedge \equiv \left(\frac{m}{n_s e^2}\right) \tag{1.60}$$

is a phenomenological parameter. The number density of electrons depends on temperature and varies from zero at T_c to a limiting value of the order n_0, the density of conduction electron at $T \to 0°\text{K}$ (Fig. 1.18).

The penetration depth λ also depends on temperature as

$$\lambda(T) = \lambda(0)\left[1 - \left(\frac{T}{T_c}\right)^4\right]^{-\frac{1}{2}}. \tag{1.61}$$

The density of super electrons n_s also varies with temperature as

$$n_s = n_0\left[1 - \left(\frac{T}{T_c}\right)^4\right], \tag{1.62}$$

where $n_0 = n(0)$

$$(\equiv n(T)\ _{T=0\mathrm{K}}|).$$

1.15 Ginzberg–Landau Theory

There are basically two theoretical approaches to describe various superconducting phenomena (1) a phenomenological theory effective through the London equations and (2) the microscopic (BCS) theory.

However, the comprehensive theoretical picture remain incomplete without considering the impact and consequences of yet another theory known as the Ginzberg–Landau (GL) theory proposed 7 years prior to the BCS theory.

According to Landau, an ordered thermodynamic phase is characterised by a non-zero order parameter, accordingly Ginzberg and Landau introduced a complex pseudo-wave function ψ as an order parameter within Landau's general theory of second-order phase transitions. This ψ vanishes at $T \geq T_c$. The GL theory has accorded a semi-phenomenological status. Near the critical temperature $|T - T_c| \leq T_c$, the theory is very much simplified and the behaviour is described by GL equations.

According to London, the wave function of the superconducting electrons is rigid, i.e. it does not change when a magnetic field is applied. In GL theory, the absolute rigidity is modified and parameter ψ is defined, such that

$$|\psi|^2 = n_s, \tag{1.63}$$

the density of super-electrons.

More physically, ψ can be thought of as the wave function of the center of mass motion of the Cooper pairs (In fact, it was shown by Gorkov in 1959, that the GL theory was a limiting form of the microscopic theory of BCS, valid near T_c in which ψ is directly proportional to the gap-parameter Δ).

Since the phenomenon of superconductivity is a second-order phase transition, there is a critical temperature T_c and a positive parameter n_s, which is zero when $T > T_c$ and is finite when $T < T_c$.

The Gibbs free energy F can be expanded as

$$F\,(T, V, n_s) = F\,(T, V, 0) + \alpha n_s + (1/2)\beta n_s^2. \tag{1.64}$$

The equilibrium condition $\partial F/\partial n_s = 0$ gives

$$\alpha + \beta n_s = 0 \quad \text{or} \quad n_s = -\frac{\alpha}{\beta}, \tag{1.65}$$

Since F is to be minimum, therefore

$$\frac{\partial^2 F}{\partial n_s^2} > 0.$$

So β is positive (from (1.64)) and α should be negative (from (1.65)). To obtain a phase transition of second kind, we assume

$$\begin{aligned} &\alpha(T_c) = 0; \ \ \beta(T_c) > 0, \\ &\alpha(T) = (T - T_c)\left(\frac{\partial \alpha}{\partial T}\right)_{T=T_c}. \end{aligned} \tag{1.66}$$

(for $T < T_c$, $\alpha(T) < 0$ and $\beta(T) > 0$).

Substituting for n_s from (1.65) into (1.64), we have

$$F_s = F_n - \frac{\alpha^2}{2\beta}. \tag{1.67}$$

$$\text{But } (F_s - F_n) = -\frac{H_c^2}{8\pi}.$$

so, we have

$$\frac{\alpha^2}{2\beta} = \frac{H_c^2}{8\pi}. \tag{1.68}$$

Here, n_s is always constant and the magnetic field enters as a term $\frac{H_c^2}{8\pi}$ in the free energy of the superconducting phase.

Since ψ is a kind of effective wave function, in presence of an external magnetic field H, the free energy will not only increase by $\frac{H^2}{8\pi}$ per unit volume, but also by an extra term connected by the gradient of ψ (because ψ is not rigid in the presence of the magnetic field). To preserve the gauge invariance, GL assumed the extra term to be

$$\frac{1}{2m}\left|-\mathrm{i}\hbar\nabla\psi + \frac{e^*}{c}\vec{A}(\vec{r})\psi\right|^2,$$

where $\vec{A}(\vec{r})$ is the vector potential of the applied field H, and e^* the effective charge. Thus,

$$F_s = F_n + \int\left\{\alpha\,|\psi|^2 + \frac{1}{2}\beta\,|\psi|^4 + \frac{H_c^2}{8\pi} + \frac{1}{2m}\left|\mathrm{i}\hbar\nabla\psi - \frac{e*}{c}\vec{A}(\vec{r})\psi\right|^2\right\}\mathrm{d}v. \tag{1.69}$$

This expression is gauge-invariant under the simultaneous transformation

$$\begin{aligned}&\psi' = \psi \exp\left(\frac{\mathrm{i}e^*}{\hbar c}\right)\phi. \qquad (1.70)\\&\vec{A}' = \vec{A} + \nabla\phi,\\&\left[\text{In fact } e^* = 2e\right].\end{aligned}$$

We now minimise the expression with respect to ψ^* and $\vec{A}$. Variation with respect to ψ^* gives

$$\delta F = \int \left\{\alpha\psi + \beta\left|\psi\right|^2\psi + \frac{1}{2m}\left[\left(-\mathrm{i}\hbar\nabla\psi - \frac{e^*\psi}{c}\right)\left(\mathrm{i}\hbar\nabla - \frac{e^*}{c}\vec{A}\right)\right]\right\}\delta\psi^*\mathrm{d}v. \tag{1.71}$$

Integrating the last term by parts gives

$$\frac{1}{2m}\left(\int \delta\psi^*(-\mathrm{i}\hbar\nabla - \frac{e^*}{c}\vec{A})^2\psi\mathrm{d}v + \iint \widehat{n}\cdot(-\mathrm{i}\hbar\nabla - \frac{e^*}{c}\vec{A})\psi\delta\psi^*\mathrm{d}a\right). \tag{1.72}$$

The surface integral vanishes because $\delta\psi^*$ is arbitrary and, therefore, the boundary condition is

$$\widehat{n}\cdot\left(-\mathrm{i}\hbar\nabla - \frac{e^*}{c}\vec{A}\right) = 0. \tag{1.73}$$

Hence, we get from (1.71)

$$\frac{1}{2m}\left(-\mathrm{i}\hbar\nabla - \frac{e^*}{C}\vec{A}\right)^2\psi + \alpha\psi + \beta\left|\psi\right|^2\psi = 0. \tag{1.74}$$

Note that this is analogous to the Schrödinger equation for a free particle, but with a nonlinear term. This equation describes the equilibrium spatial variation of ψ. Variation with respect to $\vec{A}$ yields,

$$\nabla\times\nabla\times\vec{A} = -\nabla^2 A = \frac{4\pi}{c}\vec{J} \tag{1.75}$$

(using the gauge $\nabla\cdot\vec{A} = 0$), where

$$\vec{J} = -\frac{\mathrm{i}e^*\hbar}{2m}(\psi^*\nabla\psi - \psi\nabla\psi^*) - \frac{e^{*2}}{mc}\left|\psi\right|^2\vec{A} \tag{1.76}$$

is the same as the usual quantum mechanical current expression for particles of charge e^* and mass m.

So the fundamental equations of the GL theory are

$$\frac{1}{2m}\left[-\mathrm{i}\hbar\nabla-\frac{e^*}{c}\vec{A}\right]^2\psi+\alpha\psi+\beta\left|\psi\right|^2\psi=0 \tag{1.77}$$

and

$$\vec{J}=\frac{e^*\hbar}{2\mathrm{i}m}(\psi^*\nabla\psi-\psi\nabla\psi^*)-\frac{e^{*2}}{mc}\left|\psi\right|^2\vec{A}\,. \tag{1.78}$$

With this formalism, Ginzberg and Landau were able to treat two features, which were beyond the scope of the London theory, namely

(1) Nonlinear effects of fields strong enough to change n_s (or $|\psi|^2$) and
(2) The spatial variation of n_s

This will be discussed in the subsequent section, while considering the variation of $|\psi|^2$ in type-I and type-II superconductors. Thus, GL theory embodies in a simple way the macroscopic quantum mechanical nature of the superconducting state.

1.16 Type-I and Type-II Superconductors

Both coherence length and penetration depth diverge in the same way near $T=T_\mathrm{c}$. So, a constant k is defined

$$\text{as } k=\frac{\lambda}{\xi}, \tag{1.79}$$

which will remain finite as $T\to T_\mathrm{c}$.

This is known as *Ginzberg–Landau parameter* and can be considered as a characteristic of a material. The magnitude of k defines two kinds of superconductors. For $k\ll 1$ (i.e. $\lambda\ll\xi$), we have type-I superconductors and superconductors having $k\gg 1$ (i.e. $\lambda\gg\xi$) are type II superconductors. Figure 1.19a, b depicts spatial dependence of the order parameter $\psi(x)$ and the magnetic field $H(x)$ at the superconductor-normal interface, for respectively type-I and type-II superconductors.

Consider a plane boundary between the superconducting (S) and normal (N) regions in the same material. At the boundary, the magnetic flux density must rise from zero in the superconductor to H_c in the normal region, over a distance $\sim$ penetration depth λ (as required by the condition for thermodynamic equilibrium). Likewise, the superconducting wave function ψ, and hence the density of paired electrons must fall to zero over a distance $\sim\xi$ (the coherence length). Thus, the formation of a S–N boundary involves an increase in energy (or loss of condensation energy $\approx\xi_0\left(\frac{\mu_0H_\mathrm{c}^2}{2}\right)$ per unit area and a reduction in the magnetic energy $\approx\lambda_0\left(\frac{\mu_0H_\mathrm{c}^2}{2}\right)$ per unit area).

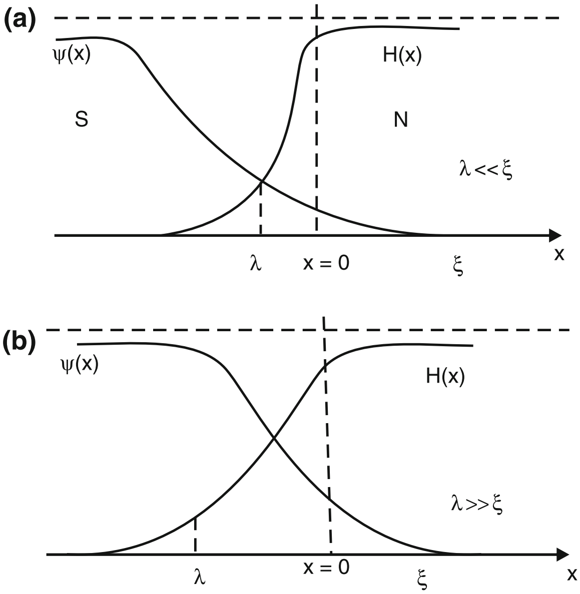

Fig. 1.19 **a** type-I and **b** type-II superconductors

The sign of the surface energy

$$\sigma_{\mathrm{s}} = (\xi - \lambda)\frac{\mu_0 H_{\mathrm{c}}^2}{2} \tag{1.80}$$

is then determined by the relative magnitudes of the coherence and perpetration lengths. Thus, a type-I superconductor has a positive surface energy and type-II superconductor has a negative surface energy in an applied magnetic field. Type-I superconductors show complete Meissner effect. The magnetisation versus applied magnetic field is shown in Fig. 1.20. The magnetisation drops suddenly at the critical field $H = H_{\mathrm{c}}$ (Fig. 1.21).

In type-II superconductor, magnetisation drops earlier, before reaching the critical field $H = H_{\mathrm{c}}$. There starts penetration of flux in the specimen at a field value H_{c1} (which is lower than H_{c}). The electrical properties in the superconducting state are also seen upto a field H_{c2} (which is greater than H_{c}). H_{c1} and H_{c2} are known as the lower and upper critical fields respectively.

The state between H_{c1} and H_{c2} is known as the mixed state or *vortex state* (because there is partial flux penetration and there are both superconducting and normal regions in the form of vortices). At $H \geq H_{\mathrm{c2}}$, the superconductivity is destroyed. The phase change at H_{c} represents a first-order transition. The transitions at H_{c1} and H_{c2} are of second-order.

$$\text{The free energy } F_{\mathrm{n}} > F_{\mathrm{s}}. \tag{1.81}$$

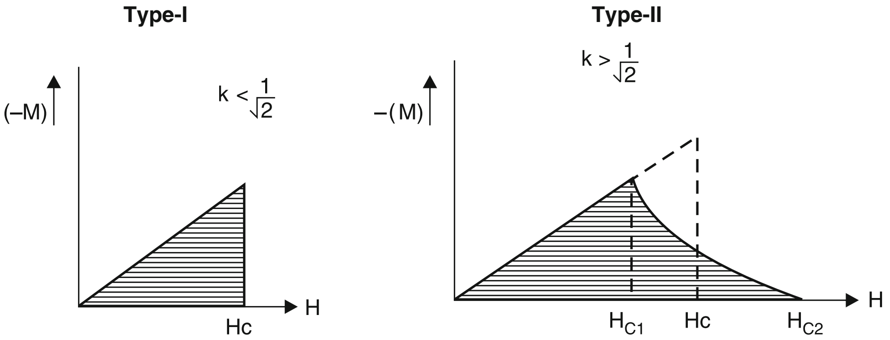

Fig. 1.20 Magnetisation versus applied magnetic field for type-I and type-II superconductors

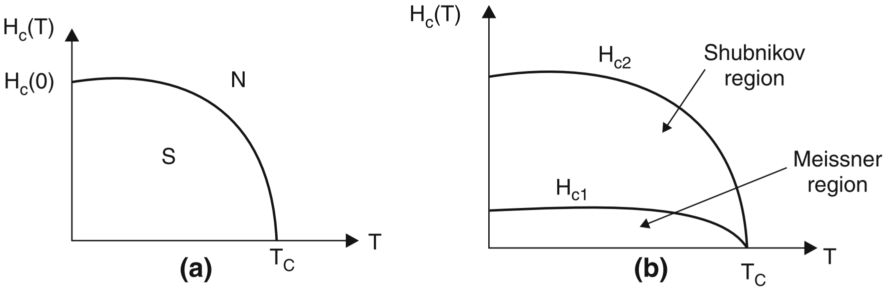

Fig. 1.21 Critical magnetic field as a function of temperature for **a** type-I and **b** type-II superconductors

The free energy cost per unit surface area ($F_\text{n} - F_\text{s}$) results from sacrificing the condensation energy in a layer of width ξ (the coherence length), i.e.

$$\Delta F_\text{cost} \text{ varies as } \left(\frac{H_\text{c}^2}{2\mu_0}\right)\xi, \tag{1.82}$$

where H_c is known as the thermodynamic critical field. The free energy of a superconductor increases in an applied field. The free energy-gain derives from allowing the field to invade a distance equal to the penetration depth λ, i.e.

$$\Delta F_\text{gain} \sim -\left(\frac{H_\text{app}^2}{2\mu_0}\right)\lambda. \tag{1.83}$$

Clearly ΔF_gain dominates for $\lambda > \xi$ as in a type-II superconductor. When H exceeds H_c1, the free energy is lowered by maximising the S/N interface area ($H > H_\text{c1} \Rightarrow B \neq 0$).

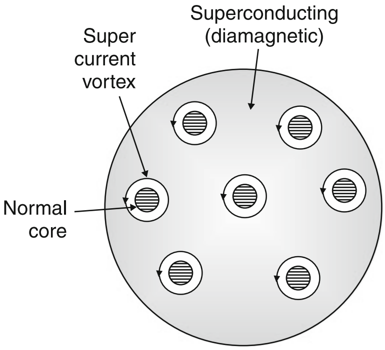

Fig. 1.22 The *triangular* lattice of vortices in the mixed state

Flux enters at $H > H_{c1}$ and according to Abrikosov, it does so in the form of flux vortices, which assume a triangular lattice structure to minimise their interaction energy. For $H_{c1} < H < H_{c2}$, we have this intermediate phase or Shubnikov phase.

At H_{c1}, the first vortex is nucleated and with increasing field, their equilibrium separation is reduced, such that at H_{c2} the normal cores overlap and then, bulk of the material turns normal (Fig. 1.22).

A vortex consists of a normal core (a cylinder of normal region parallel to the applied magnetic field) carrying a flux quantum $\phi_0 = 2.07 \times 10^{-15}$ Webers and diameter 2ξ. This microscopic normal region is surrounded by circulating super-electrons. At the centre of the core, the field is maximum and it drops to $1/e$ of its maximum value over a distance λ. A flux vortex is also known as a *fluxoid* (Fig. 1.23).

In the space between the vortices, the material remains superconducting; this is where the electric current flows, so the electrical resistance is still absent.

1.16.1 How a Normal Core is Formed in Mixed State?

With the application of the field $H > H_{c1}$, normal cores are nucleated, each carrying a quantum of flux ϕ_0. A core is surrounded by a circulating current (of super-electrons), whose super-fluid velocity is quantised to the value

$$v_{s0} = \frac{\hbar}{2m\xi}. \tag{1.84}$$

The super-electrons revolve around the vortex-axis like current in a superconducting ring. The closer the superelectron to the vortex-axis, the faster it circulates. At a shorter distance from the axis, the speed exceeds the critical value v_{s0} and superconductivity is destroyed (inside normal core).

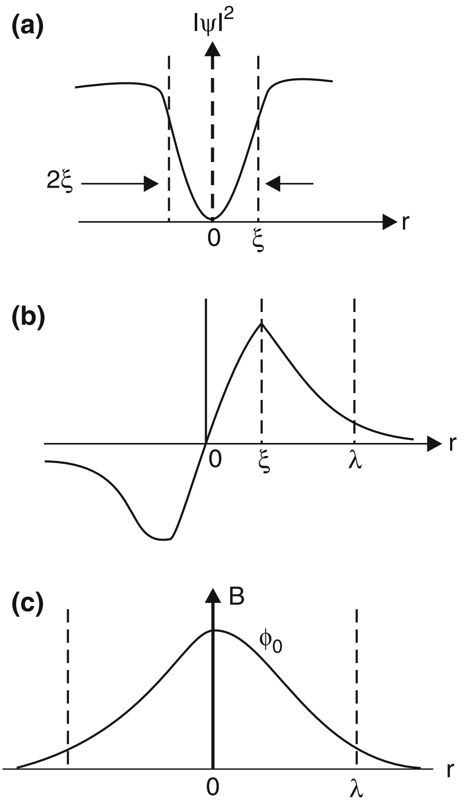

Fig. 1.23 Structure of a *vortex line* **a** order parameter **b** current density **c** local field

1.16.1.1 The Upper Critical Field

If the number density of vortex lines is n in a specimen, then spacing “a” between the neighbouring lines is given by

$$a = \left(\frac{n}{3}\right)^{\frac{1}{4}} \left(\frac{\phi_0}{B}\right)^{\frac{1}{2}}. \tag{1.85}$$

With increasing field, the density of flux lines approaches the value such that $Ba^2 \sim \phi_0$. Clearly, when “a” reaches the value ξ, the whole sample is comprised of touching normal cores, so that we may identify the upper critical field H_{c2} with this limit and

$$H_{c2} = \frac{\phi_0}{2\pi\xi^2}. \tag{1.86}$$

It is to be mentioned here that around the surface of a normal core, there are screening currents flowing in the surface in the opposite sense to the circulating persistent currents, as a result, the diamagnetism of the bulk is maintained.

From Fig. 1.23, it is seen that $|\psi|^2$ is reduced to a small value over a length ξ and the magnetic field of a flux line is spread over a region of size λ. Thus, there is a gain of energy by letting the magnetic field in over an area λ^2 and a loss of energy, because it is not superconducting effectively over an area ξ^2. Therefore, flux penetration is energetically favoured, if $\lambda > \xi$ (Type-II superconductor). However, if $\lambda < \xi$, fluxoids are not energetically favoured (for type-I superconductor). The lower critical field H_{c1} is defined as the value of the applied field at which it is energetically favourable to form an isolated fluxoid.

$$H_{c1} = \frac{H_c}{k\sqrt{2}} \quad \text{where } k \text{ is GL parameter.} \tag{1.87}$$

For the formation of an isolated fluxoid, the necessary condition is $\lambda > \xi$. A detailed treatment modifies this to

$$k > \frac{1}{\sqrt{2}}. \tag{1.88}$$

The value of k increases with normal state resistence ρ and in the dirty-limit (i.e. when $\ell << \xi_0$ where ℓ is mean free path)

$$k = k_0 + 2.4 \times 10^6 \rho \gamma^{\frac{1}{2}}, \tag{1.89}$$

where k_0 is the pure material value and γ is Sommerfeld constant. That is, many alloys and compounds have $\lambda > \xi$ and exhibit type-II superconductivity, but since both λ and ξ are affected by the electron mean free path (ℓ), type-I material (elements) can be made type-II by appropriate alloying (to reduce ℓ).

1.17 Why Materials with High T_c Tend to Fall in Type-II Category?

The reason qualitatively is as follows. The coherence length represents extension of the order parameter (the wave function of the super electrons). Using the position momentum uncertainty relation, we write

$$\xi = \frac{\hbar}{\Delta p}, \tag{1.90}$$

where Δp is the uncertainty in momentum. But a super-electron lies within an energy interval $k_B T_c$ from the Fermi surface and hence, the uncertainty of its energy is

$$\Delta E \cong k_B T_c. \tag{1.91}$$

Since $E = p^2/(2m)$, it follows that

$$\Delta E = p\frac{\Delta p}{m} \tag{1.92}$$

or $\Delta p \sim \Delta E = k_B T_c$ which, when substituted into (1.1) gives

$$\xi \propto \frac{1}{T_c}. \tag{1.93}$$

Therefore, the greater the T_c, the shorter the coherence length.

Transition metals and alloys usually fall in the type-II category. Their coherence length is shortened by the relatively large amount of scattering present.

Nearly 25 years ago, all known superconductors were having $T_c < 20\,\mathrm{K}$.

1.18 Why It is Extremely Difficult to Obtain Higher T_c?

From the microscopic (BCS) theory, the T_c is given by

$$k_B T_c = (\hbar\omega)e^{-1/\lambda_{\mathrm{eff}}}, \tag{1.94}$$

$$\text{or} \quad k_B T_c \cong (k_B\theta)e^{-1/\lambda_{\mathrm{eff}}}, \tag{1.95}$$

$k_B\theta$ denotes the energy-range near the Fermi level, in which conduction electrons attract to form Cooper pairs.

(1) If “attraction” is due to interaction with phonons, then $\theta = \theta_D$, the Debye temperature of the material.
(2) $k_B\theta_D$ is of the order of $\hbar\omega_D$, i.e. energy of highest frequency of phonons that can propagate in the substance.
(3) λ_{eff} characterises the attractive force within the framework of the BCS theory (i.e. in the weak coupling limit).

$$\lambda_{\mathrm{eff}} = N(0)V \ll 1, \tag{1.96}$$

where $N(0)$ is density of states in normal phase at the Fermi level, V is average matrix element of the interaction energy U between the electrons. λ_{eff} is a measure of the attractive force (Fig. 1.24).

The BCS model (the weak coupling case) gives

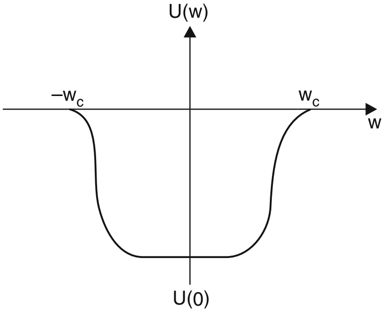

Fig. 1.24 Interaction energy between the electrons

$$\frac{2\Delta(0)}{k_B T_c} = 3.53 \tag{1.97}$$

$$\text{and} \quad \Delta C = 1.43\, T_c, \tag{1.98}$$

where ΔC is specific heat jump at T_c and γ is coefficient in the law

$$C_n = \gamma T$$

for electronic specific heat in normal state.

If the coupling is weak, then, within the phonon-mechanism

$$T_c \ll \theta_D. \tag{1.99}$$

Specifically for $\lambda_{eff} = 1/2$ and $\theta = \theta_D$, the T_c is $0.135\,\theta_D$, i.e.

$$T_c < 40\,\text{K} \quad \text{for} \quad \theta_D < 300\,\text{K}. \tag{1.100a}$$

With an increase in λ_{eff}, phonon frequencies become lower, θ_D falls

$$\therefore T_c \sim 20 - 40\,\text{K}. \tag{1.100b}$$

References

1. Steglich et al., Phys. Rev. Lett. **43**, 1892 (1979)
2. Jerome et al., J. Phys. Lett. **41L**, 195 (1980)
3. J.G. Bednorz, K.A. Muller, Z. Phys. **B64**, 189 (1986)
4. M.K. Wn, C.W. Chu, Phys. Rev. Lett. **58**, 908 (1987)
5. H. Maeda et al., Jpn. J. Appl. Phys. **27**, L209 (1988)
6. Z.Z. Sheng, A.M. Hermann, Nature **332**, 55 (1988)
7. Hebard et al., Nature **350**, 600 (1991)

Chapter 2
Crystal Structure of High Temperature Superconductors

2.1 Introduction

It has been shown by several groups of scientists including Hazen et al. [1] that the new high temperature superconductors (HTSCs) are structurally flawed members of a crystallographic family known as perovskites.

2.1.1 *Perovskite Structure*

Perovskites are ceramics (solid materials combining metallic elements with non-metals, usually oxygen) that have a particular atomic arrangement. In their ideal form, described by generalised formula ABX_3, they consist of cubes made up of three distinct chemical elements (A, B and X) that are present in a ratio 1:1:3. The A and B atoms are metallic cations (positive) and X atoms are non-metallic anions (negative). An A cation—the largest of the two kinds of metals—lies at the centre of each cube, the B cations occupy all the eight corners and the X anions lie at the mid-points of cube's twelve edges (Fig. 2.1).

2.2 The Structure of $YBa_2Cu_3O_{7-x}$

The compound $YBa_2Cu_3O_7$ is superconducting ($T_c = 90\,K$) and has orthorhombic symmetry and, the structure has two Cu–O sheets in the *ab* plane and Cu–O chains along the *b*-axis. The structure can be described as a perovskite with an oxygen deficit. In Fig. 2.1, B is the metallic cation Cu (small radius), surrounded by six oxygen ions occupying site X. The metallic cation site A is occupied by yttrium (large radius than B). By eliminating oxygen atoms from the ideal perovskite lattice, we obtain $YBa_2Cu_3O_7$ (Fig. 2.2a). Its unit cell contains.

A. K. Saxena, *High-Temperature Superconductors,* Springer Series
in Materials Science 125, DOI: 10.1007/978-3-642-28481-6_2,

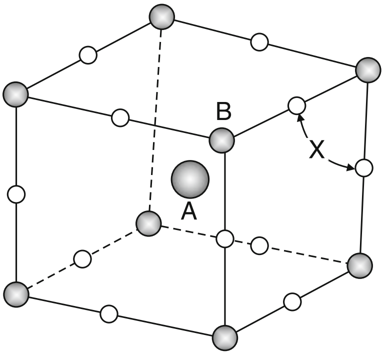

Fig. 2.1 The perovskite structure ABX_3

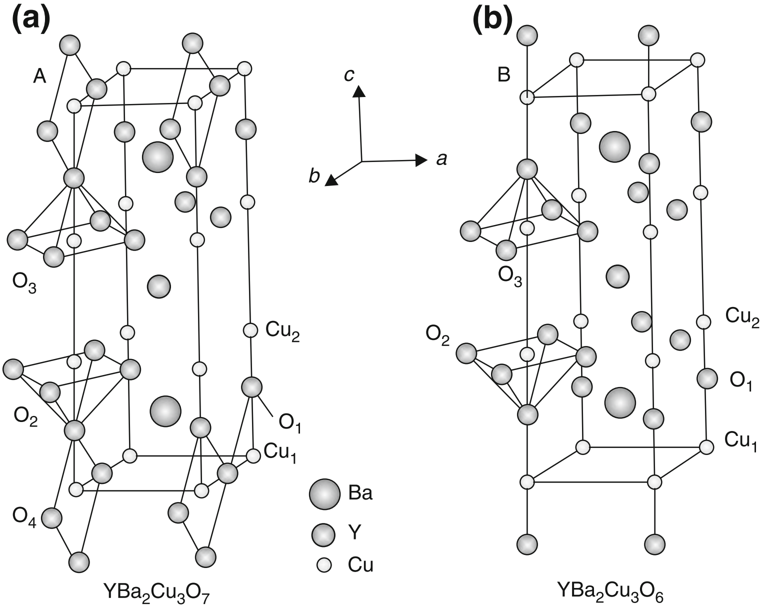

Fig. 2.2 The structure of YBCO (**a**) orthorhombic structure ($a_0 = 3.823$ Å, $b_0 = 3.885$ Å, $c_0 = 11.7$ Å) (**b**) tetragonal structure ($a_0 = b_0 = 3.86$ Å, $c_0 = 11.7$ Å)

- A layer of Cu−O having copper (Cu 1) surrounded by four oxygen ions
- A layer of BaO
- A layer of Cu−O, where (Cu 2) is surrounded by five oxygen ions forming a polyhedron
- A layer of yttrium, short of four oxygen

Thus, the stacking sequence of the (*ab*) planes is Y−CuO−BaO−CuO_2−BaO−CuO_2−Y (we will see in this Chap. 5-that the configuration of copper–oxygen planes

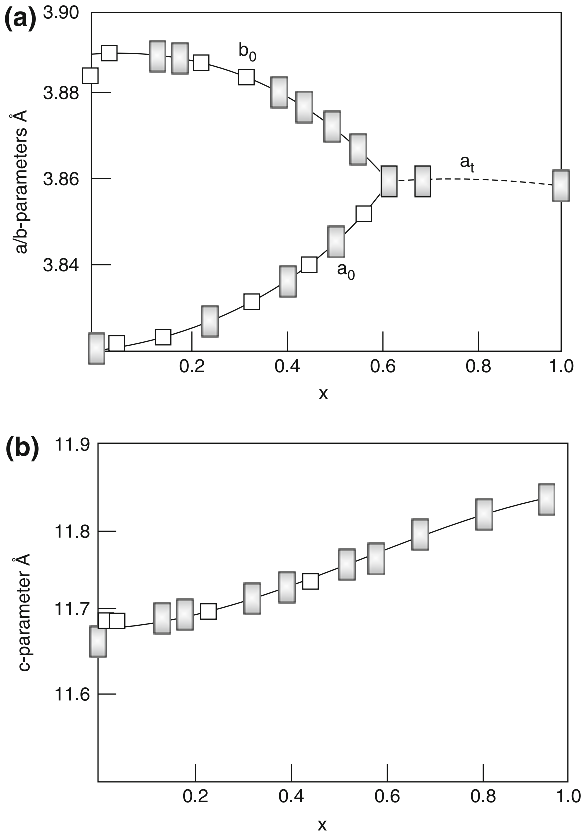

Fig. 2.3 Variation of the unit cell parameters of $Y_1Ba_2Cu_3O_{7-x}$ with the oxygen stoichiometry x. The oxygen deficiency leads to departure from orthorhombicity $\left(\frac{b-a}{b+a}\right)$

is $Cu-O_2$). It is to be noted that there are Cu–O chains along the *b*-axis. The presence of oxygen atoms in these chains are essential for superconductivity.

The general formula of the compound is $Y_1Ba_2Cu_3O_{7-x}$ where $0 \leq x \leq 1$. The lattice parameters vary with the oxygen content (x-value) and for $x \geq 0.6$, the structure is tetragonal. In $Y_1Ba_2Cu_3O_6$ ($x = 1$), there are no chain (O4 sites) oxygen and Cu in *b*-axis is in the 1^+ state. (Non-superconducting state). Thus, the unit cell parameters vary with the value of x in $Y_1Ba_2Cu_3O_{7-x}$ (i.e. a, b and c parameters vary with the oxygen-stoichiometry). This has been depicted in Fig. 2.3. The structure is orthorhombic for $x = 0$ (Fig. 2.4).

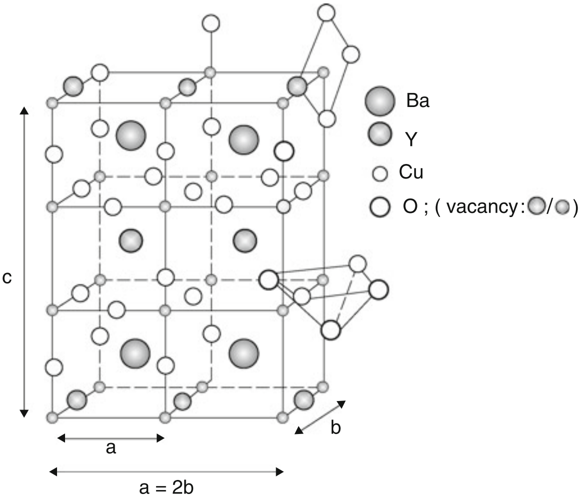

Fig. 2.4 Crystal structure with oxygen disappearing from alternate chains in $YBa_2Cu_3O_{6.5}$ and complete disappearance of oxygen from $YBa_2Cu_3O_{7-x}$ to give $YBa_2Cu_3O_6$. (It has been shown using neutron diffraction techniques and high resolution electron microscopy that the oxygen deficit is situated in the CuO_4 square plane layers and not in the CuO_5 pyramids.) Every $1/x$th chain oxygen is missing for $YBa_2Cu_3O_{7-x}$

2.2.1 *Variation of T_c with Oxygen Stoichiometry*

The critical temperature T_c of $Y_1Ba_2Cu_3O_{7-x}$ also varies with x-value and the material becomes non-superconducting at $x \cong 0.6$ (Fig. 2.5).

The T_c remains around 90 K from $x = 0$ to $x \approx 0.2$ (for $x = 0.25$, there are alternately "full" and half oxygen chains) and then shows a plateau at 60 K when $x = 0.3{-}0.4$. T_c is 45 K, when $x = 0.5$. Structural studies have revealed that oxygen vacancies may be ordered when $x = 0.5$ and 0.75 and no clear oxygen vacancy ordering has been found in the $x = 0.3{-}0.4$ range, (i.e. in the plateau region). For $x = 0.5$ (i.e. $YBa_2Cu_3O_{6.5}$), fully oxygenated Cu−O chains (as in $YBa_2Cu_3O_7$) are present along *b*-axis, alternating with fully vacant O_4 sites (as in $YBa_2Cu_3O_6$) (see Fig. 2.4).

Thus, for $x = 1.0$, there are no chain oxygen atoms and T_c is zero. The value of x in a particular sample depends on the processing conditions, especially temperature and oxygen partial pressure. Even though x itself is temperature and atmosphere dependent, under equilibrium conditions at high temperatures, the transition appears always to occur at $x = 6.5$.

Figure 2.6 shows the cell-parameters for the orthorhombic structure of Y−Ba−Cu−O. The double CuO_2 layers are a feature common to all the HTSCs and are believed to be the key to the occurrence of high temperature superconductivity in these oxides.

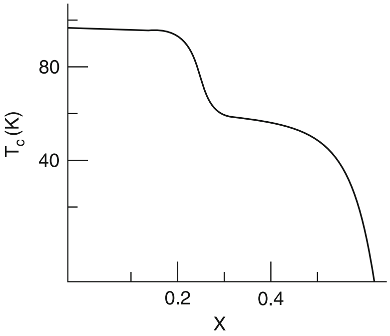

Fig. 2.5 Variation of the superconducting transition temperature T_c of $YBa_2Cu_3O_{7-x}$ with the oxygen stoichiometry x

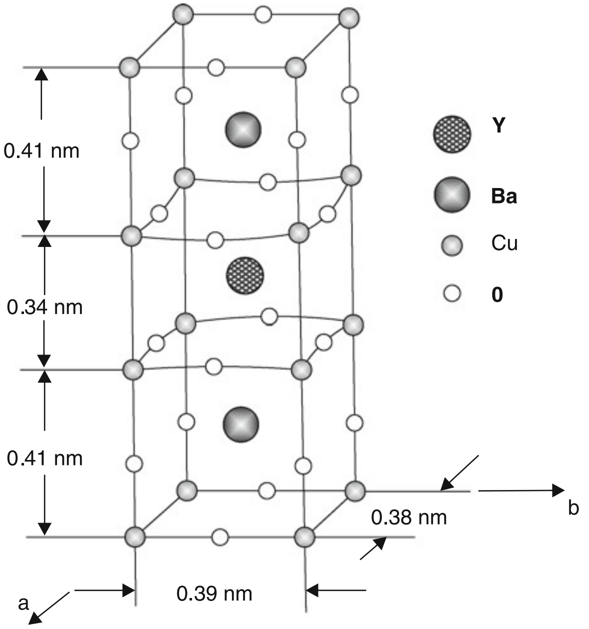

Fig. 2.6 The orthorhombic (distorted) crystal structure of YBCO superconductor

The anisotropic structure of these compounds is reflected in the anisotropy of the relevant intrinsic electronic properties of these materials, as shown in Table 2.1.

2.3 The Structure of $La_{2-x}M_xCuO_4$

Unlike YBCO (which have their structure derived from ideal perovskite by an ordered removal of oxygen atoms), La-, Bi-, or Tl-based cuprates have structures derived

Table 2.1 Relevant intrinsic properties of $YBa_2Cu_3O_{7-x}$

	Parallel to *c*-axis	Parallel to *ab*-plane
ξ(Å)	∼2–3	∼15–20
λ(Å)	1,500	7,500
J_C(Acm^{-2} at 77 K)	10^4	10^6
H_{c2}	150 T	30 T

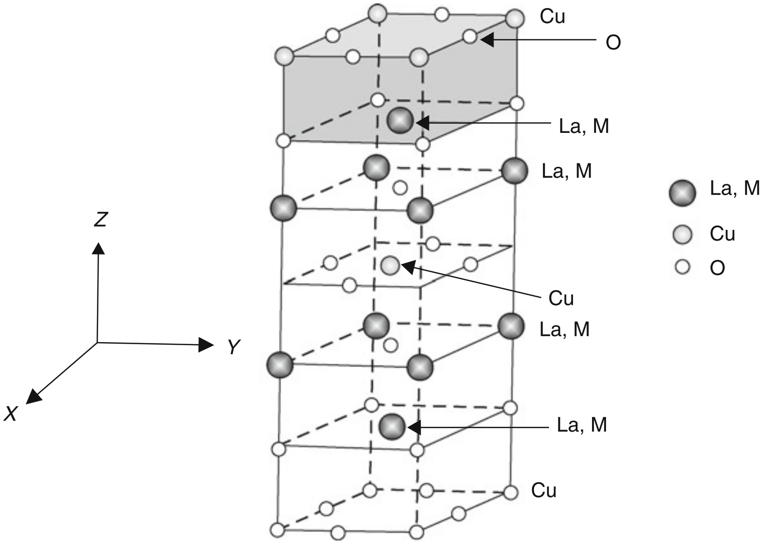

Fig. 2.7 The crystal structure of $La_{2-x}M_xCuO_4$ (M = Ba or Sr). For $x = 0$, $a = b = 3.77$ Å, $c = 13.25$ Å. M atoms occupy La site in La_2CuO_4

from ideal perovskite structure through an intergrowth phenomenon. Structure of $La_{2-x}M_xCuO_4$ is shown in Fig. 2.7.

M is the alkaline earth element (Sr or Ba). It can substituted on the La-site. $La_{1.85}Sr_{0.15}CuO_4$ has a tetragonal K_2NiF_4 type of layered perovskite structure. The structure can be viewed as a stacking of

$$-CuO_2-LaO-LaO-CuO_2-LaO-LaO-CuO_2-$$

$La_{2-x}M_xCuO_4$ shows the highest T_c around a critical value of x (0.15 for Sr and 0.2 for Ba with T_cs of 30 and 35 K respectively).

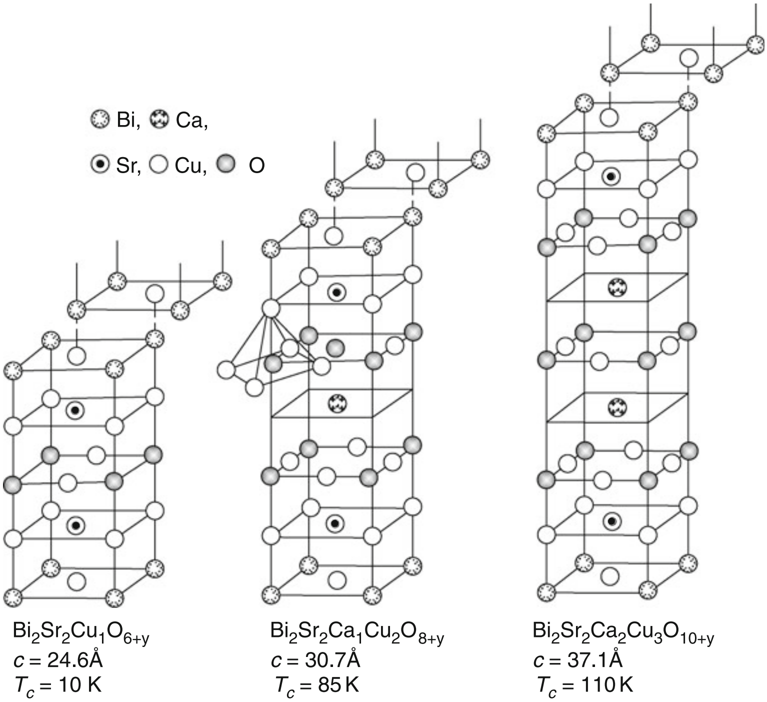

Fig. 2.8 The crystal structures of the Bi phases of general formula $Bi_2Sr_2Ca_{n-1}Cu_nO_y$ with $n = 1$, 2 and 3

2.4 The Structure of Bi-Based Cuprate Superconductors

The discovery of the high T_c superconductor $La_{2-x}(Ba/Sr)_xCuO_4$ with $T_c \sim 40$ K and $YBa_2Cu_3O_{7-x}$ with T_c of ~90 K led to an intensive search for new oxide superconductors of still higher T_cs (>100 K). No new superconductor with T_c higher than that of $YBa_2Cu_3O_{7-x}$ was reported upto January 1988. In May 1987, Michel et al. [2] reported the discovery of superconductivity between 7 and 22 K in rare-earth-less material Bi–Sr–Cu–O. Because of the intense interest in the 90 K material YBCO, at that time, their report did not attract widespread interest. However, attention quickly focused on the Bi-containing cuprate superconductors in January 1988, when addition of Ca to the Bi–Sr–Cu–O ternary led Maeda et al. [3] to the discovery of bulk superconductivity at 85 K and evidence of superconductivity upto 110 K in the Bi–Sr–Ca–Cu–O system. The compound with formula $Bi_4Sr_3Ca_3Cu_4O_{16}$ was found to be responsible for superconductivity at 85 K in the Bi-system and its structure was established [4, 5].

The crystal substructure can be viewed as a three dimensional packing of $Bi_2Sr_2Ca_1Cu_2O_8$ slabs along the c-axis, with the main feature being the presence of the two Bi–O layers separated by 3.0 Å and shifted, with respect to each other (crystallographic shear) along the diagonal direction of the perovskite sub-cell. Tarascan et al. [6] showed the evidence that the 100 K phase has the Bi-2:2:2:3 formula and its structure contains three CuO_2 layers: The three phases of Bi−Sr−Ca−Cu−O can be represented by the general formula $Bi_2\ Sr_2Ca_{n-1}Cu_nO_y$ ($n = 1$, 2 and 3) and have a pseudo-tetragonal structure (Fig. 2.8), which can be described as a stacking of a basic $Bi_2Sr_2CuO_6$ unit with either zero, one or two $CaCuO_2$ slabs inserted. The c-lattice parameter increases from 24.6 to 30.6 Å and finally to 37.1 Å in going from $n = 1$ to 2 and 3, and the increase results from the progressive addition of 2×1 and 2×2 (doubled because of the crystallographic shear) $CaCuO_2$, each about 3 Å thick, to the stacking sequence in the unit cell.

For $Bi_2Sr_2Ca_1Cu_2O_8$, the stacking sequence is

$$\mathrm{Bi-Sr-Cu-Ca-Cu-Sr-Bi.}$$

In $Bi_2Sr_2Ca_2Cu_3O_{10}$, the layer sequence is

$$\mathrm{Bi-Sr-Cu-Ca-Cu-Ca-Cu-Sr-Bi.}$$

The Bi-based high T_c superconductors ($Bi_2Sr_2Ca_{n-1}Cu_nO_y$ for $n = 2$ and 3) are superior to the YBCO in respect of higher T_c. This class of superconductors (unlike YBCO) are resistant to water or humid atmosphere and have the advantage of compositional/oxygen stability, e.g. some of its superconducting phases do not gain or lose oxygen, when the material is annealed at $\sim$850 °C. Another advantage of the BSCCO materials relates to the fact that BiO layers being Vander Waal bonded, this material can be easily rolled. This property has been utilised successfully for tape-casting and its texturing.

2.5 Structure of Thallium-Based Cuprate Superconductors

The discovery of 30 K superconductivity in the La–Ba–Cu–O system stimulated a worldwide search for even higher T_c superconductors. Elemental substitutions proved to be most effective in raising the transition temperature. Substitution of Sr for Ba produced 40 K superconductivity in the La–Ba–Cu–O system and substitutions of Y for La produced the high T_c ($\sim$90 K) superconductor Y–Ba–Cu–O, and it became clear immediately that substitutions of other rare-earths for Y would produce superconductors.

Two approaches for rare-earth substitution were taken. One approach was the choice of the rare-earth with small or no magnetic moment, such as Lu and Yb, as a small concentration of magnetic ions is known to depress significantly, or even to destroy superconductivity in conventional superconductors. Another approach was the choice of the rare-earths with ionic radius close to that of Y, such as Gd and Ho, inspite of their large magnetic moment. After all the rare-earths were substituted, it was concluded that

(1) Substitution of magnetic rare-earths for Y in $Y_1Ba_2Cu_3O_{7-x}$ did not influence significantly the transition temperature
(2) Ionic radius of rare-earths was important to superconductive behaviour of the (RE) $Ba_2Cu_3O_{7-x}$ compounds, e.g. substitution of La (the rare-earth with largest ionic radius) for Y produced superconductor with a relatively low transition temperature, usually below liquid nitrogen temperature, and the Lu-containing superconductor (Lu is the rare earth with smallest ionic radius) was difficult to be prepared in single phase, and
(3) The valence of the substituted rare earth was crucial to the superconductivity of (RE) $Ba_2Cu_3O_{7-x}$ compounds (Ce, Pr and Tb with both 3^+ and 4^+ valences did not form superconducting compounds)

The above mentioned facts strongly suggest that the valence and radius of rare-earth ions are more vital to the formation of rare-earth containing superconductors than the local magnetic effects.

Logically one would expect that other elements with 3^+ valence and similar ionic radius could also form similar superconducting compounds. Sheng and Hermann (University of Arkansas, Fayetteville) inspected the periodic table that the elements in Group IIIA were also characterised by a 3^+ valence and in particular Tl (thallium), the heaviest one in Gr IIIA, had an ionic radius (in 3^+ valence state) of 0.95 Å, similar to those of rare-earths (0.85–1.016 Å) and same as that of Eu^{3+}. These considerations motivated them to completely replace rare-earths in the (RE)–Ba–Cu–O system with thallium. Thus, the superconductivity in the Tl–Ba–Cu–O system was observed for the first time in October 1987 by Sheng and Hermann. Their samples contained no Ca, their nominal compositions were $Tl_2Ba_2Cu_3O_{8+x}$ and $TlBaCu_3O_{5.5+x}$. The sample consisted of many components and showed zero resistance above 80 K [7]. Soon after this, they added Ca to their samples and discovered superconductivity above 100 K in Tl–Ba–Ca–Cu–O system [8]. Their sample consisted of many chemical components. The superconducting phases were identified in Sheng and Hermann's sample by Hazen et al. [9]: $TlBa_2CaCu_2O_8$ and $Tl_2Ba_2Ca_2Cu_3O_{10}$. Then, Parkin et al. [10] changed the processing conditions to greatly increase the amount of $Tl_2Ba_2Ca_2Cu_3O_{10}$ phase and produced a material with bulk superconductivity at 125 K.

Ten perovskite-related oxides have been identified in Tl–Ba–Ca–Cu–O system. These are $Tl_1Ba_2Cu_1O_5$, $Tl_1Ba_2Ca_1Cu_2O_7$, $TlBa_2Ca_2Cu_3O_9$, $Tl_1Ba_2Ca_3Cu_4O_{11}$, $Tl_1Ba_2Ca_4Cu_5O_{13}$, $Tl_1Ba_2Ca_5Cu_6O_{15}$, $Tl_2Ba_2Cu_1O_6$, $Tl_2Ba_2CaCu_2O_8$, $Tl_2Ba_2Ca_2Cu_3O_{10}$ and $Tl_2Ba_2Ca_3Cu_4O_{12}$. For brevity, these phases are referred to as Tl:1201, Tl:1212, Tl:1223, Tl:1234, Tl:1245, Tl:1256, Tl:2201, Tl:2212, Tl:2223 and Tl:2234. The crystal structures of these phases, which form the homologous series are represented by general formula:

$$Tl_mBa_2Ca_{n-1}Cu_nO_{2(n+1)+m}$$
$$(m = 1, 2 \text{ and } n = 1-6)$$

as shown in Figs. 2.9 and 2.10.

All of these oxide have a tetragonal structure at room temperature. The oxides with Tl–O mono-layers have primitive tetragonal cells, whereas the oxides with Tl–O bilayers have body-centered tetragonal cells.

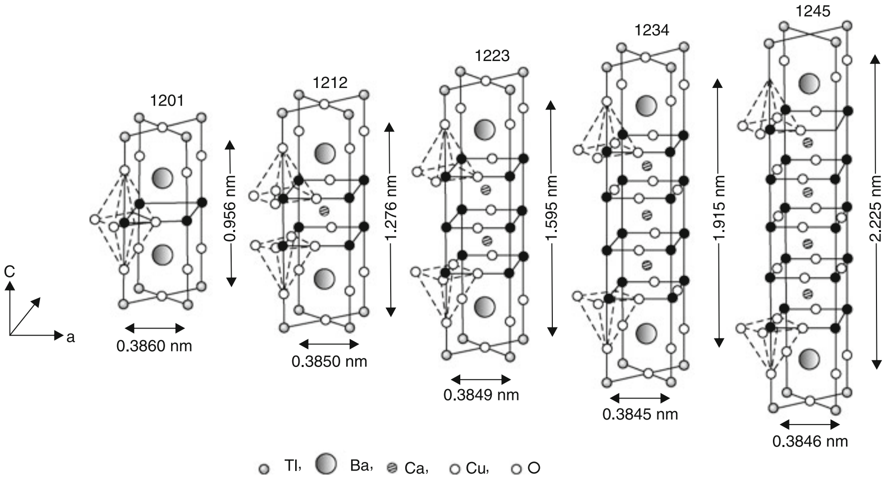

Fig. 2.9 Crystal structures of Tl monolayer superconducting oxides $TlBa_2Ca_{n-1}$ Cu_n O_{2n+3} ($n = 1-5$)

2.5.1 Comparison of Bismuth and Thallium Based Cuprates

Bismuth cuprates

(1) Are orthorhombic
(2) Show modulation in *ab* plane (with 4*b* periodicity)
(3) Possibility of intergrowth of members (of the series) at the unit cell level

Here, modulation is related to the oxygen content and structure of the Bi–O layers. There is never phasic purity because of (3).

In thallium cuprates, the phasic inhomogeneity is due to the co-occurrence (or intergrowth) of the different members of the series. Absence of twins is definitely established in these cuprates (Fig. 2.11).

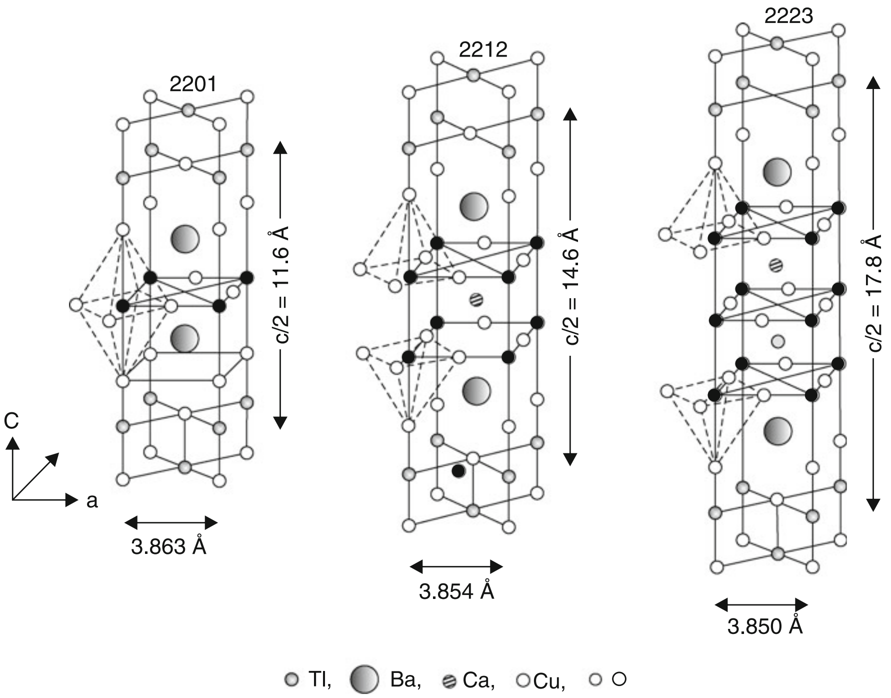

Fig. 2.10 Structure model of $Tl_2Ba_2Ca_{n-1}Cu_n$ O_{2n+4}($n = 1-3$)

2.6 Mercury Based Cuprate Superconductors

Mercury bearing compound $HgBa_2RCu_2O_{6+\delta}$ (Hg:1212), where R is a rare-earth element, was synthesised by Putilin et al. [11]. It has a structure similar to the thallium bearing superconductor $TlBa_2CaCu_2O_7$ (Tl-1212), which has one TlO layer and two CuO_2 layers per unit cell and $T_c \sim 85\,K$ [12]. But inspite of the resemblance to Tl:1212, Hg:1212 was found to be non-superconducting. In 1993, Putilin et al. [13] reported the synthesis of the compound $HgBa_2CuO_{4+\delta}$ (Hg:1201) with only one CuO_2 layer per unit cell. It was found to be superconducting below 94 K. Its structure is similar to that of Tl:1201 ($T_c \leq 10\,K$), but its T_c is considerably higher. The availability of such a material with high T_c and a single metal-oxide (HgO) layer may be important for technological applications, because a smaller spacing between CuO_2 planes leads to better superconducting properties in a magnetic field.

The structural arrangement of $HgBa_2CuO_{4+\delta}$ is similar to that of Tl Ba_2CuO_5, except for the oxygen stoichiometry of the HgO_δ and $TlO_{1-\delta}$ layers, respectively. For the former, δ is very small and for the latter, the $TlO_{1-\delta}$ layer is only slightly oxygen depleted. These different requirements for attaining the optimal concentration of holes (carriers) are due to the different preferred coordination geometries of the Tl^{3+} and Hg^{2+} cations. The rare-earth based Hg:1212 compounds were not found to be

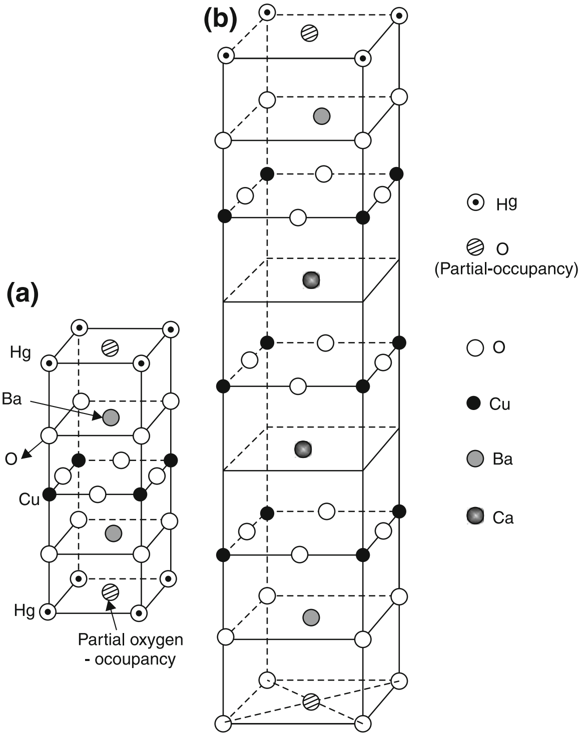

Fig. 2.11 Atom cluster model for central cell of (**a**) Hg-1201 and (**b**) Hg-1223 superconductors

superconducting because the hole concentration in these phases might not be high enough for inducing superconductivity. Putilin et al. [14] replaced the trivalent rare-earth cation by divalent Ca^{2+} and obtained a superconductive transition temperature of above 120 K in Hg $Ba_2CaCu_2O_{6+\delta}$.

In 1993, Schilling et al. [15] reported their discovery of superconductivity above 130 K in a material containing $HgBa_2Ca_2Cu_3O_{8+\delta}$ (with three CuO_2 layers per unit cell) and $HgBa_2CaCu_3O_{6+\delta}$ (with two CuO_2 layers per unit cell) and an ordered superstructure comprising a defined sequence of the unit cells of these phases. A maximum transition temperature of ~133 K had been obtained which was distinctly higher than the previously established value of 125–127 K observed in $Tl_2Ba_2Ca_2Cu_3O_{10}$.

In September 1993, a record T_c of ~150 K in $HgBa_2Ca_2Cu_3O_{8+\delta}$ at quasi-hydrostatic pressure of 150 K-bar was obtained by Chu (Texas Centre for Superconductivity, U.S.A.). Such pressure effect on T_c might also be duplicated by chemical means, i.e. “chemical pressure” imposed by other “element” substituted on Hg-site (published in Nature) (Previous record of $T_c \sim 135$ K in Hg:1223 was at ambient pressure). Table 2.2 gives lattice parameters of Hg-superconductors.

It has been found that electronic structure for $\delta = 0$ reveals that

1. Total density of states $N(E_F)$ per cell at E_F is 36 states Ryd^{-1} per cell. It is close to the value (40) for $Y_1Ba_2Cu_3O_{6+x}$. Also, it is much larger than 16 states Ryd^{-1} per cell for $La_{1.85}Sr_{0.15}CuO_4$ (Note: $N(E_F)$, is mainly from the Cu $3d_{x^2-y^2}$ and O_2p orbital in the CuO_2 layers.)
2. The two-dimensionality of the electronic structure of Hg:1223 is higher than that of $La_{1.85}Sr_{0.15}CuO_4$ (i.e. the carriers tend to move mainly in the CuO_2 layers).
3. The DOS curves of Ba and Ca are almost above the Fermi energy and, therefore, indicate that this stabilises the crystal structure and hence, Ba and Ca serve as electron-reservoirs.

It is to be noted that Hg:1201 is overdoped and only slightly excess oxygen (i.e. $\delta > 0$ and $\delta \ll 1$) introduces holes into the CuO_2 layers. In contrast to this, Cu atom oxidation state in Tl:1.201 is itself high (=+3).

2.7 Characteristics of High Temperature Superconductors

Some of the common characteristics of oxide high T_c cuprate superconductors are as follows:

(1) They have their structure derived from ideal perovskite structure (therefore, termed as defect perovskite structure), either through an intergrowth phenomenon or by an ordered removal of oxygen atoms.
(2) They have a layered crystal structure consisting of one or more CuO_2 layers. Each copper atom in a $Cu-O_2$ plane is strongly covalently bonded, in a nearly square-planar arrangement, with four oxygen atoms at a distance of 1.9 Å (the Cu–O bond length).
(3) Copper is present in the mixed valence state involving a partial oxidation of Cu^{2+} to Cu^{3+}.
(4) There is a charge transfer, to and from the CuO_2 layers, which is induced by doping near the metal-insulator phase boundary (in the phase-diagram) existing in all oxide high T_c superconductors.
(5) The sign of Hall coefficient is positive, indicating that the charge carriers are holes in all oxide HTSCs, except $Nd_{2-x}Ce_xCuO_4$, which is an electron superconductor. Hall coefficient for a magnetic field H parallel to the *ab* plane is much smaller than for H parallel to the *c*-axis.
(6) When rare-earth (RE) ions replace Y in $YBa_2Cu_3O_7$, T_c remains virtually unchanged and most of the transport properties are unaffected. However, the specific heat data of (RE) $Ba_2Cu_3O_7$ compounds, which are within 2 % of the $YBa_2Cu_3O_7$ for $T > T_c$ show drastic differences at low temperatures. This arises due to the magnetic interactions between the paramagnetic ions as well as between these ions and the crystal field. This establishes that superconductivity and magnetism can coexist in the RE compounds and the RE ions do not participate in superconductivity.

(7) The normal state transport properties are highly anisotropic. In YBCO, there is a linear dependence of the *ab* plane resistivity (ρ_{ab}). But the *c*-axis resistivity (ρ_c) shows a semiconducting dependence ($\propto 1/\mathrm{T}$) for less oxygenated samples and $\rho_c \propto T$ for well oxygenated samples. $\rho_c/\rho_{ab} \sim 30$ at room temperature. Similar anisotropic behaviour is observed for other HTSCs.

(8) All of them are type II superconductors. The lower critical field H_{c1} and the upper critical field H_{c2} are highly anisotropic.

$$H_{\mathrm{c2}}^{\prime\prime}(0) = 120\,\mathrm{T} \quad \text{and} \quad H_{c2}^{\perp}(0) = 510\,\mathrm{T} \quad \text{for} \quad \mathrm{YBa_2Cu_3O_7}.$$

(9) The two fundamental superconductivity parameters viz. the coherence length ξ and the penetration depth λ are also highly anisotropic. $\xi_{ab} = 20\text{–}30\,\text{Å}$ and $\xi_c = 2\text{–}3\,\text{Å}$ for $\mathrm{YBa_2Cu_3O_7}$, Further, the magnitude of coherence length is quite small as compared to that for conventional superconductors.

(10) There is near absence of isotope effect in high T_{c} superconductor.

(11) The value of $2\Delta(0)/(k_{\mathrm{B}}T_{\mathrm{c}})$ is smaller for tunnelling of pairs perpendicular to the *ab*-plane (i.e. it is in the range of 3.8–4), while its value parallel to the plane is 5.8–6.0.

(12) The low temperature specific heat of HTSCs in the superconducting phase is due to three contributions:

- $\mathrm{C} = \alpha\mathrm{T}^{-2} + \gamma\mathrm{T} + \beta\mathrm{T}^3$.
- The first term gives a Schottky-like anomaly and arises from magnetic impurities. The second is a linear contribution similar to that for free electrons in a metal. The third is Debye contribution from the lattice. The absence of the exponential dependence of the electronic specific heat (expected on the basis of the BCS theory) is a major departure from the properties of the conventional superconductors. The linear term is now believed to arise from the presence of impurities.

(13) The phononic mechanism of superconductivity (the BCS theory) has certain limitations in theoretically explaining the mechanism of superconductivity in the cuprate high T_{c} superconductors. Various other mechanisms have been proposed (e.g. Anderson's RVB model, Schrieffer's spin-bag model, bipolaron model, etc.) but still, no suitable mechanism is able to explain satisfactorily various normal-state and superconducting properties of these materials.

2.7.1 Resemblance Between HTSC and Conventional Superconductors

The following are the points of resemblances:

1. Superconducting state is made up of paired carriers
2. Presence of a true energy gap ($\Delta\,(k) \neq 0$ for all values of k)
3. Jump in specific heat at $T = T_{\mathrm{c}}$

4. The pair wave function has s-wave symmetry
5. Presence of a Fermi-surface

2.7.2 Unusual Properties of HTSCs

(1) Small coherence length ξ (this reduces the pinning energy implying weak pinning)
(2) Large penetration depth λ [this softens the flux line lattice (FLL)]
(3) Large energy gap (Δ)
(4) Large anisotropy (cf. $\xi_{ab} > \xi_c$) (this is due to layered structure)
(5) Small Fermi energy (E_F)
(6) High T_c (~90 to 130 K)
(7) Smaller carrier concentration (there are only ≤ 5 pairs per coherence volume as compared 10^4 pairs per coherence volume for BCS superconductor)
(8) High $H_{c2}\left(=\phi_0/2\pi\xi^2\right)$, which is anisotropic and much larger when applied parallel to the planes than when applied perpendicular to the planes ~1 M Gauss (for YBCO), which is 3–5 times the fields available presently
(9) Heat transport dominated by lattice

$$(k_{\text{el}} \ll k_{\text{lat}})$$

(10) The jump in heat capacity is not sharp
(11) (a) Sound velocity (elastic constants) is dramatically affected at T_c (unaffected for conventional superconductors)
    (b) Presence of low-lying optical phonon modes
(12) The ratio $\frac{\Delta(0)}{E_F}$, which indicates fraction of electrons paired, is much larger than in conventional superconductors.

It may be mentioned here that in HTSCs, the existence of pairs is reflected experimentally by

1. ac Josephson effect
2. Direct measurement of ϕ_0 (flux quantum) and
3. Little–Parks oscillations (Table 2.3).

2.8 Fermi Energy and Fermi Velocity of Superconductors

One of the most unusual fundamental properties of HTSCs is that one particle excitations are characterised by low values of Fermi-energy (E_F) and Fermi velocity v_F (see Table 2.4).

Table 2.4 shows effective mass m^*, Fermi wave vector k_F, Fermi velocity v_F and Fermi energy E_F for a conventional and high T_c superconductor.

Table 2.2 Lattice parameters of Hg based superconductors

Cuprate	T_c^a(K)	Lattice parameters
Hg-1201	94	$a(=b) = 3.85\,\text{Å}, c = 9.5\,\text{Å}$
Hg-1212	120	$a(=b) = 3.85\,\text{Å}, c = 12.6\,\text{Å}$
Hg-1223	133	$a(=b) = 3.85\,\text{Å}, c = 15.7\,\text{Å}$

[a] At ambient pressure

Table 2.3 The comparison of estimated parameters for Hg-1223 and Y-123

Parameters	Hg-1223	Y-123
T_c	133 K	90 K
H_{c1}(o) along c-axis	290 Oe	1×10^4 Oe
H_{c2}(o) along c-axis	190×10^4 Oe	120×10^4 Oe
$\lambda_{ab}(0)$	1,650 Å	1,300 Å
$\xi_{ab}(0)$	13 Å	10–15 Å
$\gamma(= \lambda_c/\lambda_{ab})$ (anisotropy parameter)	17	6
$2\Delta/k_B T_c$ (4.2 K)	4.2	6–8
$\Delta C_p/T_c^a$	27 mJ mole^{-1}K^{-2}	45–65 mJ mole^{-1}K^{-2}

[a] Size of discontinuity in electronic contribution to specific heat

Note The expected value for $\Delta C_p/T_c$ for 100 % single phases of Hg-1223 is 45 mJ mole^{-1}K^{-2}

Table 2.4 Some physical parameters of La-Sr-Cu-O

Quantity	Conventional metals	$La_{1.8}Sr_{0.2}CuO_4$
m^*	$(1-15)\, m_e$	$5\, m_e$
k_F(cm^{-1})	10^8	3.5×10^7
v_F(cm s^{-1})	$(1-2) \times 10^8$	8×10^6
E_F(eV)	(5–10)	0.1

The ratio $\Delta(0)/E_F \sim (10^{-4})$ for low T_c superconductors, where as it is $\sim(10^{-1})$ for high T_c materials.

The ratio $\Delta(0)/E_F$ is an important superconducting parameter. It shows what faction of the electronic states are directly involved in pairing. The small value in ordinary superconductors means that only a small number of states near the Fermi-surface are involved in pairing. However, large value of $\Delta(0)/E_F$ for cuprates corresponds to a significant faction of the carriers being paired up. Naturally, this implies a short coherence length.

Since in conventional superconductors $\frac{\Delta(0)}{E_F} \ll 1$, pairing can occur only near the Fermi surface (Cooper's theorem). Thus, the states on the Fermi surface form a two-dimensional system in momentum space. This is important because in 2D, any attraction will lead to the formation of a bound state (pairs). The possibility of having a large value of $\frac{\Delta(0)}{E_F}$ and a short ξ is directly related to the quasi-two-dimensional structure of the cuprates (layered structure). Quasi-two-dimensional carrier motion forms a favourable condition for pairing. Thus, this makes pairing possible, even for states that are distant from the Fermi surface. (The *Fermi surface* is a locus in momentum space, where the occupation of the electronic states drops abruptly and where the energy required to create particle-hole excitations vanishes.)

2.9 Comparison of High T_c Cuprates with Typical Metals in Relation to Normal State Resistivity

In the normal state (of HTSC cuprates), the in-plane resistivity ρ_{ab} increases with temperature (i.e. metallic behaviour) whereas ρ_c decreases with temperature. Thus, the system is metallic in *ab*-plane and non-metallic, perpendicular to it. (Extrapolated zero temperature value of ρ_{ab} is nearly zero in very clean samples). Resistivity in typical metals is due to

1. Scattering of electrons by lattice vibrations
2. Other electrons
3. Imperfections

None of these yields the observed temperature dependence for cuprate superconductors.

The linear temperature dependence in cuprates imply that inverse life-time (or decay rate) of a carrier is proportional to its excitation energy. Further, the normal state (i.e. above T_c), arising out of the motion of oxygen $2p$-holes in a background of magnetic copper d-holes (with which they mix), is poorly understood.

This family of materials cannot be considered as standard metals or as standard anti-ferromagnetic insulators.

The normal state properties of high T_c cuprates are anomalous, in the sense that they do not fit in with conventional Fermi-liquid[1] theory.

References

1. R.M. Hazen et al., Phys. Rev. **B35**, 7238 (1987)
2. C. Michel et al., Z. Phys. **B68**, 421 (1987)
3. H. Maeda et al., Jpn. J. Appl. Phys. **27**, L209 (1988)
4. J.M. Jarascan et al., Phys. Rev. **B37**, 9382 (1988)
5. S.A. Sunshine et al., Phys. Rev. **B38**, 893 (1988)
6. J.M. Tarascan et al., Phys. Rev. **B38**, 8885 (1988)
7. Z.Z. Sheng, A.M. Hermann, Nature **332**, 55 (1988)
8. Z.Z. Sheng, A.M. Hermann, Nature **332**, 138 (1988)
9. R.M. Hazen et al., Phys. Rev. Lett. **60**, 1657 (1988)

---

[1] *Fermi-liquid* characterizes the metallic state with non-interacting quasi-particles. The low-energy excitations (i.e. quasi-particles are in many ways analogous to electrons. Quasi-particles determine the properties at low temperature. The quasi particles are strongly modified (renormalized) by the many electron interactions and by interaction with phonons.

10. S.S.P. Parkin et al., Phys. Rev. Lett. **60**, 2539 (1988)
11. S.N. Putilin et al., Mater. Res. Bull. **26**, 1299 (1991)
12. S.S.P. Parkin et al., Phys. Rev. **B38**, 6531 (1988)
13. S.N. Putilin et al., Nature **362**, 226 (1993)
14. S.N. Putilin et al., Physica **C212**, 266 (1993)
15. A. Schlling et al., Nature **363**, 56 (1993)

Chapter 3
Critical Current

3.1 Introduction

By critical current, J_c is meant the maximum lossless current, a superconductor can sustain before the voltage develops.

In general, there can be two contributions to the current flowing on the surface of superconductor. Consider, for example, a superconducting wire along which we are passing a current from some external source. We call this, the transport current (because it transports charge into and out of the wire). If the wire is in an applied magnetic field, screening currents circulate so as to cancel the flux inside. These screening currents are superimposed on the transport current, and at any point, the current density is

$$\overrightarrow{J_t} = \overrightarrow{J_i} + \overrightarrow{J_H}, \tag{3.1}$$

where $\overrightarrow{J_t}$ is due to transport current and $\overrightarrow{J_H}$ arises form screening current.

The superconductivity breaks (i.e. a resistance appears), if the magni- tude of total current density $\overrightarrow{J_t}$, at any point, exceeds the critical current density J_c.

If the total current flowing is sufficiently large, the current density at the surface will reach the critical value J_c and the associated magnetic field strength at the surface will have a value H_c. Conversely, a magnetic field of strength H_c at the surface is always associated with a surface super-current density J_c. This leads to the hypothesis:

"A super-current loses its zero resistance at any point on the surface, when the total magnetic field strength, due to transport current and applied magnetic field, exceeds the critical field H_c."

Clearly the stronger the applied magnetic field, the smaller is the critical current. If there is no applied magnetic field, the only magnetic field will be that generated by any transport current. In that case, the critical current will be that which generates the critical magnetic field H_c at the surface. This special case (of above) is known as *Silsbee*'s *rule*. H_c is known as bulk or thermodynamic critical field.

A. K. Saxena, *High-Temperature Superconductors,* Springer Series
in Materials Science 125, DOI: 10.1007/978-3-642-28481-6_3,

3.2 Critical Current of a Wire

Consider a long superconducting wire of circular cross-section with radius $a \gg \lambda$, carrying a current I. This current produces a circumferential self-field (at the surface) of magnitude

$$H = \frac{2I}{ca}. \tag{3.2}$$

When this field reaches the critical field H_c, it will destroy the superconductivity, which is known as the *Silsbee-criterion*. Thus, the critical current will be

$$I_c = \frac{caH_c}{2}, \tag{3.3}$$

which scales with the perimeter, and not the cross-sectional area of the wire. This current flows in a surface layer of a constant thickness λ. Since the cross-sectional area of this surface layer will be $2\pi a\lambda$, the critical current density will be

$$J_c = \frac{I_c}{2\pi\lambda a} \tag{3.4}$$

$$= \frac{cH_c}{4\pi\lambda} \equiv J_d \quad \text{(The depairing current density.)} \tag{3.5}$$

(The *depairing current density* sets an upper limit to the J_c and is defined by the energy at which super-electrons are excited over the superconducting gap.)

The thermodynamic critical field (H_c) for pure element is small (of the order of a few hundred Oersteds). Niobium, Lead or tin are not useful for high field magnets, although zero field J_d is very large. For Pb–Bi alloy, it was found (during 1928) that a field of 25 kOe (2.5 Tesla) was necessary to quench superconductivity. But, a solenoid of this alloy proved disappointing as it did not conduct as expected from Silsbee's rule.

From (3.4), it is seen that the critical current J_c is inversely proportional to the radius of the sample and represents the current at which vortices first enter the sample. The critical current occurs, when the surface field is equal to H_c. This is called *Silsbee*'s *rule*.

Some typical figures for high performance conventional type II superconductors are given in Table 3.1.

The figures in Table 3.1 are to be borne in mind for use of high temperature superconductors in cryogenic technology.

Table 3.1 Critical current and upper critical field

Alloy	J_c	H_{c2}
NbTi	3×10^5 A cm^{-2} at 5 T	11 T (4.2 K) 15 T (0 K)
Nb_3Sn	10^6 A cm^{-2} at 5 T	28 T (0 K)
V_3Ga	2×10^6 A cm^{-2} at 5 T (highest J_c)	–
$PbGd_{0.2}Mo_6S_8$	–	54 T (42 K) 60 T (0 K) (highest)

3.3 Critical Current in Mixed State

The resistance-less current in a homogeneous type-II superconductor is limited to a value, which just produces field H_{c1} at its surface, as given by Silsbee's rule. Above H_{c1}, the sample contains magnetic vortex lines threading through bulk of the same in the form of a triangular lattice called flux line lattice (FLL).

Now, if we pass a current (called transport current) $\vec{J}$, which is perpendicular to the vortex-cores, a Lorentz driving force equal to $\frac{1}{c}\left(\vec{B} \times \vec{J}\right)$ acts on the vortices, tending them to move. If the vortex lines move in response to the Lorentz force, they will dissipate the energy in the flowing current, specifically the dissipation induces a voltage, and thus, resistance in a sample known as flux-flow resistance (Fig. 3.1).

In a homogeneous wire, there is no counteracting force preventing this. Clearly to carry a large current with resistance, the vortices must be pinned, so that their motion is inhibited there.

3.4 Flux Pinning

If the fluxoid lattice is regular and uniform, the field within the superconductor must also be uniform. From the relation curl $\vec{H} = \mu_0 \vec{J}$, it follows that there cannot be any macroscopic current in the system. Experiments on pure well annealed samples of type II superconductors show this to be true. Super-currents can only be made to flow on the surface and resulting critical currents are extremely small. To produce a technologically useful material, which is able to carry macroscopic currents throughout its volume, the distribution of fluxoids must be made non-uniform, so that a finite curl is possible. Then, due to mutually repulsive force between fluxoids, a concentration density gradient will give rise to a net force per unit volume called as driving force given by

$$\left|\vec{F}_L\right| = \frac{B}{\mu_0}\frac{dB}{dx}, \tag{3.6}$$

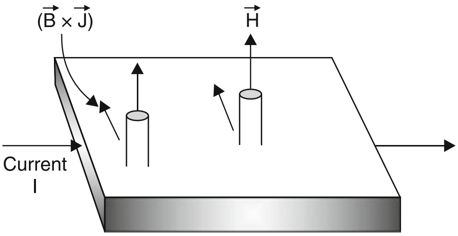

Fig. 3.1 Lorentz driving force acting in a current carrying superconductor in mixed state

where B is flux density and $\frac{dB}{dx}$, the gradient. In three dimensions, the relation is

$$\vec{F}_L = \frac{1}{\mu_0} \vec{B} \times \text{curl}\, \vec{B} = \vec{B} \times \vec{J} \,. \tag{3.7}$$

That is, the force is equivalent to the Lorentz force. To pin the FLL and maintain a current density, the crystal lattice must supply an equal and opposite pinning force per unit volume $\vec{F}_p$. Critical current corresponds to the point, at which the FLL starts to move and we define critical pinning force

$$\vec{F}_{pc} = \vec{B} \times \vec{J}_c \left(\text{Nm}^{-3}\right). \tag{3.8}$$

Then, flux-pinning is thought to be caused by forces between fluxoids and certain inhomogeneties in the crystal known as *pinning centres*, e.g. if normal core of a fluxoid resides on a small “normal” metal inclusion, its energy will be lowered because there is no longer any need to derive a previously superconducting region normal.

3.4.1 Role of Inhomogeneties

The pinning of FLL can occur through their interaction with various types of microstructural inhomogeneties, such as dislocation networks, different types of inter- and intra-grain boundaries, composition fluctuations, precipitates of a second phases, etc. They give rise to local variations in superconducting properties either through “core interaction” or the “magnetic interaction” with a flux vortex, characterised by normal core radius (ξ) and super-current circulation spread (λ) respectively (generally, magnetic pinning is more important in low k materials).

The interaction between an isolated defect and FLL results in elementary pinning force f_p, which when properly summed over all the pinning entities per unit volume, (taking into account the elastic properties of FLL) gives rise to the volume pinning force F_p. The critical current, then, is governed by force balance equation

$$\vec{F}_L = \vec{B} \times \vec{J} = -\vec{F}_p \,. \tag{3.9}$$

3.4.2 *Flux Pinning (Pinning of Flux-Vortices in Conventional Superconductors)*

Two materials, in particular, have been predominantly involved with high field and high current superconducting technology. These are the alloy $Nb_{40}Ti_{60}$ and the compound Nb_3Sn. In the Nb–Ti alloy, flux lines are pinned by tangles of dislocations, which form during drawing of the wire. In Nb_3Sn, the highest critical current is obtained in material with the smallest grain-size, indicating that grain boundaries are the cause of flux pinning. Their metallurgical properties are quite different: the alloy is strong and ductile and can be readily drawn down in large quantities to a diameter of $\approx$0.2mm, while in contrast, Nb_3Sn is brittle and weak and the fabrication of a conductor in a form suitable for winding into magnet-coils present a number of technical problems. The first superconducting magnets in the 1960s were found to have performances, which were not in accordance with measurements made on short samples of the same wire. A coil would revert to the normal resistive state at a quarter of its expected current value by a process known as quenching. It was recognised that some precautions were necessary to prevent a local quench (caused by a small region of the winding exceeding the critical current density), from propagating and causing a full-scale quench with the possible destruction of the magnet insulation through very large induced voltages. A simple solution to this problem was to clad the superconductor with a low-resistance normal conductor, such as copper. This forms a temporary alternative path for the current in the event of a local resistive region being formed in the superconductor. Composite conductors consisting of strands of superconductor embedded in a matrix of copper have been successfully used for the partial stabilisation of small magnets carrying up to 100 A, but for large magnets, additional cryostatic stabilisation is required. The ratio of copper to superconductor in the windings is greatly increased ($\sim$20:1), and helium is channelled through the winding, so as to be able to remove the heat generated by a local quench, without a catastrophic rise in temperature. The fully stabilised conductors have the disadvantage that J_c reduces to about $10^3\ \mathrm{A\,cm^{-2}}$ (Fig. 3.2).

3.5 Depinning of Flux Vortices

When driving force just exceeds the pinning force, depinning occurs and the current reaches the critical value. Depinning process can be accelerated by thermal activation.

At any finite temperature $T < T_c$, thermal activation added by Lorentz driving force can cause pinned flux lines to hop out of the free energy wells of depth U_0 (the pinning energy) and produce dissipation even when $F_L < F_p$ (Fig. 3.3). This phenomenon is known as *flux creep*. (This name is given because of analogous behaviour of dislocations in solids subjected to a load at elevated temperatures.)

A pinned vortex has to surmount energy barrier U_0, before it is free to move under Lorentz force. A moving vortex will generate heat until it is trapped at another pinning

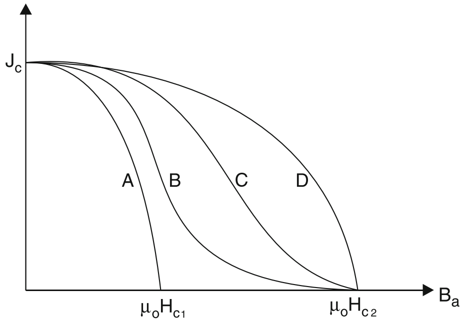

Fig. 3.2 Critical current versus applied field for samples of the same material with increasing amount of flux pinning (from A to D)

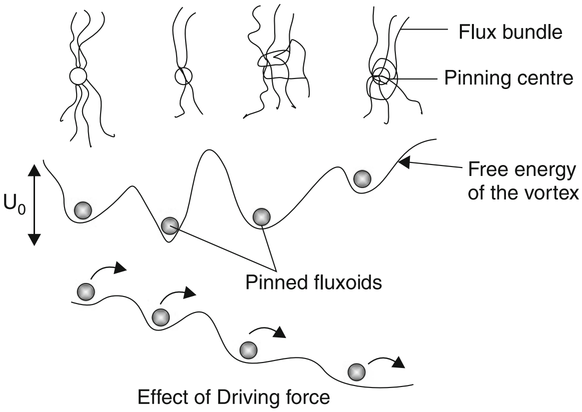

Fig. 3.3 Flux pinning (and depinning) [1, 2]

site. This heating in turn enhances the likelihood that nearby vortices can exceed the activation barrier and the pinning force itself is temperature dependent, leading to a highly nonlinearly coupled system with positive feedback. This thermally activated vortex motion is *flux creep*. As a result, at a relatively lower value of the driving force, depairing effect can become detectable and rate of depairing

$$R = R_0 \ \exp\left[-\frac{(U_0 - F_\mathrm{L} V_x)}{k_\mathrm{B} T}\right],$$

$$k_\mathrm{B} T \ell n \left(\frac{R_\mathrm{c}}{R_0}\right) = -(U_0 - F_\mathrm{L} V_x)_\mathrm{crit}. \tag{3.10}$$

$$(F_\mathrm{L})_\mathrm{crit} = \frac{1}{c}\left(\vec{B} \times \vec{J}\right). \tag{3.11}$$

$$(F_\mathrm{L})_\mathrm{crit} = \left[U_0 - k_\mathrm{B} T \ell n \left(\frac{R_0}{R_\mathrm{c}}\right)\right] \frac{1}{V_x}. \tag{3.12}$$

R_c is the maximum detectable rate. However, when T is small and U_0 is large, the factor $k_\mathrm{B} T\ \ln(R_0/R_\mathrm{c})$ is negligibly small and the creep effect is not very important. However, when U_0 is small and T is large, the flux creep can significantly reduce J_c.

3.6 Critical Current in High Temperature Superconductors

Two crucial virtues for the success of Nb–Ti and Nb_3Sn materials are that they develop strong flux pinning and are not granular. The tendency of granular superconductors to subdivide into regions of strong superconductivity separated by weak superconducting interfaces (weak-links) is bad for applications. The critical transport current density (J_ct) for transmitting current over useful lengths is then very much less than the local critical current density J_c in the strong superconducting regions with good flux pinning.

In addition to the granular structure, another phenomenon that controls the magnitude of critical current in HTSCs is the flux creep; it is important owing to the possibility of working at quite high temperatures.

3.6.1 Effect of Structure

The first studies on the critical current of sintered HTSCs have brought out some intriguing problems. It was found that

(1) Critical current density given by transport experiments is low and very much magnetic field dependent.
(2) That measured from magnetisation is larger up to a very high magnetic field ($\sim$20 T).
(3) The magnetisation is sample size independent, which is not predicted from Bean theory [3].

The paradoxical data are only consequences of the transport and magnetic measurements not being sensitive to the same contributions: so, the transport current depends chiefly on the current between the grains and, therefore, on the connection between them. It has been shown that in high T_c ceramics, the sintered grain boundary behaves as a weak-link, i.e. as a Josephson junction. So, high T_c superconductors exhibit the behaviour of a granular superconductor. However, the physics of HTSCs is quite different from that of a low T_c superconductor. In low T_c superconductor, grain size is smaller than ξ and λ. In HTSC, the grain sizes are large compared with λ and ξ and so, the high T_c ceramic superconductor has to be understood as a "composite". Clem [2], has proposed that a HTSC can be modelled by considering an array of

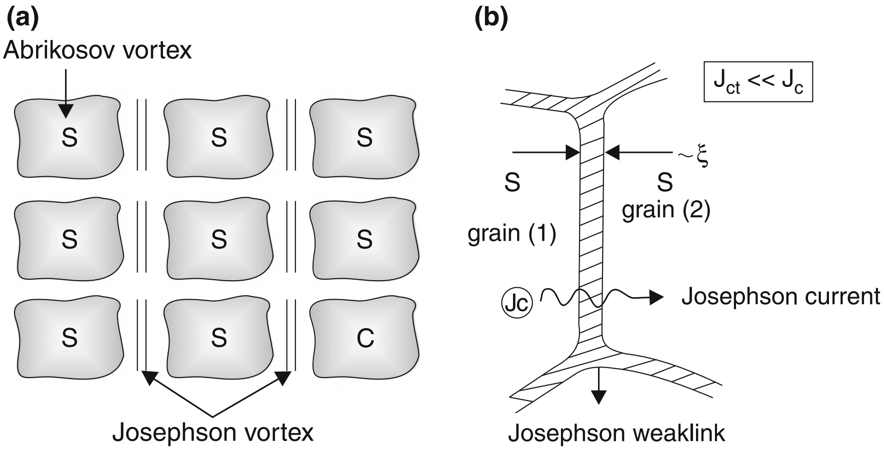

Fig. 3.4 Flux creep model of **a** HTSC, **b** a Josephson junction between two grains

Josephson junction (JJs) linking grains of type II superconductors. In HTSCs, very rapid flux creep has been reported [4], which is the manifestation of the presence of the Josephson junction array (weak-links), whose activation energy is ϕ_0. However, in the grain and in a single crystal, it has been shown that activation energy is lower than in low T_c superconductors and is magnetic field dependent. Thus, for the temperature range near T_c, the flux creep phenomenon is a major limiting influence on the critical current (Fig. 3.4).

3.7 RSJ Model of an HTSC (High T_c Superconductor)

Unlike conventional (i.e. low T_c) superconductors, grain boundaries play an important role in HTSCs. Due to small coherence length (ξ) and large gap (Δ), the order parameter (therefore, pair potential) is very sensitive to crystallographic defects, particularly grain boundaries.

An HTSC may be viewed to be consisting of strong superconducting grains weakly interconnected by grain-boundaries acting as resistively shunted Josephson junctions (Fig. 3.5).

At 0 ° K, the inter-grain coupling energy is

$$E_J = \frac{\hbar i(0)}{2e \cos \delta}, \tag{3.13}$$

where

$$\hbar = \frac{h}{2\pi} \quad \text{and} \quad i\,(0) = \frac{\pi \Delta(0)}{2eR_n}. \tag{3.14}$$

Fig. 3.5 RSJ model of HTSCs

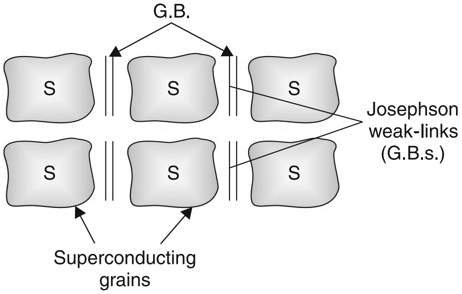

R_n is the normal state resistance of the grain boundary.

Equation (3.13) can be written as

$$E_J = \frac{h}{2\pi}\frac{1}{2e}\frac{\pi\Delta(0)}{2e\,R\,\cos\delta} = \frac{h\Delta}{8e^2}\frac{1}{R\,\cos\delta}$$

or Josephson coupling energy,

$$E_J = \frac{\Delta R_Q}{2R}, \tag{3.15}$$

where

$$R_Q \equiv \left(\frac{h}{2e^2}\right)\Big/\cos\delta \tag{3.16}$$

is the quantum pair resistance.

At a finite temperature (T), $i(0)$ changes to

$$i_c(T) = \frac{\pi\Delta(T)}{2eR_n}\tan h\left[\frac{\Delta(T)}{2kT}\right]. \tag{3.17}$$

Then

$$E_J(T) = \frac{h\Delta(T)}{8e^2R_n\cos\delta}\tan h\left(\frac{\Delta(T)}{2kT}\right). \tag{3.18}$$

Here, R_n should be small.

In fact, the behaviour of grain boundaries in HTSC is not well described by the Ambegaokar–Baratoff theory due to following three facts:

(1) $I_c\ R_n$ product is $\ll \Delta$ (the band gap)
(2) There is anomalous temperature dependence of $I_c\ R_n$ product:

$$I_cR_n \propto (T_c - T)^2$$

(3) I_c R_n product is not a constant, but scales with R:

$$I_c R_n \propto \left(\frac{1}{R}\right)$$

Further, I_c $R_n(\equiv V_c)$ is one- to two-orders of magnitude lower than expected from Ambegaokar–Baratoff relation

$$V_C = \left(\frac{\pi\sqrt{\Delta_1\Delta_2}}{2e}\right).$$

For granular superconductors, like BSCCO, inter-granular coupling is better modelled as an S–N–S type weak-link than as a tunnel junction, because the short coherence length allows a continuous depression of the superconducting order parameter near the interface connecting two bits of ideal materials. Thus, the Josephson coupling energy E_j and the critical current I_c are expected, in general, to be less than that implied for the same normal resistance by the ideal Ambegaokar–Baratoff relation (3.18) and (3.17). To get a feel for the numbers, if the inter-granular resistance adds $\sim 10^{-4}\ \Omega-$cm to the normal resistivity, and if the grain size "a" is $\sim 1\ \mu$m, it follows that the resistance of a typical inter-granular link is $\sim 1\ \Omega$. For ideal Ambegaokar–Baratoff junctions of YBCO, this would imply a link critical current (at $T = 0$) of $I_c(0) \sim 10^{-2}$A or $J_c(0) \sim 10^6$ A cm^{-2}. This value is comparable with J_c in crystals, but ceramic samples usually have J_c of only 10^3–10^4 A cm^{-2}, indicating a sizeable reduction below ideal values. Further, if there is a considerable variation in the strength of the Josephson coupling from grain to grain, the properties of the sample may be dominated by relatively few percolating paths of particularly strong junctions.

For HTSC, we can write

$$I_c R_n \propto \left(1 - \frac{T}{T_c}\right)^2 \frac{\pi\Delta(T)}{2e} \tanh\left[\frac{\Delta(T)}{2kT}\right] \exp\left(\frac{-2d_n}{\xi_n}\right)$$

where d_n is the thickness (intergrain separation) and for SNS like interface ($R_n \propto 1/d_n$). Further the grains and grain boundaries separating the grains behave like SNS interface if $2d_n < \xi$. In the dirty limit, for a grain boundary, we have

$$\xi_n = \left(\frac{h v_{FN} l_N}{12\pi^2 kT}\right)^{\frac{1}{2}}$$

However, if $2d_n$ exceeds ξ, there is a significant reduction in the $I_c R_n$ product.

3.8 Effect of Granularity on Superconductivity

Both nominally uniform and granular thin films tend to lose their zero resistance state at a normal state sheet resistance R_N, which is close to the quantum pair resistance.

$$R_\text{Q} = \frac{h}{(2e)^2}. \tag{3.19}$$

Uniform films undergo a sharp superconductor to insulator transition near R_Q. A truly insulating state is not seen in granular films, until $R_\text{N} \gg R_\text{Q}$.

In contrast to uniform films, the S–I transition in granular films is mediated by a competition between

(1) Grain charging and
(2) Josephson coupling

To put an electron on an isolated grain (of capacitance C), costs an electrostatic energy

$$E_\text{c} = \frac{e^2}{2\text{C}}, \tag{3.20}$$

which can become very large, if grains are small. This energy barrier is known as *Coulomb-blockade* and will be detrimental to Josephson (i.e. pair) tunnelling, if E_c is comparable to, or large than the Josephson coupling energy E_J.

Transport properties of the films are dominated by the nature of inter-grain coupling. In low resistance films, $R_\text{N} < R_\text{Q}$ and "global" superconductivity is established via inter-grain Josephson (i.e. pair) tunnelling. However, as R_N is increased above R_Q, Josephson coupling energy

$$E_\text{J} = \Delta\left(\frac{R_\text{Q}}{2R_\text{N}}\right) = \frac{\Delta h}{8e^2}\left(\frac{1}{R_\text{N}}\right) \tag{3.21}$$

becomes small when compared with the characteristic inter-grain dephasing energy E_c and, therefore, the global superconductivity is lost.

At high enough sheet resistance R_N, E_J is diminished to the point that what were formally Josephson junctions become more characteristic of S–I–S tunnel junction with the current being primarily carried via quasi-particle tunnelling. Since the quasi-particle tunnelling is attenuated at temperatures lower than T_c, the film would exhibit quasi-entrance and super-resistive behaviour at $T < T_\text{c}$ (Fig. 3.6).

Consider two nearby superconducting grains. Energy cost for a quasi-particle to tunnel from one grain to the other is $(2\Delta + E_\text{c})$, while a Cooper pair tunnelling cost is $4E_\text{c}$. Quasi-particle tunnelling will become favourable, if $4E_\text{c} > (2\Delta + E_\text{c})$ or if E_c is of the order of Δ.

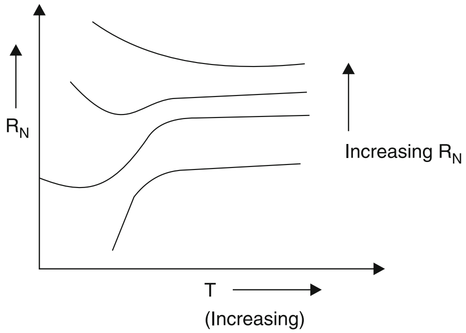

Fig. 3.6 Super-resistive behaviour

3.9 Measurement for J_c

High angle grain boundaries reduce the inter-granular transport. After an extensive investigation of various misorientations, the IBM group [5] concluded that all grain boundaries misoriented by greater than 5 ° are intrinsic weak-links and such junctions are extremely undesirable.

Critical current can be measured in two ways:

(1) Transport current density (J_{ct})

J_{ct} is limited by the weakened properties of the grain boundaries and not by the strong flux pinning properties of the grain interiors. A transport measurement, therefore, represents the lowest value of J_c that can be defined.

(2) Critical current from magnetisation measurements (J_{cm})

The measure of critical current relies on the fact that magnetic moment is equal to the circulating current enclosed into area.

In a granular medium, this can lead to difficulty, because the appropriate area is not the area of the whole sample. Therefore, J_c is sometimes insecurely defined.

3.10 Flux Flow and Defining J_c

For transport currents above a depinning threshold, the statistically averaged sum of the Lorentz forces on the vortex array exceeds the total pinning force, and therefore, the entire array moves laterally at a steady velocity. This is known as *flux flow*.

The motion of the vortex-lattice results in significantly higher energy dissipation and heat generation by inducing an electromotive force, which drives current through the normal core of the vortex. In a Bardeen–Stephen model, this leads to a velocity dependent force on the vortex.

$$\vec{f}_{\mathrm{v}} = -\eta \vec{v}, \tag{3.22}$$

where η is a viscosity coefficient and v is the vortex velocity. Thus, above the depinning current, there is a force balance given by

$$\eta\vec{v} = \vec{f}_{\mathrm{L}} - \vec{f}_{\mathrm{p}}. \tag{3.23}$$

The flux motion produces an electric field

$$E = \eta v\,\phi_0 = vB, \tag{3.24}$$

where B is the average magnetic induction.

Combining these results, a differential flux flow resistivity

$$\rho_{\mathrm{f}} = \frac{dE}{dJ_{\mathrm{T}}} = \frac{\phi_0 B}{\eta}, \tag{3.25}$$

can be defined which can be obtained from the linear portion of I–V characteristic in a field for currents above the depinning current.

For an operational threshold voltage criterion in a transport measurement, the onset of the linear portion of the I–V curve defines J_c.

In conventional materials, since $\rho_{\mathrm{creep}} \ll \rho_{\mathrm{f}}$, establishment of a working criterion for defining J_c is not a problem.

A second defining characteristic of flux flow is the scaling of the resistivity ρ_{f} with normal state resistivity ρ_{N} as

$$\frac{\rho_{\mathrm{f}}}{\rho_{\mathrm{N}}} = \frac{H}{H_{c2}(T)}. \tag{3.26}$$

Because of the high normal state resistivity of the HTSCs, it is clear that there will be substantial energy dissipation at fields H near H_{c2}.

3.11 Anisotropies in High T_c Superconductors

There are various anisotropies in HTSCs. This is shown in carrier concentration. Coherence length $\xi \propto \nu_{\mathrm{F}}$

where Fermi velocity

$$v_{\mathrm{F}} = \frac{\hbar}{n}(3\pi^2 n)^{\frac{1}{3}}, \tag{3.27}$$

$$\frac{\xi_{11}}{\xi_{\perp}} = \left[\frac{n(11)}{n(\perp)}\right]^{\frac{1}{3}}, \tag{3.28}$$

where ξ_{11} is coherence length parallel to *ab* plane. $\xi_{\perp}$ is perpendicular to *ab* plane.

Table 3.2 Comparison between parameters of conventional and high T_c super-conductor Y-Ba-Cu-O

	Nb_3 Ge	$PbMO_6S_8$	$Y_1Ba_2Cu_3O_7$
$\xi(0)$	3,500 Å	4,000 Å	10–30 Å
$\lambda(0)$	35 Å	25 Å	1,400 Å
$H_c(0)$	4 kOe	1.5 kOe	10 kOe
$H_{c2}(0)$	340 kOe	550 kOe	1,200 kOe
$J_d(0)$	8×10^7 A cm^{-2}	3×10^7 A cm^{-2}	6×10^8 A cm^{-2}
J_c(4 K, 0H)	7×10^6 A cm^{-2}	2×10^5 A cm^{-2}	2×10^7 A cm^{-2} (thin film) 2×10^6 cm^{-2} (77 K in thin film)
J_c(4 K, 5 T)	4×10^6 Acm^{-2}	10^4 A cm^{-2}	1.5×10^4 A cm^{-2} (sintered compact)

Experimentally,

$$\frac{\rho_\perp}{\rho_{11}} = \frac{n(11)}{n(\perp)} = 300. \tag{3.29}$$

Therefore,

$$\frac{\xi_{11}}{\xi_\perp} = (300)^{1/3} \approx 6.5, \tag{3.30}$$

$$\left.\begin{aligned} H_{c2}(11) &\propto \left(\frac{1}{\xi_\perp \xi_{11}}\right) \\ H_{c2}(\perp) &\propto \left(\frac{1}{\xi_{11}^2}\right) \end{aligned}\right\} \Rightarrow \frac{H_{c2}(11)}{H_{c2}(\perp)} \propto \frac{\xi_{11}}{\xi_\perp \xi_{11}} \quad \text{or} \quad \frac{H_{c2}(11)}{H_{c2}(\perp)} = \frac{\xi_{11}}{\xi_\perp} \approx 6.5. \tag{3.31}$$

The Table 3.2 gives the characteristic parameters of Y–Ba–Cu–O compared with some important conventional high field superconductors.

It is clear that a high upper critical field alone is not enough to make the material technologically attractive. Pb Mo_6S_8 did not succeed because of disappointing J_c.

Y–Ba–Cu–O has the highest depairing current density J_d (o). The zero-field J_c values (at 4 K) for thin films are about an order of magnitude close to $J_c(0)$. But the sintered compacts have J_c value 2–3 orders of magnitude lower. The highest zero field J_c (at 77 K) of the material sintered and heated above its melting temperature is 7.4×10^3 A cm^{-2} (which is again low) (The bulk single crystals are found to possess J_c values intermediate between thin films and polycrystalline sintered compacts).

Low $J_c(H)$ value suggests that bulk pinning in these materials is low and conventional defects like twin-boundaries, grain boundaries etc. (which although present in abundance) are not providing effective pinning (FLL is extremely stiff and difficult to pin).

Many findings suggest that in sintered compacts, the pinning at $T \ll T_c$ is provided by inter-grain connections serving as proximity type pinning centres. (The

Table 3.3 FL Lattice melting temperatures of some HTSCs

HTSC	T_c (K)	Lattice melting temperature (K)
YBCO	92	75
BSCCO	110	30
TBCCO	125	

proximity connections are in the dirty-limit.) The number of effective pinning proximity centres increases with decreasing temperature. At T close to T_c, current is essentially weak-link like. The exponential decrease of J_c with H reported for some bulk and thin film specimens is indicative of dominance of surface pinning and near absence of bulk pinning. In suitably oriented films containing field H_0, where J_0 is high and is much less sensitive to J_c, the effect is attributed to a larger coherence length ξ_{11} in *ab* plane along which the current flows and, therefore, inter-grain weak-links are not so effective. J_c is, therefore, no longer strongly sensitive to imposed field and high J_c values upto 1.5 T could either be due to strong surface pinning effect or favourably aligned defects like twin boundaries or grain boundaries providing more effective bulk pinning.

For low temperature superconductors, FLL melting temperature is well above the critical temperature. So FLL melting does not affect superconductivity. Table 3.3 gives FLL melting temperatures of some HTSCs.

It should be noted that flux pinning is a complex and imperfectly understood field of study. The details are extremely sensitive to the particular material and its defect population.

When the defects range from the visible (e.g. grain boundaries, twin boundaries, dislocations, voids and particles of second phase) to the invisible (e.g. cation disorder or oxygen vacancies), it is not surprising that there is a little agreement on what determines flux pinning.

It is to be noted here that Bi-and Tl-based materials are not likely to be useful at liquid N2 temperatures in applications that demand a magnetic field, unless in some way pinning is provided. Many of the projected applications involve magnetic fields, therefore, the Y:123 compounds (with even their lower T_c but higher lattice melting temperature) become the material of choice for many uses. Table 3.4 gives a comparison of parameters of Hg- and Y-based superconductors.

3.12 Flux Pinning in High Temperature Superconductors

Any spatial variation in H_{c2} or k (the GL parameter) will produce a binding energy δE between a fluxoid and the defect, which is given by

$$\delta E = \int \mu_0 H_c^2 \left(-\frac{\delta H_{c2}}{H_{c2}} |\psi|^2 + \frac{1}{2} \frac{\delta k}{k^2} |\psi|^4 \right) dv, \tag{3.32}$$

Table 3.4 Thermodynamic superconducting state parameters of Hg-based superconductors compared with that of YBCO

Quantity/phase	$HgBa_2Ca_{n-1}Cu_nO_{2(n+1)+\delta}$			YBa_2Cu_3
	Hg-1201	Hg-1212	Hg-1223	O_{7-x}
$T_c(K)$	96	127	135	92.2
$\lambda_{ab}(0)$(nm)	268	209	155	89
$\xi_{ab}(0)$Å	21.1	16.6	19.3	16.4
$k_{11c}(0)\ (=\lambda_{ab}(0)/\xi_{ab}(0))$	127	126	80	74
$(H_{c1})_{11c}$ (0) Oe	123	201	33.5	900
$(H_{c1})_{11c}$ (5 K) Oe	350	320	380	530
$(H_{c2})_{11c}$ (0) Tesla	72	113	88	122
$H_{c(0)} \approx \left[\frac{(H_{c1})_{11c}(0)(H_{c2})_{11c}(0)}{\ell n\ k_{11c}(0)}\right]^{1/2}$ Oe	4,300	6,900	8,200	16,000
$(H_{c2})_{11c}$ (80 K) Tesla	30	68	68	25

where H_c is the thermodynamic critical field that defines the superconducting condensation energy $U_0 = 1/2\mu_0 H_c^2$. v is the volume of the pinning reaction and ψ is the order parameter.

HTSCs exhibit flux creep much more strongly than older superconducting materials. The basic phenomenon underlying flux creep is the thermal activation of fluxons out of their pinning wells (U_0) at a rate proportional to exp $(-U_0/k_B T)$. The maximum well depth is obtained when fluxoid cores find normal regions, because, then the entire condensation energy $1/2\mu_0 H_c^2 v$ is saved. One may expect U_0 to be large, because of the higher critical fields than LTSCs, but coherence length is also much smaller. This implies that the interaction volume is low. Since T_c is high, and temperature enters exponentially in the Boltzmann factor for thermal activation of fluxons, therefore, even a small increase in U can enormously reduce the creep rate.

On one hand, if the defects are small (of the order of ξ), this will favour a high J_c. On the other hand, if the defects are $>\xi$, the superconductivity will be locally disrupted. One of the key goals is to engineer pinning centres that are extended in one- or two-dimensions so that their increased volume can make U bigger, however, without inducing granularity or decreasing the pin density too much. This implies that flux creep effects can be reduced through addition of appropriate defects, which should be small when compared to coherence length and not too abundant, otherwise, they will reduce T_c and also not too few, otherwise there may be significant motion of the vortices leading to lower J_c.

3.13 Columnar Defects and Flux Pinning

The laminar character of the high T_c cuprates dictates that they can pin the vortices only in the form of pancakes rather than as infinite cylinders perpendicular to the CuO_2 layers (Fig. 3.7).

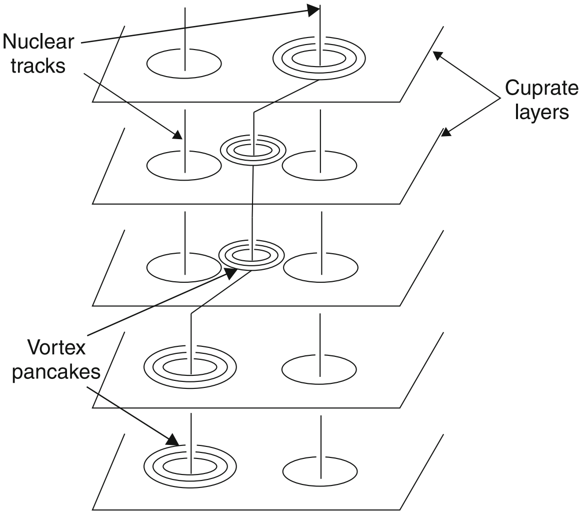

Fig. 3.7 Flux pinning in the form of pancakes

As a result, these materials define an *irreversibility line* that demarks the boundary between two regions in the mixed state zone of the B–T plane:

(a) In the region of low magnetic field B and low temperatures T (no flux flow), the electric current can flow without energy dissipation. In this region, T_c is non-zero and magnetisation is irreversible.
(b) At large B and T (the second region), the flux is staggering and any current will dissipate energy. In this region, the critical temperature vanishes and magnetisation behaviour is reversible.

The reversibility line is lower in BSCCO than in YBCO. This implies that BSCCO is more anisotropic and consequently planes are less coupled in BSCCO.

Figure 3.8b depicts magnetic moment as a function of temperature. After being cooled in zero field (ZFC), M vs. T is measured in a field $H > H_{c1}$ with increasing temperature. Then, $M = -1/(4\pi)$ (or less) is obtained at low temperature and $M(T)$ as indicated. If the sample is cooled in a field (FC), then different $M(T)$ is obtained.

Below T_c, there is a temperature T_{irr}, where $M(T)$ of the ZFC and FC results are the same. These measurements can be performed for different magnetic fields and $T_{irr}(H)$ determined. The line of $T_{irr}(H)$ in the H–T plane is called the irreversibility line. Above and to the right of this line, the sample has reversible magnetic behaviour. Below and to the left of this line, the sample has irreversible behaviour (Fig. 3.8a).

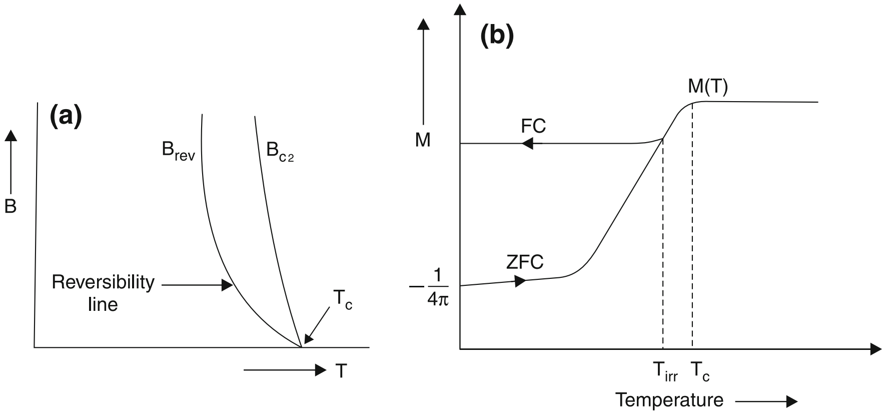

Fig. 3.8 **a** (B, T) diagram for a high T_c superconductor. **b** Magnetic moment versus temperature

3.13.1 Flux Pinning in HTSCs by Vortex Pancakes

The common feature of HTSCs is the presence of double/triple layers of CuO_2 planes, which are believed to be the superconducting planes. The coherence length along the planes is <2 nm. In case of YBCO, this leads to the weak-link problem, probably because T_c of this material decreases considerably with oxygen deficiency, which especially occurs at grain boundaries. The distance between the superconducting layers is relatively large and is responsible for the large, to very large anisotropy of the superconducting parameters. Consequently, the pinning in these materials is also very anisotropic, partially because

$$F_{\mathrm{p}} \propto B_{\mathrm{c2}}^{n}\,(T)\,b^{p}\,(1-b)^{q}$$

and

$$B_{\mathrm{c211}} \gg B_{\mathrm{c2}_{\perp}}, \quad (b = B/B_a)\,,$$

but also because of the very anisotropic nature of the vortex lattice itself.

When the decoupling between the layers is large (as in Bi- and Tl-compounds), the super-currents are confined to the layers and the vortices are segmented into vortex-pancakes with weak electromagnetic and Josephson coupling between them. This is demonstrated in Fig. 3.9, where two different representations are given for a flux-line in an applied field making an angle θ with the normal to the superconducting layers (c-axis).

In Fig. 3.9, the ellipses lying in the *ab* plane depict superconducting screening current. To the left, is the continuous flux line picture for very anisotropic superconductor, to the right, the segmented flux-line picture with pancake vortices valid for Josephson coupled superconducting layers. (Note that the magnetisation is directed along the c-axis.) The segmentation is indicated by current loops in the CuO_2 (i.e. *ab*)

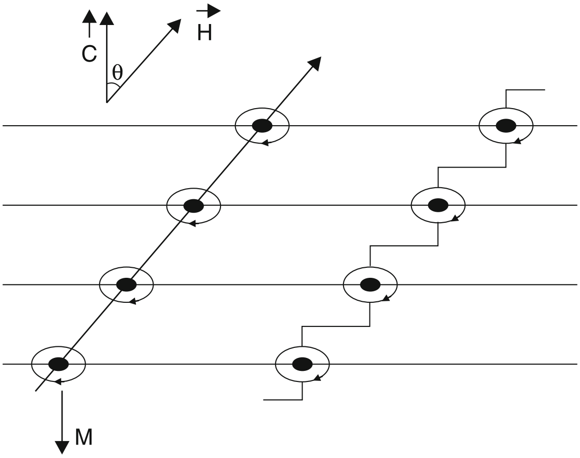

Fig. 3.9 Schematic view of two representations of flux lines intersecting CuO_2 double layers. (*Horizontal lines*) when the field $\vec{H}$ makes an angle θ with the *c*-axis

planes. The magnetic moment related with the screening current is oriented along the normal, which leads to a net torque on the sample when θ deviates from either $\theta = 0$ or $\theta = \pi/2$. This provides an accurate way to measure the anisotropy parameter. The zeros of the order parameter and the vortex cores are depicted by black dots. The representation at left shows the vortex in the anisotropic 3D picture, while the zigzag line at right represents the vortex in the quasi-2D case. (The latter applies below the cross-over temperature.) The vortex consists of 2D pancake vortices in the layers and Josephson vortices along the layers. Flux-line cutting in such a system leads to quasi-2D behaviour above a cross-over field B_{2D} defined by

$$B_{2D} = \frac{\varphi_0}{t_a s^2},$$

where t_a = anisotropy parameter and s = entropy density

For Bi = 2212, $B_{2D} \approx 0.3\,T$

and for Tl:2212, $B_{2D} \approx 10\,mT$

(according to $s \approx 1.5\,nm$ and $t_a = 3 \times 10^3$ and 10^5 respectively).

In many respects, the properties of the vortex lattice for $B > B_{2D}$ may be considered as if a thin superconducting film of thickness s in a perpendicular field is studied.

The different behaviour of J_c in Y:123 and Bi:2212 is caused by the large difference in anisotropy of both materials [6, 7].

Magnetisation experiments have shown that the anisotropy of J_c and irreversible magnetic field (B_{c2}) of the BSCCO system is much larger than that of the YBCO system. J_c decreases drastically, when the magnetic field deviates from the *ab*-plane for a YBCO thin film. A *c*-axis oriented BSCCO thin film has a strongly enhanced J_c, when the field is parallel to *ab*-plane. For the Tl films at 77 K, it has been found that when B is parallel to *ab* plane, the J_c values are 1.2×10^4 and 1.5×10^3 A cm^{-2} at 5 tesla and 16 tesla, respectively. However, when B is perpendicular to *ab* plane, J_c decreases drastically to 1.3×10^3 A cm^{-2} at 0.7 tesla. This anisotropy of J_c indicates the existence of strong pinning centers parallel to the *ab*-plane, which could be explained using the intrinsic pinning model proposed by Tachiki and Takahashi [8]. The structure of Tl:2223 is composed of CuO_2 layers (superconductive) and other layers (Tl–O double layers), which are weakly superconductive or insulators. Then, the weakly superconductive or insulator layers work as strong pinning centers for flux lines parallel to the layers.

3.14 Experimental Results on Introduction of Flux Pinning Centers in HTSCs

In 1991, by scanning tunnelling microscopy, it was discovered at Los Alamos and IBM Ruschlikon that in epitaxial films there were large number of screw dislocations $\left(\approx 10^9/\text{cm}^2\right)$ much more than in substrate ($SrTiO_3$). This led to an understanding that these screw dislocations may pin the vortices leading to large critical currents.

Subsequently, we will consider results on

(1) Melt textured growth
(2) Chemical inhomogenity (in the form of precipitates of second phase)
(3) Production of extended defects (columnar defects) by (1) heavy ion beam or (2) neutron irradiation.

3.14.1 Melt Textured Growth

A significant improvement in J_c of YBCO ceramic has been obtained by radical change in the processing method. Instead of conventional solid phase sintering, the technique involves partial or complete melting and controlled solidification. This results in a dense material with a microstructure consisting of locally aligned, high aspect ratio grains with short dimensions ~2–5 μm. The short grain axis is parallel to the c-axis. Adjacent grains are only slightly misoriented with respect to each other (low angle grain boundaries predominate). Due to slow cooling of the melt, a platelet morphology is obtained. That is, in melt textured growth, two dimensional structure of YBCO favours its oriented growth in two specific crystal directions (*a* and *b*), thus, avoiding the formation of boundaries in the copper layers.

One may think of melt textured growth method as a compromise between chemistry aimed at producing perfect single phase sample of Y:123 and ceramic processing aimed at making a perfect ceramic without cracks. This method has been extensively developed using either a thermal (temperature) gradient [9, 10] or more recently, a magnetic field gradient [11].

3.14.2 Introduction of Second Phase (Chemical Inhomogeneity)

Murakami and his colleagues at ISTEC in Tokyo [12] have been very successful in strengthening the flux pinning of melt-processed YBCO by introducing progressively smaller ($\sim 0.1\,\mu$m) insulating Y_2BaCuO_5 particles as pinning sites. The particles are still large by fluxoid diameter standards. The ISTEC group has succeeded in raising J_c (77 K), pushing the irreversibility line to higher fields and reducing the flux creep rate.

3.14.3 Extended Defects (Columnar Defects)

In 1989, Bernard Raveau and his colleagues, began bombarding samples of YBCO with heavy ions to enhance flux pinning by creating extended defects. Others undertook studies with heavy ion beams [13] and neutron irradiation [14]. The advantage of high energy heavy ions over other modes of irradiation is that, they create amorphous columnar defects of widths comparable to the coherence length in the copper layers (nuclear track is generated by bombarding with 5.3 GeV Pb ions coming perpendicular to copper layers). The structure of such tracks consist of an almost amorphous region forming a cylinder of 7 nm diameter (which is $\approx$ the vortex core radius). Thus, energetic heavy ions are efficient projectiles for modifying and tailoring the superconducting properties of high T_c cuprates. They generate columnar defects perpendicular to the copper layers that act as efficient flux pinning centres provided that ion species, its energy and the beam fluence are carefully chosen. Such extended defects play a crucial role in controlling the magnetic hysterisis and, thus, give huge enhancement of J_c.

3.15 Magnetic Phase Diagrams of HTSCs

Figure 3.10 compares the magnetic phase diagrams of a conventional type II superconductor and a high temperature superconductor.

It has been suggested by Mathew Fisher (a theorist at IBM) that if there are enough pinning defects (centres) in the material, the superconductor may arrange itself into a vortex-glass state, in which the flux vortices do not move, i.e. there is no flux creep (converse of lattice melting).

For HTSC, the vortex solid is either a lattice (FLL for clean superconductors) or a (vortex) glass (for “dirty” superconductors). At Bell communications Research,

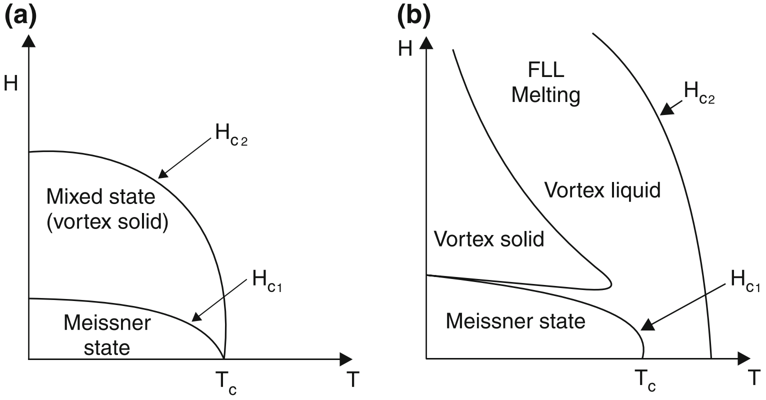

Fig. 3.10 Magnetic phase diagram of **a** conventional (type-II) superconductor and **b** an HTSC

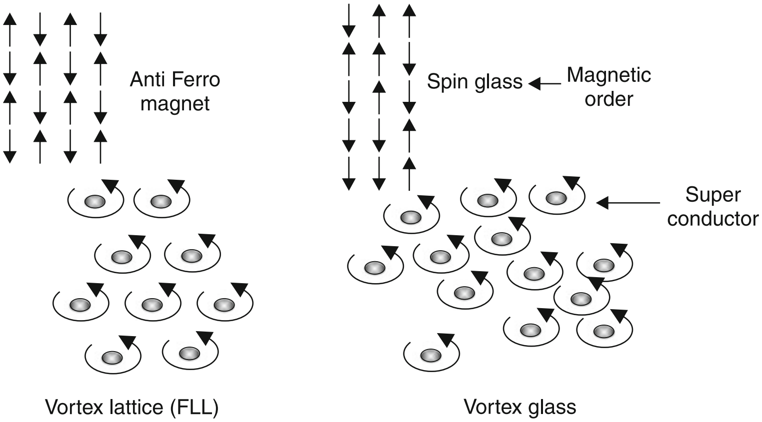

Fig. 3.11 Magnetic order versus superconductor analogy

Steve Gregory and Charles Rogers have done sensitive "vibrating reed" experiments, in which a thin film of superconductor is mechanically vibrated in a magnetic field and observed as oscillations die out. These experiments imply that superconducting films were in a vortex glass state. They interpret the state as arising from an entanglement of the flux lattice lines (FLL). If the lines were flexible enough, they may twist around each other like a tangled pile of spaghetti. This tangling may then allow the entire flux lattice to be pinned with many fewer defects than would be necessary, if the lines were free of each other (as if in lattice) (Fig. 3.11).

In absence of thermal fluctuations, the upper critical field for a type-II superconductor is given by

$$H_{c2} = \frac{\phi_0}{2\pi\xi^2}. \tag{3.33}$$

Thus, small coherence length for HTSCs should give rise to large H_{c2} ($\sim$100 T). In presence of thermal fluctuations, the temperatures are higher. Consequently, energies to create and move vortices are lower.

Energy for movement is determined by temperature and energy to create vortices is determined by field (and therefore ξ and λ). The relevant energy scale is that required to create a piece of vortex line, whose length is ξ (i.e. one coherence length). So this energy $\sim(\xi/\lambda^2)$ is much lower for HTSCs (because of small ξ and large λ). Smaller coherence length and large penetration lengths reflect that density of (mobile) pairs is relatively low.

The effects of enhanced thermal fluctuations are found in presence of an applied magnetic field. It is marked by the presence of vortex-liquid regime between the H_{C2} (T) and the vortex solid phase in the phase diagram.

On cooling, in a field $H < H_{c2}$, the electrons start to pair up and vortices form in the pair wave function near H_{c2}. In the vortex-liquid state, vortices are mobile and have only short-range correlations in their positions, like atoms in a conventional fluid. This regime extends to lower temperature in more and extremely anisotropic HTSCs (like BSCCO), particularly when the applied magnetic field is directed perpendicular to the Cu–O_2 layers. In this case, the vortex lines actually consist of strings of “points” or “pancake” vortices in each superconducting Cu–O_2 layer with only weak correlations between pancake vortices of different layers.

It has been found for BSCCO that in fields $\geq$5 T, it does not become a better conductor than copper even upto 30 K, inspite of the expectation that its resistivity should have vanished at a temperature $T_c\,(H_2) = 80\,\text{K}$. This fact is explained quite naturally by the large vortex-liquid regime in case of BSCCO. It is a natural analogue of the disordered paramagnetic phase of magnetic materials, when heated above the Curie (or Neel) temperature. Vortex motion scrambles the phase of the pair wave function disrupting any possible long-range coherence (→no superconductivity).

3.16 Melting of the FLL Because of Reduced Size of $\xi_{GL}(T)$

For $T \ll T_c$, $\xi_{GL}(T)$ is between 0.5 and 30 Å. At $T \leq T_c$.

$$\xi_{GL}\,(T) = \xi_{GL}\,(0)/(1 - T/T_c)^{1/2}\,, \tag{3.34}$$

since $\xi_{GL}(T)$ is $\ll \lambda_L$ (type II superconductor).

So, we have extremely high low-temperature value for H_{c2}. Associated with the short ξ is weak pinning of fluxoids compared with the pinning in the conventional superconductors. This decreased flux pinning diminishes the size of J_c.

3.16.1 Effect of Reduced Size of $\xi_{GL}(T)$

As the sample is warmed up, the shear modulus of the fluxoid lattice goes to zero at a temperature below T_c. This melting may account for an upward curvature (i.e. a positive second derivative) in the graph of the $B(T)$ curve at which electrical resistance appears.

Although the flux pinning is weak at temperatures comparable with T_c, it is large enough at lower temperatures to make measurements of the H_{c1} very difficult. (Values in literature for H_{c1} of Y:123, e.g. range from 1 to 5,000 Oe.)

Flux pinning is responsible for the measured magnetic susceptibility being different, when measured on a sample cooled in a constant magnetic field than on one cooled in a zero field, and exposed to field after the lowest temperature is reached. In the former case, the fluxoids move out of the sample as it is cooled, whereas in the latter, they move into it as it is heated; in each case, flux pinning impedes the motion. These two types of data are frequently referred to as “Meissner data” and “Zero field-cooled data” respectively.

3.17 Kosterlitz–Thouless–Berezinski Transition

If the superconductor-film thickness is comparable to the coherence length, then at any finite temperature (even at zero field) there are vortices present in the film. Because energy necessary to create a vortex is very small if the length of a vortex is less than the coherence length, therefore, there is always a significant number of thermally excited vortices in very thin films, and there is also an equal number of anti-vortices, so that there is no net field at any significant distance from film. Thus, in addition to Cooper-pairing, another phase transition occurs due to pairing of vortices and anti-vortices, which is complete at a temperature represented as T_{2D}, (T_{2D} is $< T_{c(0)}$). (This effect has also been observed in two-dimensional helium films.) $T_{c(0)}$ is the bulk transition temperature. This two-dimensional transition to zero resistance in films occurs at a temperature below the bulk transition temperature of the parent material. The difference $(T_{c(0)} - T_{2D})$ is proportional to the sheet resistance of the 2D film.

For T_{2D} to be closer to $T_{c(0)}$, the sheet resistance should be low. At T_{2D}, there would be a sharp increase in superfluid density, and this would manifest itself in any property sensitive to n_s (e.g. kinetic inductance). If, either the thin film is granular or has a low carrier concentration, the T_{2D} will be significantly different from $T_{c(0)}$, because of large sheet resistance. This vortex pairing transition implies reduced dissipation. To study this transition, granular films are nice, because of lesser pinning than homogenous films.

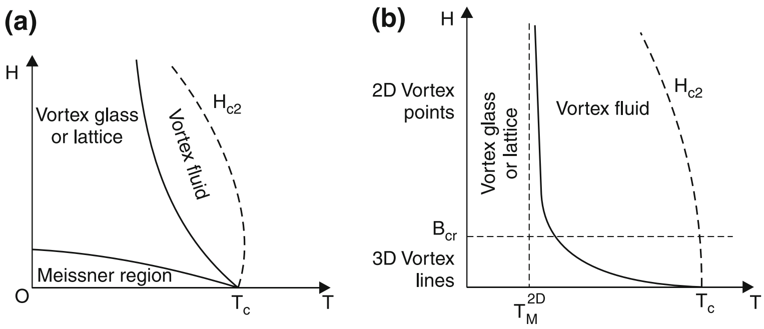

Fig. 3.12 Schematic phase diagram for melting of FL solid for **a** YBCO and **b** BSCCO

3.18 Anisotropy and Change Over from a 2D to 3D Behaviour

For highly anisotropic Bi- and Tl- based compounds (in the absence of external magnetic field), the superconducting transition corresponds closely to the Kosterlitz–Thouless transition for 2D systems. Thermal fluctuations are very important in HTSCs. In applied magnetic fields, thermal fluctuations modify the field-temperature (i.e. B–T) phase diagram with respect to the mean field one, which is dependent on anisotropy also.

The layered structure of the materials leads to the existence of a critical value for the magnetic induction B_{cr} which separates regions of 2D and 3D behaviour of the vortex system and hence, different regimes of vortex-lattice melting.

Figure 3.12 compares the phase diagrams for melting of the flux line solid for a 3D material YBCO with that of a highly layered material BSCCO. The results for BSCCO are with $\vec{B} \parallel \vec{c}$. The melting line starts near T_{c}, rising initially as $(T_{\text{c}}–T)^2$ until B_{m} reaches a value B_{cr} at $T \sim T_{\text{m}}^{2\text{D}}$, after which B_{m} rises almost vertically.

Figure 3.12 shows the contrasting behaviour of the two HTSCs. It is to be mentioned here that the melting temperature $T_{\text{m}}^{2\text{D}}$ (which marks the cross-over flux density B_{cr} for BSCCO) is at inaccessibly high fields for the 3D material YBCO.

3.18.1 High Field Regime ($B \gg B_{\text{cr}}$)

The interaction energy between 2D vortices in the same layer is stronger than the interaction energy between vortices which belong to different layers. This results in a quasi-2D behaviour of the vortex system, which can be considered as made of only weakly interacting 2D vortex lattices in different layers. In this case, the melting temperature is close to the strictly 2D (Kosterlitz–Thouless) melting temperature, which is field independent.

$$T_m^{2D} = \left(\frac{A}{8\pi\sqrt{3}}\right)\left[\frac{d\varphi_0^2}{(4\pi\lambda_{ab})^2}\right] \tag{3.35}$$

$(A \approx 1)$
where $d =$ inter-planar distance
$\varphi_0 =$ flux quantum
$\lambda_{ab} =$ in plane component of London penetration depth.

For Bi:2212, the above equation gives

$$T_{\mathrm{m}}^{2D} \approx 25\text{–}30\ \mathrm{K}$$

in real systems. In presence of field

$$T_{\mathrm{m}}(B) = T_{\mathrm{m}}^{2D}\left[1 + \frac{b}{\ell n^{2.70}\left(\frac{B}{B_{\mathrm{cr}}}\right)}\right], \tag{3.36}$$

where b is a constant ($\approx$1).

3.18.2 Weak Field Region ($B \ll B_{\mathrm{cr}}$)

The relative displacement of 2D vortices in adjacent layers is much smaller than the displacement due to fluctuations (disorder) and the vortex-lattice follows a 3D behaviour. In this case,

$$T_{\mathrm{m}}(B) = \left(\frac{c_{\mathrm{L}}^2}{2^{3/2}}\right)\frac{d\varphi_0^2}{(4\pi\lambda_{ab})^2}\left(\frac{B_{\mathrm{cr}}}{B}\right)^{\frac{1}{2}}, \tag{3.37}$$

where $0.1 \geq c_{\mathrm{L}} \leq 0.4$.

$T_{\mathrm{m}}(B)$ in this equation indicates the melting temperature from a 3D vortex lattice to a liquid of 3D vortex lines. A further increase of temperature results in dissociation of vortex lines into 2D vortices which are free to move independently in each layer at a temperature

$$T'(B) = T_{\mathrm{m}}(B)\left(\frac{B_{\mathrm{cr}}}{B}\right)^{\frac{1}{2}} (>T_{\mathrm{m}}(B)). \tag{3.38}$$

3.18.3 The Cross-Over Field B_{cr}

Average inter-vortex distance in the plane is

$$\approx \left(\frac{\varphi_0}{B}\right)^{\frac{1}{2}} \tag{3.39}$$

and Josephson length

$$= (\gamma d) \tag{3.40}$$

where anisotropy parameter

$$\gamma = \left(\frac{\lambda_c}{\lambda_{ab}}\right). \tag{3.41}$$

λ_c is out of plane penetration length, d is the inter-plane distance. This implies

$$B_{\text{cr}} \approx \frac{\varphi_0}{(\gamma d)^2} \tag{3.42}$$

The behaviour of real materials is very sensitive to anisotropy: the parameter γ in Bi:2212 depends on the oxygen content, for a fixed value of the reduced temperature $t = (t/T_{\text{co}})$, J_{c} is found to increase with increasing oxygen content. This effect can be explained with the reduction of effective anisotropy (γ) and, therefore, with a more 3D character of vortex fluctuations in oxidised samples.

3.19 The Effect of Anisotropy Parameter γ on the Vortex Phase Transitions

An increase of γ results in decrease of B_{cr} $\left(\sim 1/\gamma^2\right)$. This implies melting temperature of the vortex lattice decrease with decrease in oxygen content, for a fixed value of the applied field. In strongly reduced samples, the cross-over field can be so close to H_{c1} that (3.37 and 3.38) would have no temperature range of validity. Figure 3.13 shows the behaviour of the magnetic irreversibility line for two different oxidation states of BSCCO film.

The B_{cr} values were found to be ~1,000 and 100G, respectively for oxidised and reduced states. Such changes in B_{cr} correspond to a large variation of the anisotropy parameter γ (from 80 to 300 respectively).

The transition temperature to the vortex glass phase (T_{g}), decreases as the anisotropy factor γ increases reaching $T_{\text{g}} = 0$ at $\gamma = \infty$ (pure 2D). In the presence of finite inter-layer coupling, the 2D vortex glass correlation length grows resulting in a transition to 3D vortex glass phase at sufficiently low temperatures $T_{\text{g}} \sim (1/\gamma^{\text{n}})$ $(n > 0)$.

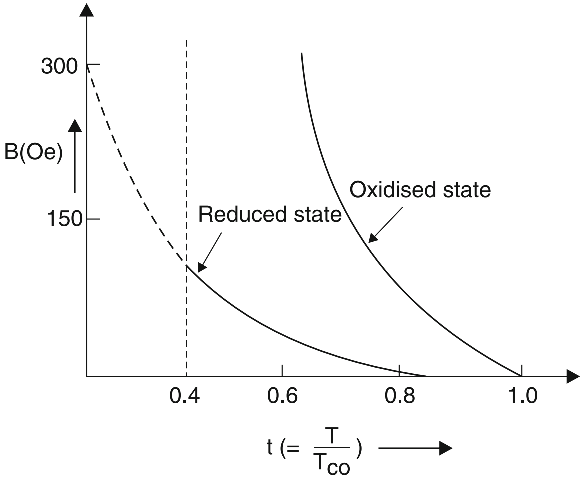

Fig. 3.13 Behaviour of magnetic irreversibility line for two different oxidation states of BSCCO film

3.20 Desired Microstructure Synthesis for High Critical Current Density in High T_c Superconductors

3.20.1 Some Inherent Problems (Weak-Links and "Flux Lattice Melting")

When the initial euphoria regarding the discovery of HTSCs subsided, and attempts regarding the deployment of HTSCs in devices started, it became evident that certain practical problems will have to be solved. One of the major (practical) problem relates to the low critical current density (with or without applied magnetic field) for the as synthesised HTSC materials. The lower value of critical current densities arises due to both inter-grain (weak-link) and intra-grain (flux lattice melting) effects. There have been speculations that the above effects are inherent in certain specific properties of HTSC materials, including those very properties that are thought to be responsible for making the new oxide superconductor as HTSCs, for example the HTSCs are known to have lower carrier densities as compared to the low T_c metallic superconductors (LTSCs). In the new oxide cuprate superconductors, according to one popular view, the charge carriers are provided by deviating the nominal valence of copper from 2^+ to $(2+\delta)^+$ where $0 < \delta < 1$. The materials, which contain divalent copper ions are insulators, despite the odd number of valence electrons expected per unit cell. The genesis of gap-formation in the conduction band is thought to be due to strong electron correlation relative to the energy corresponding to the band width. For those compositions (n_S), where superconductivity sets in, it has been known that the energy gap structure is essentially retained on doping of the carriers to a substantially high

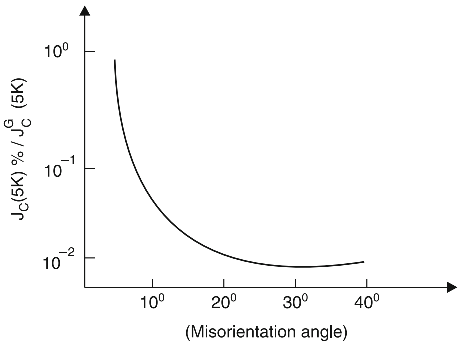

Fig. 3.14 Ratio of critical current density (grain boundary J_c) to the average value of current density J_c^G in the two adjacent grains as a function of the misorinetation angle in the basal plane

level. However, if the doping level is increased, the carrier density could be increased further, but then, the gap seems to get destroyed. The transition temperature then decreases rapidly. Because of this, the maximum useful carrier density remains in the range $\sim 2 \times 10^{21} - 5 \times 10^{21}$ cm^{-3}. This value is substantially (about 100 times) lower than that obtained for conventional superconductors. It is, therefore, apparent that low carrier density is native to HTSC materials. However, this low carrier density leads to several undesirable aspects regarding the application potential of HTSCs. One important effect of low carrier density is that it leads to a potential barrier at the grain boundary, which hinders the transmission of the electrical current across the grain boundary (GB). [15] were the first to outline the presence of potential barrier at the boundary. In a more recent study, the transport critical current (inter-grain) has been found to get reduced to varying degrees depending on the relative tilt angle between the boundaries (Fig. 3.14) [16].

Another problem related with current transport is due to flux lattice melting. This again is related to the inherent properties of HTSCs. This relates to coherence length ξ, which has its origin in the finite distribution range of momentum of the electronic states resulting in the formation of Cooper-pairs. The coherence length can be approximated as $\xi = n' v_F / (\pi\Delta)$, where ν_F is the Fermi velocity, Δ, the superconducting gap and n' the carrier density. For the case of a low carrier density material, the Fermi sphere and hence, Fermi velocity is small. The superconducting gap Δ is range in the high T_c materials (since Δ is an increasing function of T_c). In view of their large Δ and small ν_F, it is unlikely that the new materials will possess large coherence lengths. It has been estimated that for Y-123, $\xi_{ab} \cong 30$ Å and $\xi_c \cong 3$ Å and for $Bi_2Sr_2CaCu_2O_8$, $\xi_{ab} \cong 35$ Å and $\xi_c \cong 3$ Å. It may be noted that for conventional superconductors, e.g. for Nb, $\xi \cong 400$ Å. The small coherence length leads to small pinning force and hence this limits the intra-grain critical current. One possible simple way of looking at this problem is as follows: A pinning centre has an effective dimension $\sim\xi$. The energy to destroy superconductivity, i.e. the condensation energy is $H_c^2/(8\pi)$ per unit volume. Thus, if we have a non-superconducting precipitate of volume ξ^3, an excess energy of $\xi^3 H_c^2/(8\pi)$ is required to push a flux line out of the precipitate [17]. The value of H_c is larger for HTSCs (e.g. 3 T for Y:123) than for conventional superconductors (e.g. for Nb, it is ~0.2 T) However, for HTSCs, the

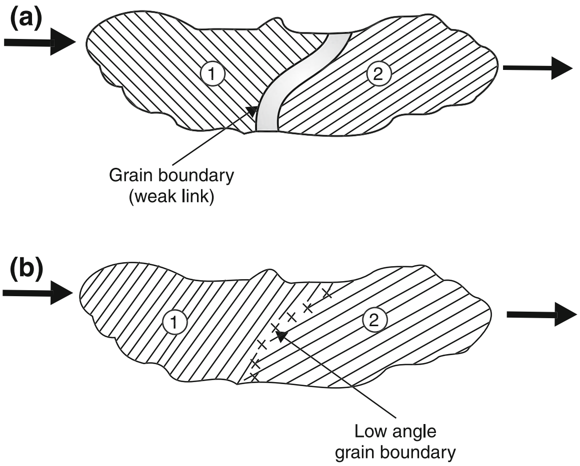

Fig. 3.15 The passage of current across **a** high angle and **b** low angle grain boundary. In case of former, there is a large but for the latter, very small decrement in current

value of ξ^3 is much smaller. For example in cuprate HTSCs, it is 5×10^{-27} m^3 (vs. 6×10^{-23} m^3 for Nb). As a result, pinning energy in cuprate HTSC is smaller than in conventional superconductor by a factor of 10^3. The pinning energy for YBCO, derived on the basis of these arguments, is 0.04 eV. (It may be pointed out that the thermal energy at 77 K is 0.006 eV.) Thus, the pinning energies are not large enough to circumvent the thermally activated depinning. As a consequence, a finite resistivity would be expected in a magnetic field even at very low current level.

In addition to the aforementioned inter-grain weak-link and intra-grain flux-lattice melting problems, yet another factor that limits the current carrying capacity of HTSCs is their anisotropy. The best current capacities are observed for current flow in the *a–b* plane, and poorer in the *c*-axis direction. The improvements to raise the capacity in this regard do not seem feasible. Thus, in the subsequent discussion, we would confine ourselves to discuss possible ways out of the "weak-link" and "flux-lattice melting".

3.20.2 Possible Ways Out of "Weak-Links"

As described previously, the weak-links correspond to grain-boundaries. Since the first forms of HTSC materials produced were polycrystalline pellets, the weak-link problems were invariably present and the transport current (across the GBs) was very low (~10 A cm^{-2}). One easy way out of the weak-link effects could be found in the earlier works on metals and alloys and also on some inorganic solids, where material forms were produced from polycrystalline versions through a process termed as "texturing". In this, the crystallites of the polycrystalline forms were provided treatments so that they adopt specific orientations, and hence, would

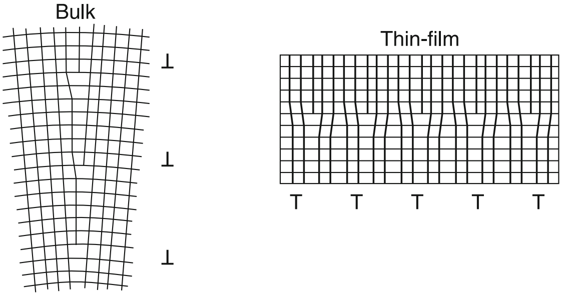

Low-angle grain boundary Epitaxial interphase boundary

Fig. 3.16 Low angle (**a**) and epitaxial inter-phase boundaries (**b**) resulting due to texturing

be separated (generally) by low angle grain boundaries (Fig. 3.15). For instance, it has been reported that the diminution in critical current decreases as the misorientation between grains decreases [18], i.e. as high angle grain boundaries yield to give rise to low angle boundaries. Thus, when electrical current passes through a polycrystalline configuration with low angle grain boundaries, the diminution in it is minimum. Thus, if texturing is imparted through a suitable process, the critical current density would get significantly enhanced, e.g. under suitable conditions, it may reach upto $\sim 10^5$–$\sim 10^6$ A cm^{-2}. It is interesting to note that the first reports of higher J_c ($\sim 10^5$ A cm^{-2}) were for thin films deposited on suitable substrates, as for instance, for $YBa_2Cu_3O_{7-\delta}$, the substrates employed corresponded to MgO, ZrO_2 and $SrTiO_3$ [18]. Considerations of thin film formation on these substrates held at elevated temperatures (300–500 °C) would reveal that they nearly satisfy the conditions of epitaxial growth in thin films. Without going into details, it may be pointed out that in this growth process, the depositing atoms/molecules lead to formation of crystal like regions, which nearly adopt the substrate crystal orientations (Fig. 3.16). Thus, in thin films, texturing is automatically provided during the film formation.

On one hand, texturing leads to similar effects in thin films and bulk, for the former, it gets naturally imparted during film formation process itself. On the other hand, for bulk, texturing has to be necessarily done after synthesis (growth) of the initial material. Being a post-synthesis process, it corresponds to an additional process step. Also, an HTSC being a multi-component material, imparting texturing is rather an involved process. Because of these factors, texturing in bulk has not yet been a routine step, although several specific texturing processes have been put forward. Out of the various texturing processes developed so far, those which seem to be important are those proposed by Murakami [19], and a more recent process—the so called "continuous" process proposed by Professor Paul Chu's group at Houston [21]. These processes are briefly discussed in the following, with emphasis on embodied principles.

The texturing process propounded by Murakani et al. is essentially a quench melt growth (QMG) process, which leads to

Fig. 3.17 Phase diagram illustrating QMG process

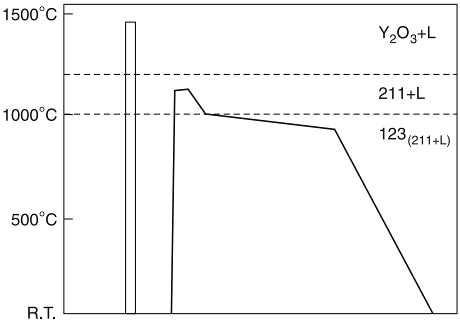

(1) Suppression of the second phase intrusions
(2) Improvement in the connectivity of the superconducting phase and
(3) Grain alignment

and thereby, the achievement of high J_c in the Y–Ba–Cu–O system. The QMG process can be described with the help of the diagram shown in (Fig. 3.17).

The QMG process is based on the known phase transformations in Y:123 material. Some salient features can be recapitulated. When the 123 bulk precursor cools from a single phase liquid region to 1,050 °C, it undergoes the transition

(Y_2O_3 + liquid) → (Y_2BaCuO_5 + liquid) → (123 + liquid of composition $BaCuO_2 + CuO$).

At around 1,050 °C, 123 forms through a peritectic solidification according to Y_2BaCuO_5 + liquid ($3BaCuO_2 + 2CuO$) → $2YBa_2Cu_3O_{6.5}$. Now, if the material is heated above the solidus temperatures (1, 020–1, 200 °C), it helps to dissolve the impurity phases, which are precipitated in the grain boundaries. In addition to this, crystal grains grow more easily in a liquid solution. Thus, the QMG texturing process consists of rapidly heating 123 above the solidus temperature (or even above the melting point) and then, slowly cooling through the peritectic temperature.

In the QMG process, first a stoichiometric $YBa_2Cu_3O_7$ pellet is heated to 1,450 °C for a few seconds, and then it is quenched to room temperature. This step creates precursor material consisting of fine Y_2O_3 particles scattered through out liquid phases of copper oxide and barium copper oxide. Then, the precursor material is heated to 1,100 °C for 20 min. This causes the Y_2O_3 particles to react with the liquid, forming a fine and homogeneously dispersed 2–1–1 phase. The material is cooled to room temperature. This causes the 2–1–1 phase to react with the liquid phases, creating a well connected 1–2–3 microstructure. Cooling of the material in a temperature gradient encourages directional growth of $YBa_2Cu_3O_7$ phase. The cooling should be done in flowing oxygen, so that enough oxygen can be incorporated to induce the tetragonal to orthorhombic transition. It is also possible to incorporate oxygen into the sample by post-annealing at around 600 °C after fast cooling from 900 to 950 °C, where the growth of the 123 phase terminates.

The above QMG process leads to alignment of grains and hence, is like a texturing process, which creates material having grains aligned within few degrees.

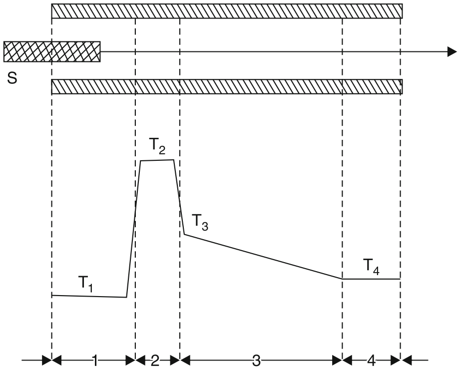

Fig. 3.18 Illustration of continuous process for step (3) in the preparation of bulk 123 sample (S)

This Murakami's process leads to textured HTSC materials with very high J_c and was verified by Salama [20], who obtained a current density of 37,000 A cm^{-2} in a magnetic field of 0.6 T.

More recently, a continuous bulk HTSC texturing process has been developed by Prof. Paul Chu's group at Houston [21]. These investigators, to allow the continuous growth of large samples of bulk 123 that are capable of carrying a high J_c and to help remove impurities, moved the 123 bulk precursor through an open tubular furnace having a pre-set temperature profile that includes a narrow hot zone (Fig. 3.18). Meng et al. have set the temperature profile in accordance with the known phase transformation in 123 material, which has already been described while dealing with Murakami process.

The temperatures are $T_1 = 500 \pm 25\,°\mathrm{C}$. The time spent in different zones are: 1 (not critical); 2: (10 ± 5 min); 3: (100 ± 50 h); 4: (20 ± 5 h). The peritectic temperature is 1,050 °C [21].

They have varied both the speed $\mathrm{d}x/\mathrm{d}t$ and the gradient $\mathrm{d}T/\mathrm{d}x$, to give the desired rate of temperature change $\mathrm{d}T/\mathrm{d}t$. Meng et al. sintered a bar of dimensions $5.2 \times 0.5 \times 0.3\,\mathrm{cm}^3$ from a 123 fine powder precursor at 940–960 °C for 24 h in an oxygen atmosphere to obtain 90 % of the theoretical density of 6.3 g cm^{-3}. The bar was heated to 1,100 °C very rapidly for a short time, before it was cooled rapidly to near the peritectic temperature (∼1,050 °C).

The specimen was then made to go through peritectic solidification very slowly. Due to narrow hot zone, zone refining occurs along the axis of travel depositing Y_2BaCuO_5 at one end of some of the samples. Small pieces from different parts of the bar were oxygenated at 500 °C for 24–48 h. The resulting bar has very good grain alignment throughout the bar. This was confirmed by scanning electron microscopy and X-ray diffraction techniques. The XRD of the samples taken through the texture processing as per the details suggested by Meng et al., clearly shows that the *a–b* plane coincides with the longitudinal fracture face along the direction of travel and that all of these planes in the sample are parallel to each other. Some typical J_c values obtained by Meng et al. at 77 K can be outlined here. For a sample of dimensions $1 \times 0.04 \times 0.05\,\mathrm{cm}$ was $2 \times 10^4\,\mathrm{A\,cm^{-2}}$ at 0 T, $1.1 \times 10\,\mathrm{A\,cm^{-2}}$ at 0.54 T and

7.5×10^3 A cm^{-2} at 0.82 T. For the case of the applied field parallel to J_c, J_c was found to be about 1.4×10^4 A cm^{-2} at 0.82 T. This clearly suggests that weak-links get largely eliminated in the texture processing carried out by Meng et al.'s process.

One significant advantage of Meng et al.'s texturing process is that it has continuous nature. Therefore, practical forms like plates, rods, ribbons and perhaps thick films can be fabricated from bulk superconductors having practical forms. The processing of the bulk 123 within the framework of Meng et al.'s process can be divided into four steps (1) the synthesis of powder precursor, (2) sintering of bulk precursor, (3) melt-textured growth and (4) oxygenation. By employing proper temperature gradients and speeds in different zones of the furnace, steps (2) and (4) can be combined into a single continuous process. Another modification, which can be done is the lowering of processing temperature. This can be done by using low melting flux comprising of $BaCuO_2$ and/or CuO and a more reducing atmosphere or halogen. This may be particularly useful for HTSC wires or ribbons, which may involve metal cladding, e.g. silver sheath.

It appears, at present, that the HTSC materials prepared by Meng et al.'s process may be somewhat inferior to that of Murakami's quench melt growth process in regard to the critical current density. However, Murakarni et al.'s process is a batch process, whereas the Meng et al.'s is a continuous process, which is of a great advantage.

3.20.3 Provision of Flux Pinning Sites

Even when the weak-links are taken care of through texturing, the flux lattice melting problem still remains and the critical current density in the magnetic field undergoes significant diminution due to flux disordering. As discussed previously, to circumvent flux disordering problem, the microstructure has to be suitably tailormade. If the microstructure contains no defects i.e. the crystal is perfect, it would not sustain any current. It is only when defects get created that a current would be–carried through. This is so since the defects can pin the flux and hence it would not disorder and disappear. This is so because the Lorentz force between the transport current and the flux lines causes the latter to move. A voltage is thus created unless the flux lines are pinned. The defects are really the glue which keeps the lattice together and without them, there would be no transport current. The defects must be of the order of coherence length (i.e. $\sim$30 Å for *ab* plane in YBCO). Thus effective flux pinning centres would correspond to localised defects with dimensions of few times the coherence length.

The "flux lattice melting" achieved serious attention after the appearance of the article "Superconductivity: Is the party over" by Pool [22] where he described the work of several investigators including David Bishop of AT and T Bell labs and brought out the limitations on J_c arising from flux lattice melting into sharp focus. The flux lattice melting has been dramatically demonstrated by Bishop [23] by comparing the electron micrograph of the flux lattices (revealed indirectly by magnetic particles attracted towards the ends of flux lines) of Y- and Bi-bearing HTSC materials. According to Bishop, the flux lattice in YBCO melts at about 75 K and that in

BSCCO, around 30 K. The ways and means of circumventing the flux lattice melting have been extensively explored. It appears that one of the effective ways to arrest the flux lattice melting is to tailor-make the HTSC materials so that they contain a second phase in the form of fine particles which are constrained to the dimensions of the coherence length. It may be found that this can be obtained by suitably adjusting melting and quenching process in the QMG (Murakami) or continuous (Chu) texturing processes. The processes of using a liquid phase in the peritectic region naturally produces second phase materials. Adjustments of quenching conditions may produce second phase particles with dimensions constrained to the dimension of coherence length. The HTSC material in such cases i.e. when QMG or continuous growth also produces second phase flux pinning centers, will have truly large J_c, since in such material forms, weak-link problem has been taken care of by texturing and FLL melting has been arrested by the second phase particles (e.g. 211 particles in the textured 123 material obtained through QMG).

In 1989, it has been shown that irradiation of 123 HTSC material with fast neutrons ($\sim$1 MeV) also leads to enhancement of intra-grain critical current density by as much as hundredfold [24]. The enhancement in the fast neutron irradiated ($\sim$1 MeV, fluence $7.9 \times 10^{16}\,\mathrm{cm}^{-2}$) 123 HTSC results due to creation of neutron irradiation induced defects which act as pinning centres. There have been several other results on the neutron irradiation induced enhancement of intra-grain critical current density J_c [24]. However in none of these investigations the nature of defects created by fast neutron irradiation has been elucidated. Janam et al. [25] made investigations on unravelling the defects created through neutron irradiation. The 123 single crystals grown by flux ($BaCO_3$ and CuO) method were tested for superconductivity ($T_c \sim$ 85–90 K). These crystals were then irradiated with 1 MeV neutrons (fluence $10^{16}\,\mathrm{cm}^{-2}$) at Dhruva reactor of Bhabha Atomic Research Centre, Mumbai. The defects created by neutron Irradiation were explored by transmission electron microscopy. TEM bright field micrograph revealed that the defects consist of linear spikes (Thermal spikes of width $\sim$100 Å). At later stages, the spike becomes displacement spike. Both the thermal spike ($\sim$100 Å) and displacement spike defect clusters ($\sim$300 Å) have dimensions $\sim$3 to 10 times the coherence length ($\xi_{ab} \sim 30$ Å). It is these defects which correspond to flux pinning centres and seem to be responsible for the enhancement of a critical current density on fast neutron irradiation of 123 HTSC single crystal [24].

3.20.4 Desired Microstructure for High J_c

From the preceding discussion, it is clear that for the viable optimum high critical current across the inter-grain (weak-link) and also intra-grain (flux lattice melting) will have to be optimised. Thus processes leading to texturing and provision of “flux pinning centres” both will have to be carried out before the new cuprate HTSC becomes a potentially viable practical material at least for the majority of more useful applications, where high critical transport currents are desired. It appears that for specialised applications, thin film forms where texturing automatically takes place, will continue to find favoured position. Here the flux pinning centres will have to be provided either through the provision of fine aggregates of a second phase or through localised defects created e.g. by neutron irradiation. An interesting aspect of the HTSC thin films is that not only texturing gets automatically imparted but due to different energetics prevalent during their formation, some non-equilibrium and/or metastable second phases (e.g. 211 in aY:123 matrix) gets formed. These phases may serve as flux pinning centres. Thus the thin films may represent desirable forms where with a little effort one can get high critical current density. However, for many general application bulk HTSC forms will be needed. Here, additional processes will have to be carried out so that the as synthesis material becomes a viable form capable of high critical current density. Based on the present state of the art, it appears that first a texturing like Murakami "QMG" or Chu "Continuous" process will have to be carried out so as to eliminate or decrease the density of weak-link. This will have to be followed by a process aimed at providing flux pinning centres e.g. second phase precipitation or defect creation through fast neutron irradiation. A schematic plan for achieving the special microstructures with textured grains and with local second phase/defect cluster configurations is shown in Fig. 3.19.

3.21 High T_c Technology

A recent study by the US department of Energy and the Electric Power Research Institute offers a detailed survey of the potential applications of high temperature superconductors once J_{ct} reaches $10^5\,\text{A/cm}^2$. The survey predicts extensive markets for HTSCs in electric motors, power electronics, transportation, heat pumps, electromagnetic pumps and materials production. These application offer the long term prospect of reducing our total energy consumption by $\sim 3\,\%$. At liquid He temperatures, the critical current of the new materials (BSCCO) exceeds $10^5\,\text{A/cm}^2$ in a 25-tesla field, besting the Nb based superconductors in their temperature regime. These results have been obtained on tapes with a high degree of crystallographic alignment, produced by repeated cycles of sintering and mechanical deformation.

Until now, Nb-Ti or Nb_3Sn have been used for very-high field magnets. The present record is 20T for powered magnets and 15 T for persistent current NMR magnets. BSCCO superconductors have the potential to function in fields exceeding 20T. A second advantage of BSCCO materials is that their critical currents vary little with temperature in the range 4–20 K. This suggests an extensive market for magnets that can be cooled by cryocoolers without requiring immersion in liquid helium such cryocoolers work very comfortably in the range 10–20 K without Joule-Thompson expansion values. Sato's Sumitomo team have already constructed a small BSCCO wire solenoid that generates 0.9 T at 4.2 K and 0.1 T at 77 K. It seems likely that we will soon see commercial superconducting magnets with cryocoolers. At liquid nitrogen temperatures, the best results for BSCCO have not yet reached 10^5 A/cm^2. The maximum critical current at 77 K are about $5 \times 10^4\ \text{A/cm}^2$ at zero field and $1 \times 10^4/\text{cm}^2$ at 1 T [26]. However the general conclusion about the long term potential of the BSCCO (and TBCCO) materials at 77 K are not yet justified because

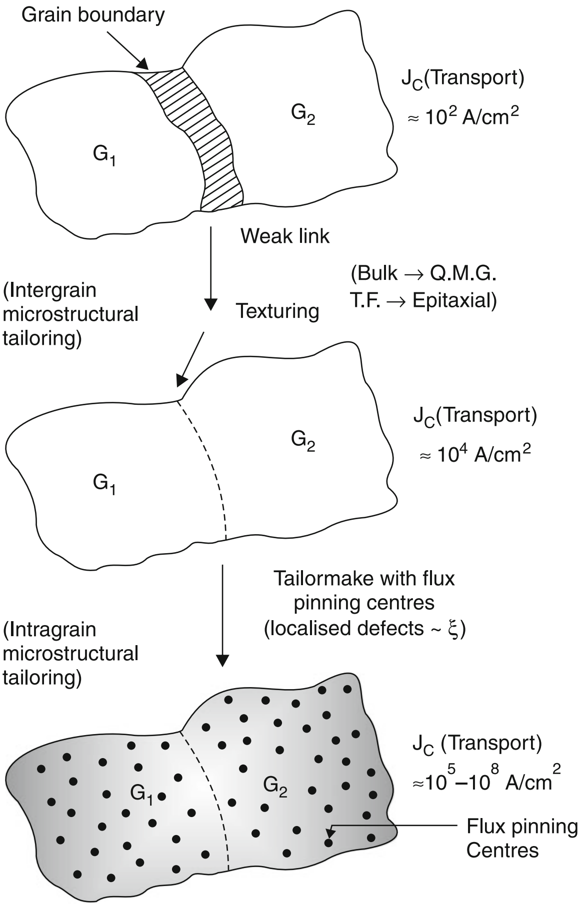

Fig. 3.19 A schematic plan for developing high critical current density bulk HTSC (after Prof. O.N. Srivastava, Banaras Hindu University, Varanasi, India)

these compounds cannot maintain strong flux pinning at temperatures above 30 K because of strong flux creep and FLL melting. At the same time, the much lower anisotropy of Y-123 superconductors and their better flux creep properties at present justify, for many, a continued push to understand and defeat the weak-link problem posed by the grain boundaries in the Y123 compounds.

3.21.1 Advantage of Weak Pinning

The weak pinning behaviour is advantageous for making devices where free flux motion is required, for example a dc transformer. A dc transformer consists of two magnetically coupled but electrically isolated granular films. By passing a dc current in film A, the vortices will move (due to Lorentz force). The vortices in film B will also move. Moving vortices always produce a voltage (and a current). So, there will be an induced dc current in film B just by passing a current in film A.

Solid	Superconductor
1. *Screw dislocation in a solid* The order advances by one lattice spacing in going around the dislocation line	1. *Vortex-line in a superconductors* The pair-phase advances by 2π in going around the vortex core
2. *Slip-plane in a solid* The atomic spacing is shifted Δa	2. *Superconducting tunnel junction* The pair-phase difference is between the two superconductors
3. In the solid, the inter-atomic forces are short range implying that low lying order fluctuation modes are phonons	3. The corresponding fluctuations of the phases in the superconductor involve fluctuations in charge density and the long-range coulomb forces give them the plasmon energy in a bulk superconductor (-Anderson)
4. A solid near its melting point	4. In 3-D, the thermal excitation of phase fluctuation modes can lead to the disintegration of the phase ordering below the "bulk" transition temperature determined by the quasi-particle excitations (i.e. melting of FLL (flux line lattice))

3.22 Comparison Between Non-Uniform Order in a Solid and That in a Superconductor

We know that in a crystalline solid, the order parameter is the atomic position, while in the superconductor; it is the pair centre-of-mass phase. The table compares some special cases of non uniform order in the two cases.

In the passing, it is worth mentioning here that for a high T_c superconductor with useful J_c values, point defects, stacking faults and probably dislocations may be too small to be good pinning centres even when their density is high. On the other hand, precipitations, voids etc above a minimum size of few tens of nanometers would provide sufficient large pinning energies (in order to reduce flux creep). First success along this way was reported by Murakami et al. (1988) who generated large precipitates of Y_2BaCuO_5 in a well connected $YBa_2Cu_3O_{7-x}$ matrix by a sophisticated heat treatment of a solidified melt and $J_c \sim 10^4 A/m^2$ was obtained at 77K and 1T which was several orders of magnitude higher than sintered materials.

References

1. A.V. Narlikar, in *Critical Current and Vortex Pinning in (High Temperature) Superconductors*, ed. by S.V. Subramanyam, E.S.R. Gopal, High Temperature Superconductors (Wiley, New York, 1989)
2. J.R. Clem, Phys. C **50**, 153 (1988)
3. C.P. Bean, Phys. Rev. Lett. **8**, 250 (1962)
4. Y. Yeshurum, A.P. Malozemoff, Phys. Rev. Lett. **60**, 2202 (1988)
5. D. Dimos, P. Chaudhuri, J. Manhart, Phys. Rev. B **41**, 4038 (1990)
6. T.T.M. Palstra et al., Phys. Rev. B **41**, 6021 (1990)
7. T.T.M. Palstra et al., Phys. Rev. B. **43**, 3756 (1991)
8. M. Tachiki, S. Takahashi, Solid State Commun. **72**, 1083 (1989)
9. S. Jin et al., Appl. Phys. Lett. **52**, 2074 (1988)
10. S. Jin et al., Appl. Phys. Lett. **54**, 584 (1988)
11. R. De Rango et al., Nature **349**, 770 (1991)
12. M. Murakami et al., IEEE Trans. Mag. **27**, 1479 (1991)
13. W.K. Chu et al., Nucl. Instr. Methods B **59–60**, 1409 (1991)
14. H. Weber et al., in *Studies of High Temperature Superconductors*, vol. 9, ed. by A.V. Narlikar (Nova Science, New York, 1991), p. 37
15. Y. Enomoto et al., Jpn. J. Appl. Phys. **20**, L661 (1981)
16. D. Dimos et al., Phys. Rev. Lett. **61**, 219 (1988)
17. K. Kitazawa, Cer. Bull. **68**, 880 (1889)
18. P. Chaudhuri et al., Phys. Rev. Lett. **58**, 2687 (1987)
19. M. Murakami et al., Jpn. J. Appl. Phys. **28**, 1189 (1989)
20. K. Salama et al., Appl. Phys. Lett. **54**, 2352 (1989)
21. R.L. Meng et al., Nature **34**, 326 (1990)
22. R. Pool, Science **244**, 914 (1989)
23. D. Bishop, in *International Conference on Superconductivity*, Bangalore, January 1990
24. R.B. Van Dover et al., Nature **342**, 55 (1989)
25. R. Janam et al., Solid State Commun. (1990).
26. K. Sato et al., IEEE Trans. Mag. **27**, 1231 (1991)

Chapter 4
Synthesis of High T_c Superconductors

4.1 Synthesis of $Y_1Ba_2Cu_3O_7$ in Bulk Form

Before going into details of preparation, it would be worthwhile to note the undermentioned properties of YBCO system, as these are of relevance in determining the preparation procedure:

1. On heating the Y:123 compound, it decomposes peritectically at about 1,020−1,040 °C into Y_2BaCuO_5, CuO and $BaCuO_2$. For this reason, all preparation steps should better be carried out at temperatures below 1,000 °C.
2. $Y_1Ba_2Cu_3O_7$ (i.e. orthorhombic phase) is unstable at temperatures higher than 650 °C.

At 900–950 °C, the oxygen content per formula unit is less then 6.5 and the structure become tetragonal. If quenched in this form, the material is non-superconducting. To regain the oxygen to the desired value (i.e. close to 7), the material should be given a long anneal in O_2 in the temperature range of 400–500 °C, to enable the oxygen pick up. Otherwise oxygen can be incorporated by annealing at $\sim$900 °C in flowing oxygen for short durations and then, slow cooling in oxygen atmosphere.

The most widely used method is the conventional ceramic technique, which comprises the following steps:

(1) Weighing the appropriate amounts of starting materials.
(2) Mixing these powders to get a homogeneous mixture.
(3) Calcining the homogeneous mixture to get the reacted material.
(4) Grinding the calcined reacted powder to get the desired particle size.
(5) Shaping the ground powder by pressing (i.e. pelletizing).
(6) Sintering the shaped material.
(7) Annealing in oxygen with a slow cool to get the superconducting material.

The starting materials are Y_2O_3, BaO_2 and CuO. Mixing is done with an agate, mortar and pestle (for small quantities $\sim$10 gm). For larger quantities, one may use ball mill.

A. K. Saxena, *High-Temperature Superconductors,* Springer Series
in Materials Science 125, DOI: 10.1007/978-3-642-28481-6_4,

Calcining is carried out in the temperature range of 880–900 °C in air. The duration of this calcining can be fixed by intermittent checking of X-ray diffraction for the complete disappearance of the lines due to the reactants. Generally, 10–20 h should be sufficient, but many workers prefer to interrupt the heating, regrind and remix the powder and heat the same again to ensure a total conversion to the desired product.

This is followed by a grinding operation (in a ball mill or mortar and pestle).

The grinding time is such that the final powder becomes approximately micron sized. This powder is then shaped into the desired forms by using a suitable die and punch. The pressure used is generally $5{,}000\ 1\mathrm{b\,in.}^{-2}$.

Sintering is done in an oxygen atmosphere at temperatures around 920–950 °C, for a period ranging from a few hours to more than 24 h. The conditions are to be optimized to get as high density as possible.

The sample is then cooled slowly in an atmosphere of flowing oxygen. The rate of cooling is generally maintained at 1–2 °C per minute (particularly in the temperature range of 600–400 °C). Below 400 °C, the sample can be cooled faster.

Platinum crucibles can be used at the calcining stage, if the temperature is lower than 900 °C, but at higher temperature, sintering should be done on fused alumina plates (because platinum reacts with the material at temperature >900 °C). Other techniques used are sol–gel method and single crystal growth.

The samples so synthesized may be subjected to various characterizations, such as T_c-measurement by Vander Pauw technique, X-ray diffraction, J_c measurement, etc.

4.2 Why Thin Films of High T_c Superconductors?

High T_c superconductivity in the bulk material suffers from low current density, if the current in a sample is increased, a breakdown of superconductivity occurs. Furthermore, since the superconductivity effect is strongly anisotropic in a polycrystalline bulk, an unavoidable averaging of the superconducting properties of all crystal orientations takes place. However, once crystal growth is epitaxial, the super-current density can be increased over that of the poly-crystalline material.

The chemical, mechanical and electrical properties of the available bulk HTSC materials, however, are suitable for only few applications and a great deal of development effect is needed. However, applications involving superconducting thin films, much as hybrid superconducting/semiconducting circuits and microwave/millimetre wave devices seem to be closer in practice than applications of bulk materials.

Thin films are also important in surface studies, nucleation and growth studies, and in the production of meta-stable structures and compositions, consequently these facts necessitate the synthesis of HTSCs in thin film forms.

4.3 Techniques for Thin Film Preparation

The basic steps involved in thin film deposition-techniques are

(a) Creation of material to be deposited in an atomic, molecular or particulate form prior to deposition
(b) Transport of materials, thus, created onto the substrate in the form of vapour, stream or spray
(c) Deposition of material on the substrate and film growth by a nucleation and growth process

The deposition techniques can be distinguished by the way these basic steps are affected. One can, in principle, get films of desired properties by properly modifying these three steps.

The thin film deposition techniques can be broadly classified as physical vapour deposition (PVD) and chemical deposition. The PVD techniques are those in which the first step involves a physical process. In PVD, the thermal energy for the melting and vaporization can be provided by any of the following procedures:

(1) Resistive Heating

This method consists of heating the material with a resistively heated filament or boat, generally made of refractory metals, such as W, Mo, Ta or Nb, with or without ceramic coatings. The choice of the support material is determined by the evaporation temperature and resistance to alloying and/or chemical reaction with evaporant.

(2) Flash Evaporation

A rapid evaporation of a multi-component alloy or compound, which tends to distill fractionally, may be obtained by continuously dropping fine particles of the material onto a hot surface, so that numerous discrete evaporations occur. Alternatively, a mixture of the components in powder form may be fed into the evaporator. The fine powder is fed into a heated Ta or Ir boat by mechanically or ultrasonically agitating the feed chute.

(3) Electron-Beam Methods

The simple resistive heating of an evaporation source suffers from the disadvantages of possible contamination from the support material and the limitations of the input power, which make it difficult to evaporate high melting point materials. These drawbacks are overcome by an efficient source of heating by electron-bombardment of the material.

The simplest electron-bombardment arrangement consists of a heated tungsten filament to supply electrons, which are accelerated by applying a positive potential to the material for evaporating. The electrons lose their energy in the material very rapidly, their range being determined by their energy and the atomic number of the material. Thus, the surface of the material becomes a molten drop and evaporates. In contrast to this simple work-accelerated e-beam arrangement, one way is to use electron-optics to focus the beam and direct it onto the material for evaporation.

(4) Molecular Beam Epitaxy (MBE)

The deposition of single crystal epitaxial thin films by the condensation of one or more beams of atoms and/or molecules from Knudsen (effusion) sources under ultra-high vacuum conditions is called molecular beam epitaxy (MBE).

The Knudsen effusion source consists of a crucible containing the evaporant, with a small orifice. The orifice dimension is smaller than the mean free path of the vapour in the source cavity and the outflow of the molecules from the source is by effusion. The effusing molecular beam has a large mean free path compared to the source–substrate distance. The flux of the beam is precisely determined by the partial pressures of the vapour species within the chamber, their molecular weight source temperature and orifice dimension. A controlled growth of the film is achieved by the MBE technique.

(5) Sputtering

Sputtering, often described as playing billiard with atoms, is the ejection of target atoms by the impingement of ions from a persistent glow discharge with kinetic energies larger than the binding energy of the target atoms. The surface atoms are sputtered, when the kinetic energy of the incident particles is transferred to the target and the sputtered atoms condense on the substrate to form a thin film.

The process is significantly influenced by the energy and the angle of incidence of the impinging ions and the target material. The sputtering yield, defined as the average number of atoms ejected from the target per incident ion, increases with the increasing energy of ions and their mass (relative to the atomic weight of the target).

(6) Pulsed Laser Deposition (PLD)

Laser deposition is based on the rapid localized heating of a volume of target material determined by the absorption depth of the laser light and the thermal properties of the target. Typically, the combination of energy absorption and heating profile results in the vaporization of the material below the surface of the target leading to the fragmentation and outward projection of a small volume of the surface material. The target material is vaporized in a broad spatial distribution and not in a point-like evaporation.

Using pulsed laser radiation of high intensity, in front of the target surface, a plasma is generated and the vaporized material is ejected in a direct jet-like plasma stream. The forward directed nature of the material ejection results from anisotropic expansion velocities of the atomic species. The physics and chemistry of the whole process is roughly divided into the regime of photon/target interaction at the target site, the regime where the plasma formation and initial isothermal adiabatic expansion takes place, the regime of the adiabatic expansion, transport, relaxation and interaction with gases in the plasma phase and finally, the condensation on the substrate.

4.3.1 Chemical Deposition Methods

Chemical methods for thin film deposition may be broadly classified in two categories-(1) electroplating and (2) chemical vapour deposition (CVD).

(1) Electroplating or electrodeposition can further be subdivided into (a) Electrolytic deposition, (b) Electroless deposition and (c) Anodic oxidation. Electrolytic deposition utilizes the principles of electrolysis. In electroless deposition, electrolytic action is achieved (without an external potential source) by a chemical reduction process. Electroless deposition is used in the well-known technique of silvering glass dewars. A large number of metals (called "valve" metals) tend to form a protective oxide film of limited thickness, when exposed to oxygen. By anodic polarization of these metals in a suitable aqueous solution (which does not dissolve the oxide), a protective high-resistance film can be grown (Anodic oxidation). The anodization process involves the migration of ions of oxygen, metal or both, depending on the material, through the existing oxide film.

4.3.2 Chemical Vapour Deposition

When a volatile compound of the substance to be deposited is vaporized and the vapour is thermally decomposed or reacted with other gases, vapours or liquids at the substrate to yield nonvolatile reaction products, which deposit (in thin film form) on the substrate. The process is called chemical vapour deposition. Due to availability of a large variety of chemical reactions, Chemical Vapour Deposition (CVD) has been versatile and flexible technique in producing deposits of pure metals, semiconductors and insulators. In CVD, if thermal decomposition of a compound is used to yield a deposit of the stable residue, it is called pyrolysis.

4.3.3 Spray Pyrolysis

In spray pyrolysis, a solution (usually aqueous) containing soluble salts of the constituent atoms of the desired compound is sprayed onto a heated substrate. Every sprayed droplet reaching the hot substrate surface undergoes pyrolytic (endothermic) decomposition and forms a single crystallite, or a cluster of crystallites of the product. The other volatile by-products and the excess solvent escape in the vapour phase. The substrate provides the thermal energy for the thermal decomposition and subsequent recombination of the constituent species, followed by sintering and re-crystallization of the cluster of crystallites. The result is a coherent film. The chemical solution is atomized into a spray of fine droplets by spray-nozzle with the help of a carrier gas, which may or may not play an active role in the pyrolytic reaction involved. The solvent liquid serves to carry the reactants and distribute them uniformly over the substrate area during the spray process.

4.4 Basic Thin Film Processes for HTSC Films

Basic processes for the deposition of perovskite thin films are as follows:

1	Amorphous phase	$T_s < T_{cr}$
2	Polycrystalline	$T_s > T_{cr}$, $T_s < T_{cr}$ and post-annealing
3	Single crystals (On single crystal substrates)	$T_s > T_{epi}$ $T_s < T_{cr}$ and post-annealing (solid phase epitaxy)

Thin films of amorphous phase are deposited at the substrate temperature T_s below the crystallizing temperature T_{cr}. The T_{cr} for the perovskite type oxides is 500–600 °C. Thin films of polycrystalline phase are deposited at $T_s > T_{cr}$. The polycrystalline phase is also achieved by the deposition of the amorphous phase followed by post-annealing at the annealing temperature above T_{cr}.

Thin films of single crystalline phase are epitaxially deposited on a single crystal substrate at the substrate temperature above an epitaxial temperature T_e ($T_e \geq T_{cr}$). The amorphous thin films deposited on the single crystal substrate will be converted into the (single) crystalline thin films, after the post-annealing at annealing temperature above T_e owing to a solid phase epitaxy.

Various experiments carried out for the deposition of the high T_c thin films are classified into three as indicated in Table 4.1.

The process for the ceramics is composed of three stages: (1) mixing, (2) annealing for crystallization and sintering, (3) annealing for the control of oxygen vacancies.

For the thin films, three processes are considered. The process (1) is deposition at a low substrate temperature followed by the post annealing. This process is commonly used for the deposition of the high T_c superconducting thin films, since the stoichiometric composition of the thin films is easily achieved. However, the resultant films are polycrystalline. The single crystal films are possibly obtained by a vapour-phase epitaxy achieved in the process (2) and (3).

Lowering the synthesis temperature is much important not only for scientific interests but also for the fabrication of the thin film superconducting devices. The maximum temperature in the process (2) is governed by the post-annealing process for the control of oxygen-vacancies, however, the oxygen vacancies control will be attained at lower temperature, when the vacancies control is conducted by an oxygen-ion bombardment on the film surface during the film-growth. The structural analyses for the YBCO ceramics suggest that the structural transition from the non-superconducting tetragonal phase into the superconducting orthorhombic phase occurs around 600–700 °C. If the substrate temperature during the deposition T_s satisfies the relation

$$T_e \leq T_s \leq T_t,$$

where T_e denotes the epitaxial temperature and T_t, the transition temperature from tetragonal to the orthorhombic phase and if enough oxygen is supplied onto the film surface, during the deposition so as to oxidize the deposited films, the as sputtered

Table 4.1 Fabrication processes for the high T_c superconductive ceramics and thin film

		Chemical composition	Crystallization (°C)	Oxygen vacancy control (°C)
Ceramics		Mixing	Sintering 850–950	Annealing [a] 850–950
Thin films	1	Deposition ($T_s < T_{cr}$)	Annealing 850–950	Annealing [a] 850–950
	2	Deposition ($T_s > T_{cr}$)		Annealing [a] 600–950
	3	Deposition ($T_s > T_{cr}$)[b]		

T_s is substrate temperature during deposition, T_{cr} is crystallizing temperature (500–600 °C)

[a] slow cooling

[b] quenching

Table 4.2 Fermi energy in 10^5-cal. mole^{-1} at 1190 K for various simple oxides

Y_2O_3	BeO	MgO	ZrO_2	Al_2O_3	SiO_2
1.11	1.15	1.12	1.04	1.03	0.79

films show single crystal phase and reasonably exhibit superconductivity without the post-annealing process through in situ process, which is characterized in process (3).

In the case of the metallic atoms of YBCO, computation shows that in the range of 1,100–1,300 °K, the largest E_F is due to Y_2O_3. Table 4.2 shows E_F in 10^5-cal. mole^{-1} at 1,190 K for Y_2O_3 and various simple oxides.

From this table, one can infer that BeO and MgO, whose E_F are larger than E_F for Y_2O_3 could be good substrates for YBCO films [1].

Thin film growth techniques can be broadly classified into the following two undermentioned categories:

	Those requiring high temperature, post-deposition annealing (Ex situ annealing)		Film is grown in correct crystalline form during growth (In situ growth techniques)
1.	The crucial growth step takes place after deposition, i.e. during annealing The film crystallizes by a solid state re-growth mechanism to form a polycrystalline but epitaxial layer	1.	Although, some low temperature annealing may be required to achieve correct oxygen stoichiometry, but it requires no substantial rearrangement of the lattice after growth:
2.	The actual technique used to deposit the layer is of only secondary importance because the crucial growth step takes place long after deposition	2.	Advantages: (a) Lower temperatures involved minimize contamination from the substrate (b) single crystal films can be grown with improved physical properties (c) film surface can be smooth
3.	All the known HTSCs can be grown by processes involving ex situ annealing All the reported films with $T_c > 100$ K have been made by careful ex situ annealing	3.	BSCCO and TBCCO are very difficult to be prepared by in situ technique

4.5 Various Techniques for Deposition of Films of High Temperature Superconductors

The synthesis of high T_c thin films involves the problem of the deposition of a large number (three to five, for the different compounds) of metallic constituents in a fairly well controlled manner as well as the crystallization in the correct structure and the oxygenation for the desired doping of holes. Hence, due to the complexity of the HTSCs with respect to the number of constituents and oxygen stoichiometry, their preparation as epitaxial films was a certain challenge for the scientists in various disciplines. It was barely a few months after the discovery of superconductivity above 77 K that the first films of these complex multi-element materials were prepared [2]. This was accomplished first by multi-element deposition techniques. Later, other techniques, such as multisource electron beam evaporation, MBE (molecular beam epitaxy), sputtering, laser ablation, chemical vapour deposition and spray-pyrolysis etc. were used efficiently for the synthesis of high quality HTSC films on a variety of substrates.

The various routes to high T_c thin films differ in the substrate temperature during deposition (T_s), or in other terms, whether the original film is grown in the form of amorphous or micro-crystalline ($T_s < 500\,°C$) or directly in the tetragonal high resistance phase ($T_s > 600\,°C$), which converts into the superconducting orthorhombic phase during cooling in an oxygen atmosphere. The former processes are termed as ex situ, whereas the latter ones are in situ techniques. Table 4.3 shows a flow chart of different preparation routes. Crystallization and oxygenation in the ex situ techniques can be accomplished by different means, such as furnace annealing, rapid thermal annealing (RTA), or low energy plasma processing for the oxygenation [3]. All these techniques have some specialized advantages, such as low thermal budget for the TA process and this minimized substrate film interaction. The heat treatment leads to an epitaxial growth starting from the substrate/film interface. Apart from the deleterious film/substrate interaction, another disadvantage of route I is the sensitivity of the film properties to complicated processing sequence for crystallization and oxidation. This results in films with low T_c and J_c.

The alternative approach of route II yields an in situ crystallization in the tetragonal phase, which upon cooling in oxygen converts to the superconducting orthorhombic phase. Here, epitaxial growth can be achieved directly, and films show superior qualities such as high T_c and sharp transition, high J_c and low surface resistance.

4.6 Preparation of Thin Films of HTSC-$YBa_2Cu_3O_{7-x}$: An Introduction

The announcement of superconductivity above 30 K in the La–Ba–Cu–O system by Bednorz and Muller and the subsequent discovery of Y–Ba–Cu–O superconductor by Wu et al. spurred the scientists world over to make an unprecedented effort to

Table 4.3 Flow chart for high T_c superconducting thin film preparation

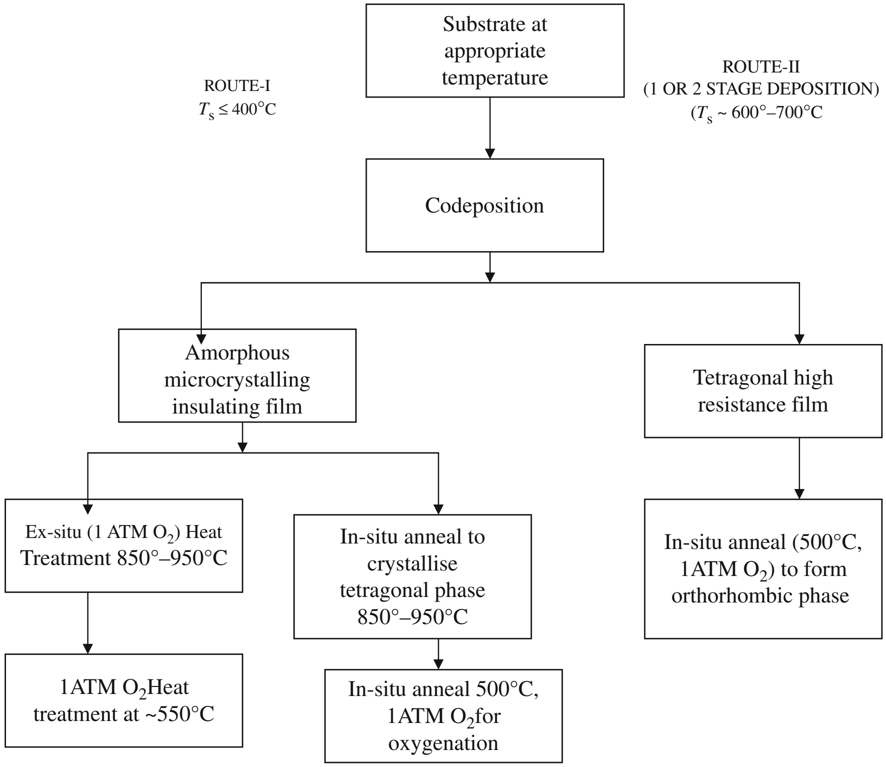

explore both the physical mechanism underlying this phenomenon and its obvious technological potential. From both viewpoints, the preparation of the superconducting films was an important step. In the beginning, the preparation of the bulk superconducting oxide samples, using conventional ceramic techniques (grinding, firing and pelletizing), became well established and was reproduced by many researchers. One drawback of the polycrystalline versions in which HTSCs were initially synthesized was low critical current density (J_c), which was about 10^2–10^3 A cm^{-2}. The usual magnitudes of J_c which, for example, is achievable from conventional superconductors is about 10^6 A cm^{-2}. Such a value would be useful for most of the devices, particularly high current ones, like high field electromagnets, lossless transmission, levitating vehicles, MRI etc. At the early stage, it was recognized that low J_c values were due to weak-link effects arising from the presence of high angle grain boundaries separating adjacent gains and also because of absence of suitable flux pinning centres within the grains. Since thin films are necessarily grown on substrates, by proper choice of substrates suitably oriented films without high angle grain boundaries could be prepared and since thin film formation is like vapour quenching, secondary phase forming flux pinning centres might get nucleated. Therefore, formation of thin films of HTSC materials held considerable promise. However, preparing thin films of these materials turned out to be a more difficult task. The first successful deposition using sputtering, from bulk materials, was reported for the $\sim$40 K superconductors [4, 5], including the preparation of microcrystalline thin films [6].

The first report on the formation of thin films of Y–Ba–Cu–O was through electron beam evaporation of individual ingredients by Chaudhari et al. [7]. Later on, other techniques like screen printing, on beam sputtering [8] and pulsed laser evaporation [9] were employed for the synthesis of thin films of these YBCO HTSCs.

4.6.1 Choice of the Substrate for Thin Film Deposition

An ideal substrate should be

(1) Chemically non-contaminating
(2) Having good lattice and thermal expansion match to the film within 5%
(3) Cheap in large size single crystals
(4) Having low dielectric constant and loss
(5) Easily cut and polished
(6) Able to withstand oxidizing atmosphere involved in the fabrication process. Strontium titanate has been the substrate of choice, since it seems to fulfill the best combination of inertness, thermal expansion and lattice matching. However, it is not a perfectly inert substrate material and its ferroelectric properties could be unsuitable in many applications. Zirconnia (ZrO_2) and MgO have much better inertness, but have poor lattice matching properties. $LaAlO_3$ and $LaGaO_3$ are recently developed substrates with improved lattice matching and dielectric properties. Crystallinity, lattice constants, thermal expansion coefficients and dielectric constant of the substrate are quite critical to the final properties, particularly morphology of the deposited films. Table 4.4 gives some details of the crystal substrates and their properties for cuprate superconductors.

Table 4.5 lists dielectric properties of $LaAlO_3$ and other commonly employed substrates.

4.6.2 YBCO Film/Substrate Interaction

One of the crucial aspects related with the formation of thin films, which decides the viability and the physical properties, e.g. texturing and the related parameter “J_c”, depends on the film–substrate interaction effect. In all film depositions, a post-deposition heat treatment is required and it is during this treatment that most of the

Table 4.4 Some selected substrate materials for deposition of high T_c superconductor films

Material	Structure	Lattice constants A^0	Thermal expansion coefficient (K^{-1})	Dielectric constant
Y–Ba–Cu–O	Orthorhombic	3.88, 3.86, 11.67	15×10^{-6}	–
$SrTiO_3$	Cubic	3.905	10×10^{-6}	180
$Y-ZrO_2$	Cubic	5.16	10×10^{-6}	7.8
MgO	Cubic	4.21	12×10^{-6}	9.7
Si	Cubic	5.43	3×10^{-6}	12
SiO_2	Hexagonal	4.91, 5.394	1×10^{-6}	3.8
Al_2O_3	Hexagonal	4.76, 12.9	6×10^{-6}	10.2
Gadolinium Gallium Garnet	Cubic	12.383	8×10^{-6}	15
$MgAl_2O_4$	Cubic	8.085	8×10^{-6}	–
$LaGaO_3$	Orthorhombic	5.52, 5.49,7.77	–	27
$LaAlO_3$	Rhombohedral	5.357, 60°6′	10×10^{-6}	15
$LiNbO_3$	Hexagonal	5.15, 13.86	–	–

Table 4.5 Dielectric properties of substrates suitable for deposition of high T_c thin films

Material	Al_2O_3	ZrO_2	$SrTiO_3$	MgO	$LaAlO_3$
Dielectric constant					
at 300 K	9.87	26.1	310	9.1	15.3
at 77 K	9.6	25.4	1900	20.5	15.3
Dielectric loss tangent					
$\tan\delta$ (300 K)	2×10^{-4}	1.7×10^{-2}	3.2×10^{-2}	2.2×10^{-5}	5.8×10^{-4}
$\tan\delta$ (77 K)	4.2×10^{-5}	7.5×10^{-3}	5.8×10^{-2}	4.9×10^{-6}	8.3×10^{-5}

film substrate interaction takes place. The interaction with substrates can further be divided into three groups:

1. Reaction between film and substrate
2. Lattice matching
3. Matching of thermal expansion coefficients between the film and substrate

A schematic representation of the interaction between the film and substrate is shown in Fig. 4.1. The film and substrate react at the interface establishing either a reaction zone where new compounds are formed with structures differing from both, the deposit and the substrate, or a zone with a composition gradient where diffusion or inter-diffusion has taken place between the film and the substrate without the formation of new structures. The new zone continues to grow with time and temperature.

Of the substrates that have been used, the best is YSZ (yttria stabilized Zirconia), followed by BaF_2, $SrTiO_3$, MgO, Al_2O_3 in order with Al_2O_3, the worst.

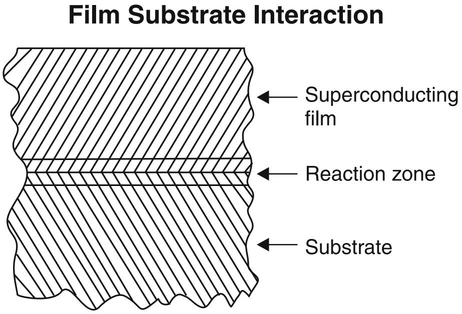

Fig. 4.1 Schematic of the interaction between the $YBa_2Cu_3O_7$ film and the substrate after annealing at ∼900°C

Table 4.6 Results for YBCO films using different buffer layers on sapphire substrate

Substrate	Deposition temperature (°C)	Buffer layer material (thickness)	T_c (k)	J_c
Al_2O_3	450	Plain (no buffer layer)	75	4×10^3 at 40 K)
Al_2O_3	450	MgO (500 Å)	78	9×10^3 (at 40 K)
Al_2O_3	450	$BaTiO_3$ (500Å)	83	4.5×10^{-4} (at 40 K)
Al_2O_3	450	Ag (thickness not known)	75	–

Many studies of YBCO thin films have shown that interdiffusion or reaction can occur with almost all substrate materials including Si, Al_2O_3, $SrTiO_3$, ZrO_2 and MgO [10–14].

In some cases, the diffusion of small amounts of metal ions from the substrate material into the superconducting YBCO should not cause a prominent decrease in T_c [15]. However, the depletion of elements from YBCO can leave behind non-superconducting material. For most substrate materials, Ba^{2+} ions diffuse most quickly to the substrate film interface, forming a Ba-enriched layer or second Phase. Cu^{2+} ions also tend to diffuse toward the interface. The degree of inter diffusion varies strongly with substrate material and the maximum temperature to which the films are exposed. MgO and Y_2O_3-stabilized cubic ZrO_2(YSZ) seem to be two of the less reactive of the materials mentioned above. YSZ buffer layers have been studied with success as a way of limiting the problem of highly reactive substrate, such as Si and Al_2O_3. Witanachchi et al. [16] have studied the effect of buffer layers on low temperature (i.e. in situ) growth of mirror-like superconducting thin films of YBCO on sapphire (Al_2O_3), utilizing plasma-assisted laser deposition. Their results are summarized in Table 4.6.

MgO and $BaTiO_3$ improved the value of T_c, while Ag showed a slightly semi-conducting behaviour near T_c. The Ag buffer also improved the normal state resistivity of the YBCO film at room temperature. Optical and scanning electron microscope (SEM) examination showed that the films were mirror-like and very smooth (surface roughness $<0.1\ \mu m$), which is in contrast with the films made by high temperature post-annealing, which showed $>1\,\mu$m micro-crystal structures intercalated in a pseudorandom fashion [17, 18]. The X-ray diffraction (XRD) patterns of the $YBCO/BaTiO_3/Al_2O_3$ showed formation of highly oriented film with c-axis perpendicular to the surface. The same results were obtained for the MgO buffer case. The directly deposited film ($YBCO/Al_2O_3$) was not well oriented and its XRD revealed diffraction peaks other than (001). Thus, the MgO and $BaTiO_3$ buffer layers improved the crystalline structure as well as the J_c of the films.

In the subsequent sections, we proceed to describe the various thin film deposition techniques employed for the synthesis of YBCO superconducting thin films.

4.7 Techniques Employed for Synthesis of YBCO Thin Films

4.7.1 Electron Beam Evaporation

This technique involves the use of thermionically produced electron beams with energies in the range of 5–10 keV, magnetically deflected and focused onto elemental, metallic or alloy or oxide targets located in water cooled holder. The constituents in a complex ceramic composite having different melting points and vapour pressures do not evaporate congruently by this method. In such cases, the deposition of non-stoichiometric films is achieved. This has been observed in the deposition of YBCO high T_c superconducting films by evaporating single phase target of Y–Ba–Cu–O material [19]. Here, the major problem encountered was that the target thermally decomposed into the original and stable oxides, such as CuO, BaO and Y_2O_3 (CuO evaporated first, followed by BaO and Y_2O_3). This resulted in yttrium-deficient films and an extra Y-layer was necessary to achieve the 123 stoichiometry. This problem was significantly overcome by evaporating constituent elements in their respective stoichiometry by precisely controlling the flux of the molecular or atomic beam independently [20]. The schematic view for typical e-beam co-evaporation systems is shown in Fig. 4.2.

Evaporation is usually done in a high vacuum chamber (pressure $= 10^{-7}$ torr). Pure Y and Cu are normally evaporated with electron guns and Ba with an effusion cell [21]. Instead of Ba-metal, which easily oxidizes, inert and easily handled compounds, such as BaF_2, or $BaCO_3$, or BaO or BaO_2 have been used. It is interesting to note that films made from BaF_2 contain only a small amount of fluorine ($<5\,\%$), which does not affect the superconducting properties.

Films deposited in ultra-high vacuum from the metal sources were very unstable in air. Exposure to a small partial oxygen pressure (10^{-3}–10^{-5} torr) caused oxidation of Y and Ba and improved the stability. However, the as deposited films were sensitive to ambient moisture and immediate annealing in oxygen atmosphere was required to stabilize the film and form the orthorhombic superconducting phase.

The metals have usually been deposited as a set of metallic tri-layers and the layer thickness adjusted so that the desired 123 stoichiometry was obtained. The number

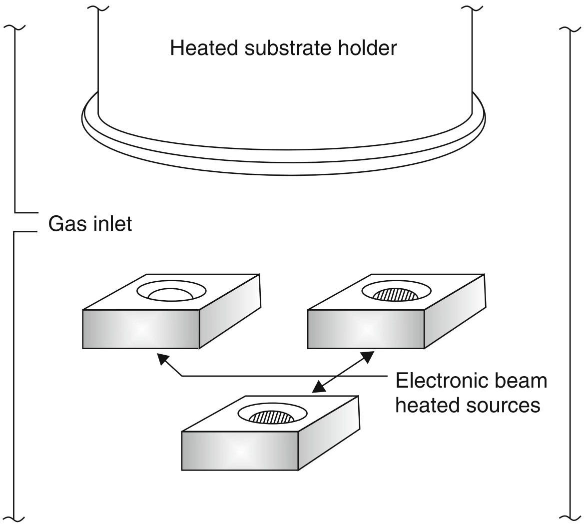

Fig. 4.2 A schematic diagram showing e-beam evaporation process

and order of the layers vary in different studies, but Cu was generally used for the first layer because it has the lowest oxygen affinity and substrate interactions may, therefore, be minimized. The sequence Ba, Y, Cu has also been used [22].

Substrate temperatures ranging from room temperature to 900 °C have been used, the most popular region being 300–500°C. According to Laibowitz [23], film stability is increased at elevated substrate temperatures (450 °C). According to Naito [10], the substrate temperature does not significantly affect T_c, but it influences J_c and the shape of R vs T curve. High J_c values were measured on samples deposited at ambient temperature on $SrTiO_3$. The reason for this behaviour lies in the orientation of the 123 phase. With high T_s (∼700–900 °C) depositions have random orientations, while at medium T_s (300–500 °C) the a-axis is perpendicular to the film. In films deposited at low temperatures, the texture is such that the c-axis is strongly and the a-axis is weakly perpendicular to the substrate. The highest J_c value reported for evaporated films is 10^6 A cm^{-2} at 81 K.

The microstructure of evaporation deposited 123 films on $SrTiO_3$ depends on the experimental conditions. Naito et al. have explained columnar structure, which indicates the c-axis is oriented perpendicular to the plane of the film.

4.7.2 Molecular Beam Epitaxy

This method has been extensively used for the deposition of epitaxial compound semiconductor thin films. Kwo and co-workers [24] applied this technique for the preparation of ceramic superconductor films. In the case of YBCO deposition, films with 123 stoichiometry have been produced by using metals as source materials. Generally, the three metals are simultaneously deposited by concentrating the vapour fluxes of three sources onto a substrate centrally located with respect to the sources symmetrically distributed on a circular area. The rate of deposition of each is first, individually calibrated, stabilized and subsequently adjusted to yield the desired 123 stoichiometry.

Oxygen was usually introduced to the growing film by a precision leak valve. The base pressures were typically $\leq 2 \times 10^{-10}$ torr. Prior to film growth, oxygen was blowed into the system and the background pressure increased to 10^{-7} torr. During film growth, the pressure above the film was $\sim 10^{-5}$ torr. The reported growth temperatures vary from ambient to 450 °, 530–560 ° or 600–750 °C. The substrates used were (100) Si, $\left(1\bar{1}02\right)$ sapphire, (100) yttria stabilized ZrO_2, (100) MgO and (100) and (110) Sr TiO_3. No superconductivity was observed on Si, while the highest transition temperatures were obtained on $SrTiO_3$ (82 and 89 K) and MgO (82K). On (100) $SrTiO_3$, MBE grown 123 films have shown strong orientation (a-axis normal to the surface). With a lower substrate temperatures (300 °C), better 123 stoichiometry was obtained with c-axis oriented perpendicular to the film [25, 26]. The c-axis oriented films have a higher degree of structural order, lower normal state resistivity and higher J_c than the a-axis oriented films.

Due to the strong orientation of the MBE grown films, the critical current values measured were high compared to average sputtered or evaporated films. The values are $\sim 10^6$ A cm^{-2} at 4.2 K and $>10^5$ A cm^{-2} at 77 K. The requirements for high T_c and J_c values are high purity (no other phases than 123), minimum number of grain-boundaries and high orientation of a-axis perpendicular to the substrate surface. Growth by MBE seems to fulfill these requirements.

4.7.3 *Sputter Deposition*

Sputtering process is the ejection of individual surface atoms from the solid surface by momentum-transfer from high energy bombarding ions to surface atoms.

The process basically involves a series of nearly elastic collisions between a projectile-atom and target atoms. A projectile atom, typically a noble gas ion (e.g. Ar^+) is accelerated towards the sputtering target. Upon impact with the target, the projectile atom may

(1) Leave the target by scattering (reflecting) backward, and transfer only part of its energy to target atoms, or
(2) Remain embedded (implanted) within the target and so transfer all of its energy to the target. The target atoms, which receive sufficient energy in the direction away from the target (to overcome their binding energy), may leave the target and traverse through the gas phase; these atoms are said to be sputtered. The sputtered atoms will generally re-condense on the first solid surface they come in contact

> with, and in this manner, a film of the target material will grow, predominantly, atom-by-atom, on surface opposite to the target.

Because of the higher kinetic energy of the sputtered flux, sputter deposited ad-atoms have higher mobilities than do evaporated adatoms, producing better morphologies and microstructures that can be advantageously exploited for superconductor thin film applications. The advantage of sputtering over evaporative methods is that high quality films with good adhesion can be obtained because, as a result of enhanced mobilities of the adatoms, it would be possible to obtain epitaxial films at much lower substrate temperatures than those obtained by other techniques.

However, its low deposition rate of 20–100 $\text{Å}\,\text{min}^{-1}$ is its main drawback as long hours of sputtering are required for preparing films of significant thickness. To use it as an effective deposition technique, a large number of incident ions must strike the target per second. The method used to generate the ion-bombardment is the distinguishing feature of the many sputtering techniques utilized. The simplest experimental set up is that of dc-diode sputtering. The ions are generated in a glow discharge plasma, a mixture of neutral gases, ions and electrons sustained by an applied potential (The name "diode" indicates that this is a two electrode discharge: target is the cathode and the substrate platform (or entire chamber) is made the anode). The negative bias applied to the target (typically $\sim 1{,}000\,\text{V}$) accelerates incoming positive ions, resulting in sputtering, secondary electron emission and noble gas reflection.

Electrons emitted from the target accelerate away due to the negative potential and may collide with gas atoms, ionizing them. These emitted secondary electrons are then mainly responsible for sustaining the plasma. In order to sustain the plasma, the pressure must be controlled and be well below the atmospheric pressure. Also, the sputtering gas must be very pure to obtain a film of high purity. The chamber is first evacuated to low pressure and then, the required pressure is achieved by flowing the sputtering gas into the system. At this point, the potential is applied to ignite the plasma and begin sputtering. The main parameters describing the sputtering process in this case are

(1) Sputtering pressure
(2) The applied voltage
(3) The sputtering (ion) current at the target

The power applied at the target may be either dc or rf, rf power is necessary when sputtering an insulating target to avoid a charge build up at the surface.

Figure 4.3 illustrates different sputtering configurations.

Other sputtering techniques commonly employed are magnetron sputtering, triode sputtering and ion beam sputtering.

The difference between magnetron and diode sputtering systems is the application of a magnetic field at the target. The magnetic field and the electric field combination very effectively confines electrons enabling more gas to be ionized per electron and so, a higher sputtering current is obtained at a lower sputtering voltage and less secondary electrons will bombard the substrate during film-growth [27].

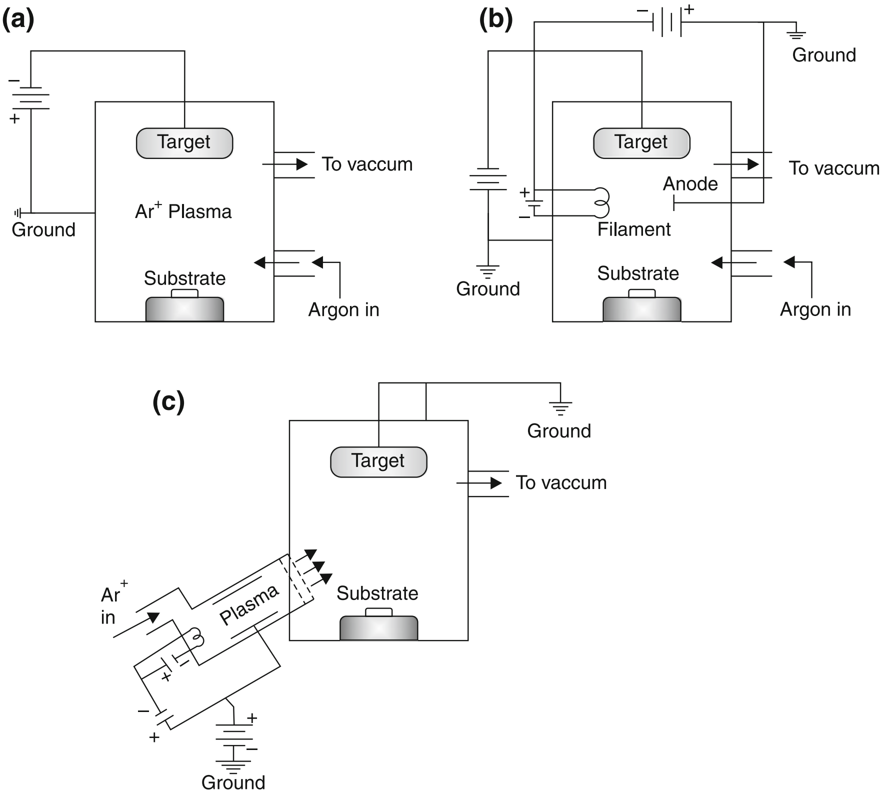

Fig. 4.3 Schematic illustrations of **a** diode sputtering **b** triode sputtering and **c** ion-beam sputtering

The magnetron has the advantage of operating with higher deposition rates and with less electron and energetic atom bombardment during growth than in diode system. Because of its good operational stability, it is generally the preferred technique.

In the triode sputtering arrangement, instead of relying on the secondary electrons emitted from the target, to sustain the plasma discharge, a third electrode (typically a hot filament cathode) is used to inject electrons into the plasma. The plasma is then sustained between the hot filament (cathode) and the anode, with the target as the third electrode, which can be biased independently. This allows more control over the process parameters, compared to the diode and magnetron systems. However, the hot filament makes the triode configuration less rugged than the other methods [28].

The ion-beam sputtering technique employs a confined ion-source, which serves to produce the plasma and to accelerate the ions towards the target. In this case, the sputtering parameters are totally independent of the target. The ion beam technique offers the control of the triode system with the advantage that no target-bias is necessary and the energy and direction of the incident ions are better defined [29].

4.7.4 Sputter Deposition of HTSC Films

Sputtering offers certain advantages over other thin film deposition techniques for the growth of high T_c films. Because of the higher kinetic energy of the sputtered flux, sputter deposited adatoms have higher mobilities than do evaporated adatoms, producing morphologies and microstructures that can be advantageously exploited for superconductor thin film applications. In addition, as a result of the enhanced mobilities of the adatoms, it is possible to obtain epitaxial films at much lower substrate temperatures than those obtainable by other techniques.

The first sputter deposited superconducting thin films were Sr–La–Cu–Oxides, but majority of studies were on the YBCO system [30]. All types of sputtering techniques, including dc diode, dc triode, rf diode, dc magnetron and rf magnetron have been employed in the studies, but rf magnetron sputtering is the most commonly used method. As a sputtering gas usually argon is used, desired chemical reactions of the sputtered atoms/ions in the plasma can be achieved by adding reactive gases to the sputtering gas.

In the case of YBCO and other multi component oxide system, tremendous problems arise from the formation of negatively charged particles at the target (cathode) side. Elements with a large electronegativity difference (e.g. oxygen and the alkaline earth metals) form negative ions, which are accelerated away from the target by the potential difference of the cathode dark space. This energetic particle flux is directed to the substrate in conventional sputtering geometries leading to selective re-sputtering of the growing film, which modifies the film composition or gives rise (in extreme cases), to etching of the substrate rather than deposition. To overcome these problems, following four different routes are used:

(1) To work at gas pressures high enough to reduce the kinetic energy of the ions striking the substrate below the binding energy [31].
(2) To place the substrate off-axis so it will not face the cathode [32].
(3) To design the system for a minimum discharge voltage [33].
(4) To adjust the target composition for a compensation of the re-sputtering effects [34].

Practically, a huge variety of different arrangements of target-substrate position and target configurations have been tried for in situ processes. The sputtering source configurations include multi-target arrangements using metal, metal alloy or metal oxide targets, single ceramic Y:123 targets, single off-stoichiometric YBCO targets and stoichiometric Y:123 hollow cylindrical targets. A comprehensive review covering the developments till 1988 has been given by Leskela [35].

Among several different sputtering techniques, magnetron sputtering offers additional advantages, in that deposition at lower sputtering pressure and target power density is possible. This, in combination with the secondary electron confinement at the target due to the applied magnetic field helps to prevent re-sputtering and heating of the growing film. Figure 4.4 illustrates popularly used magnetron sputtering employing the off-axis geometry first demonstrated by researchers at IBM.

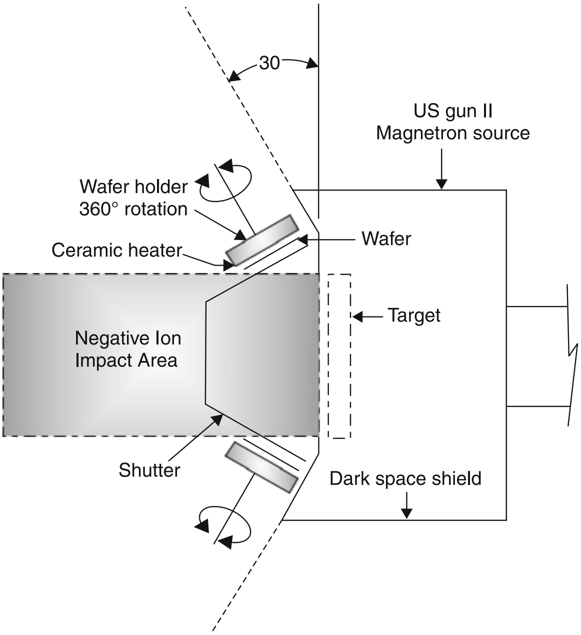

Fig. 4.4 A schematic diagram of off-axis sputtering process

Sandstorm et al. [36] have also described the use of single target rf magnetron sputtering in off-axis geometry that has allowed routine production of high T_c $YBa_2Cu_3O_{6+x}$ films from a slightly composition compensated target (+6 % Y, −7 % Ba).

The $SrTiO_3$ substrates (held at 350°C) are placed outside the region of head-on negative ion flux, but still immersed in the outer edge of the plasma region. Substrate wafers are held on individual heated holders that are rotated to facilitate the achievement of uniform thickness and composition. The sputtering process is carried out in a small chamber evacuated with a $360\,\mathrm{l\,s^{-1}}$ turbo pump and having a base pressure of 10^{-7} torr. Typical plasma parameters are 100 W of rf power at 10 MHz, ∼165 V dc self bias with a 98 % Ar, 2 % O_2 gas flow mixture at 6 m Torr total pressure. Deposition rates are 7–10 nm min, so that run durations of 40–60 min are required to yield the ∼400 nm thick films. With high temperature (850°C) ex situ anneals, completely superconducting films (at T_c∼86–89 K) were obtained. J_c at 77 K ranged from 10^4 to $8 \times 10^5\,\mathrm{A\,cm^{-2}}$.

4.7.5 Pulsed Laser Deposition

At present, it is an efficient technique for the preparation of high quality YBCO thin films and is a much faster technique than off-axis sputtering. The first application of

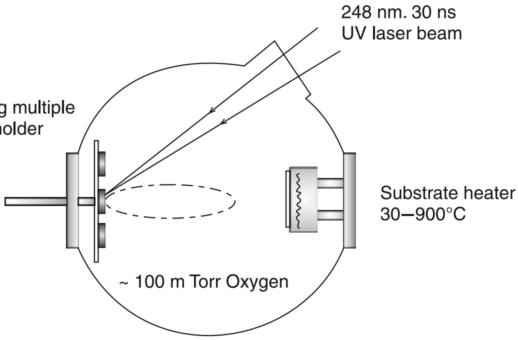

Fig. 4.5 A schematic diagram of experimental set up used in pulsed laser deposition process

pulsed lasers to the deposition of HTSC materials was demonstrated by the Bellcore-Rutgers group in 1987. Figure 4.5 illustrates schematically the Bellcore-apparatus used for laser deposition. The target, in the form of a pellet (about 2.5 cm in diameter, 6 mm thick) of YBCO, is mounted on a rotating holder in a vacuum chamber with a base pressure of about 2×10^{-7} torr and is irradiated through a quartz window by the output of 1 J pulse^{-1} KrF excimer laser. The targets are rotated during deposition to ensure that the beam always encounters fresh material. A quartz lens is used to forces the beam onto the target to achieve an energy density $\sim 1-2$ J cm^{-2}. The substrate is mounted on a heater positioned about 8 cm from the target. Film growth proceeds as material is ablated from the source disk and deposited onto the substrate. The rate of deposition is ~0.2 A° pulse^{-1} at a laser repetition rate of 5 Hz. A typical set of deposition parameters [37] is

Wavelength 248 nm [Kr F]
Energy density 1−2 J cm^{-2}
Target spot size 3 mm^2
Substrate target distance 3–4 cm
Oxygen background pressure 1 m bar
Substrate temperature 780 °C

4.7.6 Chemical Vapour Deposition

In this technique, the metal organic compounds are used as the source for the deposition of the oxide thin films. The chemical reaction is initiated at or near the substrate surface, which produces the desired material in the form of thin film. Organic precursor compounds bearing the required metal atoms are heated and an inert gas mixed with oxygen transports the resultant vapours into a reaction vessel containing a heated substrate onto which the deposition occurs (Fig. 4.6).

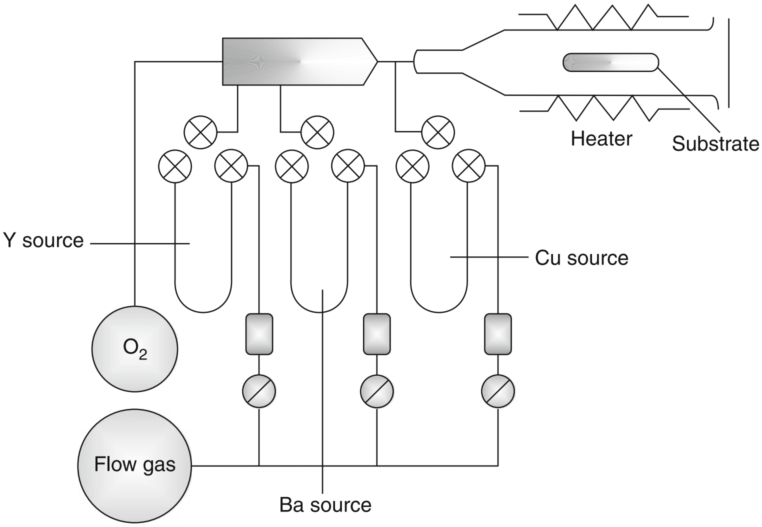

Fig. 4.6 Schematic illustrating metal organic chemical vapour deposition (MOCVD)

One of the few compounds in which both rare-earths and alkaline earths are volatile are β-diketonates, which have been used in gas-phase thin film growth. Berry et al. reported MOCVD growth of Y-123 films using β-diketonates as sources and N_2 as carrier gas. Film growth occurred via depostion of the reactant gases on a MgO substrate surface in an O_2 rich atmosphere. The as-deposited films were amorphous, but a semiconducting film with a T_c of 20 K was obtained after annealing at 890–920 °C. The quality of the film could be improved by optimizing the growth conditions.

Yamane et al. [38], Nakamori et al. [39] and Zhang et al. [40], have used the (2, 2, 6, 6-tetramethyl-3, 5-heptanedione) β-diketonate complexes of Y, Ba and Cu as source materials in their CVD experiments. Epitaxially growth films were obtained on (100) $SrTiO_3$ and yttria stabilized ZrO_2 at substrate temperatures of 650 and 900 °C. Oxidation was performed in situ after the deposition and T_c and J_c values of 84 K and 2×10^4 A cm^{-2} (at 77 K) respectively were measured.

4.8 Film Substrate Lattice Matching and Buffer Layer Considerations

High temperature superconducting films of YBCO and BSCCO were deposited on different substrates using conventional techniques like evaporation and spray pyrolysis [41]. The micro structural investigation of the films by Scanning Electron Microscopy revealed the partially oriented nature of the crystallites. In the case of

Table 4.7 Lattice mismatch calculations [41]

Substrate and substrate structure (Å)	Lattice mismatch for $Bi_2Sr_2CaCu_2O_8$ (a = 5.399 Å; b = 5.414 Å; c = 30.904 Å)		
	along a (%)	along b (%)	along c (%)
MgO (F.C.C. NaCl type) $a = 4.20A$	$M_a = 8.87$	$M_b = M_a = 8.87$	$M_c = 5.05$
$SrTiO_3$ (Perovskite cubic) $a = 3.90A$	$M_a = 1.92$	$M_b = M_a = 1.92$	$M_c = 1.08$
Y-stabilized ZrO_2 (f1ourite cubic) $a = 5.16A$	$M_a = 4.63$	$M_b = 4.92$	$M_c = 0.18$

spray-deposited film, R–T monitoring revealed a striking result that the film lattice/substrate mismatch does not affect the transition temperature: It was observed that R-T curves for the three film configurations viz. Bi-Sr-Ca-Cu-O/MgO, Bi-Sr-Ca-Cu-O/$SrTiO_3$ and Bi-Sr-Ca-Cu-O/YSZ led to the same transition temperature. The calculated values of lattice mismatch is given in Table 4.7. It may be noted that the largest mismatch is for Bi-Sr-Ca-Cu-O/MgO and the smallest value corresponds to Bi-Sr-Ca-Cu-O/$SrTiO_3$. A model of the film/substrate matching is shown in Fig. 4.7, [41]. The Jc of these films measured on some films was ~100–500 A/cm^2. The microstructural characteristics (as monitored by SEM) for spray deposited films revealed platelet characteristic of the film where the film was parallel to a–b plane in case of film deposited on Sr TiO_3. On the other hand, curled petal shaped growth morphology and some cylindrical shaped growth of crystallites were seen in films on MgO and YSZ.

It is worthy of note here that the structure of the film at an initial stage of the epitaxial growth strongly depends on the substrate crystal [42]. The lattice matching between YBCO and the substrate crystal is of essential importance.

Ultra thin films grown directly on Sr TiO_3 and MgO have distorted lattices, imperfections and discontinuity. Therefore Terashima et al. [43, 44] used a Pr-Ba-Cu-O buffer layer as a substrate. PrBCO has favourable properties for being the buffer layer for the formation of a one-unit-cell-thick YBCO layer: (i) PrBCO of the same 1:2:3 structure with lattice constants very close to those of YBCO (lattice mismatch $\leq 1.5\,\%$) is a semiconductor even in its fully oxidized state and has a high resistivity at low temperatures (ii) Flatness of the substrate surface on the atomic scale was a basis for the growth of a continuous one-unit-cell-thick YBCO layer. The films were grown by co-evaporation of the metal elements under an oxygen atmosphere, and the process was called reactive evaporation. The one-unit-cell-thick YBCO layer was a sandwich between the PrBCO layers. The underlying PrBCO layer plays the role of a *buffer layer* having a very good lattice matching. The covering PrBCO layer grown on the one-unit-cell-thick YBCO layer was found to be of significance in providing it with holes and thereby inducing superconductivity. In the recent past (1993), super lattice of (110) oriented $YBa_2Cu_3O_{7-x}$/$PrBa_2Cu_3O_{7-x}$ (i.e. YBCO/PrBCO) were

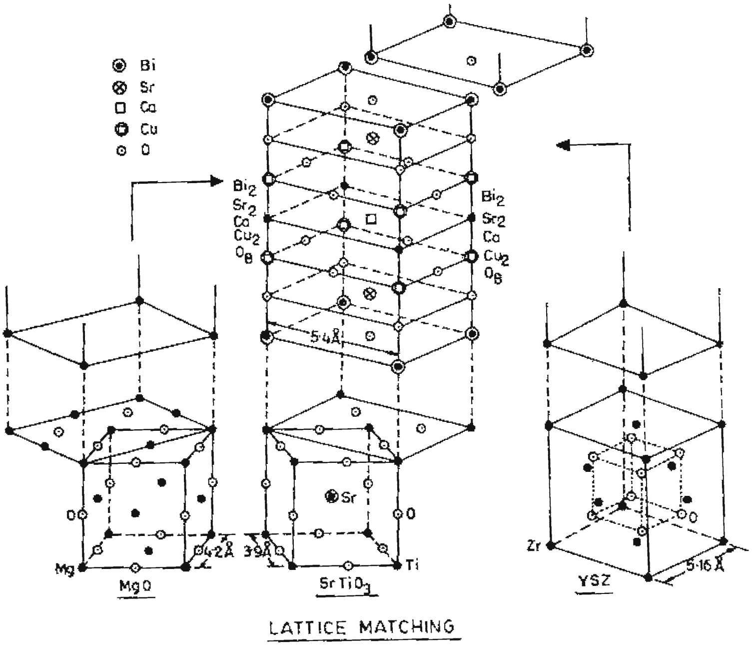

Fig. 4.7 A model of possible planes of matching for Bi-Sr-Ca-Cu-O films over MgO, $SrTiO_3$ and Yttria stabilized zirconia (YSZ) [41]

grown on $SrTiO_3$ (110) substrates by I.E. Trofimove et al [45] using in situ pulsed laser deposition technique. X-ray and Raman studies confirmed a high degree of epitaxy with no (103) or $(10\underline{3})$ grains observable. The optical and transport properties of (72/72 Å) super lattices showed considerable anisotropy. The anisotropy ratio (using dc four-probe method) was found to be $\rho_c/\rho_{ab} = 75$ at 300 K.

4.9 "Brick-Wall" Microstructure in Epitaxial $YBa_2Cu_3O_X$ Films

During past few years (i.e. 1993–1994), it became clear that reducing the oxygen content x of epitaxial $YBa_2Cu_3O_x$ thin film strongly enhances the anisotropy of the superconducting properties. A reduction of the oxygen content in the YBCO films produces more chain-site oxygen vacancies, resulting in a less effective coupling of neighboring superconducting CuO_2 planes [46]. The in plane transport properties of the epitaxial YBCO films are consistent with a 3D-2D crossover when decreasing the oxygen content at a fixed reduced temperature (T/T_c) [47]. It was, further, shown by Janossy et al. [48], that for an oxygen content $6.5 < x < 7$, the observed increase of the anisotropy with decreasing oxygen content could be described in terms of a strong enhancement (by more than two orders of magnitude) of the effective transverse mass

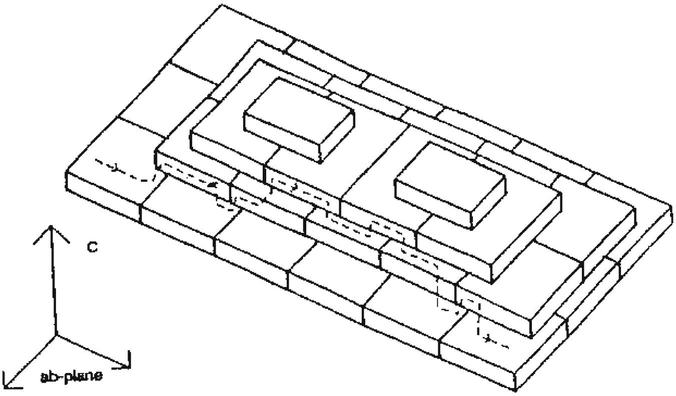

Fig. 4.8 Schematic view of the "brick wall" micro structure for epitaxial $YBa_2Cu_3O_x$ films. The *dashed line* indicates a possible path for the superconducting current which is forced out of the ab plane near the grain boundaries [49]

M of the carriers, while the in-plane effective mass is almost a constant. Within the frame work of the anisotropic Ginzberg-Landau equations, the strong enhancement of M is related to an exponential decrease of the critical current density J_c^* along the c-axis with decreasing oxygen content x:

$$J_c^* = \frac{\hbar e n_s}{2dM} \propto e^{\mathrm{x}},$$

with d, the distance between superconducting CuO_2 planes and n_s, the carrier density within these planes. Gao et al. [49] have reported detailed transport measurements of the in-plane (ab plane) critical current density J_c in epitaxial, c-axis oriented YBCO films. They observed that the variation of J_c as a function of the oxygen content x also obeys the exponential increase predicted by the above equation. They argue that this exponential dependence is consistent with a "brick wall" microstructure which is shown schematically in Fig. 4.8.

The concept of a brick wall structure was first introduced to explain the elevated critical current density in textured BSCCO [50] and TBCCO [51] material. Assuming a very poor coupling between the bricks along the *ab* direction, the super current, which is represented by the dashed line in Fig. 4.8 will be weaving around these boundaries by running locally perpendicular to the *ab* plane. Consequently, the in-plane critical current density will be limited by the current density J_c^* which is allowed to flow along the c-axis, implying that

$$J_c(x, T) \propto J_c^*(x, t) \propto e^{\mathrm{x}}.$$

with the constant of proportionality depending on the dimensions of the bricks. This brick wall picture shown in Fig. 4.8 [49] is based on their scanning tunneling microscopy images of the YBCO films which reveal that their films consist of islands with a pronounced terrace-like structure. They have conjectured that this brick wall structure (apparently) results from the overlap between terraces belonging to adjacent spiral-shaped islands.

4.10 "ABSTRACTS" of Author's Papers on Superconductivity

1. On the Formation of Y-Ba-Cu-O Superconducting Thin Films A.K. Saxena, S.P.S. Arya, B. Das, A.K. Singh, R.S. Tiwari and O.N. Srivastava [Solid State Communication **66**, No 10, 1063–1065 (1988)]

Abstract Thin film of $YBa_2Cu_30_{7-x}$ has been prepared by a spray pyrolysis technique on $LiNbO_3$substrate. Structural characterization through X-ray diffraction suggests that the film has the orthorhombic phase of $YBa_2Cu_3O_{7-x}$. Surface topography monitored by secondary electron imaging shows randomly oriented grains indicative of rough surface. The Tc-onset and Tc-zero for these films have been found to be 94 and 75 K respectively.

2. Formation of Y-Ba-Cu-O thin films by spray pyrolysis. A.K. Saxena, B. Das, S.P.S. Arya, P. Mandal, C.C. Tripathi, A.K. Singh, R.S. Tiwari & O.N. Srivastava. [Reviews of Solid State Science **2,** Nos. 2 & 3, 497–502 (1988)].

Abstract The high temperature superconducting films ($\sim 5\ \mu$m) of $YBa_2Cu_3O_{7-x}$ have been formed by the spray pyrolysis method. For the deposition of the film various substrates (e.g. $LiNbO_3$, $A1_2O_3$ etc.) have been investigated. It has been found that the films deposited on $LiNbO_3$ substrates are the optimum ones exhibiting Tc-onset and Tc-zero of 94 and 75 K respectively. The structural characterization of the films have been carried out employing XRD and electron microscopic techniques.

3. Preparation of Y-Ba-Cu-O and Bi-Sr-Ca-Cu-O superconducting films by conventional techniques. K.K. Verma, A.K. Saxena, S. Rastogi, R.S. Tiwari and O.N. Srivastava. [Bull. Mater. Sci. **14,** No. 2, 493–499 (1991)].

Abstract High temperature superconducting-films of Y-Ba-Cu-O and Bi-Sr-Ca-Cu-O have been deposited on different substrates using conventional techniques, like flash evaporation and spray pyrolysis. The microstructural investigation of the films by SEM technique reveals the partially oriented nature of the crystallites. In the case of spray-deposited Bi-Sr-Ca-Cu-O HTSC films it has been found that film/substrate mismatch is not the decisive factor for the superconducting transition temperature Tc.
Keywords HTSC films; flash evaporation; spray pyrolysis; microstructure; film substrate mismatch.

4. Preparation of high Tc superconducting thin films of TI-Ca-Ba-Cu-O by the chemical spray pyrolysis technique. K.K. Verma. A.K. Saxena, A.K. Singh, R.S. Tiwari and O.N. Shrivastava [Superconductor Science and Technology **5,** 163–167 (1992)]

Abstract Thin films of the TI-Ca-Ba-Cu-O system have been prepared on MgO and YSZ single-crystal substrates by a simple chemical process (the spray pyrolysis technique). Since TI is toxic, the TI-Ca-Ba-Cu-O films were prepared by a two step process. Firstly, precursor (Ca-Ba-Cu-O) films were prepared followed by diffusion of TI derived by vaporizing TI_2O_3 in a closed system under oxygen flow. A new feature found in the present investigation is that the Tc (R = 0) of the TI-Ca-Ba-Cu-O films has been found to depend upon the microstructural characteristics of the precursor films which can be varied by annealing these films. The Tc (R = 0) of the TI-Ca-Ba-Cu-O HTSC films prepared from the annealed precursor films has been found to be higher than in the films prepared from the as-deposited precursor films. As, for example, in the case of a film on a MgO substrate, the T_c (R = 0) has been enhanced from ~90 to 98 K. The highest Tc obtained by us for the films synthesized from the annealed precursor films on YSZ substrates correspond to ~103 K. The XRD reveals the biphasic (2223/2122) nature of the films. The microstructural characteristics of the films as monitored by SEM reveals the partially oriented nature of the Tl-Ca-Ba-Cu-O film.

5. Studies on RF SQUID effect in TI-Ca-Ba-Cu-O thin films prepared by spray-pyrolysis technique. Neeraj Khare, A.K. Gupta, A.K. Saxena, K.K. Verma & O.N. Srivastava. [Superconductor Science and Technology **7,** 402–406 (1994)].

Abstract RF SQUID behaviour in thin films of TI-Ca-Ba-Cu-O has been studied. The films were prepared by the spray pyrolysis technique. Two films (A and B) which have T_c(R = 0) values of 85 and 103 K respectively, were chosen for the RF SQUID studies. Film A consists mainly of 2122 phase with needle-like grains whereas film B mainly consists of 2223 phase with well connected plate-like-grains. RF SQUID modulations in film B were observed up to 101 K. The SQUID was also operated in flux-locked-loop mode. The RFSQUID fabricated from film B was found to exhibit better flux noise performance than that fabricated from film A.

6. The synthesis of TI-Ba-Ca-Cu-O (Ag_y) HTSC films through spray pyrolysis and evaluation of the influence of silver on the critical current density. H.K. Singh, A.K. Saxena & O.N. Srivastava [Superconductor Science and Technology **8,** 448–454 (1995)]

Abstract The synthesis of TI-Ba-Ca-Cu-D(Ag_y) HTSC films corresponding to the 2223 phase through the spray pyrolysis technique has been carried out. These films are found to possess one of the highest known T_c values for such films of ~115 K and exhibit one of the highest J_c values of 1.25×10^5 A cm^{-2} (16 K) and 0.312×10^5 A cm^{-2}(77 K) for Ag content of 0.35 corresponding to $TI_2Ba_2Ca_2Cu_3O_{10}(Ag_{0.35})$. The enhancement of J_c due to Ag addition has been found to depend on the Ag content. This dependence has been found to be explicable in terms of Ag-induced grain boundary passivation and Ag segregation at the grain boundary-grain interface.

7. The formation and characterization of TI-doped Hg-Ba-Ca-Cu-O superconducting films synthesized through spray pyrolysis. H.K. Singh, A.K. Saxena & O.N. Srivastava [Physica C **262,** 7–12 (1996)].

Abstract The Tl doped Hg-Ba-Ca-Cu-O HTSC films have been synthesised by reacting Ba-Ca-Cu-O precursor films deposited by spray pyrolysis with a mixture of Hg- Tl vapour in an evacuated sealed quartz tube. These films ($\sim 3\,\mu$m in thickness) having 1223 as the majority phase are found to possess T_c $(R = 0)$'s of 127 and 122 K on MgO (100) and ZrO_2 (100) single-crystal substrates, respectively, and $J_c \sim 10^5$ A/cm^2 (both MgO and ZrO_2 have 20 K). The observed T_c $(R = 0)$ of 127 K is the highest reported so far for Tl doped Hg-Ba-Ca-Cu-O films. Surface morphological investigations reveal the occurrence of layered spiral-like growth features.

8. Effect of Ag doping on the transition temperature and critical current density of Hg_{1-x} Tl_x Ba_2 Ca_2 Cu_3 O_{8+d} films fabricated through spray pyrolysis. H.K. Singh, A.K. Saxena O.N. Srivastava [Physica C **273,** 181–188 (1997)]

Abstract The Ag doped Hg(Tl):1223 films have been synthesised by annealing $Ba_2Ca_{2.2}Cu_{3.3}O_z(Ag_y)$; $y = 0, 0.25, 0.5, 0.75, 1.0$ precursors deposited by spray prolysis on single crystal MgO and ZrO_2 substrates, in controlled Hg-Tl vapour ambient in an evacuated sealed quartz tube at 860 °C for 720 min. The transition temperature (T_c), dc transport critical current density (J_c) and microstructure of the films have been found sensitive to Ag content. The microstructural details as revealed through scanning electron microscopy exhibit the curious characteristics of the existence of spiral like growth feature which is found to deteriorate with increasing Ag concentration. The maximum $T_c = 126$ K of the as synthesized Ag doped film with $Ag = 0.50$ is nearly the same as the $T_c = 127$ K of oxygen annealed Ag-free films, suggesting insitu oxygenation. The transition temperature has been found to decrease for higher Ag contents ($0.50 < y < 1.00$). The J_c has been observed to decrease steadily with increase in silver content, being highest (7.2×10^4A/ cm^2, 20 K) in Ag-free case. This decrease in $J_c$has been accounted for in term of formation of Ag(Hg) amalgam due to the reaction of Ag with Hg already present in the grain boundary region.

PACS 74.60M$_j$; 74.75 + t
Keywords Superconductors; Transition temperature; Critical current

References

1. P. Bernstein, Phys. C **162–164**, 611 (1989)
2. R.B. Laibowitz et al., Phys. Rev. B **36**, 4047 (1987)
3. I. Tarasaki et al., Jpn. J. Appl. Phys. **27**, L1480 (1988)
4. M. Kawasaki et al., Jpn. J. Appl. Phys. **26**, L 388 (1987)
5. N. Terada et al., Jpn. J. Appl. Phys. **26**, L 508 (1987)
6. M. Suzuki, T. Murakami, Jpn. J. Appl. Phys. **26**, L 524 (1987)
7. P. Chaudhuri et al., Phys. Rev. Lett. **58**, 2684 (1987)
8. P.N. Kobrin, Adv. Cer. Mater. **38**(Special issue), 430 (1987)
9. D. Dijkkamp, T. Venkatesan et al., Appl. Phys. Lett. **51**, 619 (1987)
10. M. Naito et al., J. Mater. Res. **2**, 713 (1987)
11. Y. Enomoto et al., Jpn. J. Appl. Phys. **26**, L 1248 (1987)
12. D.M. Hwang et al., Appl. Phys. Lett. **52**, 1834 (1988)
13. T. Venkatesan et al., J. Appl. Phys. **63**, 4591 (1988)
14. H. Nakajima et al., Appl. Phys. Lett. **53**, 1437 (1988)

15. M.F. Yan et al., J. Appl. Phys. **63**, 821 (1988)
16. S. Witanachchi et al., Appl. Phys. Lett. **55**(3), 295 (1989)
17. R.P. Gupta et al., Appl. Phys. Lett. **52**, 1987 (1988)
18. J.V. Mantese et al., Appl. Phys. Lett. **52**, 1741 (1988)
19. V. Matijasevic et al., J. Mater. Res. **6**(4), 682 (1991)
20. H.U. Habermeier, J. Less-Common Met. **151**, 257 (1989)
21. AJ.G. Schellingerhout et al., Z. Phys. B **71**, 1 (1988)
22. C.X. Qui, I. Shin, Appl. Phys. Lett. **52**, 587 (1988)
23. R.B. Laibowitz et al., Phys. Rev. B **35**, 8821 (1987)
24. J. Kwo, Phys. Rev. B **36**, 4039 (1987)
25. C. Webb, Appl. Phys. Lett. **51**, 1191 (1987)
26. J. Kwo et al., Mater. Res. Soc. Proc. **99**, 339 (1988) (ed. by MB Brodsky et al., Pittsburgh)
27. J.L. Vossen, J.J. Cuomo, in *Thin Film Processes*, ed. by J.L. Vossen, W. Kern (Academic, Orlando, 1978)
28. T.C. Tisone, P.D. Cruzon, J. Vac. Sci. Technol. **12**, 1058 (1975)
29. H.R. Kaufman, *Fundamentals of Ion Source Operation* (Common wealth Scientific Corporation, Alexandria, 1984)
30. Z.L. Bao et al., Appl. Phys. Lett. **51**, 946 (1987)
31. U. Poppu et al., Solid State Commun. **66**, 661 (1988)
32. H.C. Li et al., Appl. Phys. Lett. **52**, 1098 (1988)
33. G.K. Wehner et al., Appl. Phys. Lett. **52**, 1187 (1988)
34. S.M. Rossnagel, J.J. Cuomo, AIP Conf. Proc. **165**, 106 (1987)
35. M. Leskela et al., J. Vac. Sci. Technol. **A7**, 3147 (1989)
36. R.L. Sandstrom et al., Appl. Phys. Lett. **53**, 444 (1988)
37. H.U. Habermeir, Phys. C **180**, 17–25 (1991)
38. H. Yamane et al., Appl. Phys. Lett. **53**, 1548 (1988)
39. T. Nakamori et al., Jpn. J. Appl. Phys. **27**, L1265 (1988)
40. K. Zhang et al., Appl. Phys. Lett. **54**, 380 (1989)
41. K.K. Verma, A.K. Saxena, S. Rastogi, R.S. Tiwari, O.N. Srivastava, Bull. Mater. Sci. **14**(2), 493–499 (1991)
42. K. Kamigaki et al., J. Appl. Phys. **69**, 3653 (1991)
43. T. Terashima et al., Phys. Rev. Lett. **65**, 2684 (1990)
44. T. Terashima et al., Phys. Rev. Lett. **67**, 1362 (1991)
45. I.E. Trofimove et al., MPI-Stuttgart; High Tc update, **7**(11) (1993)
46. K.E. Gray, D.H. Kim, B.W. Veal, G.T. Seidler, T.F. Rosenbaum, D.E. Farrel, Phys. Rev. B. **45**, 10071 (1992)
47. Z.X. Gao, E. Osquiguil, M. Maenhoudt, B. Wuyts, S. Libbrecht, Y. Bruynseraede. Phys. Rev. Lett. **71**, 3210 (1993)
48. B. Janossy, D. Prost, S. Pekker, L. Fruchter, Phys. C **181**, 51 (1991)
49. Z.X. Gao, I. Heyvaert, B. Wuyts, E. Osquiguil, C. Van Haesendonck, Y. Bruynseraede, Appl. Phy. Lett. **65**(6), 770 (1994)
50. L.N. Bulaevskii, J.R. Clem, L.I. Glazman, A.P. Malozemoff, Phys. Rev. B **45**, 2545 (1992)
51. D.J. Miller, J.G. Hu, J.D. Hettinger, K.E. Gray, J.E. Tkaczyk, J. De Luca, P.L. Karas, J.A. Sutliff, M.F. Garbauskas. Appl. Phys. Lett. **63**, 556 (1993)

Chapter 5
Superconductivity in Cuprates

5.1 Mott Insulator

An insulator with a magnetic moment at each lattice site (i.e. a magnetic insulator) is known as Mott insulator. The unusuality of a Mott insulator is that strong correlations suppress the charge fluctuations, which are required for a finite conductivity. However, doping produces holes in copper–oxygen planes and it becomes susceptible to charge density wave (CDW): charge on a site changes, as the excitation moves, i.e. there is a gap for charge excitations, but no gap for spin excitations. Further, due to doping, long range antiferromagnetic order is replaced by short range order, and superconductivity emerges as the ground state.

5.2 The First Cuprate $La_{2-x}M_xCuO_4$

A crystalline solid with an odd number of electrons or holes per unit cell is, in general, a Pauli paramagnetic metal (i.e. electrons in a metal constitute a Fermion gas and exhibit a temperature independent paramagnetism). However, the compound La_2CuO_4 has one hole per unit cell is insulator and anti-ferromagnetic with an ordering or Neel temperature ~210 K. It has an orthorhombically distorted K_2NiF_4 structure and transforms to regular K_2NiF_4 (tetragonal) structure above 530 K.

Let us consider first, La_2CuO_4 as a chemical compound. The valence requirements are satisfied for Cu in the 2+ state, and hence, can be written as $[(La^{3+})_2Cu^{2+}]$ $(O^{2-})_4$. Here, Cu^{2+} has an unfilled shell configuration namely d^9 or one hole in the filled d^{10} shell. So, La_2CuO_4 has one "hole" per unit cell. $La_2CuO_{4,}$ instead of being a Pauli paramagnetic metal, is an anti-ferromagnetic insulator (at temperatures $T \leq T_N(\sim 210\,K$ for $La_2CuO_4)$, the Neel temperature, there is anti-ferromagnetic ordering of magnetic moments).

Now suppose La in La_2CuO_4 is doped by a fraction of Sr (i.e. it becomes $La_{2-x}Sr_xCuO_4$). Since Sr is divalent, therefore, one should have either Cu^{3+} or

A. K. Saxena, *High-Temperature Superconductors,* Springer Series
in Materials Science 125, DOI: 10.1007/978-3-642-28481-6_5,

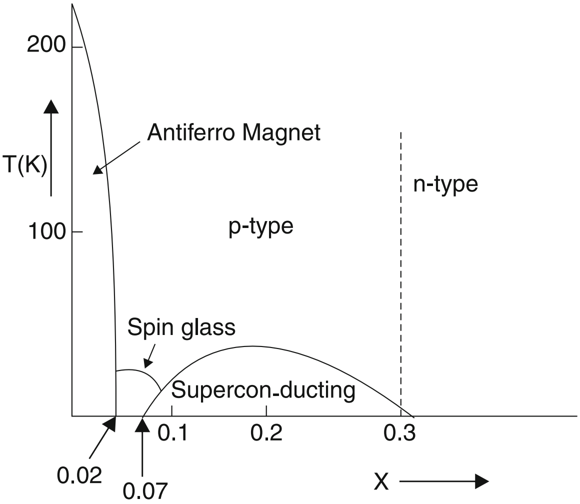

Fig. 5.1 The phases diagram of $La_{2-x}Sr_xCuO_4$ as a function of T and x

O^{1-} for each Sr^{2+}. Spectroscopic evidence shows that the latter is favoured. Therefore, the addition of a Sr atom introduces a hole in the filled oxygen p-shell and the concentration of holes is proportional to x. If these holes move, one has a metal. This is what happens at temperatures from 0 to 30 K. There is a rapid disappearance of anti-ferromagnetism with increase in x, which is absent for $x > 0.02$. Figure 5.1 shows the phase diagram of this compound in the $T - x$ plane. There is an insulator to metal transition for $x \geq 0.02$. Then, there is a phase at $T < 20$ K and for $0.02 < x < 0.06$, there are frozen disordered magnetic moments (spin glass state). This is followed by the superconducting phase, which persists for $0.06 < x < 0.30$. Hall effect measurements confirm that carriers are positively charged (i.e. holes) with their density, approximately equal to x per unit cell. Thus, $La_{2-x}M_xCuO_4$ shows the highest T_c around a critical value of x (0.15 and 0.2, respectively in case of Ba and Sr with T_cs of 30 and 35 K).

Electron doped superconductors can be produced by substituting the trivalent rare earth with a tetravalent ion, e.g. $Nd_{2-x}Ce_xCuO_4$.

5.3 The Charge-Transfer Model of a High T_c Cuprate Superconductor

All cuprate superconductors can be described by the general compositional formula:

$$(AO)_m\ (BO)_2\ (M)_{n-1}\ (CuO_2)_n\ ,$$

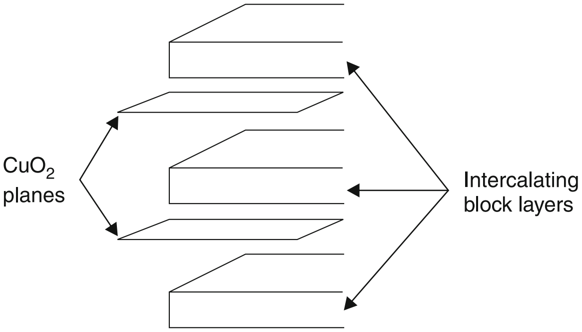

Fig. 5.2 Charge-transfer model of a high T_c cuprate superconductor. CuO_2 planes form the conduction layers whereas intercalating block layers act as charge reservoir layers

where A is Bi or Tl (or Hg) and B is La/Sr/Ba and M is Ca/Y.

Thus, $(AO)_m$ forms the rock salt block and $(M)_{n-1}(CuO_2)_n$ forms the perovskite block. The layered structure of a cuprate HTSC may be viewed, as consisting of

(1) Conduction layers (CuO_2)
(2) Charge reservoir layers: $(AO)_m(BO)_2(M)_{n-1}$

as shown in Fig. 5.2.

This is known as charge-transfer model of a high T_c cuprate superconductor. (Superconducting cuprates are generically, doped charge transfer insulators in the strong (local) correlation or Mott-limit).

Hole carriers are created in the conduction layer, when electrons are transferred to the charge reservoir layers. All superconducting cuprates have a fraction 0.05–0.30 of mobile holes per CuO_2 unit cell in the CuO_2 (i.e. *ab*) planes.

The carrier number density is controlled by (a) the overall chemistry and (b) amount of charge transferred. The amount of charge transfer depends on

(1) Structure
(2) Available oxidation states of atoms
(3) Competition between charge-transfer and oxidation/reduction of metal atoms in the charge reservoir layer

Structural oxidation–reduction chemistry, e.g. cation substitution, such as

$$Sr^{2+} \text{ for } La^{3+} \quad \text{or} \quad Y^{3+} \text{ for } Ca^{2+}$$

in the AO, BO and M layers leads to electron removal (hole doping) or electron addition (electron doping) to the CuO_2 layers.

5.4 Electron and Hole Doping of CuO_2 Layers

A CuO_2 layer with formal copper oxidation state Cu^{2+} has nine electrons to fill its d-block bands, therefore, its highest occupied band (the $x^2 - y^2$ band) is half filled (one electron/CuO_2). For a CuO_2 layer with formal copper oxidation state $Cu^{(2+\in)+}$, (where $\in > 0$), the $x^2 - y^2$ band is less than half filled, i.e. $(1 - \in)$ electrons/CuO_2. Cuprates with such CuO_2 layers are p-type superconductors with hole density

$$n_{\mathrm{H}} = \frac{\in}{\mathrm{CuO_2\ unit}} \quad (\in \text{ is hole doping}).$$

For a CuO_2 layer with formal copper oxidation state $Cu^{(2-\in)+}$, the $x^2 - y^2$ band is more than half filled (i.e. $(1+\in)$ electrons/CuO_2). Cuprates with such CuO_2 layers are n-type superconductors with electron density

$$n_{\mathrm{E}} = \frac{\in}{\mathrm{CuO_2\ unit}} \quad (\in \text{ is electron doping}).$$

The holes or electrons of the cuprates are associated with the in-plane $x^2 - y^2$ band. The charge transfer $\in$ is the linear combination of same site p_x, p_y oxygen (hole) orbitals with local $d_{x^2-y^2}$ symmetry. Hole doping of the cuprate CuO_2 layers is achieved by several means, e.g.

(1) Cation-substitution
(2) Cation-vacancy
(3) Oxygen-excess

These all are based on non-stoichiometry of chemical composition.

Rock salt layer may also acts as hole source. Holes may also be introduced into the CuO_2 layers, when the bottom of the rock salt layer bands lies below the Fermi level.

5.4.1 *Source of Hole (Carriers) in Various Cuprate Families*

It has been speculated that holes are produced

(1) In YBCO, due to mobile carriers in the Cu–O chains
(2) In BSCCO, Bi in BiO layers are insulating. Holes are created by excess O-atoms in the BiO layers, and by Sr-deficiency. For lead-doped BSCCO (i.e. BPSCCO),

$$Pb^{4+} + 2Cu^{2+} \rightarrow 2Cu^{3+} + Pb^{2+}$$

(3) TlO double rock salt layers in Tl:2212, 2223 etc. are important in creating holes in the CuO_2 planes

$$Tl^{3+} + 2Cu^{2+} \rightarrow 2Cu^{3+} + Tl^{1+}$$

(4) TlO single layers are insulating in Thallium mono-layer cuprates. Holes are produced, because copper atoms are already of high enough oxidation state:

$$\mathrm{Cu}^{2+1/n} \quad \text{where } n = 1,\ 2 \text{ or } 3 \quad \text{and}$$
$$2 + 1/n = +3.00, +2.50 \text{ or} + 2.33$$

(5) In mercury cuprates, holes are produced due to non-stoichiometry of the HgO layers. There is partial oxygen-occupancy, represented by $\mathrm{HgO}_\delta (0 < \delta < 1)$:

$$\mathrm{Hg_1Ba_2CuO_{4+\delta}}$$

Or

$$(\mathrm{HgO}_\delta)2\ (\mathrm{BaO})\ \mathrm{CuO_2}$$
$$\mathrm{Hg}^{+2}\mathrm{O}^{-\delta'}\ \ (2\mathrm{BaO})\ \ \mathrm{Cu}^{+2+\mathrm{x}}\mathrm{O}^{-2-2}$$

Due to $1 > \delta'(>0)$, a change in copper valence of $+x$ is produced. It is to be mentioned here that Hg: 1201 is overdoped. Further, since the number of Cu atoms per formula unit is more in Hg: 1212 and Hg: 1223 as compared to Hg: 1201, these are, therefore, underdoped like Bi- and Tl- cuprates.

5.5 The Conductions Plane in Cuprates

Neutral atom configurations for copper and oxygen are

$$\mathrm{Cu}^0 = (\mathrm{Ar})\,3d^{10}4s^1$$
$$\mathrm{O}^0 = (\mathrm{Be})\,2p^4$$

since $\mathrm{O}^{2-} = (\mathrm{Be})2p^6$ is a closed shell configuration (i.e. stable configuration corresponding to neon), therefore, oxygen favours the valency 2^-. This implies copper should have valency 2^+. Hence, the configuration in the *ab*- conductor plane is as shown in Fig. 5.3, i.e. the configuration is $\mathrm{CuO_2}$ per each O-atom taking $2e^{-1}$ (one each) from two closest Cu atoms)

$$\mathrm{Cu}^{2+} = (\mathrm{Ar})\,3d^9 \qquad \boxed{\uparrow\downarrow}\boxed{\uparrow\downarrow}\boxed{\uparrow\downarrow}\boxed{\uparrow\downarrow}\boxed{\uparrow}$$

Thus, copper $-3d$ and oxygen $-2p$ orbitals are the relevant ones for electronic properties of $\mathrm{CuO_2}$ planes.

The copper $3d$ orbitals combine with each other, such that there result five degenerate orbital states shown in Fig. 5.4.

The $d_{3z^2-r^2}$ along z-axis mixes well with c-axis oxygen and has lower energy than $d_{x^2-y^2}$. The energy splitting is due to

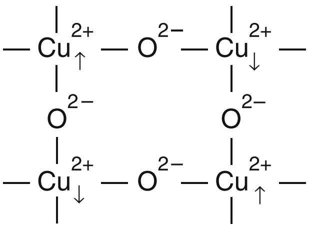

Fig. 5.3 Conduction plane in cuprates

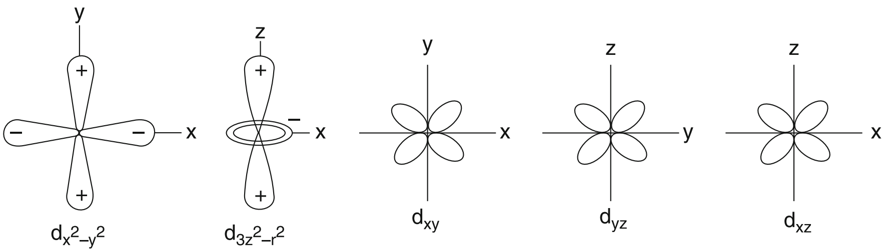

Fig. 5.4 d-orbital of copper (x and y coordinates are in the ab plane)

(1) Electrostatic field of oxygen ions at corners of octahedra.
(2) Covalent overlap (i.e. admixture) between copper-d and oxygen-p wave functions.

5.6 Octahedral Ligand Field

The crystal field theory considers the effect of ligand fields, i.e. electrostatic field due to ligands (the surrounding atoms/ions) on the d-orbitals of the central metal atom.

When negatively charged ligands approach the central atom, the electrons of the central atom are subjected to repulsive forces, which are obviously strongest in the "approach directions", i.e. to say, the energy of the orbitals, which point in these directions is, therefore, increased. So, the d-electrons will tend to occupy those orbitals that are farthest away from approach directions of ligands. The most common approach directions or rather the arrangement of ligands around a central atom are octahedral (or tetrahedral).

When a transition metal ion is surrounded octahedrally by six ligands (Fig. 5.5), their directions of approach coincide with x-, y-, z-axes (which are the directions along which d_{z^2} and $d_{x^2-y^2}$ orbitals are concentrated). Therefore, these orbitals are raised in energy. However, the d_{xy}, d_{yz} and d_{xz}, which points away from the ligands are lowered in energy. Consequently, there are two sets of higher energy, doubly degenerate d_γ and lower energy, triply degenerate $d_\in$. Energy difference Δ is the crystal field splitting. Magnitude of Δ depends on particular ligands and on the central metal ion.

Fig. 5.5 Octahedral arrangement

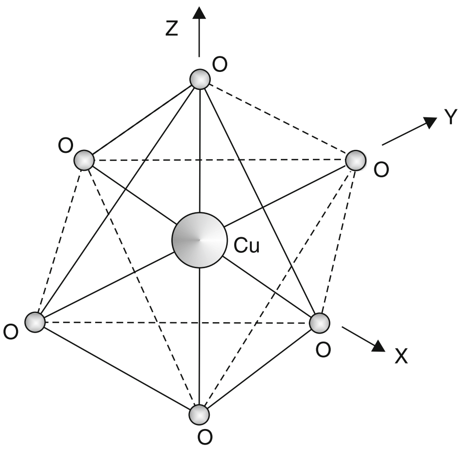

Fig. 5.6 Splitting of d-levels

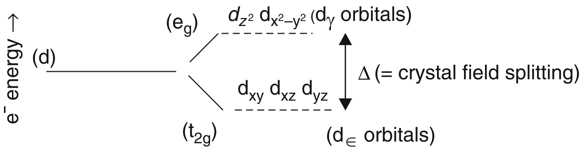

5.7 Jahn–Teller Effect

When a transition metal ion is surrounded octahedrally by six ligands, their direction of approach is along x-, y-, z-axes (i.e. along which orbitals d_{z^2}, $d_{x^2-y^2}$ are concentrated).

The arrangement of ligands is symmetrical if the electric field due to non-bonding ($d-$) electron is symmetrical. On the contrary, the octahedral arrangement is likely to be distorted.

The octahedral arrangement is distorted by a metal-ion having the configuration d^9.

d_{xy} is doubly occupied, whereas d_{xz} and d_{yz} perpendicular to the xy plane are singly occupied (Fig. 5.6).

Thus, when the ligands approach the central metal ion Cu^{2+} octahedrally, they can do so more closely along the two z-directions. As a result, the octahedron is elongated, making $d_{x^2-y^2}$ more anti-bonding and, therefore, last to be occupied. The one $d_{x^2-y^2}$ "hole" accounts qualitatively for the distortion of octahedron.

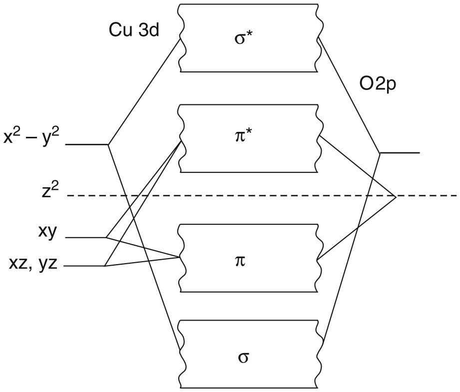

Fig. 5.7 Schematic energy bands for copper in square planar coordination

5.8 Energy Levels for Copper

A schematic energy level diagram for a square planar $Cu^{II}O_4$ unit is given in the Fig. 5.7 (for $Cu{-}O_2$ planes).

This is simply the molecular orbital diagram a chemist would anticipate, but with the energy levels broadened into bands (because of the "infinite" nature of a solid). Here, it is essential to emphasize that this bond-picture only exists as a result of a strong admixture of the Cu3d and O2p wave functions (Strictly speaking, there are no Cu3d bands or O2p bands separately in the copper oxide based phases).

5.9 Comparison of Cu^{3+} and Cu^{2+} Ions in the Oxide Octahedron

Figure 5.8 shows schematic representation of electron orbitals for octahedrally coordinated copper ions in oxides for Cu^{3+} with $3d^8$ configuration. The orbitals transforming as base functions of the cubic $\in_g$ group are half-filled, thus a singlet ground state is formed. In the presence of Cu^{2+} with $3d^9$ configuration, the ground state is degenerate, and a spontaneous distortion of the octahedron occurs to remove this degeneracy (the *Jahn–Teller Effect*).

5.10 The Hamiltonian and the Relevant Energy Levels in the Conduction Plane

All the five $3d$ orbitals are fully occupied, except $d_{x^2-y^2}$. There is one missing $d_{x^2-y^2}$ electron (i.e. a Hole) per Cu^{2+} ion. Thus, we have

$$\begin{aligned} Cu^{2+} &= (\mathrm{Ar})\,3d^9\ (\text{one hole})\,, \quad (\text{energy } \in_d), \\ Cu^{3+} &= (\mathrm{Ar})\,3d^8\ (\text{two holes})\,, \quad (\text{energy } 2\in_\mathrm{d} + \mathrm{U}) \end{aligned}$$

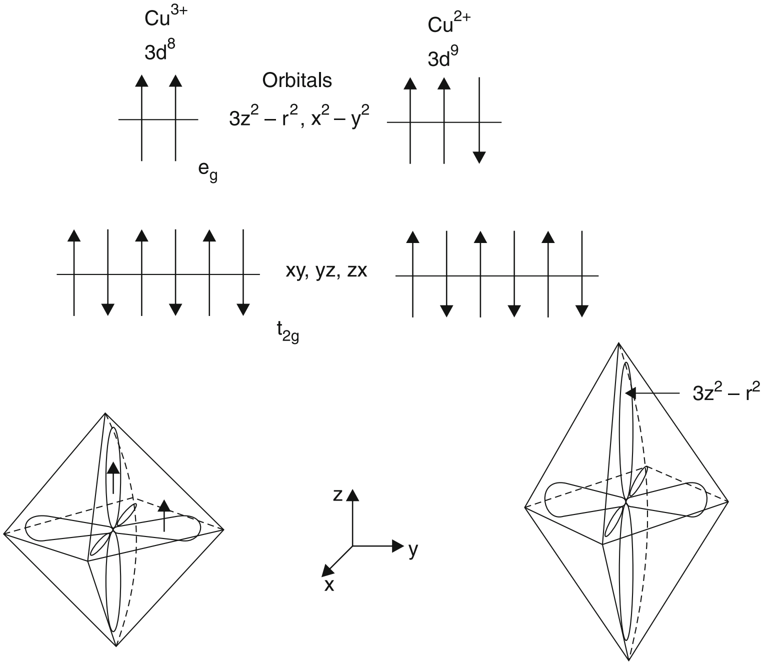

Fig. 5.8 Elongation of the octahedron (in case of Cu^{2+})

and $Cu^{+} = (Ar)3d^{10}$ (no hole), (energy zero), i.e. the single d-hole is in an orbital with local $d_{x^2-y^2}$ symmetry. All the above three states can be described by the equation

$$H_0 = \sum \in_d n_{d\sigma} + U n_{d\uparrow} n_{d\downarrow},$$

where H_0 is the energy operator (Hamiltonian) $n_{d\sigma}$ is the number of d holes with spin σ. This number has two values namely zero and one. The energy U is large ($\sim$8 eV) and positive and correlates two d holes on the same site away from each other (making d^8, unlikely) (see Fig. 5.9).

The hole wave function on one Cu site overlaps with that on the next Cu site via oxygen site intervening the two. Thus, there is an admixture of a $d_{x^2-y^2}$ hole with the surrounding (p_x, p_y) hole state. The dynamics of the admixture is characterized by

(1) The difference $\in_d - \in_p$ ($\equiv \in_{pd}$) between the energy of $(p_x - p_y)$ hole orbital and a $d_{x^2-y^2}$ hole orbital. This $\in_{pd}$ is called the *charge transfer energy*.
(2) The *hopping amplitude* $t_{pd,}$ which determines the kinetic energy of the d-holes (i.e. energy gained by their motion or delocalization)

Figure 5.9 shows the relevant energy levels of Cu and O ions in the CuO_2 planes.

The one-d hole or Cu^{2+} (or d^9) levels lie lowest, at energy $\in_d^h$ with respect to the no d-hole (or d^{10}) configuration. To add another d-hole (Cu^{3+} or d^8) costs an

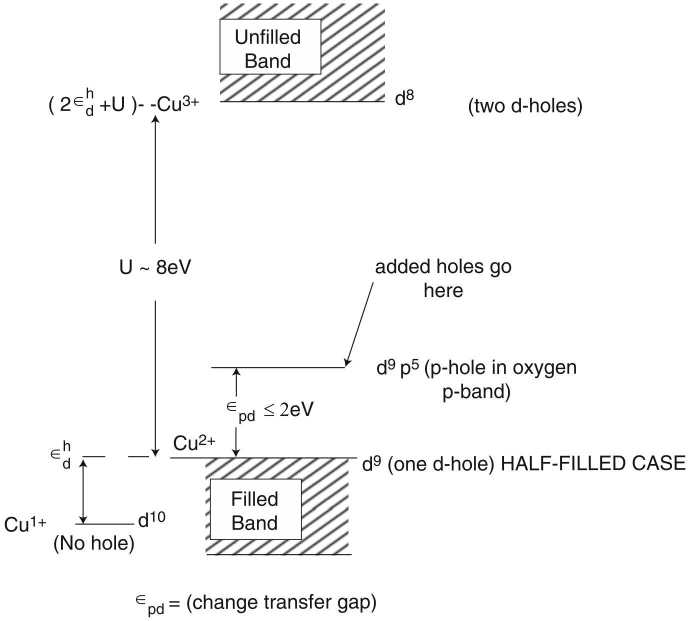

Fig. 5.9 The relevant energy levels of Cu and O ions in the Cu–O$_2$ plane [1]

extra energy $(\in_d^h + U)$, where U is the large ($\sim$8 eV) single site Mott-Hubbard repulsion energy. The large value of U leads to the stoichiometric one d-hole per site (material La$_2$CuO$_4$) and makes it an insulator. The energy U is due to Coulomb repulsion between two d holes on the same site (i.e. a spin-up and a spin-down hole on the same site). The feature that distinguishes cuprates from model one band (d band) Mott insulators is the presence of oxygen p-hole levels $\in_p^h$ between d^8 and d^9 energies, i.e. in the correlation or Mott Hubbard gap. Thus, the minimum energy required to transfer a d-hole to an unoccupied site is

$$\left(\in_p^h - \in_p^d\right) \approx 2\,\text{eV} \;\; \text{(from neutron scattering experiments)}$$

the charge transfer being to the same site linear combination of p_x, p_y oxygen hole orbitals with local $d_{x^2-y^2}$ symmetry.

Addition of holes: when holes are added to La$_2$CuO$_4$, they go into the oxygen p-hole band, and hop from site to site, both directly (with hopping amplitude $t_{pp} = 0.7\,\text{eV}$) and via admixture with d states ($t_{pd} = 1\,\text{eV}$). The ratio $|\in_{pd}|/t_{pd} = (\in_p - \in_d)/t_{pd}$ (i.e. the ratio of charge transfer energy to the hopping amplitude) determines the hole concentration. If the ratio increases, the hole concentration decreases.

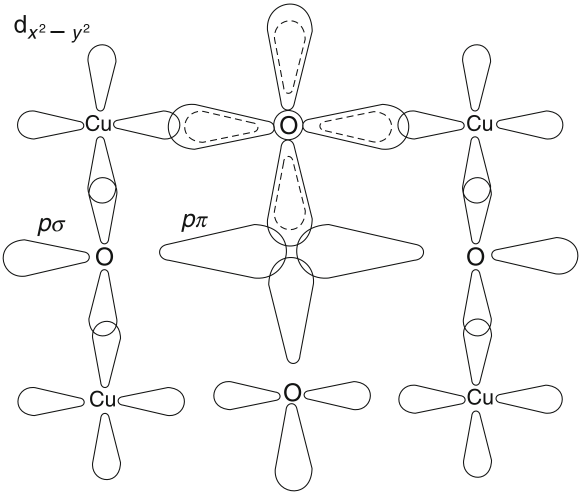

Fig. 5.10 Relevant oxygen and copper orbitals in the CuO_2 planes

5.11 Hole Superconductivity in Oxides

The essential feature of oxide superconductors is the existence of a network of anions, through which conduction occurs. Figure 5.10 shows schematically the relevant oxygen and copper orbitals in the CuO_2 planes. Conductivity in these materials occurs dominantly in the planes.

Optical experiments have shown that the O2p holes have at least 95 % $p_{x,y}$ character but have not determined whether it is $p\sigma$ or $p\pi$ orbitals. However, NMR results on ^{17}O and ^{63}Cu have unequivocally shown that BCS like superconductivity is due to oxygen holes and Cu is decoupled as far as superconductivity is concerned. Since the $p\sigma$ orbitals are strongly hybridized with the Cu $d_{x^2-y^2}$ orbitals, the combination of these observations leaves no doubt that the conduction oxygen holes that are responsible for superconductivity reside in the in plane $p\pi$ orbitals. There is a direct overlap between $p\pi$ orbitals that gives rise to conduction without involving the cation.

When an electron hops from the oxygen $p\pi$ orbital to the $p\pi$ orbital of the neighbouring O, it will drastically alter the states of the other p-electrons on these anions. This is due to the large Coulomb repulsion between that electron and the other electrons in the p-orbitals of the anions involved. The wave functions of all the remaining p-electrons on the anion, where the electron was, will contract (as they experience less repulsion), when a p-electron is removed, and the ones, where the electron hops, will expand (as shown schematically in the Fig. 5.10). This contraction of the charge density of the O^- anion relative to that of the O^{--} anion will lead to two effects, when the holes conduct through the $p\pi$ network: first, a dynamical band narrowing, as it occurs with small polarons (which is responsible for the anomalous normal state properties of these materials) and second, a pairing interaction that gives rise to a high T_c superconductivity.

5.12 Two Band and One Band Hubbard Models

For the $\mathrm{CuO_2}$ lattice, the energies of different (admixture) state are described by a two band Hubbard model with Hamiltonian:

$$H = \sum_{i\sigma} \in_d n_{d_i\sigma} + \sum_i U n_{d_i\downarrow} n_{d_i\uparrow} + \sum_{i\sigma} \in_p \, n_{pi\sigma} + \sum t_{pd} \left(\mathrm{C}^{+}_{pi\sigma} \mathrm{C}_{di\sigma} + \mathrm{C}^{+}_{di\sigma} \mathrm{C}_{pi\sigma} \right).$$

The last term describes the removal of a d hole (spin σ) at site i (destruction operator $\mathrm{C}_{di\sigma}$) and its appearance as a p-hole with the same local $d_{x^2-y^2}$ symmetry around site i (creation operator $\mathrm{C}^{+}_{pi\sigma}$). This process and its reverse $\mathrm{C}^{+}_{di\sigma} \mathrm{c}_{pi\sigma}$, both have the same hopping amplitude t_{pd} (kinetic energy of d-hole due to delocalization). The energy U tends to correlate two d-holes on the same site away from each other (It is large and positive).

The picture of crystal field levels is correct in the strong crystal field limit, i.e. when energy U of putting two holes (or electrons) in the same level (or on the same site) is much smaller than the crystal field splitting between levels. However, if U is larger than the width of the $d_{x^2-y^2}$ sub-band, the system is more stable if each hole is localized to a lattice site (i.e. the Mott insulating state). Then, the Hamiltonian can be written as

$$H = \sum_{i\sigma} \in_d n_{di\sigma} + U \sum_i n_{d_{i\uparrow}} n_{di\downarrow} + \sum_{ij\sigma} t_{ij} C^{+}_{i\sigma} C_{j\sigma}.$$

This model describes holes (or electrons) in the $d_{x^2-y^2}$ like sub-band. This is known as *one band Hubbard model*. The last term describes hopping of an electron from site i to site j; with amplitude t_{ij}.

In the *two band model*, the states p_x, p_y were having a local $d_{x^2-y^2}$ symmetry and they were considered separately (i.e. p-like and d-like states). In one band model, the $d_{x^2-y^2}$ derived band is a result of $d_{x^2-y^2}$ orbitals, formed due to $d-p$ hybrids.

In the two band model, the p hole has a tendency to bind anti-ferromagnetically to the nearest d-hole and to form a singlet. This spinless entity can be through of as a missing electron (hole) in half filling (in the one band Hubbard model). Thus, the low energy dynamics of the two models are very similar.

5.13 The Electronic Structure of Cuprates

The electronic structure of cuprates is described by two methods:

(1) Cluster approach (with Hubbard hamiltonians)
(2) A band picture (with effective one electron hamiltonians)

The first energy band calculations fail to explain the insulating nature of the cuprates having only Cu^{2+} in their $\mathrm{CuO_2}$ layers (viz. $\mathrm{La_2CuO_4}$ and $\mathrm{YBa_2Cu_3O_6}$). However, they show metallic behaviour even for $x \neq 0$ (in $\mathrm{La_{2-x}M_xCuO_4}$ and

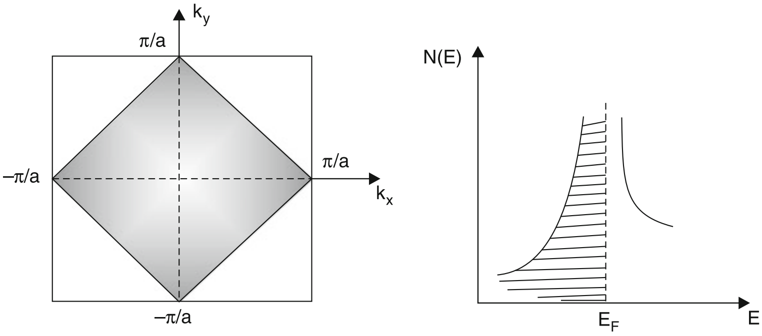

Fig. 5.11 Idealized Fermi surface for La_2CuO_4

$YBa_2Cu_3O_{6+x}$). This is seen in the density of states (DOS curves) obtained, which is non-zero at E_F, thereby representing a metal. The band structure calculations, however, which involve a one-electron approximation do not properly take into account the strong correlations between electrons due to the localization of the holes.

The idealized F.S. of a half filled square lattice is as shown in Fig. 5.11. At the points $\left(k_x, k_y\right) = (0, \pm\pi/\mathrm{a})$ and $(\pm\pi/\mathrm{a},\ 0)$, the group velocity $\vec{v}\,(\vec{k}\,) = 0$. Therefore, the DOS has a logarithmic singularity at the Fermi energy E_F.

The calculations show that the states at the Fermi energy are not spread evenly over the unit cell, but are confined strongly to the CuO networks in the layer. The charge density of the states at E_F midway between Γ and X has been calculated and plotted by Yu et al. (1987). A large fraction of this DOS has within a slab of thickness $\sim 1\,\text{Å}\ \left(\frac{c}{2} = 6.2\,\text{Å}\right)$. Moreover, instead of evenly spread, the charge stays close to the Cu and O atoms, leaving a square array of large holes in the center of the squares. The Fermi surface is roughly two-dimensional (Fig. 5.12).

In the crudest approximation, in which the bands are described by the simple pdσ bands, the Fermi surface for the half-filled band is an array of square cylinders, touching at the corners, which can be regarded as containing electrons around Γ or containing holes around X. Such a Fermi surface has perfect nesting for the wave vector $k = X = (1, 1, 0)\,\pi/a$. Strong nesting can lead to either a charge density wave (CDW) or a spin density wave (SDW), or possibly both. Which of the two occurs depends whether the charge susceptibility or the spin susceptibility diverges first as temperature decreases.

For a one band Hubbard model (a CuO_4 unit corresponds thereby to a lattice point), the conditions are

$$
\begin{aligned}
&1 - \left(\frac{2g^2}{K} - U\right) u\,(Q, T) = 0(\mathrm{CDW}),\\
&1 - U u\,(Q, T) = 0(\mathrm{SDW})
\end{aligned}
$$

respectively.

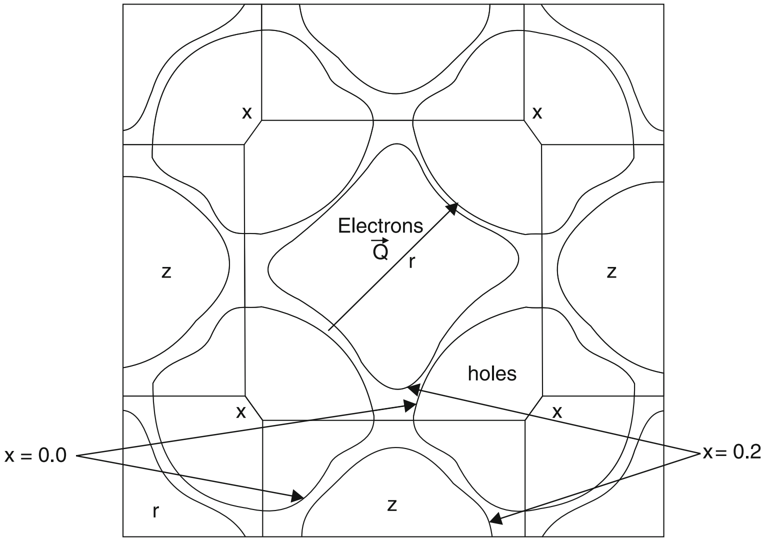

Fig. 5.12 Fermi surface of paramagnetic $La_{2-x}M_xCuO_4$ in the $k_z = 0$ plane for $x = 0.0$ and 0.20

Here g is the electron-phonon coupling constant, K is the characteristic elastic energy, U is the coulomb interaction between two electrons in a CuO_4 unit and $u\,(Q, T)$ is the *Lindhard function* for a one-dimensional system with nesting vector $\vec{Q}\left(=2\vec{k}_F\right)$. The latter has a singularity as $T \to 0$. From the experimental fact that an anti-ferromagnetic phase transition, but no CDW is found, one may conclude that $U > 2\,g^2K^{-1}$. From a Neel temperature of $T_N = 230$ K, one can estimate U to be ≈ 2 eV. The AF order is destroyed by doping (with Sr). Nesting is then no longer perfect and $u\,(Q, T)$ decreases, therefore, this shows that electron correlations are strong.

5.14 Strong Electron Correlations

A convenient measure of "Strongness" of electron correlation is the suppression of charge fluctuations by correlations.

A correlation strength parameter Σ is defined through

$$\sum = \frac{(\Delta n)_{\mathrm{SCF}} - (\Delta n)_{\mathrm{corr}}}{(\Delta n)^2_{\mathrm{SCF}}}.$$

Here, $(\Delta n)^2 = (n - \bar{n})^2$ is the mean square deviation of an orbital occupancy n from its average value $\bar{n}$. It is calculated by using the self-consistent field (SCF) ground state wave function $| \phi_{\mathrm{SCF}} \rangle$ (independent electron approximation) and the correlated wave function $| \psi_{\mathrm{corr}} \rangle$ respectively. Both are related through

$$\left| \psi_{\mathrm{corr}} \right\rangle = e^{s} \left| \phi_{\mathrm{SCF}} \right\rangle$$

where s consists of local operators, which generate a correlation-hole around every valence electron. For uncorrelated electrons $\Sigma = 0$ while in the strong correlation limit $\Sigma \to \Sigma_{\max}$, which depends on $\bar{n}$. For $\bar{n} = 1$, it is $\Sigma_{\max} = 1$. Detailed calculations show that for Cu $\left(3d_{x^2-y^2}\right)$, it is $\frac{\Sigma}{\sum_{\max}} \cong 0.85$, i.e. one is close to the strong correlation limit.

A better theoretical understanding of high T_c materials is still a fascinating problem and there is apparently no fast progress in this direction, the reason being that the strong electron correlations govern the motion of electrons in the Cu$-$O$_2$ planes.

Experimental evidences of strong correlations include:

1. Energy gap $= 7{-}8\, k_B T_c$C (for $T_c = 90\,\mathrm{K}$) and independent of T_c (as compared to BCS/Fermi liquid prediction $3.5\, k_B T_c$).
2. La_2CuO_4, inspite of a half filled conduction band, is an insulator and not a metal (strong correlations suppress the charge fluctuations necessary for a finite conductivity).
3. The behaviour of the oxygen 1s electron energy loss spectrum (EELS) of $La_{2-x}Sr_xCuO_4$ with changing doping concentration cannot be explained within a one electron band picture and shows characteristics features of strong correlations.

The standard model, which is used for describing the strong correlations (in the CuO_2 planes) is the three-band Hubbard or energy model. Strong correlations are expected from photo electron (PES) and inverse photo electron (BIS) spectra calculated from that model. The three-band Hubbard or Emery model considers only the Cu$3d_{x^2-y^2}$ and those O$2p_{x(y)}$ orbitals, which hybridize with the Cu orbitals most strongly. The parameters obtained in it can be derived from LDA calculations. One finds indeed that the coulomb repulsion of two holes at a Cu site is $U_d \approx 10.5\,\mathrm{eV}$ and, therefore, much larger than the hopping matrix element $t_{pd} = 1.3\,\mathrm{eV}$ between a Cu$3d_{x^2-y^2}$ and O$2p_{x(y)}$ orbital. Hence, strong correlations are expected from this point of view also.

5.15 Charge Density Wave and Spin Density Wave

The tendency toward Fermi-surface driven instabilities is given a general measure, in terms of the generalized susceptibility χ(Q), by

$$\chi(Q) = \frac{\sum\limits_{\underline{k}} \left(f_{\underline{k}} - f_{\underline{k}+Q}\right)}{\left(E_{\underline{k}+Q} - E_{\underline{k}}\right)},$$

where $E_{\underline{k}}$ is the band energy and $f_{\underline{k}} = f\left(E_{\underline{k}}\right)$ is the Fermi function. The susceptibility towards CDW or SDW instabilities in a crystal involves a matrix generalization of χ with appropriate matrix elements. However, the Q-dependence is usually provided by this generalized scalar form.

The insulating cuprates La_2CuO_4 and $Y_1Ba_2Cu_3O_6$ exhibit A.F—a special case of SDW, so that within a band picture, the insulating nature of these (with only Cu^{2+} in their CuO_2 layers) may be rationalized in terms of the metal-SDW transition associated with the nested Fermi surface of their half filled $x^2{-}y^2$ bands. As the extent of hole (or electron) doping increases in the CuO_2 layers, the Fermi surface no longer is quadratic, it becomes (more) circular in shape and, therefore, not nested so that electronic instability is removed (-metallic). The SDW is commensurate with the crystal lattice, its wavelength is twice the Cu–Cu distance in the *ab* planes. The first implication is that the Fermi surface (or at least a substantial portion of it) is destroyed and the instability opens up an energy gap at E_F, which transforms the system from metallic to insulating.

Thus, the instability due to nested Fermi surface is a symmetry breaking instability in which the band energy gain arising from the gap is thought to drive such a Metal (M) to insulator (I) transition by overwhelming the loss in Coulomb (and strain) energy, which favours the symmetric (M) state.

5.16 Variation of T_c with Hole Concentration

In high temperature cuprate superconductors, the mechanism of superconductivity is not known so far, T_c (critical temperature) cannot be calculated like conventional superconductors, in terms of the known parameters. Experimental facts have given certain general trends. One of the trends is that T_c scales with the hole density (Fig. 5.13). T_c reaches a maximum value around an optimal hole concentration and decrease for lower and higher values of hole concentrations. Figure 5.13 depicts the variation of T_c with hole concentration n_h for La–Sr–Cu–O and Y–Ba–Cu–O. The hole concentration can be varied by substitution (e.g. Sr or Ba by La in La–Sr–Cu–O) (Table 5.1).

It was first observed by Torrance (IBM) that T_c is a non-monotonic function of carrier concentration n_c. There is a certain optimal value n_H, which corresponds to maximum T_c (Fig. 5.13). When $n_c > n_H$, the critical temperature begins to come down and at a sufficiently large value of n_c, there is a superconductor to normal metal transition.

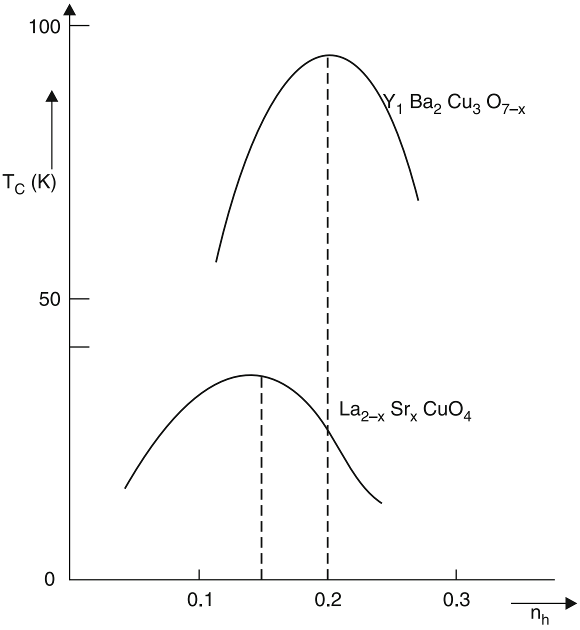

Fig. 5.13 Variation of T_c with hole concentration n_h [2]

5.16.1 *Role of* CuO_2 *Planes (Effect on* T_c*)*

To assess the effect of CuO_2 planes on T_c, it is necessary to consider the role of interlayer coupling. It has been observed that T_c is maximum for an optimum number of CuO_2 planes. Two different types of coupling may be distinguished:

(1) Intra-cell and
(2) Inter-cell coupling

In the cuprates, unlike graphite intercalation compounds (GICs), intra-cell coupling between two CuO_2 planes is much smaller (than in GIC) because of the spacer layers of Ba/Sr/Ca. However, the inter-cell coupling is much larger as evidenced by smaller anisotropy of conductivity and effective mass. Hence, in interpreting the hole concentration, it can be assumed that all the holes arise in the CuO_2 sheets. Now, why T_c does not continue to increase as n increases above 3 or 4 can be understood as follows:

If the holes are generated by transferring electrons to the intercalant layers, then screening effects will cause most of the holes to pile up on the bounding layers, i.e. those layers nearest the intercalant. Hence, any extra CuO_2 layers will have very few carriers, and will not contribute to the superconductivity.

Table 5.1 Electron configuration and other parameters of some elements

Element	Z	Configuration	Valency	Ionic radius	Pauling electronegativity
Y	39	$[Kr]4d5s^2$	+3	0.893	1.22
Ba	56	$[Xe]6s^2$	+1	1.53	0.89
			+2	1.32	
Cu	29	$[Ar]3d^{10}4s$	+1	0.96	1.90
			+2	0.72	
Bi	83	$[Xe]4f^{14}5d^{10}6s^26p^3$	+1	0.98	2.02
			+3	0.96	
			+5	0.74	
Sr	38	$[Kr]5s^2$	+2	1.12	0.95
Ca	20	$[Ar]4s^2$	+1	1.18	1.00
			+2	0.99	
Tl	81	$[Xe]4f^{14}5d^{10}6s^26p$	+1	1.47	2.04
			+3	0.95	
O	8	$[He]2s^22p^4$	−2	1.40	3.44
Pb	82	$[Xe]4f^{14}5d^{10}6s^26p^2$	+2	1.20	2.33
			+4	0.84	

5.17 Defects in Bi Based Superconductors

For the Bi based compounds, the mismatch between the dimensions of the CuO_2 and intercalating layers is so large that the structure displays an incommensurate modulation, i.e. the atom-positions no longer exhibit the ideal translational symmetry of the basic unit cell, rather they are displaced with a periodicity that is not commensurate with the underlying unit cell.

Defects in the Bi-system include

(a) Bi-atom substitution on the Sr- and Ca-sites
(b) Sr atom substitution on Ca-site
(c) Vacancies on Sr-sites
(d) Interstitial O-atoms at the end of a modulation period.

Inspite of this complexity, the calculated average oxidation state for the copper (i.e. Cu atom in the conduction layer) is 2.21, in good agreement with the optimum values for superconductivity observed in other cuprates.

Defects in the conduction layer (e.g. oxygen O^- vacancy) destroy superconductivity.

5.18 Effect of Oxygen Stoichiometry on T_c of HTSCs Bi Based and Tl Based Superconductors

A maximum T_c can be reached by optimizing the hole carrier density through manipulation of the oxygen stoichiometry. It has been found for $Y_1Ba_2Cu_3O_7$ that an oxygen deficiency relative to the nominal composition lowers the T_c. Thus, it appears that increasing the oxygen content would have a very desirable effect of raising T_c. But it is not always the case, e.g. consider the thallium cuprate $Tl_2Ba_2CuO_6$. In fact, its formula should be written as $Tl_2Ba_2CuO_{6\pm\delta}$, because it has been found that its synthesis as a pure phase with absolutely regular stacking of copper and thallium layers does not give a "superconductor". It has been found with the help of HREM (high resolution electron microscopy) that without any structural change, T_c is controlled by creating point defects (oxygen vacancies) through optimized annealing. Then, the variation of δ can be interpreted chemically as a variation of mean oxidation state of Cu between Cu^{2+} and Cu^{3+}, or in terms of physics, a variation of hole carrier density. The T_c of $Tl_2Ba_2CaCu_2O_8$ has been raised to 120 K by hydrogen annealing and $Tl_2Ba_2Ca_2Cu_3O_{10}$ appears to acquire a maximum T_c of 125 K through annealing under ambient oxygen pressure.

The effect of oxygen pressure is different for Bi-cuprates. The reversible reaction

$$Bi^{3+} + 2Cu^{3+} \Rightarrow Bi^{5+} + 2Cu^{2+}$$

affects the equilibrium population of the copper oxidation states. Starting from the air synthesized

$$Bi_{2.1}Sr_{1.9}CaCu_2O_{8+\delta} \quad (T_c = 76\,K)\,,$$

one can arrive at composition

$$Bi_{2.1}Sr_{1.9}CaCu_2O_{8.17} \quad (T_c = 90\,K)$$

by annealing at 400 °C with Argon.

Annealing in oxygen flow produces

$$Bi_{2.1}Sr_{1.9}Ca\,Cu_2O_{8.23}$$

with a T_c of only 66 K.

In double Tl–O layer based superconductor, the thallium bi-layers are conducting, so that an excess or deficiency of oxygen in these layers will affect the T_c.

In single Tl–O layer based superconductors, the Tl–O layer is insulating. But in both the cases (i.e. in single Tl–O and double Tl–O layer HTSCs), the oxygen stoichiometry in the perovskite layer (i.e. CuO_2 planes) will influence the T_c due to Jahn–Teller effect. Formation of oxygen vacancies in CuO_2 layers can yield either pyramidal or square planar configuration, instead of octahedral, i.e. a change in coordination of copper with oxygen ions.

5.19 Comparison of Bi- and Tl-Cuprates

A pair of electrons with opposite spins, which does not take part in bonding is known as *lone-pair*.

In the double rock salt layer cuprates, the bonding between the two layers may be different (i.e. Bi-double layer and Tl-double layer).

In $\mathrm{Bi_2Sr_2Ca}_{n-1}\mathrm{Cu}_n O_{2n+4}$,

(1) The Bi^{3+} $6s^2$ lone pair electrons are oriented between the sheets
(2) A Bi–O chain in one of the sheets of a double layer is located directly above (or below) a chain in the other sheet of the double layer. Consequently, there is very weak interaction between the two consecutive sheets of a double layer in Bi, accounting for the mica-like behaviour (it can be cleaved very easily)

In contrast to this, the lone-pair absence and staggered chain arrangement leads to a very strong interlayer bonding in the Tl–O layers of

$$(\mathrm{TlO})_2\,(\mathrm{BaO})_2\,\mathrm{Ca}_{n-1}\,(\mathrm{CuO}_2)_n\,.$$

The Tl–O planes are much closer together than Bi–O planes (interlayer spacing is 3.2 Å for BiO and 2 Å for TlO). Each Tl has already bonded to two close oxygens, one from the perovskite plane and other from the second TlO layer. Therefore, electron delocalization along the *c*-axis is much easier in the Thallium relative to the Bismuth phases (Table 5.2).

5.20 Comparison of Mercury Based and Thallium Monolayer Based Cuprate Superconductors

Hg:12 $(n-1)n$ has a general layered structure, similar to Tl-12 $(n-1)n$ with repeated stacking of rock salt type layers (BaO) (HgO_δ) (BaO) and perovskite type layers $(\mathrm{CuO_2})$ Ca $(\mathrm{CuO_2})$.

Difference: Tl- compound has Tl^{3+} and, therefore, rock salt type layers of (BaO) (TlO) (BaO). Mercury compound has Hg^{2+} and, therefore, (BaO) (HgO_δ) (BaO), i.e. oxygen deficient HgO_δ layers. In Hg:1201 and Hg:1212, there exist a large number of vacant oxygen sites in the Hg layer.

By fine tuning, the doping levels especially the anion doping, (e.g. oxygen) even higher T_c may be found in HBCCO.

5.21 Mercury Based Superconductors

The role of O(4) and electronic structure of Hg:1223 for $\delta \neq \mathrm{o}$:

Experiments show that the T_c of $\mathrm{HgBa_2Ca_2Cu_3O}_{8+\delta}$ rises to 134 K after oxygenation and the extra oxygen O(4) lies in the centre of the Hg-layers. Table 5.3 indicates Fermi energies and DOS of $\mathrm{HgBa_2Ca_2Cu_3O}_{8+\delta}$ for various values of δ.

Table 5.2 Comparison of Bi-and Tl based systems in regard to the source of carriers in respective cases

The HTSC system	Relative energies of $Cu_{x^2-y^2}$ and rock salt layer 6*s* or 6*p* block bands	Copper oxidation state	Remarks
$Bi_2Sr_2Ca_{n-1}Cu_nO_{2n+4}$	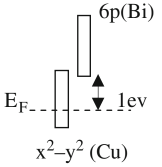 (distorted Bi-O layer)	+2	Bi 6p block bands do not act as hole source. Holes are created by excess O^- atoms in BiO layers
$Tl_2Ba_2Ca_{n-1}Cu_nO_{2n+4}$	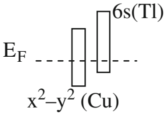	+2	TlO layers are important in creating holes in CuO_2 layers. Additional sources are excess oxygen and cation vacancy
$Tl_1Ba_2Ca_{n-1}Cu_nO_{2n+3}$	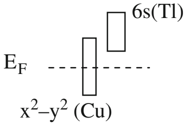	$2 + (1/n)$	Tl–O single rock salt layers do not create holes in CuO_2 layers rather, Cu atoms are itself in high oxidation state

Note In Tl-double layer HTSC, since Tl-6*s* block band is below Fermi level, it removes electrons from x^2-y^2 bands of CuO_2 layers. In Tl monolayer HTSC, Tl − 6*s* block band is above Fermi level, therefore, they do not remove electron from x^2-y^2 bands of CuO_2 layers

As δ increases, E_F is lowered, while $N(E_F)$ increases monotonically. For $\delta = 0.4$, $N(E_F)$ has increased by about 6.5 states Ryd^{-1} per cell (as compared to $\delta = 0$).

$N(E_F)$ is mainly from $Cu3d_{x^2-y^2}$ orbitals, and there is some distance between E_F and the DOS peak of $Cu3d_{x^2-y^2}$ (These are nearby for $\delta = 0$).

It has been conjectured that:

1. The oxygenation lowers E_F and $N(E_F)$ increases markedly for $\delta = 0.4$ (this has also been speculated by experiments)
2. The Cu–O band in the CuO_2 layer is strengthened further after doping O(4)
3. The Cu(2)–O(3) bond (i.e. interaction between the layers) is intensified

Table 5.3 E_F and $N(E_F)$ of Hg:1223 for various values of δ

δ	E_F(Ryd)	$N(E_F)$ (states Ryd^{-1}/cell)
0	−0.59106	35.8
0.12	−0.59810	36.8
0.2	−0.60241	38.5
0.4	−0.61022	42.3

Table 5.4 Valences of copper and oxygen in $HgBa_2Ca_2Cu_3O_{8+\delta}$ for varying δ (Rise in valence means loss of electrons)

δ	Cu(1)	Cu(2)	O(1)	O(2)	O(3)	O(4)
0	1.336	1.356	−1.619	−1.633	−1.829	–
0.12	1.396	1.419	−1.611	−1.625	−1.838	−1.911
0.2	1.435	1.460	−1.606	−1.620	−1.837	−1.911
0.4	1.511	1.525	−1.596	−1.610	−1.811	−1.877

Table 5.5 Change in the number of holes in CuO_2 layers of $HgBa_2Ca_2Cu_3O_{8+\delta}$ for various

δ	n[Cu(1)]	n[Cu(2)]	n[O(1)]	n[O(2)]	Δn
0	0.658	0.669	0.337	0.326	–
0.12	0.714	0.727	0.345	0.334	0.220
0.2	0.750	0.765	0.350	0.339	0.362
0.4	0.821	0.826	0.359	0.348	0.609

4. There is strengthening of the Hg–O(3) bond also The drop in E_F together with the strengthening of the correlation between the layers, leads to the redistribution of the carriers. This implies change in valences of each site after oxygenation. It has been found that valences of Cu and O (in CuO_2 layers) rise, while valences of other sites change little (Table 5.4)
5. Doping O(4) moves electrons from CuO_2 layers to the O(4) sites in the HgO layer, through BaO layers, and leads to an increase in hole concentration in the CuO_2 layers

Table 5.5 gives change in the number of holes for Cu3*d* (per copper atom) and O*p* (per oxygen atom) in the CuO_2 layers of $Hg_1Ba_2Ca_2O_{8+\delta}$ for various δ.

Δn is the total change in the number of holes per cell in the three CuO_2 layers. It has been suggested [3] that O(4) should induce 0.60 holes per cell (for three CuO_2) to make E_F coincide with the DOS peak. This requires that every O(4) atom has to supply two holes and for this, ideal δ would be 0.30.

However, if the effects of Hg, Ba and Ca are taken into account (they also provide some electrons) and not every O(4) would offer exactly two holes, then the ideal δ is 0.40. Thus, effects of O(4) are as hereunder:

(1) Increases $N(E_F)$
(2) Increases hole concentration in CuO_2 layers
(3) Strengthens Cu–O bond (therefore interaction) within the CuO_2 layers
(4) Strengthens correlation between the layers

These above factors are responsible for the rise in T_c after oxygenation (Table 5.6).

Table 5.6 Critical Temperature, average copper-oxidation states and lattice parameters of various high Tc superconductors

The HTSC	T_c(K)	Average Cu-oxidation state[a]	Structure (Å)	
$Y_1Ba_2Cu_3O_{7-x}$	92	+2.33	a = 3.82, b = 3.89, c = 11.70 (orthorhombic)	
$Tl_2Ba_2Cu_1O_{6+y}$	82	+2.17	a = 3.86, c = 23.2	Tetragonal
$Tl_2Ba_2Ca_1Cu_2O_{8+y}$	108	+2.16	a = 3.854, c = 29.2	
$Tl_2Ba_2Ca_2Cu_3O_{10+y}$	125	+2.11	a = 3.850, c = 35.6	
$Tl_1Ba_2Cu_1O_5$		+3.0	a = 3.86, c = 9.56	Tetragonal
$Tl_1Ba_2Ca_1Cu_2O_7$	80	+2.50	a = 3.85, c = 12.76	
$Tl_1Ba_2Ca_2Cu_3O_9$	105	+2.33	a = 3.849, c = 15.95	
$Tl_1Ba_2Ca_3Cu_4O_{11}$	120	+2.25	a = 3.845, c = 20.25	
$Hg_1Ba_2Cu_1O_{4+\delta}$	94		a = 3.85, c = 9.5	Tetragonal
$Hg_1Ba_2Ca_1Cu_2O_{6+\delta}$	120		a = 3.85, c = 12.6	
$Hg_1Ba_2Ca_2Cu_3O_{8+\delta}$	133	+2.203 (for $\delta = 0.4$)	a = 3.85, c = 15.7	

[a] optimum ideal value necessary for superconductivity is +2.2 to +2.3

5.22 Mercury Doped Tl:2223 Superconductor

Pure Tl:2223 (with ideal stoichiometry) would have all the Cu-atoms in the 2^+ state, making it an insulator. A higher copper valence state, necessary for a cuprate to be superconducting, is created via

(1) The substitutions of Tl^{3+} with Ca^{2+}
(2) Vacancies at cation sites
(3) Internal redox reaction

$$Tl^{3+} + Cu^{2+} \rightarrow Tl^{(3-\delta)+} + Cu^{(2+\delta)+}$$

(taking place because of overlapping Tl ($6s$) and Cu $(3d)_{x^2-y^2}$ bands at E_F for Tl:2223).

These above complex internal mechanisms are difficult to control experimentally during synthesis, therefore, an overall, optimized stable phase of Tl:2223 material is difficult to achieve, and the T_c also has been found to vary (113–127 K), even if the compound has an optimized oxygen concentration. However, partial substitution of Tl^{3+} with a lower valent cation (e.g. Hg^{2+}) increases the effective copper valence and brings the Tl:2223 system from an under-doped regime to an optimally doped regime promoting the formation of Tl:2223 phase with a maximized T_c.

5.23 Hubbard Model and Band Structure

The Table 5.7 gives electron-configurations of selected atoms useful for band-structure calculations of superconductors.

The Cu^{2+} ion ($3d^9$) may be looked upon as a filled d-shell ($3d^{10}$) plus one 3d hole, and in the cuprates this hole is a d_{x2-y2} orbital in the CuO_2 plane.

The various s, p and d wave functions (called orbitals) have the analytical form given in Table 5.8.

Figure 5.4 shows the spatial electronic charge distribution of the d orbitals and Fig. 5.10 shows the sigma (σ) bonding between oxygen p_x and p_y orbitals and copper d_{x2-y2} orbitals in the CuO_2^- plane of a cuprate HTSC (For a three state model, each copper contributes a d_{x2-y2} orbital and each oxygen contributes either a p_x or a p_y orbital).

The orbitals $\phi(\mathrm{r}-\mathrm{R})$ used in band structure calculations are normalized

$$\int \phi^*(\mathrm{r}-\mathrm{R})\phi(\mathrm{r}-\mathrm{R})\mathrm{d}^3\mathrm{r}$$

for an atom located at position R. The overlap integral $\beta\,(\mathrm{R}-\mathrm{R}')$

$$\beta(\mathrm{R}-\mathrm{R}') = \int \phi^*(\mathrm{r}-\mathrm{R})\phi(\mathrm{r}-\mathrm{R}')\mathrm{d}^3\mathrm{r}$$

is a measure of the extent to which the orbitals of atom at positions R and R′ overlap. The Coulomb integral

$$\mathrm{U(R)} = \int \phi^*(\mathrm{r}-\mathrm{R})\mathrm{V_c(R)}\phi(\mathrm{r}-\mathrm{R})\mathrm{d}^3\mathrm{r}$$

provides the Coulomb repulsion energy associated with orbital $\phi\,(\mathrm{r}-\mathrm{R})$ on an atom at position R.

The simplest model of correlated electrons is the one-band Hubbard model which (despite its simplicity) exhibits many properties characteristic of superconductors.

The Hamiltonian, written in terms of creation (a_σ^+) and annihilation (a_σ) operators of spin σ associated with atoms at positions R′ and R has the form

$$\begin{aligned} H = &- t \sum_{R,R',\sigma} \left[a_\sigma^+(R)a_\sigma(R') + a_\sigma^+(R')a_\sigma(R)\right] \\ &- \mu \sum_{R,\sigma} a_\sigma^+(R)a_\sigma(R) + U \sum_{R} n_+(R)n_-(R) \end{aligned}$$

Here the Coulomb repulsion term $U > 0$ is defined as above equation and the hopping amplitude $t > 0$ is a measure of the contribution from an electron hopping from one site to another. The chemical potential μ takes into account changes in the number of

Table 5.7 Electron configuration of selected atoms

Atomic numbers	Symbol	{core}$^{(*)}$Atom configurations	No. of valence electrons	Ion	Ion config. urations	No. of electrons in ion
8	O	{Be}, $[2s^2]2p^4$	4	O^{1-}	$2p^5$	5
				O^{2-}	$2p^6$	6
20	Ca	{Ar}, $4s^2$	2	Ca^{2+}	–	0
29	Cu	{Ar}, $3d^{10}4s^1$	11	Cu^{1+}	$3d^{10}$	10
				Cu^{2+}	$3d^9$	9
				Cu^{3+}	$3d^8$	8
38	Sr	{Kr}, $5s^2$	2	Sr^{2+}	–	0
39	Y	{Kr}, $4d^1 5s^2$	3	Y^{3+}	–	0
56	Ba	{Xe}, $[5p^6]6s^2$	2	Ba^{2+}	–	0
57	La	{Xe}, $5d^1 6s^2$	3	La^{3+}	–	0
80	Hg	-78, $[5d^{10}]6s^2$	2	Hg^{2+}	$[5d^{10}]$	0
81	Tl	-78, $[5d^{10}]6s^2p^1$	3	Tl^{3+}	$[5d^{10}]$	0
82	Pb	-78, $[5d^{10}]6s^2p^2$	4	Pb^{4+}	$[5d^{10}]$	0
83	Bi	-78, $[5d^{10}]6s^2p^3$	5	Bi^{3+}	$[5d^{10}]6s^2$	2
				Bi^{4+}	$[5d^{10}]6s^1$	1
				Bi^{5+}	$[5d^{10}]$	0

(*)The core of Hg, Tl, Pb and Bi is Xe plus the rare earth ($4f^{14}$) and ($5d^{10}$) closed shells (Xe = 54).

Table 5.8 Unnormalized analytical expressions for the s, p and d orbitals

Orbital	Cartesian form	Polar form
s	1	1
p_x	x/r	$\sin\theta\cos\phi$
p_y	y/r	$\sin\theta\sin\phi$
p_z	z/r	$\cos\theta$
d_{xy}	xy/r^2	$\sin^2\theta.\sin\phi.\cos\phi$
d_{yz}	yz/r^2	$\sin\theta.\cos\theta.\sin\phi$
d_{zx}	zx/r^2	$\sin\theta.\cos\theta.\cos\phi$
d_{x2-y2}	$(x^2-y^2)/r^2$	$\sin^2\theta(\cos^2\phi-\sin^2\phi)$
d_{z2}	$(3z^2-r^2)/r^2$	$(3\cos^2\theta-1)$

electrons and is zero if there is no doping. This Hamiltonian exhibits an electron-hole symmetry, which is of some importance to high T_c cuprates because most HTSCs are hole-type with a close to half-full band [31].

5.24 Arrangement of Atoms in p-Type Superconductors

In cuprate superconductors, CuO_2 layers are built from corner sharing square-planar CuO_4units and copper can be bonded to another O-atom, creating a square pyramidal environments or to two additional O-atoms, giving an axially elongated octahedral surrounding. Compositionally, these superconductors have the formula $(AO)_m(BO)_2M_{n-1}(CuO_2)_n$ and are often referred to as m2(n−1)n phases (Fig. 5.14). The number of CuO_2 layers stacked consecutively can be as high as 5. When $n = 1$ only distorted CuO_2 octahedra are present. With $n = 2$, all of the Cu atoms are square pyramidal. For $n > 3$, the copper atoms of the outer two CuO_2 layers are square pyramidal and those of the inner ones are square planar. M is typically Ca, Y or rare earths and is situated between adjacent CuO_2 sheets. A BO layer with B = La, Sr or Ba is located directly above and below the $(CuO_2)_n$ layers. Up to two AO layers can be stacked together: m = 2 for A = Bi, m = 1 or 2 for A = Tl aNdm = 0 for B = La (e.g. La_2CuO_4). The superconductors $YBa_2Cu_3O_7$ and Y $Ba_2Cu_4O_8$ are special cases of the m2 (n − 1)n series: The AO layer is replaced by a layer composed of CuO strings for m = 1 and CuO double strings for m = 2 [i.e. $(CuO)_m(BaO)_2Y_1(CuO_2)_2$]. Structural oxidation–reduction chemistry (e.g. cation substitution of Sr^{2+} for La or Y^{3+} for Ca^{2+}) in the AO, BO and M layers leads to electron removal from (i.e. hole doping) or electron addition to (i.e. electron doping) the CuO_2 layers.

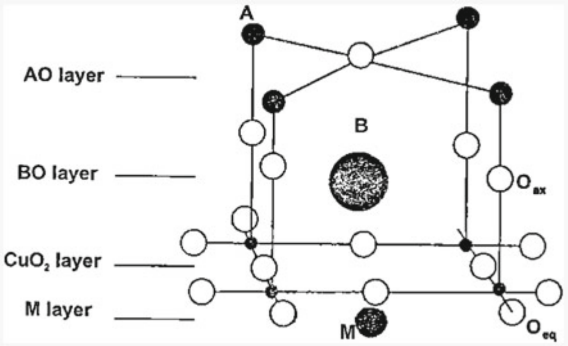

Fig. 5.14 Schematic diagram showing the arrangement of atoms around a 9-coordinate site in p-type cuprate superconductors. The cations are represented by *shaded circles*. (A = Bi, Tl; B = La, Ba, Sr; M = Y, Ca) [4]

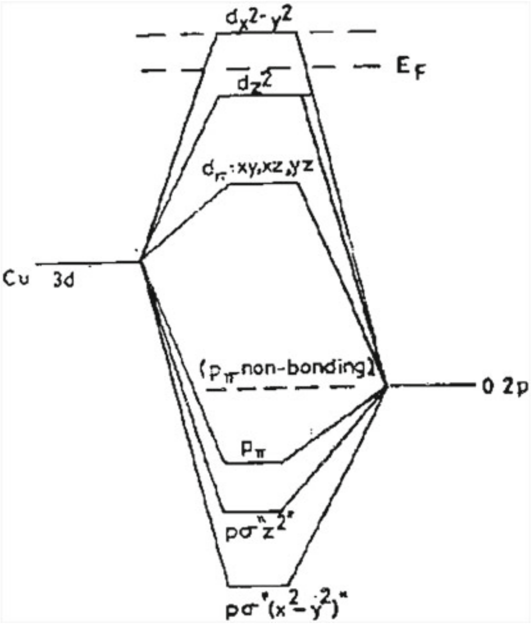

Fig. 5.15 Ligand field split levels of Cu3d in a distorted octahedral coordination similar to that in cuprates. These levels schematically describe the energy states of a single octahedral CuO_6 cluster [2]

5.25 Electronic Structure of the CuO_2 Layer

The holes or electrons of the cuprate superconductors are probably all associated with the “in-plane” $x^2 - y^2$ band, because this band lies significantly higher than the other d-block bands (Fig. 5.15).

(The d_{x2-y2} orbital is partly p-like, i.e. the wave function is a mixture of d_{x2-y2} and p_σ (or $p_x - p_y$) orbitals, the latter with d_{x2-y2} symmetry around the Cu site).

The electronic structures of cuprates are described by two methods [5]

1. Cluster approach (with Hubbard Hamiltonians)
2. A band picture (with effective one-electron Hamiltonians)

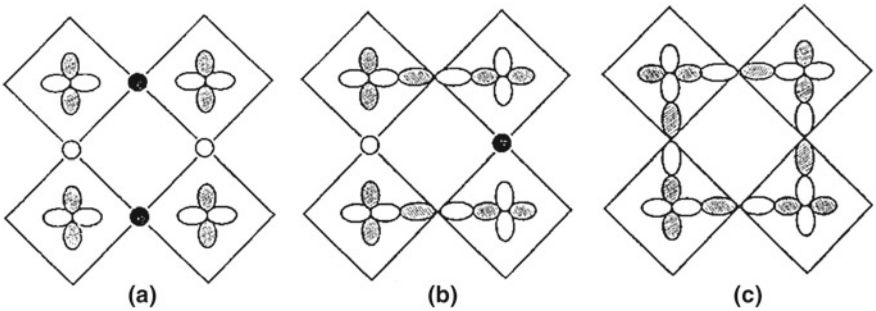

Fig. 5.16 The orbitals in bottom (**a**), middle (**b**), and top (**c**) of the $x^2 - y^2$ band

Here (1) readily incorporates correlation energies and explains high energy excitations (e.g. photo electron spectroscopy) well. However, the delocalized nature of the conduction electrons in the normal metallic state is not well described.

(2) does not properly incorporate correlation energies and hence fails to explain the details of high energy excitation spectra and the insulating nature of these cuprates with only Cu^{2+} ion in ptheir CuO_2 layers (e.g. La_2CuO_4 and $Y_1Ba_2Cu_3O_6$). However, the normal metallic state (corresponding to Cu oxidation state differing from +2)
is well described by a band picture because it accounts for the delocalized nature of the conduction electrons.

In the $x^2 - y^2$ band of a layered cuprate, the copper $x^2 - y^2$ orbitals make σ antibonding interaction with the oxygen orbitals. The extent of this antibonding increases gradually as the energy level is raised from the bottom to the top of the $x^2 - y^2$ band. For instance, the bottom, middle and top levels of this band are described by the orbitals (Fig. 5.16a, b and c, respectively) [6, 7]. Infact, photoemission spectroscopy studies on cuprate superconductors have revealed that the states around their Fermi levels have extensive copper 'd' and oxygen 'p' orbital hybridization [5]. Due to the δ-symmetry of the $x^2 - y^2$orbital along the Cu-O_{ax} direction, the s and p orbitals of O_{ax} do not overlap with the $x^2 - y^2$ orbitals of the CuO_2 layer copper atoms and therefore do not contribute to the $x^2 - y^2$ band.

Consequently, hole doping ($n_H > O$) or electron doping ($n_E > O$) into the Cu-O layers affects electronically only the in-plane Cu-O bonds. The out-of-plane Cu-O bonds are not electronically modified by hole or electron doping. That hole-or electron doping in the cuprate systems involves only the σ antibonding in-plane band (i.e. the $x^2 - y^2$ band) of their CuO_2 layers, has important geometrical consquences [4]. Substitution of the larger cation La^{3+} for the smaller cation Nd^{3+} in $Nd_{2-x}La_xCuO_4$ increases both the 'a' and 'c' unit cell parameters [8]. This cation substitution does not alter the copper oxidation state and the stesic effect of the larger La^{3+} cation expands both the 'a' and 'c' parameters, which are associated with the in-plane and the out of -plane Cu-O bond lengths respectively. Substitution of the larger cation Sr^{2+} for the smaller cation La^{3+}in $La_{2-x}Sr_xCuO_4$ increases the 'c' parameter but decreases the ‘a’ parameter [8]. The latter is due to the electronic factor: substitution of Sr^{2+} for La^{3+} creates holes in the CuO_2 layer i.e. removes electrons from the σ antibonding $x^2 - y^2$ band. Similarly substitution of the smaller cation Ce^{4+} for the larger cation Nd^{3+} in $Nd_{2-x}Ce_xCuO_4$ decreases the ‘c’ parameter but increases the ‘a’ parameter [8], the latter being caused by the electronic factor of addition of electrons in the antibonding $x^2 - y^2$ band.

5.26 Rock-Salt Layer in Cuprates as Hole-Source

Hole doping of the cuprate CuO_2 is achieved by several means, which include cation substitution, cation vacancy and oxyten excess. All of these are based upon nonstoichiometry of chemical compositions. Holes may also be introduced into the CuO_2 layers when the bottom of the rock-salt layer bands lies below the Fermi-level. This possibility becomes important for the cuprates containing Bi–O and Tl–O rock salt layers because the 6p-block bands of the Bi–O layers and the 6s-block bands of the Tl–O layers lie close to the CuO_2 layer $x^2 - y^2$ bands. According to band-structure calculations on $Bi_2Sr_2Ca_{n-1}Cu_nO_{2n+4}$ with an ideal structure for the Bi–O double rock salt layer, the bottom of the Bi 6p bands lie below the Fermi level [9]. This leads to a chemically unreasonable implication that Cu^{2+} is oxidized by Bi^{3+}. However, calculations with distorted Bi–O rock-salt-layer structures show [10] that the bottom of the Bi 6p block bands of $Bi_2Sr_2Ca_{n-1}Cu_nO_{2n+4}$ lies more than 1eV above the Fermi level (see Fig 5.17a), and thus the Bi-6p block bands do not act as a hole source. This finding has been confirmed by experimental observations [11, 12]. Holes in $Bi_2Sr_2Ca_{n-1}Cu_nO_{2n+4}$ are in part created by excess oxygen atoms in the Bi–O layers and in part by strontium deficiency [10]. According to hand structure calculations [13], on $Tl_2Ba_2Ca_{n-1}Cu_nO_{2n+4}$ with an ideal structure for the Tl–O double rock-salt layers, the bottom of their Tl 6s-blck bands lies only slightly below the Fermi level, thereby suggesting that the Tl–O double rock salt layer is not an important hole source. However, calculations with distorted Tl–O double rock-salt-layer structures reveal [14] that the bottom of the Tl 6s-block bonds lies significantly below the Fermi-level (see Fig. 5.17b). Therefore, the Tl–O double rock-salt layers are important in creating holes in the CuO_2 layers. $Tl_2Ba_2CuO_6$ exhibits [15] a $T_c$nearly as high as that of $YBaCu_3O_7$ (∼92K) although it has only one CuO_2 layer/formula unit. This may reflect the fact that $Tl_2Ba_2CuO_6$ readily achieves a high copper oxidation state by the Tl 6s block band/Cu $x^2 - y^2$ band overlap plus additional hole sources such as excess oxygen and cation vacancy.

In sharp contrast to the case of the Tl–O double rock-salt-layer phases $Tl_2Ba_2Ca_{n-1}Cu_nO_{2n+4}$, however, band-structure calculations on the Tl–O single rock-salt-layer phases $TlBa_2Ca_{n-1}Cu_nO_{2n+3}$show [14] that the bottom of their Tl 6s-block bands lies well above the Fermi level (Fig. 5.17c). Therefore, the Tl–O single rock-salt layer of $TlBa_2Ca_{n-1}Cu_nO_{2n+3}$ do not create holes in the CuO_2 layers. This finding is consistent with the observation that stoichiometric $TlBa_2Ca_{n-1}Cu_nO_{2n+3}$already has copper atoms of high enough oxidation state (i.e. 2+ (1/n)), in contrast to stoichio-

Fig. 5.17 Schematic representation for the relative energies of the CuO_2 layer $x^2 - y^2$ and the rock-salt-layer 6s-or 6p block bands in (**a**) $Bi_2Sr_2Ca_{n-1}Cu_nO2_{n+4}$ (**b**) $Tl_2Ba_2Ca_{n-1}Cu_nO_{2n+4}$ and (**c**) $TlBa_2Ca_{n-1}Cu_nO_{2n+3}$

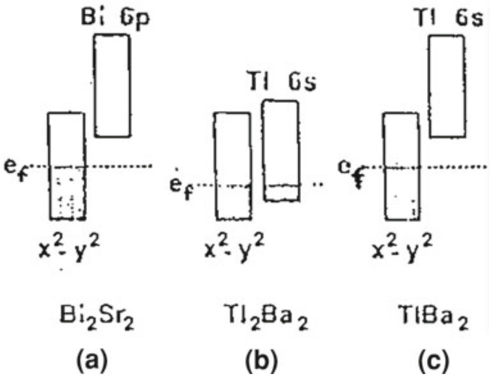

metric double layer phases $Tl_2Ba_2Ca_{n-1}Cu_nO_{2n+4}$and $Ba_2Sr_2Ca_{n-1}Cu_nO_{2n+4}$for which the copper oxidation state is +2 [4].

5.27 Phase Diagram (T_c Versus Hole Concentration)

Carrier density in the CuO_2 plane, or deviation of the formal Cu valence from 2+ ($Cu^{+2+\delta}$), is a primary parameter to control T_c in individual members of the high T_c family. Change of properties with varying carrier density is also of central concern for the experiments and theories aiming to elucidate the high T_c mechanism. Figure 5.18 illustrates phase diagrams for three representative materials. All the high T_c cuprates are expected to show similar behaviour. Although there is some ambiguity in the δ-values in the cuprates other than $La_{2-x}Sr_xCuO_4$, where $\delta = x$, T_c becomes maximum near $\delta = 0.2$ in every system. It should be emphsized that the normal state resistivity near $\delta = 0.2$ shows the T-linear dependence from T_c to high temperatures (∼1000 K).

With increasing oxygen content, Y123 covers the phase from antiferromagnetic (AF) insulator to the slightly overdoped superconducting region as shown in Fig. 5.18. $Tl_2Ba_2CuO_{6+y}$ is expected to play a complementary role to Y123 in study of the overdoped region, where the system is a nonsuperconducting metal [17].

With reducing oxygen content, the Tl compound goes into the superconducting phase with maximum $Tc \sim 90$ K, nearly the same as that in Y123.

In both Y123 and Tl compounds, the oxygen content does not give an absolute scale of carrier density. In this respect $La_{2-x}Sr_xCuO_4$ (La 214) continues to be a prototypical system. La214 is the only system by which all the three phases can be covered [18] and in which the carrier density δ is definitely equal to the composition x.

It becomes progressively evident that the phase diagram of La 214 has a singularity at $x = 0.125(=1/8)$ [19] and possibly at $x \sim 0.20$ [20]. The singularity shows

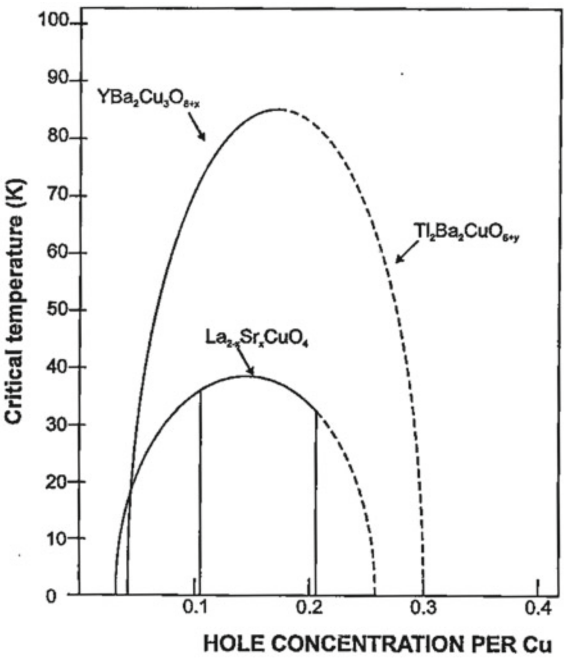

Fig. 5.18 T_c versus hole concentration for three representative cuprate systems. The scales for the hole concentration in Y123 and Tl2201 have some uncertainty [16]

up most markedly in $La_{2-x}Ba_xCuO_4$with x = 0.125, at which superconductivity disappears and instead, an AF magnetic order is restored [21]. This temperature incidentally coincides with the structural transformation from the orthorhombic to the low-temperature tetragonal (LTT) phase. In the case of Sr substitution the structural change is not seen above T_c, but an indication of T_c suppression is anticipated in the T_c vs x curve around x = 0.125 [22, 23]. It is not yet clear that the anomaly is driven by some electronic instability inherent to the material with be hole density x = 1/8 or whether it is related to the lattice instability.

Another singular point is at x ~0.20, above which the structural phase transition from high temperature tetragonal (HTT) to low temperature orthorhombic (LTO) symmetry is suppressed to zero temperature and at the same time superconductivity disappears [24]. This feature, together with the singularity at $x = 0.125$ indicates that superconductivity is observed only in the orthorhombic phase. (There should be some pair breaking effects in both HTT and LTT phases).

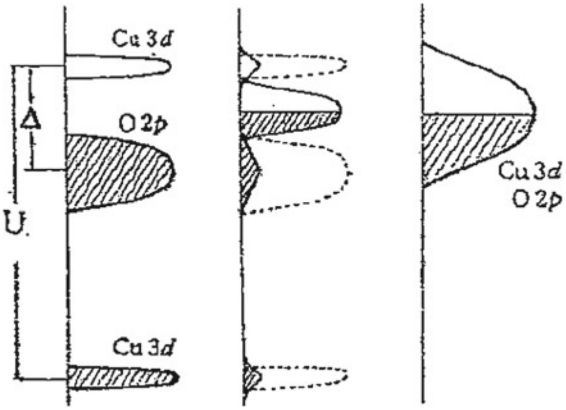

Fig. 5.19 Schematic energy diagrams of undoped, moderately doped and heavily doped CuO_2 planes (from *left* to *right*) [16]

5.28 Electronic Structure of Doped CuO_2 Plane from Spectroscopic Studies

The optical spectrum of undoped compounds such as La_2CuO_4 and Nd_2CuO_4 is characterized by the O2p-Cu3d charge transfer (CT) excitation with a threshold energy in the 1.5–2.0 eV range [25]. Doping causes a drastic change in the optical spectrum. The CT excitation is rapidly suppressed and instead, an edge shows up around 1.0 eV in the reflectivity spectrum, indicating that the spectrum is dominated by low-energy excitations in the energy range lower than 1.0 eV [26]. The optical conductivity spectrum demonstrates that the conductivity above 1.5 eV in case of La 214 decreases, but it increases below 1.5 eV as doping proceeds, so that the spectral weight of the CT excitation is transferred to low-energy excitations. This is commonly observed in N-type and other P-type cuprate systems. The implication of this spectral change is that the states O2p and Cu3d, initially separated by a CT energy gap due to large U, are redistributed upon doping to form new states in the original CT gap region [27]. These "in-gap" states are reminiscent of p-d hybridized bands, as the spectrum is eventually transformed into the Drude-type in the overdoped region (Fig. 5.19). In particular, the Electron Energy Loss Spectroscopy (EELS) results for a series of La 214 have clearly demonstrated [27] that upon doping, new states are formed in the gap region along with the reduction of the lowest empty states, i.e. the upper Hubbard band, of La_2CuO_4.

Photoemission results are suggestive of the in-gap states located in the mid-gap region [29, 30]. They show that the Fermi-level does not exhibit an appreciable shift with the transition from P- to N-type doping, and that the states near the Fermi-level are formed by a rearrangement of both conduction-and valence band states of the parent insulators.

5.29 Some Peculiar Normal Properties of Cuprates

The carrier concentration of all these compounds are much smaller than for typical metals. The carrier concentration ranges from 10^{21} to 10^{22} carriers per cubic centimeter. (Those of typical metals are one to two orders of magnitude higher). The Hall effect measurements by which most of the carrier concentrations are derived have some unusual features as well. The Hall constant has a significant temperature dependence in the Y123 compound but is much less temperature dependent for the La214 superconductor.

The thermal conductivity in these materials differs from that in most metals. As is known, thermal conductivity $\kappa = \kappa_{\mathrm{el}} + \kappa_{\mathrm{lat}}$ i.e. it is made up of electron and lattice contributions. In usual metals, $\kappa_{\mathrm{el}} \gg \kappa_{\mathrm{lat}}$. But cuprates represent a different case, for cuprates $\kappa_{\mathrm{el}} \ll \kappa_{\mathrm{lat}}$ and heat is mainly transported by the lattice.

The temperature dependence of electrical resistance observed in the cuprates differs from that in normal metals because of the peculiarities of transport phenomena in these materials due to reduced dimensionality and low carrier concentrations.

The temperature dependence of the electrical resistivity in the ab plane in the normal phase varies essentially as T rather than as the universal T^2 of the Landau theory. The question is how to account correctly for this from the properties of familiar metallic solids.

There are some inherent limitations in applying the common experimental tools of metal physics (Fermiology) such as cyclotron resonance, the de Haas-Van Alphen effect and magneto-resistance to these materials. The complications have to do with the fact that all these methods require good crystal of the normal metal at a low temperature (close to $\mathrm{T} = 0\,{}^{\circ}\mathrm{K}$)

At higher temperatures, relaxation processes become strong, and all resonance signals are washed out. However, superconductors become normal only above T_c, which is very high for the cuprates i.e. the high critical temperatures are, in this case, an obstacle to the application of the traditional methods. However, although the materials are exotic, the presence of a Fermi surface shows that by definition, we are dealing with a ‘metal’. After all, metal is nothing but a solid with a Fermi surface.

Neutron spectroscopy has identified low-lying optical phonon modes. For example in La-Sr-Cu-O, the modes are at $\omega 1 \approx 100\,\mathrm{cm}^{-1}$ and $\omega_2 \approx 200\,\mathrm{cm}^{-1}$. The presence of such low modes is an interesting and unique property of the cuprates. Another important feature of the lattice dynamics in these materials is the strong anharmonicity. Note that this feature is typical for ferroelectrics; this provided the motivation for Bednorz and Muller in their search for high T_c in the oxides. Raman effect data show that there is a continuum of electronic states in the low-energy part of the spectrum.

In addition, a layered conductor possesses a set of peculiar plasmon branches, which together form a plasmon band. Particularly important is the low energy part of the plasmon spectrum, which contains the phonon-like acoustic branch. This branch can provide an additional attraction between carriers and weaken the direct Coulomb repulsion (It is to be noted here that plasmons, in a certain sense, are similar to phonons: both describe collective vibrational motion. Phonons represent vibrational motion of the lattice whereas plasmons correspond to collective vibrational motion of the carriers relative to the lattice. This motion represents charge fluctuations and is due to Coulomb correlations in the metal). (see also Appendix A and B).

References

1. T.V. Ramakrishnan, J. Ind. Inst. Sci. **72**, 279 (1992)
2. T.V. Ramakrishnan, C.N.R. Rao, *Superconductivity Today* (Wiley Eastern, New Delhi, 1992)
3. D.L. Novikov, A.J. Freeman, Physica C **216**, 273 (1993)
4. M.H. Whangbo, C.C. Torardi, Acc. Chem. Res. **24**, 133–139 (1991)
5. W.J. Allen, C.G. Olson, MRS Bull. **34**, (1990)
6. M.H. Whangbo et al., in *High Temperature Superconducting Materials: Synthesis, Properties and Processing*, ed. by W.E. Halfield, J.H. Miller (Marcel-Dekker, New York, 1988), p. 181
7. M.H. Whangbo et al., Inorg. Chem. **26**, 1829 (1987)
8. E. Wang, Phys. Rev. B **41**, 6582 (1990)
9. M.S. Hybertsen, L.F. Mattheiss, Phys. Rev. Lett. **60**, 1661 (1988)
10. J. Ren et al., Physica C **159**, 151 (1989)
11. T.J. Wagener et al., Phys. Rev. B **39**, 2928 (1989)
12. M. Tanaka et al., Nature **339**, 691 (1989)
13. J. Yu, S. Massidda, A.J. Freeman, Physica C **152**, 251 (1988)
14. D. Jung et al., Physica C **160**, 381 (1989)
15. C.C. Torardi et al., Phys. Rev. B **38**, 225 (1988)
16. S. Uchida, Jpn. J. Appl. Phys. **32**(pt 1, No. 9A), 3784 (1993)
17. Y. Kubo, Y. Shimakawa, T. Manako, T. Satoh, S. Iijima, T. Ichihashi, H. Igarashi, Physica C **162–164**, 991 (1989)
18. J.B. Torrance, Y. Tokura, A.I. Nazzal, A. Bezinge, T.C. Huang, S.S.P. Parkin, Phys. Rev. Lett. **61**, 1127 (1988)
19. A.R. Moodenbaugh, Y. Xu, M. Suenaga, I.J. Folkers, R.J. Shelton, Phys. Rev. B **38**, 4596 (1988)
20. H. Takagi, B. Batlogg, H.L. Kao, J. Kwo, R.J. Cava, J.J. Krajewski, W.F. Peck Jr., Phys. Rev. Lett. **69**, 2975 (1992)
21. G.M. Luke, L.P. Le, B.J. Sternlieb, W.D. Wu, Y.J. Uemura, J.H. Brewer, J.S. Riseman, S. Ishibashi, S. Uchida, Physica C **185–189**, 1175 (1991)
22. H. Takagi, T. Ido, S. Ishibashi, M. Uota, S. Uchida, Phys. Rev. B **40**, 2254 (1989)
23. M. Oda, T. Ohguro, N. Yamada, M. Ido, J. Phys. Soc. Jpn. **58**, 1173 (1989)
24. H. Takagi, R.J. Cava, M. Marezio, B. Batlogg, J.J. Krajewski, W.F. Peck Jr, P. Bordet, D.E. Cox, Phys. Rev. Lett. **68**, 3777 (1992)
25. Y. Tokura, S. Koshihara, T. Arima, H. Takagi, T. Ido, S. Ishibashi, S. Uchida, Phys. Rev. B **41**, 11657 (1990)
26. S. Uchida, T. Ido, H. Takagi, T. Arina, Y. Tokura, S. Tajima, Phys. Rev. B **43**, 7942 (1991)
27. S. Maekawa, Y. Ohta, T. Tohyama, in *Physics of High Temperature Superconductors*, ed. by S. Maekawa, M. Sato (Springer, Berlin, 1991), p. 29
28. H. Romberg, M. Alexander, N. Nucker, P. Adelman, J. Fink, Phys. Rev. B **32**, 8868 (1990)
29. J.W. Allen, C.G. Olson, M.B. Maple, J.S. Kang, L.Z. Liu, J.H. Park, R.O. Anderson, W.P. Ellis, J.T. Markert, Y. Dalichaouch, R. Liu, Phys. Rev. Lett. **64**, 595 (1990)
30. H. Namatame, A. Fujimori, Y. Tokura, M. Nakamura, K. Yamaguchi, A. Misu, H. Matsubara, S. Suga, H. Eisaki, T. Ito, H. Takagi, S. Uchida, Phys. Rev. B **41**, 7205 (1990)
31. C.P. Poole Jr (ed.), *Handbook of Superconductivity* (Academic Press, New York, 2000)

Chapter 6
The Proximity and Josephson Effects

Suppose one superconductor is separated from another by a thin layer of insulator, then such a $S_1 - I - S_2$ junction is called a weak-link or a Josephson junction. The Cooper pairs can tunnel across the narrow insulator from one superconductor to the other superconductor.

The effects of pair tunnelling are classified under two categories:

1. *DC Josephson effects*. A dc current flows across the junction in the absence of any electric or magnetic field.
2. *AC Josephson effects*. A dc voltage applied across the junction causes rf current oscillations across the junction. Further, an rf voltage applied with the dc voltage can cause a dc current across the junction.

6.1 DC Josephson Effects

Consider a superconductor insulator with superconductor junction $S'_1 - I - S'_2$ (insulator I is thin). Let ψ_1 be probability amplitude of electron pairs in S'_1 and ψ_2 be the amplitude in S'_2. Let both S'_1 and S'_2 be identical and both be at zero potential. Then,

$$\psi_1 = \sqrt{n_1} e^{iS_1}$$

and

$$\psi_2 = \sqrt{n_2}\, e^{iS_2}. \tag{6.1}$$

Here, n_1 and n_2 are super-electron concentrations in S'^1_1 and S'^1_2, respectively (i.e. there are $n_1/2$ and $n_2/2$ pairs) and S_1 and S_2 are the phase functions in S'^1_1 and S'^1_2, respectively (Fig. 6.1).

The time dependent Schrodinger equation applied to the amplitudes ψ_1 and ψ_2 gives

$$i\hbar \frac{\partial \psi_1}{\partial t} = \hbar T \psi_2$$

A. K. Saxena, *High-Temperature Superconductors,* Springer Series
in Materials Science 125, DOI: 10.1007/978-3-642-28481-6_6,

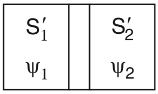

Fig. 6.1 $S_I{-}I{-}S_2$ junction

and

$$i\hbar\frac{\partial\psi_2}{\partial t} = \hbar T\psi_1. \tag{6.2}$$

Here $\hbar T$ represents the effect of electron pair coupling (or transfer interaction) across the insulator. T has the dimensions, inverse of time. It is a measure of the leakage of ψ_1 into the region 2 and of ψ_2 into region 1. If insulator is thick, $T = 0$ (no pair tunnelling). Using (6.1) and (6.2),

$$\frac{\partial\psi_1}{\partial t} = \frac{1}{2}n_1^{-1/2}\mathrm{e}^{\mathrm{i}s_1}\frac{\partial n_1}{\partial t} + \mathrm{i}\psi_1\frac{\partial S_1}{\partial t} = -\mathrm{i}T\psi_2, \tag{6.3}$$

$$\frac{\partial\psi_2}{\partial t} = \frac{1}{2}n_2^{-1/2}\mathrm{e}^{\mathrm{i}s_2}\frac{\partial n_2}{\partial t} + \mathrm{i}\psi_2\frac{\partial S_2}{\partial t} = -\mathrm{i}T\psi_1. \tag{6.4}$$

Multiply (6.3) by $n_1^{1/2}\mathrm{e}^{-\mathrm{i}s_1}$, to obtain

$$\frac{1}{2}\frac{\partial n_1}{\partial t} + \mathrm{i}n_1\frac{\partial S_1}{\partial t} = -\mathrm{i}T\,(n_1n_2)^{1/2}\,\mathrm{e}^{\mathrm{i}\delta}, \tag{6.5}$$

where $\delta = (S_2 - S_1)$.

Similarly, multiply (6.4) by $n_2^{1/2}\mathrm{e}^{-\mathrm{i}s_2}$, to obtain

$$\frac{1}{2}\frac{\partial n_2}{\partial t} + \mathrm{i}n_2\frac{\partial S_2}{\partial t} = -\mathrm{i}T\,(n_1n_2)^{1/2}\,\mathrm{e}^{-\mathrm{i}\delta}. \tag{6.6}$$

Now,

$$\mathrm{e}^{\pm\mathrm{i}\delta} = \cos\,\delta \pm \mathrm{i}\,\sin\,\delta.$$

Equating the real parts and imaginary part on the two sides of (6.5) gives

$$\frac{\partial n_1}{\partial t} = 2T\sqrt{n_1n_2}\,\sin\,\delta, \tag{6.7}$$

$$\frac{\partial S_1}{\partial t} = -T\sqrt{\frac{n_2}{n_1}}\,\cos\,\delta. \tag{6.8}$$

Similarly from (6.6)

$$\frac{\partial n_2}{\partial t} = -2T\sqrt{n_1n_2}\,\sin\,\delta, \tag{6.9}$$

$$\frac{\partial S_2}{\partial t} = -T\sqrt{\frac{n_1}{n_2}}\cos\,\delta. \tag{6.10}$$

If $n_1 = n_2$ (identical superconductors), we have from (6.8) and (6.10)

$$\frac{\partial S_1}{\partial t} = \frac{\partial S_2}{\partial t} \quad \text{or} \quad \frac{\partial}{\partial t}(S_2 - S_1) = 0. \tag{6.11}$$

From (6.7) and (6.9)

$$\frac{\partial n_1}{\partial t} = -\frac{\partial n_2}{\partial t}, \tag{6.12}$$

i.e. density of pairs changes at equal and opposite rates when there is a super-current flow across the junction. The current density per unit area J_s is given as

$$\begin{aligned} J_s &= e^* \frac{\partial}{\partial t}\,|\psi_2|^2 \\ &= e^* \frac{\partial}{\partial t}\,\left|\left(\psi_2\psi_2^*\right)\right| \\ &= e^* \frac{\partial}{\partial t}\left[n_2 e^{is_2} e^{-is_2}\right], \end{aligned} \tag{6.13}$$

or

$$J_s = \left(e^* \frac{\partial n_2}{\partial t}\right) = -e^* \frac{\partial n_1}{\partial t},$$

or

$$\begin{aligned} J_s &= -2e^* T\sqrt{n_1 n_2}\,\sin\,(S_2 - S_1) \\ &= -2e^* T\,(n_1 n_2)^{1/2}\,\sin\,\delta \end{aligned} \tag{6.14}$$

or

$$J_s \equiv J_0\,\sin\,\delta\ \text{(D.C. Josephson effect)}, \tag{6.15}$$

where $J_0 \equiv -2e^* T\,(n_1 n_2)^{1/2}$ is the maximum zero voltage current that can be passed by the junction. J_0 is proportional to the transfer interaction T and depends upon the details of the overlap of the two wave functions.

With no applied voltage, the dc current J_s flows across the junction with a value between J_0 and $-J_0$ (see Fig. 6.2).

Equation (6.15) shows that the current (a macroscopic quantity) is determined directly by the phases of the wave functions (i.e. a quantum mechanical quantity). This equation characterises the DC Josephson effect. It was first predicted theoretically by Josephson in 1962 and observed by Anderson and Rowell in 1963.

The amplitude of the tunnelling current (J_0) is temperature (T') dependent and is described by Ambegaokar–Baratoff formula given as

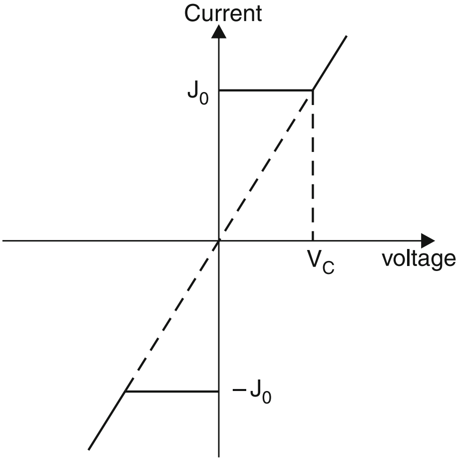

Fig. 6.2 Current voltage characteristic of a Josephson junction. At voltage above V_c, the junction has a finite resistance

$$J_0 = \frac{\pi\Delta}{2eR_N} \tan h \left(\frac{\Delta}{2T'} \right), \tag{6.16}$$

where R_N is the junction resistance in normal state.

At 0 °K, maximum zero voltage current is

$$J_0 (0) = \frac{\pi\Delta (0)}{2eR_N}, \tag{6.17}$$

i.e. $J_0(T')$ is maximum at $T' = 0\,°K$.

As $T' \to T_c$, the amplitude J_0 decreases because $J_0 \propto \left(T_c' - T'\right)$.

The sign of J_s is determined by noting that for small phase difference δ, electrons will flow into the superconductor with large phase and super-current flows in the opposite direction.

J_0 is equal to the current that would flow, if both superconductors were made normal and a voltage equal to $\pi/2$ times the energy gap parameter was applied.

Pendular Model. To examine the relation $J_s = J_0 \sin\delta$ (or $I = I_0 \sin\delta$), consider a pendular model having one pendulum linked to the other by a weak spring. When the oscillations of one pendulum leads in phase the oscillations of the other, the spring transfers energy of the first to the second. The energy flux transfer reaches maximum at a phase difference of $\pi/2$.

In the Josephson junction, Cooper pairs move from one conductor into the other through the barrier and then, return to the first conductor over the external circuit. The magnitude and direction of current are determined by the same phase relationships as for the weakly bound pendular systems.

6.2 Some Types of Josephson Junctions

Figure 6.3a–c shows possible arrangements that yield a weakly coupled contact (Josephson junction) between two superconductors.

Figure 6.3a shows a junction, which consists of two superconducting thin films separated by an insulating oxide film. This insulating layer is an oxide of one of the superconductors and may be intentionally created or simply be the natural oxide film, which exists on the surface of most of the metals exposed to the atmosphere. In this type of junction, the two superconductors are coupled by tunnelling process (tunnelling of Cooper pairs).

Figure 6.3b is essentially two pieces of superconductors connected by a very small bridge with dimensions of the order of a coherence length. It is usually an evaporated thin film, with the bridge formed by evaporating through an appropriate mask or by photo-etch techniques. The mechanism by which two superconductors are coupled is not simply Cooper-pair tunnelling.

Figure 6.3c shows a point contact junction. It is simply a small area contact between a micro-size sharp point on one piece of superconductor and another piece of superconductor. It may be of particular interest, because it is extremely simple to fabricate. It can behave like a weak-link or tunnel junction, depending on the contact pressure and the nature of oxide films on the superconductors at the contact (critical current can be adjusted by varying applied pressure).

6.2.1 Typical Current Voltage Characteristics for the Above Types of Junctions

The $I-V$ characteristic for a thin film tunnel Josephson junction displays a zero voltage current (DC Josephon current), followed by switching along the circuit load line to the single particle tunnelling curve. If the two superconductors are identical, this consist of a very small current at voltages below $2\Delta/e$. At the gap voltage, there is a sharp rise in current followed by an asymptotic approach to the linear normal state $I-V$ curve (Fig. 6.4).

The $I-V$ characteristic for a weak-link junction displays a zero-voltage current followed by a smooth transition to the normal state current.

It is worthwhile to mention here that the Josephson tunnelling was observed for the first time by Meissner and Holm in 1932. They observed that the contact resistance between two metals vanishes as soon as both become superconductors, a manifestation of Josephson tunnelling.

(a) Thin film tunnel-junction

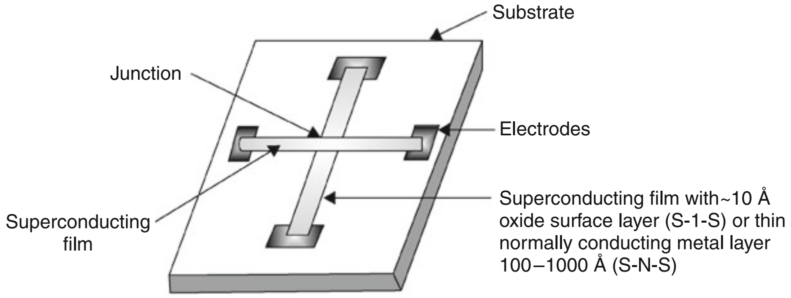

(b) Thin film weak link

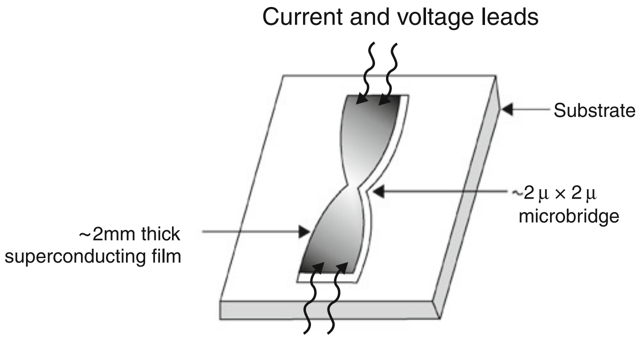

(c) Point Contact

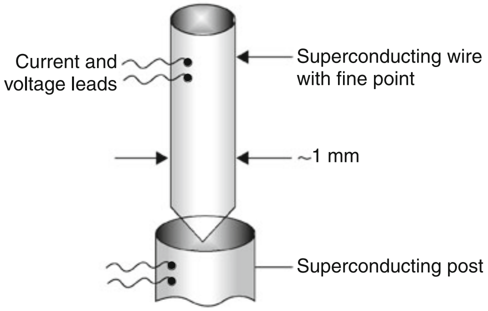

Fig. 6.3 Some Josephson junctions **a** thin film tunnel junction, **b** thin film weak-link, **c** a point contact [1]

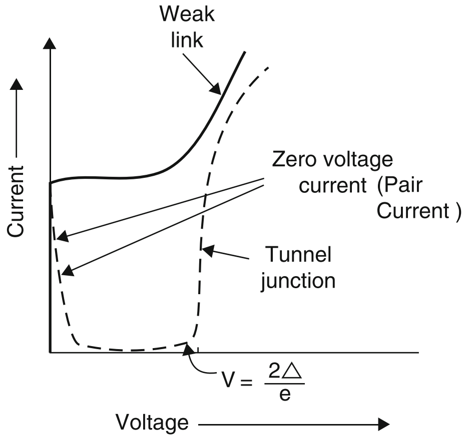

Fig. 6.4 Current voltage characteristics

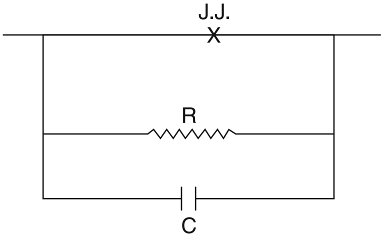

Fig. 6.5 Equivalent circuit of a Josephson junction

Table 6.1 The range of circuit elements for practical junctions

Junction	I_j	1/G (for $V < 2\Delta$)	C
Thin film tunnel junction	10 μA	>100 ohm	100–1000 pF
Point contact	10 μA	10–100 ohm	1–1000 pF
Microbridge thin film	10 μA	<1 ohm	1 pF

6.3 Equivalent Circuit of a Josephson Junction

A Josephson junction may be represented by the parallel combination of an ideal junction (one carrying a super-current only) and a resistance and a capacitance (Fig. 6.5a).

The main difference between tunnel junction, point contact and micro-bridge are in the respective values of these circuit elements (see Table 6.1).

Thus, for thin film bridge, both R and C are low.

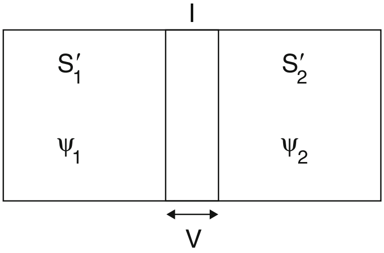

Fig. 6.6 A S–I–S junction with an applied voltage V

6.4 AC Josephson Effect

Consider a S−I−S junction, to which a voltage V is applied (it can be applied because the junction is an insulator). Let both the superconductors be identical. Then,

$$\psi_1 = \sqrt{n_2}\,\mathrm{e}^{\mathrm{i}s_1}, \quad \psi_2 = \sqrt{n_2}\mathrm{e}^{\mathrm{i}s_2}.$$

Here n_1 and n_2 are super-electron concentrations in the two superconductors. S_1 and S_2 are the phase functions in S_1' and S_2', respectively (Fig. 6.6).

An electron pair of charge $q = -2e$ will experience a potential energy difference of qV while passing across the junction, i.e. a pair on one side is at potential energy $(-eV)$ and a pair on the other side at $(+eV)$. The Schrödinger equations of motion are

$$\mathrm{i}\hbar\frac{\partial\psi_1}{\partial t} = \hbar T\psi_2 - eV\psi_1, \tag{6.18}$$

$$\mathrm{i}\hbar\frac{\partial\psi_2}{\partial t} = \hbar T\psi_1 + eV\psi_2 \Rightarrow \frac{\partial\psi_1}{\partial t} = \frac{1}{2}{n_1}^{-1/2}\mathrm{e}^{\mathrm{i}s_1}\frac{\partial n_1}{\partial t} + \mathrm{i}\psi_1\frac{\partial s_1}{\partial t} \tag{6.19}$$

$$= -\mathrm{i}T\psi_2 + \mathrm{i}\frac{eV}{\hbar}\psi_1 \tag{6.20}$$

$$\frac{\partial\psi_2}{\partial t} = \frac{1}{2}{n_2}^{-1/2}\mathrm{e}^{\mathrm{i}s_2}\frac{\partial n_2}{\partial t} + \mathrm{i}\psi_2\frac{\partial s_2}{\partial t} = -\mathrm{i}T\psi_1 - \mathrm{i}\frac{eV}{\hbar}\psi_2. \tag{6.21}$$

Multiply (6.20) by $n_1^{1/2}\mathrm{e}^{-\mathrm{i}s_1}$ to obtain

$$\frac{1}{2}\frac{\partial n_1}{\partial t} + \mathrm{i}n_1\frac{\partial S_1}{\partial t} = \mathrm{i}e\frac{Vn_1}{\hbar} - \mathrm{i}T\,(n_1n_2)^{1/2}\,\mathrm{e}^{\mathrm{i}\delta}, \tag{6.22}$$

where $\delta = (S_2 - S_1)$.

Equation (6.22) breaks up into the real part
(which is without voltage)

$$\frac{\partial n_1}{\partial t} = 2T\,(n_1 n_2)^{1/2}\,\sin\,\delta \tag{6.23}$$

and the imaginary part

$$\frac{\partial s_1}{\partial t} = \left(\frac{eV}{\hbar}\right) - T\left(\frac{n_2}{n_1}\right)^{1/2}\cos\,\delta. \tag{6.24}$$

Further, from (6.21), we get

$$\frac{1}{2}\frac{\partial n_2}{\partial t} + \mathrm{i}n_2\frac{\partial s_2}{\partial t} = \mathrm{i}e\frac{Vn_2}{\hbar} - \mathrm{i}T\,(n_1 n_2)^{1/2}\,\mathrm{e}^{-\mathrm{i}\delta} \tag{6.25}$$

Therefore,

$$\frac{\partial n_2}{\partial t} = -2T\,(n_1 n_2)^{1/2}\sin\,\delta$$

and

$$\frac{\partial S_2}{\partial t} = -\left(\frac{eV}{\hbar}\right) - T\left(\frac{n_1}{n_2}\right)^{1/2}\cos\,\delta. \tag{6.26}$$

From (6.24) and (6.26), both with $(n_1 = n_2)$, we have

$$\frac{\partial\,(S_2 - S_1)}{\partial t} = \frac{\partial\delta}{\partial t} = \frac{2eV}{\hbar}. \tag{6.27}$$

By integration of (6.27), we see that with a dc voltage across the junction, the relative phase of the probability varies as

$$\delta\,(t) = \delta\,(0) - \left(\frac{2eVt}{\hbar}\right). \tag{6.28}$$

The current is now given by

$$J = J_0\,\sin\,\delta(t)$$

or

$$J = J_0\sin\left[\delta\,(0) - \left(\frac{2eVt}{\hbar}\right)\right]. \tag{6.29}$$

The current oscillates with a frequency $\omega = 2eV/\hbar$. This relation implies that a photon of energy $\hbar\omega = 2eV$ is emitted or absorbed, when an electron pair crosses the barrier. A dc voltage of 1 μV produces a frequency of ~484 MHz.

Physically, the ac Josephson effect may be understood as follows:

We have seen that in case of a constant potential difference across the gap, a high frequency electromagnetic energy emanates from it. This points to the fact that not only a direct current but also a high frequency rf (or ac) current flows in the circuit. This phenomenon is also known as the non-stationary Josephson effect.

With a potential difference established between two superconductors, the energies of Cooper pairs on both sides differ by $2eV_0$ (where $2e$ is charge of a pair). Since the relation between the energy of particles and frequency of de Broglie waves is $E = h\nu$, the de Broglie frequency difference $\Delta\nu = (2eV_0/h)$ will appear on the two sides of the junction and the phase difference will grow continuously.

$$\delta = 2\pi\,(\Delta\nu)\,t = 2\pi t\left(\frac{2eV_0}{h}\right) = t\left(\frac{2eV_0}{\hbar}\right)$$

$\Rightarrow I = I_0 \sin\delta$ (superconducting current)

$$I = I_0 \sin\left(\frac{2eV_0 t}{\hbar}\right).$$

Thus, when a Josephson junction is biased into a finite voltage state, ac Josphson super-current flows across the junction, due to the time evolution of the phase of the superconducting wave function.

The production of an ac signal from a dc voltage may be understood as due to the conversion of energy of electron pair into photons (radiation).

It is to be noted in DC Josephson effect, the barrier in Josephson tunnelling behaves as a weak superconducting link between the two superconductors. The phases of the superconducting wave function become locked and in effect, the two superconductors become a single coherent system. An energy $hI_c(0)/2e$ where $I_c\,(0)$ is zero-field super-current) is associated with the coupling of the pair wave functions. The system is stable against thermal fluctuations (for $T < T_c$), if the barrier is very thin (thickness <10 Å) The junction then acts as a weak superconductor.

6.5 Giaever Tunnelling/Tunnelling of Quasi-Particles

If there is thin oxide insulator separating a superconductor from a normal metal, quasi-particle tunnelling may takes place depending on the position of the Fermi level on the two sides. This is known as *Giaever tunnelling* (first observed experimentally by Giaever in 1960). This exemplifies a quantum mechanical tunnelling. There is a non-zero tunnelling probability, if the electron ends up in an allowed state of energy lower than, or equal to, the energy of the initial state. Figure 6.7 shows a superconductor film separated from a normal metal film, by a thin insulating layer (i.e. a S—I—N tunnel junction).

Figure 6.7 shows the energy diagram in absence of the applied voltage. The lowest single particle energy in the superconductor lies at an energy Δ_0 above the Fermi-energy μ (which will be the same in the normal, in superconducting metals). Under such circumstances, no tunnelling current can appear, since because of the presence

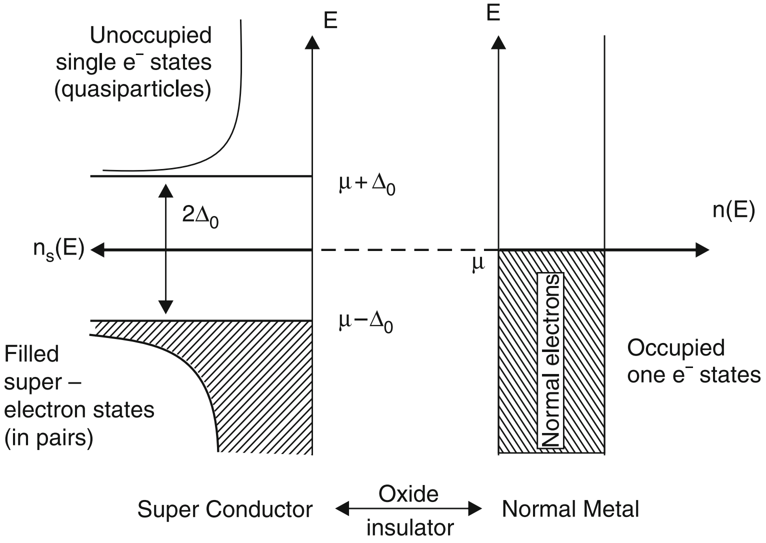

Fig. 6.7 S–I–N junction in absence of applied field (energy diagram)

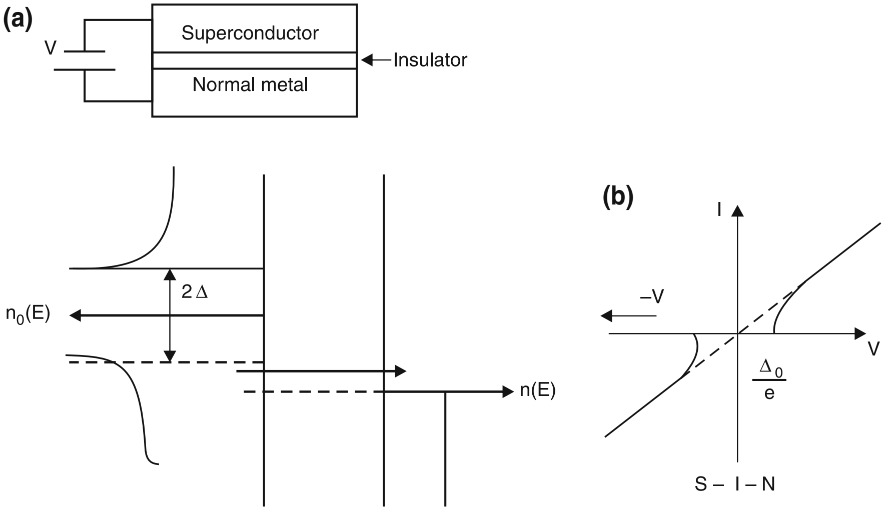

Fig. 6.8 **(a)** Energy diagram in presence of applied field **(b)** $I-V$ characteristics (the *dashed line* corresponds to N–I–N case)

of energy gap (in the superconductor), there are no states available for tunnelling transitions.

In order to make tunnelling possible, it is necessary to apply an external electric field, which will alter the positions of the Fermi-levels on the two sides (Fig. 6.8).

The tunnelling current appears only if (at zero temperature) a finite voltage V is applied such that the product $eV = \Delta_0$ (the energy gap). This V is in the order of millivolts. The absence of tunnelling current at small voltages is an experimental proof that there exists an energy gap for superconductors. In Giaever experiments, the tunnelling current was negligible, until a sufficient voltage was applied and this gave a direct voltmeter measure of the energy gap parameter. At higher voltages, the curve approaches the dependence characteristic of a tunnelling junction between two normal metals (Fig. 6.8b), as if when both films are in the normal state.

In the normal metal (on the r.h.s), all one electron states are occupied for $\in < \mu$. In the superconductor (on the l.h.s), there are no one electron states below the energy $(\mu + \Delta_0)$. Above $(\mu + \Delta_0)$, there are excited states, which are all empty at $T = 0\,\mathrm{K}$ with a density

$$n_\mathrm{s}(E_\mathrm{k})dE_\mathrm{k} = \frac{2}{(2\pi)^3}4\pi k_\mathrm{F}^2 \frac{dE_\mathrm{k}}{dE_\mathrm{k}/dk} = \left(\frac{mk_\mathrm{F}}{\pi^2\hbar^2}\right)\frac{E_\mathrm{k}}{(\in_\mathrm{k} - \mu)}dE_\mathrm{k},$$

where $E_\mathrm{k} = \sqrt{(\in_\mathrm{k} - \mu)^2 + \Delta^2}$ and $n_\mathrm{s}\,(E_\mathrm{k})\,dE_\mathrm{k}$ are density of unoccupied quasi-particle states. One can obtain this density of excited states, for $\in_\mathrm{k} \ \geq \mu$ (and therefore, $E_\mathrm{k} \geq \Delta_0$).

Now, let T denote the probability of tunnelling (called tunnelling matrix element). Taking T as independent of energy near the Fermi energy (the onset of superconductivity does not modify these one electron matrix elements), we obtain the tunnelling current I from the superconductor with an applied voltage V, to be

$$I = \frac{2\pi}{\hbar}\,(-e)\,T^2 \int dE_\mathrm{k} n_\mathrm{s}\,(E_\mathrm{k})\,n\,(E_\mathrm{k} + eV)\,f_0\,(E_\mathrm{k}) \times [1 - f_0\,(E_\mathrm{k} + V)]\,,$$

where n_s is density of quasi-particles states in superconductor, n is density of states in normal metal and f_0 is Fermi distribution function (for an electron being in an energy E_k), $(1 - f_0)$ is the probability function for an electron state being vacant.

We now neglect the variation of $n(E)$ with energy in the normal metal and consider the current at zero temperature, then $f_0 \approx 1$ (a step function), in an energy range of width eV (Fig. 6.9).

A particularly useful quantity is the dynamic conductance

$$\frac{dI}{dV} = \left[\frac{2\pi}{\hbar}e^2T^2n\,(\mu)\right]n_\mathrm{s}\,(-eV)\,.$$

It is directly proportional to the density of quasi-particle states in the superconductor. The $I_\mathrm{vs}V$ curve shows that at a temperature well below T_c $(\rightarrow 0\,K)$, the current is zero, until the applied voltage equals Δ/e, and then jumps sharply.

At finite temperatures, the function f_0 is not a step function. Further, there is weak structure in experimental curves, which is interpreted as variation of the energy gap parameter (Δ_k) with energy.

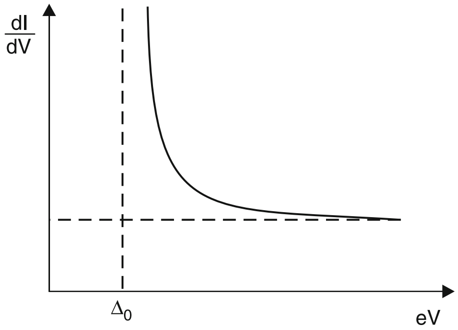

Fig. 6.9 Variation of dynamic conductance with voltage

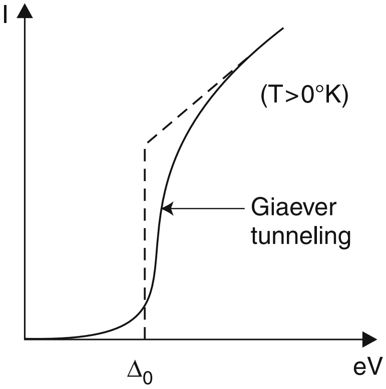

Fig. 6.10 Tunnelling current versus voltage

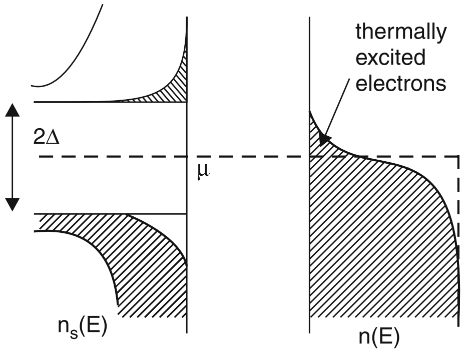

Fig. 6.11 Energy diagram for S–I–N junction for $T > 0\,°\mathrm{K}$

Figures 6.10 and 6.11 show the effect of temperature on quasi-particle tunnelling current and the energy diagrams.

It is worthwhile to mention here that at sufficiently high temperatures, quasi-particles collide so often that they do not have enough time to reveal their identity between two collisions. Quasi-particles no more play the role of elementary excitations and not being applicable to describing the properties of solids. The lower the

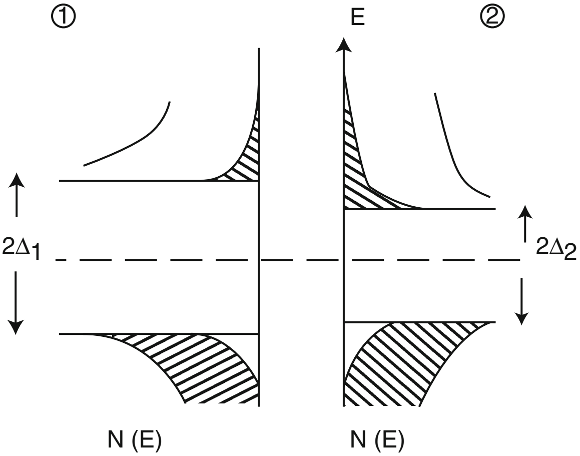

Fig. 6.12 Density of states curves for $T = 0\,^{\circ}\mathrm{K}$

temperature of a solid, the lower the frequency of collisions, the more individual is the life of each quasi-particle. This is why the concept of quasi-particles is mostly used to describe properties of solids at low temperatures.

6.6 Superconductive Tunnelling in a S–I–S Junction

Instead of metal insulator superconductor junction, if we have a S–I–S junction, coherent tunnelling is obtained instead of quasi-particle tunnelling and super-current (electron pairs) flow across the junction. In coherent tunnelling, the strength of the pairing interaction is sufficient to preserve the phase correlations of the electrons as they pass through the barrier and to re-establish coherence on the other side.

For a S–I–S junction, the effects observed depend on the thickness of the insulating barrier: if thickness $<2\,\mathrm{nm}$, a weak super-current will flow for zero voltage bias (Josephson tunnelling). Electron or quasi-particle tunnelling is observed, when the barrier thickness is 5–10 nm. In a S–I–S junction having two superconductors of different energy gaps, the Fermi level is in the middle of the gaps.

A negative voltage applied to one superconductor raises its Fermi level with respect to the other superconductor and thus, a current flows (Figs. 6.12 and 6.13).

The tunnel current is proportional to the product of the density of electrons at a particular energy in the emitter and the density of unoccupied states at the same energy level in the absorber. The tunnel current from (1) to (2) is given by

$$I_{1\to 2} = c_{12} \int_{-\infty}^{+\infty} \rho_1(E)\,\rho_2(E+eV)\,[f(E) - f(E+eV)]\,dE,$$

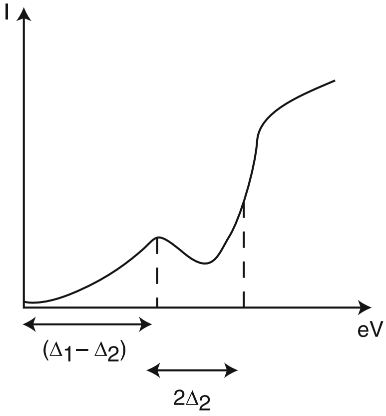

Fig. 6.13 I versus V curve for S–I–S junction of Fig. 6.12. There is a negative resistance for $\frac{(\Delta_1-\Delta_2)}{e} < V < \frac{(\Delta_1+\Delta_2)}{e}$

where c_{12} is the conductance when both metals are normal, $f(E)$ is Fermi function, E is energy measured from Fermi level, V is applied voltage, ρ_1 and ρ_2 are the ratios between the superconducting and normal densities of states. The density of states of a superconductor (in BCS theory) is given by

$$N_\mathrm{s} = N_\mathrm{n}\frac{E}{\left(E^2 - \Delta^2\right)^{1/2}}.$$

(The energy gap is 2Δ).

The superconductors (1) and (2) have energy gaps $2\Delta_1$ and $2\Delta_2$ respectively. There are some electrons above the gap in superconductor 2 and hardly any, because of larger gap in superconductor 1. When a voltage is applied, a current will flow because more and more of the thermally excited electrons in superconductors 2 can tunnel into the available states of superconductor 1. When the applied voltage reaches $(\Delta_1 - \Delta_2)/e$, it has become energetically possible for all thermally excited electrons to tunnel across the empty states of absorber. If the voltage is increased further, the current decreases, since the number of electrons capable of tunnelling is unchanged but they now face a lower density of states. When the voltage becomes greater than $(\Delta_1 + \Delta_2)/e$, the current increases rapidly as electrons below the gap can begin to flow (the main body of unexcited electrons in one is brought opposite the empty states of the other). If $\Delta_1 = \Delta_2$, the initial rise of the current is observed only when $V = 2\Delta/e$ (Fig. 6.14).

Figure 6.15 shows how the tunnelling characteristics of a symmetric S–I–S junction change as the temperature is lowered below the common transition temperature of the two superconductors. At $T = 0\,K$ (no normal electrons), the current would be zero up to a voltage V. The existence of energy gap and the requirement of the energy to be conserved, combine to prevent any single particle current flow, until the bias voltage satisfies the condition $V = 2\Delta(0)/e$. At this point, current flow becomes possible as electrons from the ground state are excited into the normal electron states

Fig. 6.14 $I_{vs} V$ for $\Delta_1 = \Delta_2$

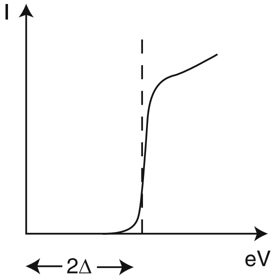

Fig. 6.15 Typical $I-V$ characteristic for a symmetric S–I–S tunnel junction at different temperatures

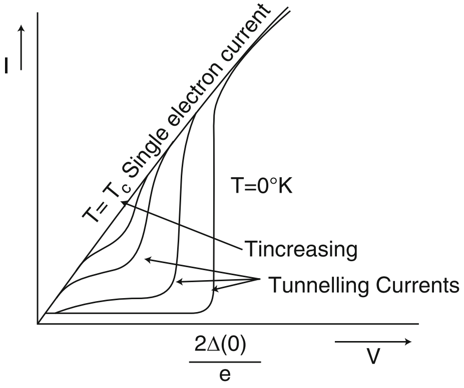

and there is a discontinuity in the characteristic. At $T > 0\,K$, we note that the discontinuity become less pronounced and moves to a lower bias voltage (indicating the temperature dependence of Δ) and also, the current flow occurs at all voltages as the number of thermally excited normal electrons increases.

6.7 Quasi-Particle Tunnelling for a Symmetric S–I–S Junction

The $I-V$ characteristics are influenced by the density of states on either side of the barrier.

In a superconductor, the energy gap in the excitation spectrum causes a displacement of states for a range Δ above and below the Fermi surface. The BCS theory shows that the missing states are concentrated immediately above the gap and $D(\in)$ has the form

$$D(\in) = 0 \quad \text{for} \in < \Delta,$$
$$\frac{D(\in)}{D(0)} = \frac{\in}{(\in^2 - \Delta^2)^{1/2}} \quad \text{for} \in > \Delta,$$

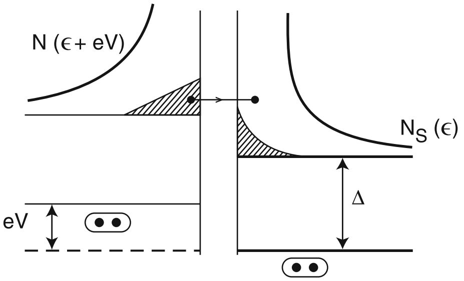

Fig. 6.16 $eV < 2\Delta(T)$ A thermally excited particle from an occupied state (*shaded*) tunnels across the barrier to an unoccupied state

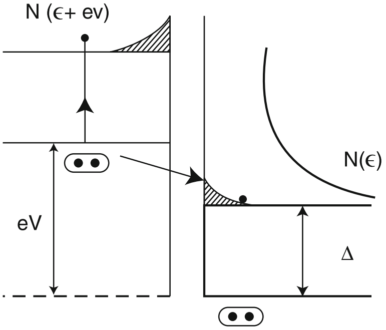

Fig. 6.17 $eV \geq 2\Delta(T)$. A pair is destroyed on the *left* with the production of two quasi-particles, one of which appears on the *right*

with a singularity at $\in = \Delta$. $D(0)$ is normal metal density of states at the Fermi level. Figures 6.16 and 6.17 illustrate the tunnelling process at $T > 0$ for two different bias voltages. The shaded region represents the occupied quasi-particle states. For $V < 2\Delta/e$, the current flow is restricted to tunnelling by thermally excited particles as shown by the horizontal transition at constant energy (Fig. 6.16). For $V \geq 2\Delta/e$, a second tunnelling process becomes possible by the destruction of a Cooper pair on the left side and the injection of a quasi-particle into each superconductor (Fig. 6.17).

In both processes, the tunnelling current will involve products of density of states function $D(\in)$ and $D(\in')$ and appropriate Fermi factors. The sharp rise in current at $V = 2\Delta/e$ is a direct consequence of the singularity in $D(\in)$ at $\in = \Delta$, and this feature makes possible the direct and accurate measure of $\Delta(T)$. Rather different $I - V$ characteristics are measured for non-symmetric junctions (e.g. SIS′ on SIN). Particularly valuable information can be obtained from derivatives of the characteristics, if *dI/dV* (or *dV/dI*) is plotted against V. For the case of a SIN junction

$$\frac{D(I)}{D(V)} \propto D_{\mathrm{S}}(\in).$$

Deviations from the simple BCS expression for $D(\in)$ are to be expected, since the true electron–electron interaction is not a constant, but reflects the metals' density of phonon states. Indeed for the strong coupling superconductors (e.g. Pb, Hg) in

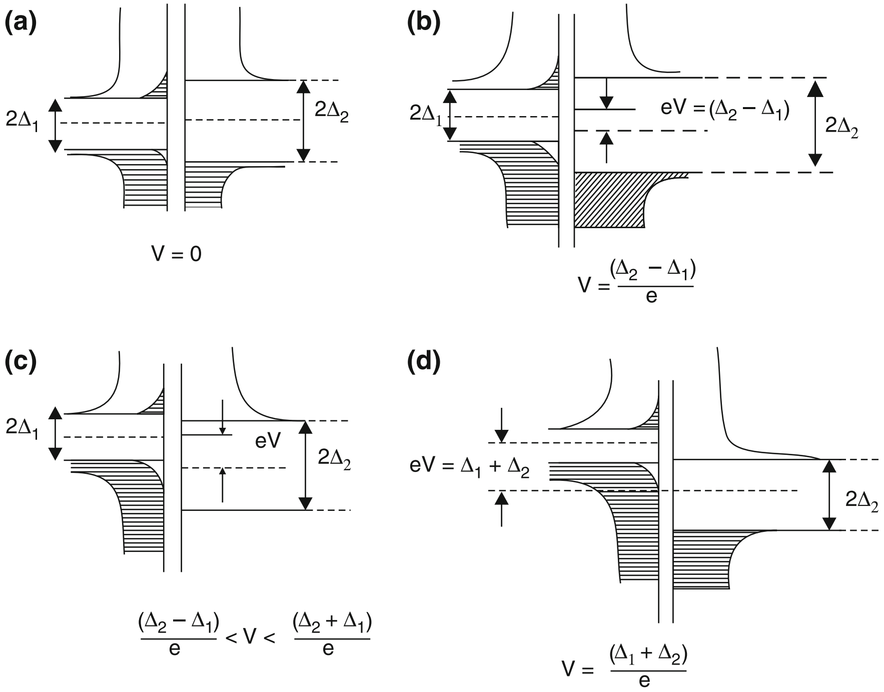

Fig. 6.18 Energy band diagrams (at a finite temperature) of a S_1-I-S_2 junction

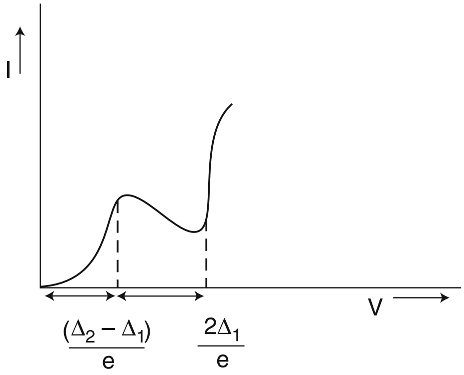

Fig. 6.19 $I-V$ characteristic of the S_1-I-S_2 junction (shown in Fig. 6.18b)

which the ration $k_B T/\hbar\omega_D$ is relatively large, measurement of $D_s(\in)$ can be used to determine the phonon density of states. Thus, tunnelling played a remarkable role in the development of strong coupling theory of superconductivity. Tunnelling measurement of Giaever on Pb–insulator–Mg at a voltage corresponding to Debye energy in lead gave $2\Delta(0)/(k_B T_c) \cong 4.3$ for lead, instead of the BCS value 3.52. k_B is Boltzmann constant (Figs. 6.18 and 6.19).

6.7.1 *Effect of Thickness of Insulator in S–I–S Junction*

If there is a rather thick insulator between two superconductors, then the phase coherence is broken. The phases of the two superconductors bear no relation between each other. If the insulator is very thin (or absent), the phases must be locked. If the insulator is thin and present, then there is still a strong tendency to fix the phase (inspite of presence of insulator). If phase-locking wins, there is a zero voltage current. If phase locking loses, the energies of electron-pairs will be different on the opposite sides of the insulator. Thus, the phase difference across the junction will not be a constant but the phases will be related to each other.

6.8 Properties of Josephson Junction

1. For an electromagnetic input, it can give a dc output
2. For a dc input it can give an electromagnetic output
3. It has two stable states
4. The maximum super-current across it is sensitive to magnetic fields
5. It can produce harmonics and sub-harmonics
6. It has a variable reactance
7. It can be produced in a number of forms, including the thin film form suitable for large scale manufacturing. Thus, it is the most versatile single device that has come our way, since the invention of pn junction.

6.9 Flux Quantisation

Consider a superconducting ring. Let there be a magnetic field $\vec{B}$ threading the ring. But, in the superconducting state, the field will be zero within the body of the ring (due to Meissner effect). Since the fields are zero, the current density $\mu_0 \vec{j}_{\mathrm{s}} = \nabla \times \vec{B}$ must also be zero. The currents are restricted to a depth λ (i.e. penetration depth) from the surface. We define a path of integration around the ring within its interior, such that the current density is everywhere zero along the path, i.e. $\int \vec{j} \cdot d\vec{\ell} = 0$.

The general form of the London equation is

$$\vec{j}_{\mathrm{s}} = \frac{n_{\mathrm{S}}}{2}\left(\frac{e}{m_{\mathrm{e}}}\right)\left(\hbar \nabla S - 2e\vec{A}\right)$$

where S is the phase of the wave function. In a solid block of superconductor, the wave function must be single valued, i.e. $\Delta S = 0$, but when the superconductor is a ring (i.e. has a hole passing through it), the change in phase around a closed path l

Fig. 6.20 A superconducting ring

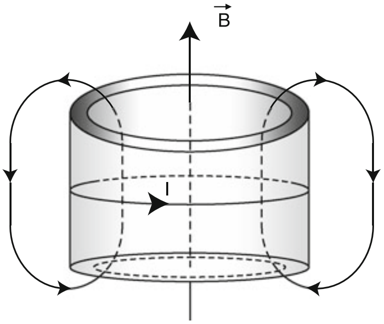

(as shown in Fig. 6.20) must be zero, i.e. S can increase or decrease by multiples of 2π (without altering $\psi = \psi_0 e^{iS(r)}$). Then,

$$\oint \vec{j}_S \cdot d\vec{\ell} = \frac{n_s}{2}\left(\frac{e}{m_e}\right)\left[\oint \hbar \nabla S \cdot d\vec{\ell} - \int 2e\vec{A} \cdot d\vec{\ell}\right]$$

(the l.h.s. is zero)

and

$$\oint \nabla S \cdot d\vec{\ell} = 2\pi n$$

$$\therefore 2\pi n\hbar = 2e \oint \vec{A} \cdot d\vec{\ell}$$

or

$$2\pi n = \frac{2e}{\hbar} \int\int \left(\nabla \times \vec{A}\right) \cdot d\vec{a}$$

(using Stokes theorem)

or

$$2\pi n = \frac{2e}{\hbar} \int\int \vec{B} \cdot d\vec{a}$$

or

$$2\pi n = \frac{2e}{\hbar}\phi \equiv \frac{\phi}{\phi_0},$$

where ϕ is the magnetic flux and $\phi_0 = \frac{\hbar}{2e} \equiv 2 \times 10^{-15}$ Webers is called the *flux quantum*.

Thus, although the flux is excluded from the bulk of the superconductor, the flux can pass through a hole in it, and in units of $\hbar/(2e)$. This flux quantisation was

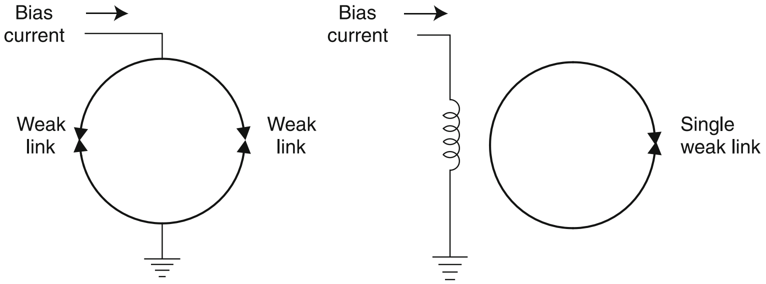

Fig. 6.21 Schematic representation of DC and rf SQUIDs

discovered by Deaver and Fairbank (and Doll and Nabuer) in 1961. The most striking characteristic feature of Josephson tunnelling is the sensitivity of the super-current to small magnetic fields. We will now consider a superconducting ring containing two Josephson junctions and placed in a magnetic field.

6.10 SQUIDs

A superconducting ring containing either one or two Josephson junctions can be used as a very sensitive flux meter. Such a device is known as a superconducting quantum interference device or SQUID. There are two types of SQUIDs (Fig. 6.21).

1. A DC SQUID, contains two Josephson junctions in a superconducting ring and is operated by direct current. The critical current of the SQUID oscillates as a function of the externally applied flux (ϕ) with a period of one flux quantum (ϕ_0). If the SQUID is biased with constant current, the voltage across the SQUID is also periodic in ϕ. Hence, essentially, it is a flux-to-voltage transducer.
2. An rf SQUID, contains only one Josephson junction in the superconducting ring, which is coupled to a tank circuit and is operated by rf current. The rf voltage across the tank circuit is also periodic in ϕ.

6.11 DC SQUID (A Superconducting Loop with Two Josephson Junctions)

This problem was investigated by Mercereau and coworkers [2] in detail. Since the Josephson effect arises because of the phase coherence between the two superconductors, it is expected that a two-junction device, consisting of a pair of Josephson tunnel junctions connected by superconducting links, would exhibit interference behaviour similar to an optical interference in so far as the critical current for the device is concerned.

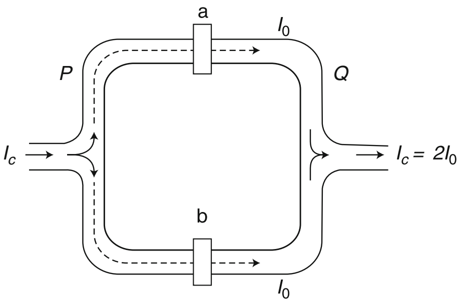

Fig. 6.22 Superconducting ring with two weak-links. There is no applied field

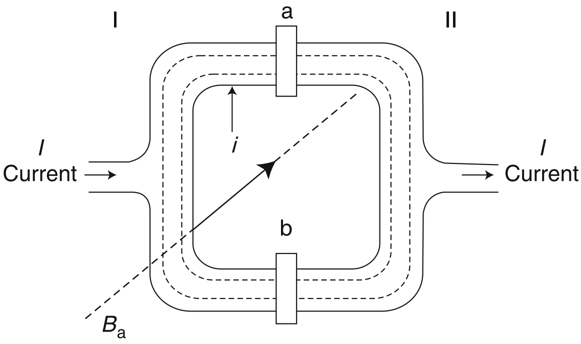

Fig. 6.23 Superconductors I and II with two weak-links (**a**) and (**b**). A magnetic field B is applied

Case I. The junctions are identical and there is no applied magnetic field (Fig. 6.22).

(Bias) current I_c from an external source divides equally between the two possible paths so that the phase difference across the junctions is the same ($S_a = S_b$), so that no voltage appears between P and Q and

$$I_c = 2I_0. \tag{6.30}$$

Case II. There is an externally applied magnetic field. An applied magnetic field perturbs the situation in two ways (Fig. 6.23).

1. A circulating current i flows along the inner surface of the loop. This current would prevent any flux from passing through the loop and we would find that

$$Li = \phi_a = (B_a) \times (\text{area of the loop})\,, \tag{6.31}$$

if there were no weak-links in the circuit. L is the self inductance of the loop.

For a single loop with millimetre dimensions, L is very small and flux cancellation is not possible in the circuit containing weak-links, because i will quickly exceed the critical currents I_0 of individual junctions. At this stage, we assume $LI_0 \ll \phi_0$, the flux quantum, i.e. $L \ll \phi_0/I_0$, so that flux through the loop (i.e. LI) is exactly equal to the applied flux ϕ_a.

2. Second effect is to produce an imbalance in phase difference across the junctions.

In order to determine how the critical current I is modified, we need to calculate the phases S_a and S_b. we find

$$\Delta S = 2\pi n = \frac{2e}{\hbar}\int A \cdot dl + S_a + S_b$$

or

$$S_a + S_b = 2\pi n - 2\pi\frac{\phi_a}{\phi_0}. \tag{6.32}$$

S_a and S_b are no longer equal, because the currents through the two junctions are different, being $(i + 1/2)$ and $(i - 1/2)$ when measured in the same clockwise direction. This imbalance in phase can be expressed as

$$S_a = \left(\pi n - \frac{\pi\phi_a}{\pi\phi_0}\right) - S_0, \tag{6.33}$$

$$S_b = \left(\pi n - \frac{\pi\phi_a}{\pi\phi_0}\right) + S_0, \tag{6.34}$$

where $(S_b - S_a) = 2S_0$, is the total phase shift. Here $S_\mathbf{a}$ and $S_\mathbf{b}$ are phases at (**a**) and (**b**) in presence of flux ϕ_a. Equations (6.32–6.34) show that the phases S_a and S_b and, therefore, the phase difference can be controlled by varying the applied flux ϕ_a. The situation is identical to that of two coherent light beams, which are made to interfere (over paths a and b). The phenomenon of super-current interference becomes evident, if we consider the total current I due to the currents I_a and I_b in presence of magnetic field.

So in (6.33) and (6.34), there is a constant phase shift which depends on the nature of the barriers (a) and (b) and the applied voltage.

$$I_a \cong I_0 \sin S_a, \tag{6.35}$$

$$I_b \cong I_0 \sin S_b, \tag{6.36}$$

$$\begin{aligned} I &= (I_a - I_b) = I_0\left[\sin S_a - \sin S_b\right], \\ &= I_0\left\{\sin\left[\pi\left(n - \frac{\phi_a}{\phi_0}\right) - S_0\right] - \sin\left[\pi\left(n - \frac{\phi_a}{\phi_0}\right) + S_0\right]\right\}, \\ &= I_0\left[2\cos\left(\pi\left(n - \frac{\phi_a}{\phi_0}\right)\right)\sin S_0\right] = 2I_0\cos\pi\left(n - \frac{\phi_a}{\phi_0}\right)\sin\ S_0, \end{aligned} \tag{6.37}$$

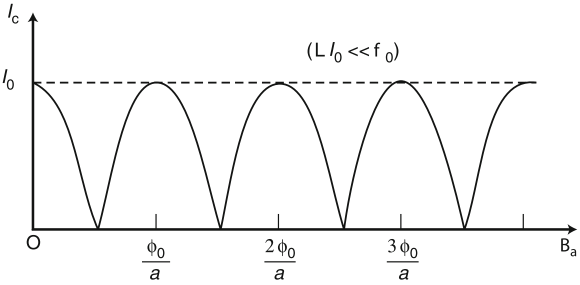

Fig. 6.24 The variation of critical current in a dc SQUID as a function of applied magnetic field. "*a*" is the area of the loop hole [3]

or

$$I = \left(2I_0 \cos \frac{\phi_a}{\phi_0}\right) \sin S_0, \tag{6.38}$$

that is, critical current is now given by

$$I_c = 2I_0 \left(\cos \frac{\phi_a}{\phi_0}\right). \tag{6.39}$$

Hence, the super-current through two Josephson junctions in a superconducting ring varies as the cosine of the magnetic flux through the ring. The maximum values of current I_c are obtained, whenever the loop contains an integral number of flux units. Figure 6.24 shows how the maximum current that flows (without a voltage appearing across the circuit) is modulated by applied flux threading the loop. However, this pattern is not observed in practice, since the circulating current does provide some screening of applied flux and coupled flux is $\phi' = \phi - Li$. Then, the interference pattern is unchanged, but the depth of modulation is reduced because the current minima are no longer zero. The modulation of interference pattern is optimum when

$$2\,(I_c)_{\max} \propto \phi_0/L \quad \text{(where L is ring inductance)}$$

or

$$(2LI_c/\phi_0) \equiv \beta_c.$$

β_c is known as the *modulation parameter* of a SQUID.

Figure 6.25 shows experimentally measured current through a pair of Josephson contacts as a function of the magnetic field through the loop. We may write

$$I\,(\phi_a) = I_c\,(0) \cos\left(\phi_a/\phi_0\right), \tag{6.40}$$

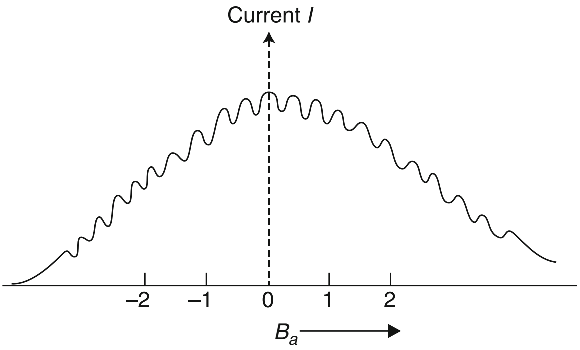

Fig. 6.25 Interference and diffraction effects

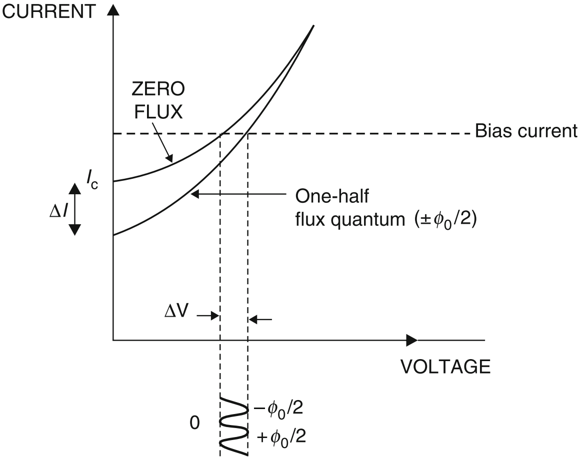

Fig. 6.26 Characteristic curve for a dc SQUID

where

$$I_c(0) = 2I_0 \sin S_0 \tag{6.41}$$

is the zero-flux critical current for the loop. The important difference between this case and that of a single junction is that, in this case, the appropriate area is the loop area and not area of a single junction, so that the magnetic field sensitivity is increased manifold.

In Fig. 6.25, the oscillations each correspond to a flux quantum and result from the cosine interference term. Thus, the interference between the Cooper pair tunnelling currents of two parallel Josephson junctions can be exploited to produce extremely sensitive magnetometers (SQUIDs).

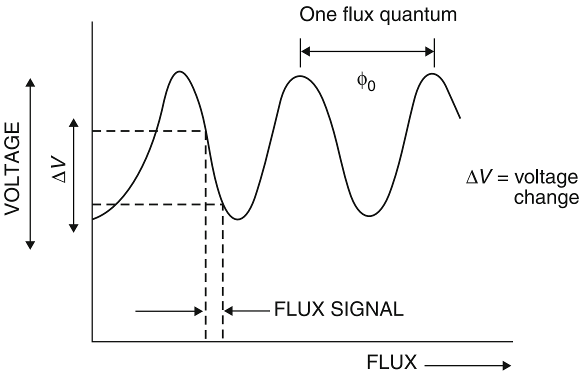

Fig. 6.27 Voltage oscillations when a magnetic flux is applied

6.11.1 The Characteristics of an Ideal DC SQUID

The SQUID, in essence, is a flux to voltage transducer; a tiny charge in magnetic flux is converted into a voltage.

The dc SQUID consists of two Josephson junctions arranged on a superconducting ring. A current applied to the SQUID, called as bias current, divides between the junctions, and if greater than the critical current, produces a voltage across the SQUID. Plotting this current against the voltage yields the characteristic curve as in Fig. 6.26.

For a fixed bias current fed into the ring, the voltage across it is modulated, as the magnetic field is changed. The voltage (critical current) is maximum for zero flux or an integral number of flux quanta and a minimum for a half integer number of flux quanta. The period of these oscillations is the flux quantum (Fig. 6.27).

Voltage modulation $\Delta V = R_D \times (\Delta I_0)$, where ΔI_0 is the critical current modulation and R_D is the dynamic resistance of the SQUID (I_0 is the critical current for individual junction). The depth of critical current modulations ΔI, depends on the product LI_0. L must be kept small to reduce the effect of thermal noise, but not so small as to limit the flux-input coupling. I_0 must also be small to avoid hysterisis in the weak-links, again, with a lower limit determined by the size of ΔI and the dynamic resistance R_D, which falls with decreasing I_0.

For these reasons, a value of

$$\frac{LI_0}{\phi_0} \approx \frac{1}{2}$$

is chosen and the modulation depth is then about 50 % or $\phi_0/2L$. The device is usually operated in the finite voltage regime with $I > I_c$.

Then

$$\Delta V = R_D \times \Delta I_0$$

or

$$\Delta V = R_{\mathrm{D}}\left(\frac{\phi_0}{2L}\right).$$

The variation ΔV with applied flux is approximately triangular and, thus, the flux sensitivity

$$\frac{\Delta V}{\Delta\phi} = \left(\frac{R_{\mathrm{D}}}{L}\right).$$

The SQUID is to be operated on the steep part of the $V - \phi$ curve, where $dV/d\phi$ is maximum.

The signal amplitude per ϕ_0, (i.e. $\Delta V/\phi_0$) is called the transfer function, which depends on the SQUID geometry, temperature and bias current. Thus, an output voltage is produced in response to a small input flux.

6.12 The rf SQUID

An rf SQUID consists of a single Josephson junction (JJ) in a superconducting ring, which is coupled inductively to an external (rf tuned) circuit. No dc current is fed to the ring, but in this, the circulating current is an oscillating function of the applied flux. Since the SQUID ring response is detected through the behaviour of the coupled rf tuned circuit, this JJ device is referred to as an rf SQUID.

6.12.1 Principle

A single JJ element is shorted at dc by the superconducting loop. This is monitored at a radio frequency ~20–30 MHz by coupling an rf current from a coil (I_{rf}), which forms a part of a tank circuit resonant at a particular frequency supplied by a constant rf drive current I_{rf} (Fig. 6.28).

The magnitude of the rf loss from the resonant circuit due to its coupling to the loop depends periodically on the *dc* flux enclosed by the loop with period ϕ_0. This flux modulated rf loss modulates the Q of the tank circuit and, hence, the magnitude of the rf voltage v_{rf} across it. This rf voltage is detected to provide the flux dependent readout from the device.

6.12.2 Working

The tuned circuit (also called tank circuit) is fed from a current source at an rf frequency ~20 MHz and the effect of the inductively coupled superconducting circuit is to produce a load, which varies periodically with the applied (*dc*) flux.

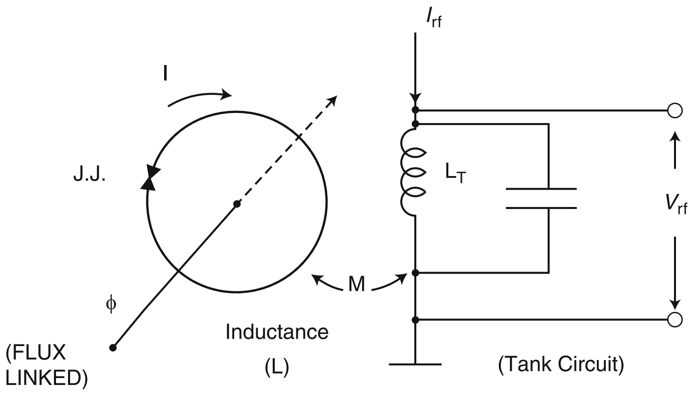

Fig. 6.28 Basic circuit for a rf SQUID

To understand how the device works, we need to find a relationship between the flux linking the superconducting ring (ϕ) and the applied flux (ϕ_a). The flux through the ring can be expressed as

$$\phi = \phi_a - LI \tag{6.42}$$

where $L =$ SQUID ring inductance, I is the circulating screening current in the ring.

$$I = I_0 \sin\left(\frac{2\pi\phi}{\phi_0}\right), \tag{6.43}$$

ϕ_0 is the flux quantum.

The coupled equations (6.42 and 6.43) may be solved to find ϕ in terms of ϕ_a, but the behaviour depends on the parameter

$$\frac{LI_0}{\phi_0} \equiv \beta.$$

For $\beta \ll 1$, there is no screening and $\phi = \phi_a$. For $\beta \gg 1$, the screening is complete and $\phi = 0$ for all values of ϕ_a.

For values $\beta \geq \pi/2$, the ϕ versus ϕ_a curve has regions with negative slope as shown in Fig. 6.29.

The negative resistance regions (in the Fig. 6.29) are unstable and for increasing or decreasing applied flux, the coupled flux ϕ will only follow those parts of the curve with a positive slope.

ϕ_b is a small background *dc* flux, which is not entirely screened by the circulating current I (This corresponds to the point A in the figure).

As the rf flux increases from zero, the flux through the loop and the circulating current will increase. At point B, the slope ($d\phi/d\phi_a$) is infinite and the system becomes unstable. The weak-link behaves like a gate, which opens to allow a single

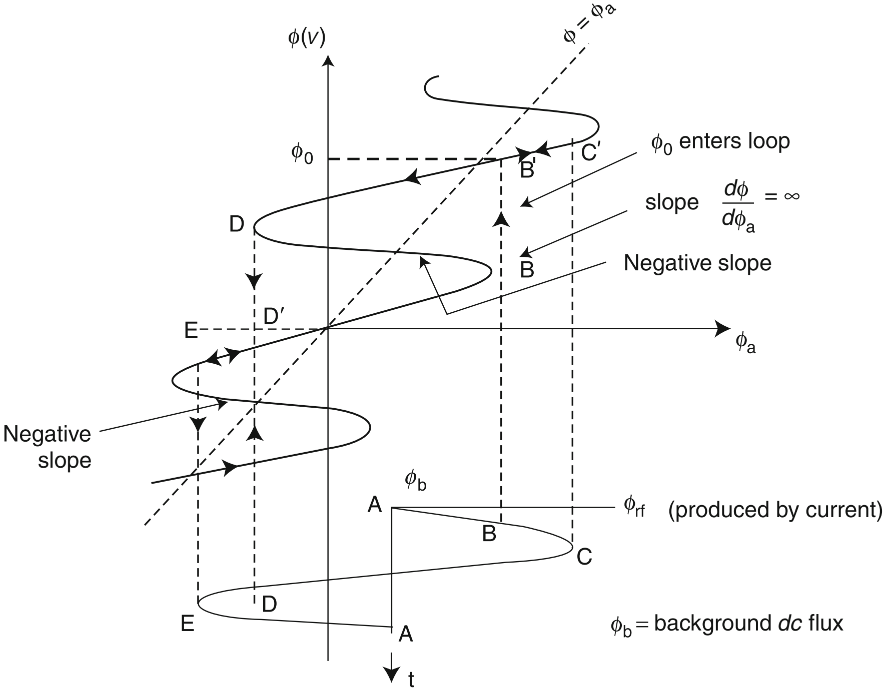

Fig. 6.29 Flux through an rf SQUID as a function of applied flux for $\frac{LI}{\phi_0} \geq \pi/2$

flux quantum ϕ_0 to enter the loop during the upward transition from B to B′ (i.e. a flux ϕ_0 jumps in when ϕ_a first exceeds the maximum screening field LI_0). The circulating current also changes discontinuously and reverses its direction (between B and C); the flux ϕ_{rf} and the current I once more increase. As ϕ_{rf} is reduced, the path is not reversed and the flux quantum ϕ_0 is not expelled from the circuit, until the point D is reached when there is a downward transition in ϕ (D to D′) and another reversal of I. For the remainder of the cycle (i.e. DEA), the flux follows the reversible path along the lower branch (then $\phi_a = \phi_0 - LI_0$).

The net effect of taking the SQUID around the hysterisis loop is to cause energy dissipation and a reduction in the effective Q-factor of the tank circuit. This is a threshold effect. As the rf current bias increases, the amplitude of the oscillatory voltage V_{rf} across the tuned circuit is linear in I_{rf}, while the amplitude of ϕ is less than a value corresponding to point B in the cycle, i.e. flux linking the loop limits the amplitude of ϕ_{rf} or ϕ_a given by

$$\phi = \frac{\phi_a}{2\pi} \cos^{-1}\left[\frac{\phi_a}{I_0 L}\right].$$

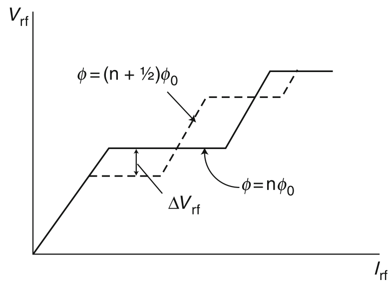

Fig. 6.30 Relation between V_{rf} and I_{rf} for the cases of integral and half integral numbers of flux quanta. For intermediate values of flux, the voltage steps occur at intermediate values of V_T [4]

Due to onset of hysterisis, level of oscillation ϕ_{rf} in the tank circuit is reduced, therefore, $\langle V \rangle_{time}$ remains constant, until the rf current I_{rf} has been increased sufficiently (at a rate $I_{rf} V_{rf}$) to overcome the additional energy loss in the secondary (i.e. superconducting) loop. As a result, the resulting $\langle V \rangle$ versus I_{rf} characteristic curve is a staircase pattern, with a series of plateau region, which occurs every time ϕ_{rf} is increased sufficiently to cause to SQUID to go round an additional hysterisis loop. The value of threshold voltage and current for each step will depend on the magnitude of background flux ϕ_b (a d.c. flux) coupled into the ring (Fig. 6.30).

It is to be noted here that if the amplitude ϕ_{rf} of the rf drive flux is too small, no flux jumps and hysterisis loss can occur. Jumps and hysteresis loss start to occur, when $\phi_a = \phi_b + \phi_{rf}$ (mod ϕ_0) exceeds the maximum screening flux LI_0. For the two extreme cases, in which ϕ_b is an integral or half integral multiple of ϕ_0, this occurs at $\phi_{rf} = LI_0$ and $LI_0 - \phi_0/2$ respectively. To relate this to an observable quantity, we note that

$$\phi_{rf} = MI_{rf} = MV_{rf}/(\omega L_T)$$

where M is the mutual inductance.

Thus, if one monitors V_{rf} as the drive current I_{rf} to the tank circuit is increased from zero, V_{rf} rises linearly with I_{rf}, until V_{rf} reaches $(\omega LI_0/M)$ for the integer flux case, or $(\omega LI_0/M)\,(1 - \phi_0/2LI_0)$ for the half integer case.

The plateaus in Fig. 6.30 correspond to the hysteritic break downs in the tank circuit. Further, V_{rf} will be modulated by

$$\Delta V_{rf} = \omega\phi_0\, L_T/(2M)$$

between integer and half integer values of ϕ_b, if the SQUID is operated with I_{rf}, fixed at a value for which a step in V_{rf} exists at both the integer and half integer flux values and, therefore, at all those values in between.

As one increases (or decrease) the flux, each step splits into two, with a maximum separation in voltage occurring for a flux of $(n \pm 1/2)\,\phi_0$. As the flux is further increased to $(n + 1)\,\phi_0$, (or decreased to $(n - 1)\,\phi_0$), the I_{rf} versus V_{rf} curve is restored to the solid line in Fig. 6.30. Thus, at a constant value of I_{rf}, V_{rf} oscillates as the flux is gradually increased or decreased, with the period of oscillations being

Fig. 6.31 Variation of ⟨V⟩ with applied flux ϕ_a

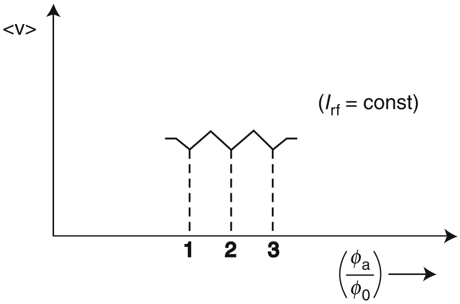

ϕ_0 (Fig. 6.31). In other words, if the SQUID is biased at the middle of one of the steps and if the value of the applied dc magnetic flux ϕ_a is varied, the value of $\langle V \rangle$ will oscillate (with ϕ_a) as a triangular waveform of period ϕ_0.

6.13 Applications of SQUIDs

A SQUID is essentially a flux to voltage transducer, so it can be used to measure magnetic flux, changes in flux, current or voltage. SQUIDs find the following applications:

1. Medical diagnosis (e.g. activities of brain)
2. Measurement of diamagnetism of new HTSCs
3. Sensing geological changes deep within the earth crust (for ore deposits)
4. Prospecting to submarine hunting
5. Earthquake scientists may, one day, use to predict likely earthquake periods by magnetically monitoring strain build up deep beneath the earth.

6.14 HTSC SQUIDs

SQUID effects in HTSCs have been reported by several groups of scientists. These include both dc and rf SQUIDs. For observing dc SQUID-effect, a superconducting ring interrupted by two Josephson junctions is required, whereas for rf SQUID effect one Josephson junction in a superconducting ring is needed.

Soon after the discovery of HTSCs, it was established that grain boundaries in these materials act as Josephson junctions and these could be utilised to fabricate the SQUIDs.

The behaviour of grain boundaries (weak-links) on an average depends on the preparation conditions of the material and behaviour of any particular weak-link is quite unpredictable. Thus, realisation of two identical grain boundary weak-links

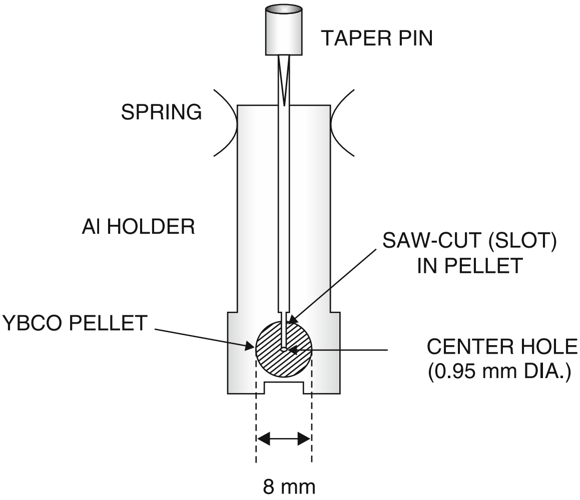

Fig. 6.32 Break junction rf SQUID [5]

for the dc SQUID in HTSCs is rather difficult, which results in very low yield of fabrication of HTSC dc SQUIDs. If the characteristics of the two weak-links are not identical, it may lead to irregular $V - \phi$ behaviour. However, it is easier to get one weak-link in a superconducting ring with a characteristic feature suitable for an HTSC rf SQUID. The observation of the rf SQUID effect does not require any direct contact, so the problem of contact resistance does not come into the scenario.

6.15 Some Practical rf SQUIDs

6.15.1 Break Junction rf SQUIDs

Figure 6.32 shows the experimental set up used for realising a break junction in a cryogenic atmosphere. A disc of YBCO with about 1 mm dia hole drilled through its centre has been glued on an aluminum holder. A slot is cut radially from the perimeter towards the hole leaving a small bridge of the material. Break junction is realised by forcing a tapered pin into the slot, which causes the YBCO pellet to break in the bridge region (slot). The pin is slightly withdrawn, then YBCO surfaces on the two sides of the crack come together (due to springs) forming a point contact junction. This entire operation is done inside the liquid nitrogen atmosphere. The rf SQUID so formed is coupled to a resonance circuit and can be operated in the usual way.

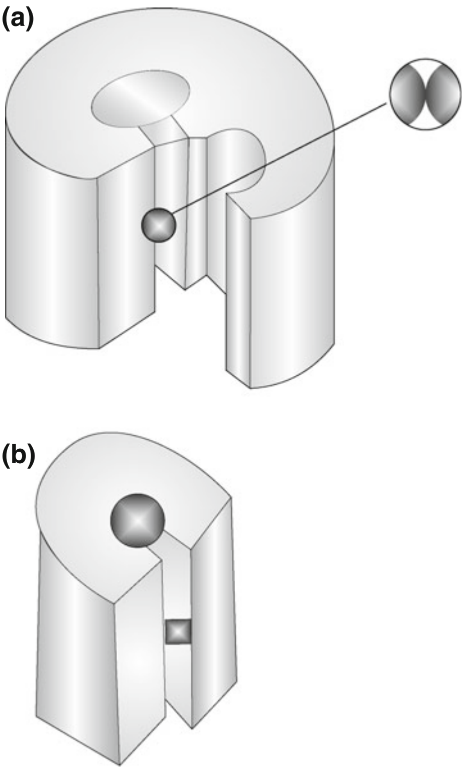

Fig. 6.33 **(a)** Two-hole and **(b)** one-hole rf SQUIDs [6]

6.15.2 Two- and One-Hole rf SQUIDs

The $V - \phi$ behaviour (which is periodic) of break junction rf SQUIDs is similar to that of a conventional low T_c rf SQUID. But, fragile nature of the weak-link makes it not very useful for practical applications. More stable rf SQUIDs have been obtained by using naturally present grain boundary weak-links in a micro-bridge of polycrystalline YBCO pellet (Fig. 6.33).

The two-hole geometry is fabricated by drilling two holes of diameter of the order of 1 mm in a pellet leaving a bridge between the holes. This bridge is eroded carefully to get a micro-bridge weak-link. In single hole geometry, one hole is drilled in the pellet and then, micro-bridge is created by eroding the wall on one side of the hole (erosion of bridge is done mechanically with fine needle files or with diamond coated wires). The minimum dimensions of the micro-bridge required for observing the periodic rf SQUID characteristic feature depends on the quality of the pellet, such as density, critical current density and grain size ($>10 \times 10(\mu\text{m})^2$).

The dense pellets having micro-bridge dimensions $\sim 100 \times 100\,\mu\text{m}^2$ do not show SQUID behaviour, if the critical current density is also very high. Then, reduction of micro-bridge dimensions to $50 \times 50\,\mu m^2$ or less is required to get the SQUID behaviour.

In principle, the micro-bridge should contain only one grain boundary junction for observation of good rf SQUID behaviour, but even small micro-bridge fabricated manually in the two-, or one-hole geometry may contain more than one grain boundary junction. For reducing the parallel weak-links, it is desirable to use local thermal treatment instead of further erosion. Local heating of the bridge results in the reduction of some of the parallel weak-links and, thus, reduction of the critical current of the micro-bridge. Thermal cycling of the sample between room temperature and liquid-N_2 temperature may result in reduction of parallel weak-links at the surface of the micro-bridge, whose T_c may be reduced to less than 77 K.

6.16 SQUIDs Fabricated from Films

In the two-hole or one-hole bulk rf SQUIDs, the micro-bridge does not have any base support, so the thermal shock can easily result in development of a crack in the micro-bridge. On the contrary,

1. It is easier to prepare micro-bridge of smaller dimensions in a film, using suitable patterning technique, and
2. It is easier to control the grain size also and its orientation in the film as compared to the bulk.

6.16.1 SQUIDs Using Polycrystalline Films

The rf SQUIDs based on polycrystalline film are fabricated by patterning a hole shunted with a micro-bridge type of structure on the film as shown in Fig. 6.34.

Most of the early rf SQUIDs were fabricated using polycrystalline films. Recent reports indicate that it is advantageous to fabricate SQUIDs using epitaxial films, which have lower flux noise.

In case of polycrystalline films, naturally present grain boundary acts as a Josephson junction. However, in good epitaxial films, grain boundaries suitable for SQUID effect are nearly non-existent and thus, an artificial grain boundary or some other suitable structure (for Josephson junction) needs to be fabricated.

6.16.2 SQUIDs Using Epitaxial Films

The polycrystalline film based rf SQUIDs have serious drawbacks:

1. SQUID parameters cannot be fully controlled and
2. Presence of grain boundaries in the superconducting ring may introduce low frequency noise due to flux hopping.

Fig. 6.34 A BSCCO film with a hole and a micro bridge [7]

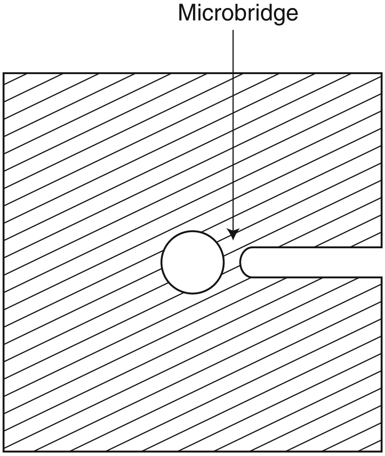

Fig. 6.35 Artificial GB grown on a bicrystal substrate. This gives low noise SQUIDs

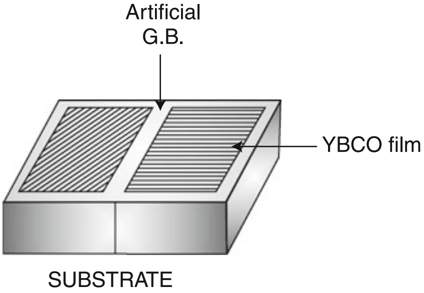

Fig. 6.36 Edge junction

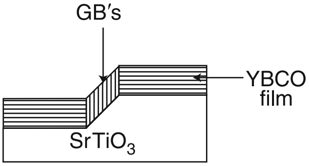

Fig. 6.37 Film deposition by biepitaxy

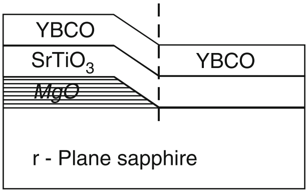

Thus, it is desirable to fabricate rf SQUIDs from epitaxial films with a well defined weak-link structure.

Various types of weak-link fabricated, using epitaxial films, are shown in Figs. 6.35, 6.36, 6.37, 6.38, 6.39 and 6.40.

Fig. 6.38 A S–I–S edge junction

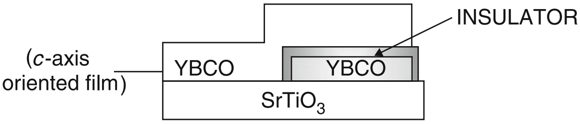

Fig. 6.39 SNS edge junction

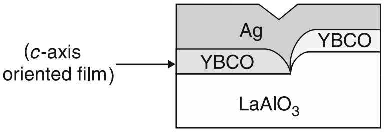

Fig. 6.40 Planar SNS structure

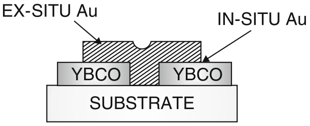

Figure 6.37 shows an edge junction, where an epitaxial film has been deposited on a single crystal substrate having a sharp edge (this is a successful technique).

Figure 6.37 shows a Josephson junction realised by film deposition by bi-epitaxy process using a seed layer.

The ideal Josephson junction for the SQUIDs is thin film S–I–S type tunnel junction. But to date, no tunnel junction suitable for electronic applications has been fabricated using HTSCs. Physical and chemical imperfections occurring either during film deposition or subsequent processing, combined with short coherence length has made realisation of good quality S–I–S junction very difficult and challenging. As coherence length of HTSCs along *ab* plane (15–30 Å) is much large than along *c*-axis $\left(\sim 3\,\text{Å}\right)$, it is desirable to use *a*-axis oriented film (and not *c*-axis oriented film) for fabricating S–I–S sandwich type tunnel junction. Some groups have reported fabrication of edge junctions using *c*-axis oriented films (in both SIS and SNS configurations). Similarly, planar SNS junctions have also been fabricated using *c*-axis oriented films.

In all cases viz. film on bicrystal, film on edge junction and film deposited by biepitaxy, a GB junction showing Josephson characteristics can be fabricated by patterning a micro-bridge across the grain boundary.

The ideal Josephson junction for device application is sandwich type, i.e. thin film SIS tunnel junction. For this, the tri-layer structure must be deposited in situ (to avoid oxygen deficiency at film surface and avoid interdiffusion of film with barrier layer material). The material of the barrier layer must be lattice matched to the HTSC material layers and it should not react with the HTSC film at the deposition temperatures, so that interfaces are sharp within the coherence length.

The sandwich type junctions fabricated from *c*-axis oriented films do not show Josephson effect, whereas sandwich type structures (SIS) fabricated using *a*-axis oriented film show Josephson effect. However, their characteristics are similar to those of SNS junctions.

The SIS and SNS type edge junctions fabricated on edge of c-axis oriented films have characteristics similar to that of SNS type junctions, The tunnelling current (across the edge junction) is in ab plane.

6.17 How SQUIDs are Used for Flux Measurements

It is already known that zero voltage super-current of a Josephson junction is strongly affected by small magnetic fields.

$$I_\mathrm{c}\left(\phi\right) = I_0 \left|\frac{\sin\left(\pi\phi/\phi_0\right)}{\left(\pi\phi/\phi_0\right)}\right|, \tag{6.44}$$

where ϕ is the applied flux $\left(= \vec{B} \cdot \vec{A}\right)$ and ϕ_0, the flux quantum.

In case of a Josephson junction in a loop (i.e. a SQUID), we have

$$I_\mathrm{c}\left(\phi\right) = I_0 \left|\cos\left(\frac{\phi\pi}{\phi_0}\right)\right|, \tag{6.45}$$

where ϕ is total flux enclosed in the loop and I_0, the zero flux critical current. The important difference between (6.44) and (6.45) is that in case (6.45), the appropriate area is not that of the junctions in the loop but that of the loop containing the junctions. As a result, the sensitivity to flux changes is remarkably higher. In fact, the actual resolution of such a device can be much better than single flux quantum. The normal approach to make a practical device is to apply a dc bias current that is close to the critical current at zero flux, whereas an ac (I_rf) flux modulation to the rf SQUIDs via a small coil coupled to the SQUID loop, about one ϕ_0 in amplitude and at a sufficient frequency to be about an order of magnitude above the maximum frequency that is going to be measured. A small input (dc) or low frequency flux produces a modulation of the critical current, which can be detected as a voltage modulation across the input.

A small flux (input) to be detected is, if applied to the input coil, this will try to charge the feedback current and this change in feedback current will be proportional to the input flux.

A flux change $\delta\phi$ produces a voltage V_m across the SQUID, which is feedback to the SQUID itself through the coil coupled to the SQUID. As a consequence, a flux $(-\delta\phi)$ is generated and the SQUID will not experience any flux, but the feedback current increases linearly with the applied flux. Therefore, voltage fed back is proportional to the applied flux (*the feedback voltage appears across the feedback resistor*).

The phase-sensitively detected dc output voltage across the feedback resistor will then be a direct measure of the input flux (from, V vs ϕ characteristic) (Fig. 6.41).

Bias changes from p to p′ as a result of external flux. For p′, voltage output V_m is at the modulation frequency.

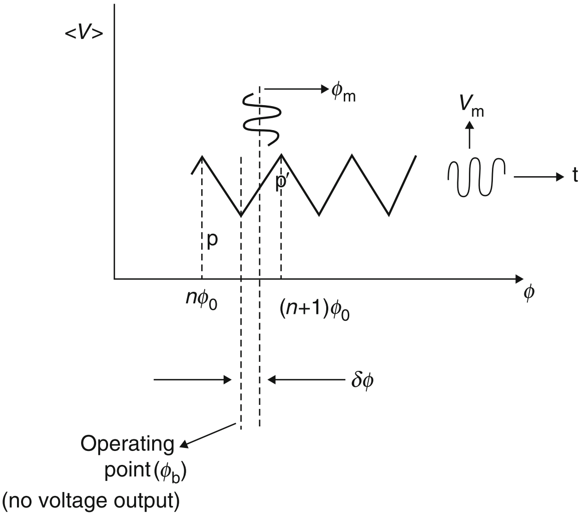

Fig. 6.41 Variation of average dc output voltage with variation in input flux

$|V_m|$ is a measure of $\phi'_p - \phi_p$. Due to feedback, the bias point is brought back from P′ to P. To obtain a dc output voltage (which should be varying linearly with the ϕ_m), an rf SQUID can be operated in the flux locked loop mode, employing a feedback circuit consisting of a coil and a feedback resistor. The SQUID remains "locked" to the minima of the $V - \phi$ characteristic.

In the flux locked loop mode, one can detect flux much less than ϕ_0 as well as several ϕ_0 with the same high sensitivity.

6.17.1 Superconducting Flux Transformers

Since SQUIDs are employed to measure small changes in magnetic field, it requires to screen the SQUID from other external sources. The flux to be measured is coupled into the SQUID ring via a superconducting flux transformer.

For screening, a superconducting enclosure is used. The screening device works on the principle that in a closed superconducting circuit, the flux is constant and remains fixed at the value contained in the circuit when the material becomes superconducting. In its simplest form, the flux transformer has two coils:

1. *Coupling coil*. which is inductively coupled to SQUID loop.
2. *Input coil* (*or Pick up coil*). This is exposed to the flux to be measured SQUID and the part of flux transformer coupled are screened inside the superconducting shield, which preserves the magnetic environment during measurement (Fig. 6.42).

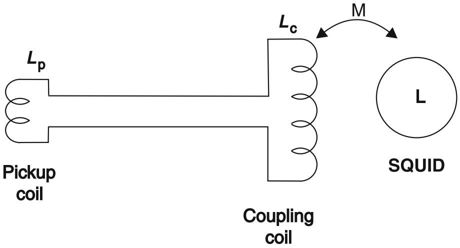

Fig. 6.42 Superconducting flux transformer

The flux input to the pickup coil causes a super-current to flow around the transformer coil. This super-current flow imposes a magnetic field on the SQUID, which is proportional to the flux input to the pick up coil.

Let ΔB_i denote the input field coupled to the pick up coil. Then current induced in the flux transformer is

$$\Delta i = \frac{\Delta B_\mathrm{i} A_\mathrm{p}}{(L_\mathrm{p} + L_\mathrm{c})},$$

where A_p is area of pickup coil.

The change in field at the coupling coil is

$$\frac{\Delta i L_\mathrm{c}}{A_\mathrm{c}} = \frac{\Delta B_\mathrm{i} A_\mathrm{p}}{(L_\mathrm{p} + L_\mathrm{c})} \left(\frac{L_\mathrm{c}}{A_\mathrm{c}}\right).$$

If $L_\mathrm{c} = L_\mathrm{p}$, then change in field,

$$= \frac{\Delta B_\mathrm{i} A_\mathrm{p}}{2 A_\mathrm{c}}.$$

If $A_\mathrm{p} \gg 2A_\mathrm{c}$ (as is usually the case), then there can be significant field multiplication.

$$\phi_\mathrm{a} = \left(L_\mathrm{p} + L_\mathrm{c}\right) \Delta i.$$

The flux coupled into the SQUID will depend on the mutual inductance M between L_c and the SQUID ring, therefore,

$$\begin{aligned} \phi_\mathrm{SQUID} &= \frac{\phi_\mathrm{a} M}{(L_\mathrm{p} + L_\mathrm{c})} \\ &= M \Delta i \\ &= \left(\frac{\Delta B_\mathrm{i}}{L_\mathrm{p} + L_\mathrm{c}}\right) A_\mathrm{p}. \end{aligned}$$

Figure 6.43 shows several possible configurations for the pick up coil.

A magnetometer detects total flux and provides no spatial discrimination (Fig. 6.43a). A gradiometer detects $\frac{\partial H_z}{\partial z}$, whereas an off diagonal gradiometer detects

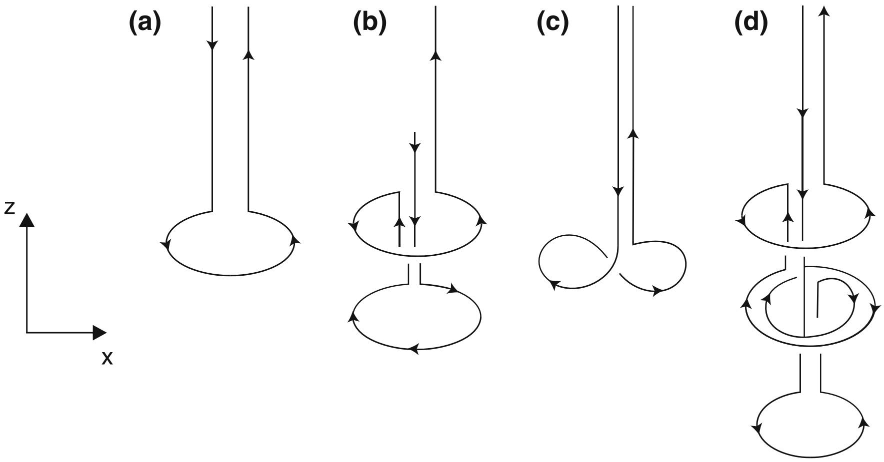

Fig. 6.43 **(a)** Magnetometer, **(b)** gradiometer **(c)** off diagonal gradiometer, **(d)** second derivative gradiometer [8]

$\frac{\partial H_z}{\partial x}$ (Fig. 6.43b, c respectively). Both Fig. 6.43b and c are the first derivative gradiometer and insensitive to uniform fields.

A second derivative gradiometer detects $\frac{\partial^2 H_z}{\partial z^2}$ (Fig. 6.43d). It is insensitive to uniform field and uniform field gradients.

6.18 Design and Noise Aspects of SQUIDs

Design of SQUIDs to achieve high sensitivity requires careful attention to obtain appropriate values for SQUID ring and junction parameters. For the ring, most important quantity is self inductance L_{sq} (dependent on its diameter). For Josephson junction, the important parameters are

Critical current (I_c)
Capacitance (C) and
Shunt resistance (R)

6.18.1 Choice for Critical Current I_c of J.J.

For larger I_c, no SQUID response is observed and for very small I_c values ($<1\,\mu$A), the coupling energy $I_\mathrm{c}\phi_0/2\pi$ will become much smaller than the thermal energy $k_\mathrm{B}T$. For a SQUID, a Γ-parameter is defined as

$$\Gamma = \left(\frac{2\pi k_B T}{I_c \phi_0}\right).$$

For observing quantum interference effect,

$\Gamma < 1$ preferably $\Gamma \cong 0.1$

$$\Rightarrow I_c \cong (10-100)\ \mu A,$$

for operation at 77 K.

6.18.2 Choice for the Inductance of the Ring

Thermal fluctuations put a limit on the largest value of $L_{sq}.k_B T/2$ per degree of freedom generate a mean square fluctuation in the SQUID $= \phi_n^2/L_{sq}$, where ϕ_n is equivalent flux noise. SQUID effect can be observed only if

$$\begin{aligned}\phi_n &< \phi_0/2\\ \Rightarrow \frac{\phi_n^2}{L_{sq}} &< \frac{\phi_0^2}{4L_{sq}}\end{aligned}$$

Then, the condition for observing rf SQUID response is

$$k_B T < \frac{\phi_0^2}{4L_{sq}}.$$

This imposes a condition

$$L_{sq} < 10^{-9} H$$

for operation at 77 K.

From the equivalent circuit for JJ, useful design parameters for SQUIDs are

$$\begin{aligned}\beta_c &= \frac{2\pi I_c R^2 C}{\phi_0},\\ \beta_L &= \frac{2L_{sq} I_c}{\phi_0}\ \text{(for dc SQUID)},\\ \beta_L &= \frac{2\pi L_{sq} I_c}{\phi_0}\ \text{(for rf SQUID)}.\end{aligned}$$

The optimum sensitivity of the SQUID for instrument design purpose is usually obtained for

$$\beta_c < 1\ \text{(typically} \sim 0.3)$$

and $\beta_L \approx 1$.

β is known as hysterisis parameter. If β is >1, rf SQUID operates in the hysteritic mode, then best rf SQUID response is at resonance frequency. For $\beta < 1$, it operates in the non-hysteritic mode. Best rf SQUID response occurs when tank circuit is slightly detuned on either side of the resonance frequency.

6.18.3 *Noise, Noise Energy and Energy Resolution of SQUID*

The sensitivity of a SQUID is limited by the random voltage (noise) S_V, which generates in the absence of a signal.

S_V depends on f (frequency).

The voltage noise spectrum $\sqrt{S_V(f)}$ is measured with the help of a spectrum analyser (a dynamic signal analyser). It can be expressed as an equivalent flux noise S_ϕ, which has a spectral density

$$\sqrt{S_{\phi(f)}} = \frac{\sqrt{S_V(f)}}{\delta V/\delta\phi}$$

or

$$S_\phi(f) = \left\{\frac{S_V(f)}{(\delta V/\delta\phi)^2}\right\}^{1/2}$$

at frequency f. Here $\delta V/\delta\phi$ is the transfer function of the SQUID. Typically, $\sqrt{S_\phi(f)}$ is frequency independent white noise down to a frequency where it scales as $1/f$, i.e. $\sqrt{S_\phi(f)}$ is the frequency dependent flux noise. Another figure of merit for comparing the performance of different SQUIDs is the flux noise energy

$$\varepsilon(f) = \frac{S_\phi(f)}{2L_{sq}}.$$

The input energy is

$$\varepsilon = \frac{1}{2}L_c(\delta I)^2,$$

where L_c is inductance of coupling coil and δI is the current in input coil, which can just be resolved by the SQUID. This minimum current is limited by the flux noise, which when expressed as a spectral density S_ϕ is related to δI by

$$\sqrt{S_\phi} = M\delta I$$

where

$$M = \alpha\sqrt{L_\mathrm{c}L_\mathrm{sq}},$$

α given by $\alpha = \frac{M}{\sqrt{L_\mathrm{c}L_\mathrm{sq}}}$

$$(\delta I)^2 = \frac{S_\phi}{M^2} = \frac{S_\phi}{\alpha^2 L_\mathrm{c}L_\mathrm{sq}}$$
$$\Rightarrow \varepsilon = \frac{1}{2}L_\mathrm{c}\,(\delta I)^2 = \frac{S_\phi}{2\alpha^2 L_\mathrm{sq}}$$

or

$$\varepsilon(f) = \frac{S_\phi(f)}{2\alpha^2 L_\mathrm{sq}}$$

6.18.3.1 DC SQUIDs

For an optimised dc SQUID with

$$\beta_\mathrm{L} = \frac{2L_\mathrm{sq}I_\mathrm{c}}{\phi_0} \approx 1$$

and for a value of bias current (I) where the SQUID transfer function

$$\begin{aligned} V_\phi &= \left(\frac{\delta V}{\delta\phi}\right) \text{ is maximum,} \\ V_\phi &\approx (R/L)\,, \\ S_\mathrm{V}(f) &\approx (16k_\mathrm{B}TR)\,, \\ \varepsilon(f) &= \left(\frac{9k_\mathrm{B}TL_\mathrm{sq}}{R}\right). \end{aligned}$$

From the expression for β_c, we obtain the value of R as

$$R^2 = \frac{\beta_\mathrm{c}\phi_0}{2\pi I_\mathrm{c}C} = \frac{\beta_\mathrm{c}L_\mathrm{sq}}{2\left(\frac{L_\mathrm{sq}I_\mathrm{c}}{\phi_0}\right)C\pi}$$

or

$$R^2 \approx \frac{\beta_c L_\mathrm{sq}}{\pi C} \quad \left(\frac{L_\mathrm{sq}I_\mathrm{c}}{\phi_0} \approx 1\right)$$

or

$$R = \left[\frac{\beta_\mathrm{c}L_\mathrm{sq}}{\pi C}\right]^{1/2}.$$

Therefore, $\varepsilon(f) = \frac{9k_{\mathrm{B}}TL_{\mathrm{sq}}}{R}$,

$$= 9k_{\mathrm{B}}TL_{\mathrm{sq}}\left[\frac{\pi C}{\beta_{\mathrm{c}}L_{\mathrm{sq}}}\right]^{1/2}$$

or

$$\varepsilon(f) = 9k_{\mathrm{B}}T\left[\frac{\pi CL_{\mathrm{sq}}}{\beta_{\mathrm{c}}}\right]^{1/2}.$$

Thus, one should reduce T, L_{sq} and C to improve the energy-resolution of dc SQUIDs.

For a commercially available dc SQUID,

$$\sqrt{S_\phi} \approx \frac{2\times 10^{-5}\phi_0}{\sqrt{Hz}}; \quad \varepsilon \cong 10^{-30}\frac{J}{Hz} \text{ at } 4.2\,\mathrm{K}.$$

For high T_{c} dc SQUID, flux noise energy can be predicted by the preceding equations. One can assume $R = 5\Omega$ (which is close to values achieved experimentally for high T_{c} grain boundary junctions), with

$$\begin{aligned} L_{\mathrm{sq}} &= 0.2\times 10^{-9}\,\mathrm{H},\\ T &= 77\,\mathrm{K},\\ R &= 5\,\Omega,\\ \varepsilon &= 4\times 10^{-31}\,\mathrm{J\,Hz^{-1}}. \end{aligned}$$

This value is somewhat better than that of a commercially available (4.2 K) dc SQUID and about two orders of magnitude lower than that of a commercially available 4.2 K rf SQUID. However, this value is only about one order of magnitude higher than that of a typical Nb-based thin film dc SQUID operating at 4.2 K.

The excess noise, typically with a spectral density scaling as $1/f$ can substantially reduce the sensitivity of SQUIDs at low frequencies. Although this $1/f$ noise has been known earlier in low T_{c} SQUIDs, it has been particularly severe in high T_{c} devices. In the case of the dc SQUIDs (both low and high T_{c}), the origin of $1/f$ noise has been extensively studied and two sources have been identified

1. Fluctuations in critical current I_{c} generated by the trapping of electrons or by atomic reconfigurations in the barrier.
2. Thermally activated hopping of flux vortices between pinning sites in the body of the SQUID with magnitude depending on quality of the superconducting material.

The contribution 1 can be reduced in the flux modulated and flux locked dc SQUIDs. Although the critical current fluctuations are accompanied by resistance fluctuations, the latter usually play no significant role under typical bias conditions for the SQUID. Noise contribution 2 cannot be reduced by any bias modulation scheme. It is also to be noted that, although rf SQUID were the first to become commercially

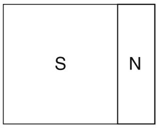

Fig. 6.44 Superconductor-normal proximity system

available, for typical operating frequencies ($\sim$20 MHz), the resolution in fractions of flux quantum/$\sqrt{Hz}$ of rf SQUID is not as good as that of the dc SQUID. A much higher frequency bias would be required to become equal in resolution to the dc SQUID.

Further, flux noise in epitaxial *c*-axis films is about half the flux noise in polycrystalline *c*-axis films, which is very less than flux noise in random oriented films.

6.19 Proximity Effect (Induced Superconductivity)

Consider a sandwich consisting of two films, with a superconductor and a normal metal (i.e. a S–N sandwich), e.g. Nb–Cu (Fig. 6.44).

Copper itself is not a superconductor, but as a part of S–N sandwich, it begins to display superconducting properties due to the influence of neighbouring superconducting film. This has been observed experimentally that when this Nb–Cu is placed in a magnetic field, copper exhibits Meissner effect.

Cooper pairs from S-film penetrate into the N-film, therefore, the pair wave function $\psi(r)$, called the order parameter, becomes non-vanishing in the N-film also.

The transition of a Cooper-pair from S-film to N-film, can be considered as reflection of the pair off the S–N boundary, with an electron incident on the boundary and a hole reflected (Andreev reflection, quasi-particles of a pair are of opposite momentum in Andreev scattering, (1964)). Such a reflection is equivalent to an electron-pair vanishing from the S-film and going into the N-film. When describing the disappearance of an electron-pair at the boundary, we can picture the entire process as disappearance of one electron accompanied by creation of one hole. This picture of Andreev reflection conveniently describes the processes taking place at the S–N interface.

The degree of proximity effect depends on

1. Quality of the contact
2. Thickness of the films.

Increasing the thickness of N-film weakens the effect. Decreasing the temperature diminishes chaotic thermal motion, which facilitates pair-penetration.

The proximity effect is strongest at temperatures far from T_c and close to 0 K.

There are two approaches for the theory of the proximity effect

1. P.de. Gennes et al. (Orsay group)
2. Mc Millan's tunnelling model (1968).

The former is based on Ginzberg Landau theory and is applicable only near T_c. According to Mc Millan's theory, the proximity effect is generated by electrons tunnelling through the barrier formed by the interface region. Interface quality affects the magnitude of so-called tunnelling matrix element. To describe the tunnelling process, one introduces the quantities T^s and T^N such that

$$T^{\alpha} = |T|^2 v_{\alpha}$$

$(\alpha = S\ or\ N)$.

Here, T is tunnelling matrix element and ν is density of states.

An effective coherence length ξ_N can be introduced such that, according to Clarke (1969)

$$\xi_N = \frac{h V_F^N}{T},$$

where V_F^N is the Fermi velocity in the N-film.

It is to be noted here that McMillan's theory is valid at all temperatures.

A proximity system is characterised by a single critical temperature T_c with $T_C^{\beta} < T_C < T_C^{\alpha}$.

For S–N system,

$$T_C(T) = T_C^S \left(\frac{T_C^S}{T} \right)^{\frac{v_N L_N}{v_S L_S}}$$

assuming $T > T_C^S$,

L are the film thicknesses. Here,

$$L_N \ll \xi_N, \quad L_S \ll \xi_S.$$

Since in proximity effect, the superconductivity can be induced in materials that are not superconductors by themselves, therefore, in doing so, one can utilise both the superconductivity and intrinsic properties of the normal (N) material (say a semiconductor). For instance, by varying the carrier concentration in the semiconductor (N), one can significantly affect the critical temperature T_c. This can be seen as

$$v_N \sim p_F^N \sim n_N^{1/3},$$

where p_F^N is the Fermi momentum in the N-film (carrier concentration can be affected by either radiation or employing the field effect).

In order to have tunnelling effects, the conductance of the junction should be low and the critical voltage ($I_c R$ product) should be high (where R is normal state resistance of junction).

6.19.1 S–I Junction

Experiments on break junction BSCCO have shown that even in favourable direction (parallel to *ab* plane), zero conductance is achieved only at the Fermi level and conductance (otherwise) is very large.

6.20 S–N Junction

1. *Junction $\perp$ to ab plane*. Show small but finite I_c with $I_\mathrm{c}R$ product about two order of magnitude lower than expected.
2. *Junction parallel to ab plane*. No I_c could be measured on YBCO/Au/Nb junction, which was unexpected as otherwise large ξ of Au (normal metal) could have remedied problem arising from short ξ of cuprate. This depression of $I_\mathrm{c}R$ arises due to larger conductance and larger carrier density of the normal metal as compared to the cuprate (The limitation is of fundamental nature and not arising due to metallurgical problems).

6.20.1 Fundamental Properties of S–N Contacts

These can be described by two parameters

1. Pair potential Δ
2. Pair amplitude $F = (\Delta/V)$.

V is the BCS interaction parameter. In a normal metal in contact with a superconductor $F \neq 0$, which gives rise to induced superconducting properties (like Meissner effect). Theory of proximity effect predicts that when a relatively clean normal metal is in contact with a cuprate, the pair amplitude in N at the interface is strongly reduced compared to that in S.

In a S–N–S junction, if N is a conventional normal metal (Ag or Au), there is a strong depression of the pair amplitude in N at the S/N interface. This implies low $I_\mathrm{c}R$ product (this is due to short ξ and low carrier density of S). A large $I_\mathrm{c}R$ product can be obtained by using for N either

1. A low carrier density metal or
2. A heavily doped semiconductor.

6.20.2 Boundary Conditions for Pair Amplitude (F)

In the absence of any significant boundary resistance, the boundary conditions for F, at the interface are

$$\frac{F}{N\,(0)} \text{ continuous} \tag{6.46a}$$

$$D\left(\frac{\mathrm{d}F}{\mathrm{d}x}\right) \text{ continuous} \tag{6.46b}$$

$N(0)$ is normal state density of states
D is coefficient of diffusion
x-axis is taken $\perp$ to the interface
Not too close to the interface, F decays exponentially in N with a decay length K^{-1}
If $V_N = 0$, in clean limit $l_N > K^{-1}$.

with

$$K^{-1} = \frac{\hbar V_{FN}}{2\pi k_B T_C} \tag{6.47a}$$

and in the dirty limit

$$K^{-1} = \left(\frac{\hbar D_N}{2\pi k_B T_C}\right)^{1/2}. \tag{6.47b}$$

If $V_N > 0$, N side becomes superconducting at some finite temperature T_{CN}.

Near T_{CN}, $K^{-1} \propto (T - T_{CN})^{-1/2}$, i.e. K^{-1} is temperature dependent.

For a given value of above $|T - T_{CN}| \ll T_{CN}$, $K^{-1}(T)$ above T_{CN} is $>\xi_N(T)$ below T_{CN} by a factor $\sqrt{2}$.

$$\left(\text{i.e. } K^{-1}|_{T>T_{CN}} = \sqrt{2}\xi_N|_{T<T_{CN}}\right)$$

coupled with the normal state conductivity $\sigma = 2e^2 \mathrm{N}(0) D$, the boundary condition is

$$\frac{1}{F} = \left(\frac{\mathrm{d}F}{\mathrm{d}x}\right)\sigma \text{ be continuous} \tag{6.48}$$

For a semi-infinite N

$$b = \left(\frac{\sigma_s}{\sigma_N}\right) K^{-1}$$

where $b^{-1} = \frac{1}{F}\left(\frac{\mathrm{d}F}{\mathrm{d}x}\right)$.

For a normal metal N of finite thickness d_N,

$$b = \left(\frac{\sigma_s}{\sigma_N}\right) K^{-1} \quad \cot h\,(K d_N)$$

6.20.3 *Effect of a Finite Boundary Resistance*

Now (6.46a) and (6.46b) do not hold. Large boundary resistance occurs if the interface has been contaminated by a non-conducting material (such as thin oxide layer) or less trivially, if normal state properties of S and N are very different. The relevant parameter describing importance of boundary resistance R_B is

$$\upsilon_B = R_B \sigma_N K,$$

where K is given by (6.47b) (the dirty limit value). Equations (6.46a) and (6.46b) are valid for $\upsilon_B \ll 1$. An expression for R_B is given by

$$\frac{1}{R_B} = \frac{e^2}{2\pi^2 \hbar}(k_F)^{-2} t,$$

where k_F is smaller of the Fermi wave vectors of S and N, t is transparency coefficient (<1) given by

$$t = \frac{V_{FS}}{V_{FN}}; \quad (V_{FS} < V_{FN})$$

Two cases arise:

6.20.3.1 Case (1) $k_{FN} < k_{FS}$

(carrier concentration in N $<$ that in S)
then

$$\upsilon_B = \frac{4}{3}(\ell_N K) t^{-1}$$

the condition $\upsilon_B < 1$ is ensured only in the dirty limit $l_N K < 1$, which is not the case for usual metals.

6.20.3.2 Case (2) $k_{FN} > k_{FS}$

(carrier concentration in N $>$ carrier concentration in S)
then

$$\upsilon_B = \frac{4}{3}\left(\frac{k_{FN}}{k_{FS}}\right)^2 \ell_N K t^{-1}$$

or if

$$t^{-1} = \left(\frac{V_{FN}}{V_{FS}}\right)$$

then

$$\upsilon_{\mathrm{B}} = \frac{4}{3}\left(\frac{n_{\mathrm{N}} m_{\mathrm{S}}^{*}}{n_{\mathrm{s}} m_{\mathrm{N}}^{*}}\right) \ell_{\mathrm{N}} K,$$

where n is carrier concentration and m^{*} is effective mass.

We note that if $\left(\frac{n_{\mathrm{N}} m_{\mathrm{S}}^{*}}{n_{\mathrm{s}} m_{\mathrm{N}}^{*}}\right) \gg 1$ and if $l_{\mathrm{N}} K < 1$, we shall have $\upsilon_{\mathrm{B}} \gg 1$, then F will be strongly discontinuous at the interface and induced superconducting properties in N are much weakened.

6.20.4 (Cuprate -S)/N Interface

The above considerations are sufficient to explain the weak superconductivity induced in Ag layer by YBCO electrodes.

1. Since $\frac{\sigma_{\mathrm{S}}}{\sigma_{\mathrm{N}}} \ll 1$ (Typically $\approx$1)
   $\therefore b \ll K^{-1}$
   (in fact $b < \xi_{\mathrm{s}}$).
   Thus, even without considering the boundary resistance, F is significantly reduced at the interface.
2. $\left(\frac{n_{\mathrm{N}}}{n_{\mathrm{S}}}\right) \approx 10$; $\left(\frac{m_{s}^{*}}{m_{N}^{*}}\right) \approx 4$; $\ell_{\mathrm{N}} K \sim 1$

$$\Rightarrow \upsilon_{\mathrm{B}} \approx 50$$

(the contact is then in Mc Millan limit. Gap induced in N layer is small and $I_{\mathrm{c}} R$ product is small).

There are two ways to remedy the situation, first, using a very dirty normal metal, ensuring both $b > K^{-1}$ and $\nu_{\mathrm{B}} \approx 1$.

This situation may arise in YBCO/Ag/YBCO junction due to inter-diffusion resulting from high temperature treatment, as indeed noticed by Cohen and Polturak [9].

Another more controllable solution is as proposed by Deutscher and Simon [10]. They noticed that problem basically arises due to smaller n_{s}. The solution obviously consists in using a heavily doped semiconductor, such as $\mathrm{SrTiO_3}$ doped with Nb, as used by Van Duzer [11]. Another possibility is to use doped cuprates (such as Pr YBCO), which has a lower carrier concentration and a lower conductivity than YBCO electrode. In both experiments, conditions $b > K^{-1}$ and $\nu_{\mathrm{B}} < 1$ are achieved.

In agreement with proximity effect theory, the critical current is observed to decrease exponentially with d_{N}. The deduced decay length is $\sim$100 Å in agreement with the theory. For $d_{\mathrm{N}} \sim K^{-1}$, the $I_{\mathrm{c}} R$ product approaches the gap. An interesting property of PrYBCO alloy is that it is itself superconducting at $T_{\mathrm{cN}} \approx 40\,\mathrm{K}$. One can then observe the divergence of K^{-1},

$$K^{-1} \propto (T - T_{\mathrm{cN}})^{-1/2}$$

as predicted by theory.

6.21 Grain Boundary Junctions

It is well known that in low T_{c} superconductors (LTSCs), GBs do not play an important role. Situation is quite different in cuprates where GBs behave as Josephson junctions. This is understood as resulting from much smaller ξ, which renders the pair potential sensitive to crystallographic defects on the atomic scale.

The behaviour of GB junctions is not well described by Ambegaoker–Baratoff theory in three respects:

1. $I_{\mathrm{c}}R$ product is, in general, much smaller than the gap.
2. $I_{\mathrm{c}}R$ has an anomalous temperature dependence $I_{\mathrm{c}}R \propto (T_{\mathrm{c}} - T)^2$.
3. $I_{\mathrm{c}}R$ product is not a constant, rather it scales with R.

The physical properties of GB junctions are difficult to establish and may not be universal. Yet, the above three features are apparent quite generally. It has been proposed that these three are related to short coherence length ξ [12]. A direct consequence of short ξ_{S} is that the pair potential is depressed not only at an S/N interface but also at an S/I interface. In this case, equation for b has to be replaced by

$$b = \frac{\xi_{\mathrm{S}}^2(0)}{a},$$

where a = inter-atomic distance.

Since in oxides, $\xi_{\mathrm{S}}(0)/a$ is not much larger than unity, the parameter $b/\xi_{\mathrm{S}}(T)$ that governs the depression of F at the interface is less than one in a significant temperature range near T_{c}. Hence, irrespective of whether the inter-grain material is insulating or metallic, the law

$$I_{\mathrm{c}}R \propto (T_{\mathrm{c}} - T)^2$$

is expected. While for low T_{c} (large ξ) superconductors, this law is characteristic of S–N–S junctions.

The proximity effect approach to the properties of GB junctions also explains the scaling of $I_{\mathrm{c}}R$ product with R.

In the limit where

$$Kd_{\mathrm{N}} < 1 \quad \text{and} \quad (b/\xi_{\mathrm{S}}) < 1.$$

The value of the pair potential at the interface is

$$\Delta_{\mathrm{i}} \propto K^2 d_{\mathrm{N}},$$

from which it follows that in the dirty limit

$$I_c R \propto (\rho_N d_N)^{-1}.$$

Hence,

$$I_c R \propto R^{-1},$$

a behaviour that appears quite universally.

All HTS Josephson devices exhibit properties reminiscent of SNS proximity weak-links with I–V characteristics of resistively shunted junction (RSJ) or flux flow type.

The critical voltage $V_c = I_c R_n$ is of the one to two orders of magnitude lower than that expected from Ambegaokar–Baratoff relation

$$V_c = \frac{\pi\sqrt{\Delta_1 \Delta_2}}{2e}$$

In all useful devices, S electrode/N interface cannot be orthogonal to the c-axis [because Josephson current flows along CuO_2 (i.e. *ab* planes)].

The main categories of potentially useful high T_c Josephson devices are

1. GB junctions artificially nucleated in epitaxial (c-axis) films at defined substrate locations
2. Junctions with artificial barriers
3. Microbridges with a weakened (SIS) type/normalised (SNS) superconductor link

SIS configuration would give quasi-particle I–V characteristics (as due to presence of electronic states within the gap). Such characteristics are unsuitable for device purposes; however, exceptions are Bi (2212) break, and SIN junctions.

6.22 Requirements for Josephson Devices

The under-mentioned requirements should be satisfied:

1. SNS junction with V_c approaching Ambegaokar–Baratoff value $V_c = 0.1$–$1\,\text{mV}$ (at 77 K).
2. Ideally $\frac{L_N}{\xi_N} \approx 1$.
   where L_N is "normal" barrier length and ξ_N coherence length in "N".
3. Since $J_c \propto \exp\left(-\frac{L_N}{\xi_N}\right)$,
   therefore, short barriers are required, which have precisely set L_N.
   L_N should be $\sim 100\,\text{nm}$ for long carrier mean free path l (for metals) and $\sim 1\,\text{nm}$ for short l (for semiconductors).
4. $\nu = \left(\frac{\rho_S \xi_S}{\rho_N \xi_N}\right)$ should be small, where ρ is resistivity in normal state. (This is required by boundary condition at S–N interface, for a maximum V_c).

5. Specific resistance R_B should be zero (ideally) to minimal.
6. A high plasma frequency (requires high J_c, low junction capacitance, low white noise, low $(1/f)$ noise).

For low white noise, ratio of (I_c/I_f) must be high, where noise current

$$I_f = \frac{2\pi kT}{\phi_0}.$$

To maintain the same ratio at 77 K, as used at 4.2 K, an $I_c \sim 20$ times higher is required.

For I_c tolerance to be ±2 %, a very precise control of L_N is required.

A true Josephson junction should meet under-mentioned two simple tests

6.22.1 Small Junctions Free of Self Shielding Effects

Small junctions, free of self shielding effects, i.e. having a width $w < \lambda_J$, the Josephson penetration depth, and should have a spatially uniform J_c.

The uniformity test for J_c is provided by I_c dependence upon a weak magnetic field (in the barrier)

$$I_c(H) = I_{c0}(H/H_0)^{-1} \sin(H/H_0)$$

with

$$H_0 = \phi_0/\{w(L_N + 2\lambda_J)\},$$

when $w/\lambda_J < 1$, I_c(H) dependence is represented by the Fraunhoffer diffraction pattern. A deviation from it indicates current non-uniformity.

6.22.2 Test for the ac Josephson Effect

The second test is the presence of Shapiro steps in I–V characteristics at

$$V_n = (nhf/2e)$$

where f is the frequency of external microwave excitation and $n = 1, 2, 3, \ldots$. In a flux flow weak-link, steps will also be followed at sub-harmonic frequencies.

References

1. A.K. Saxena, *Principles of Modern Physics* (Alpha Science International, Oxford, 2007)
2. J. Mercereau et al., Phys. Rev. Lett. **12**, 274 (1964)
3. A.K. Saxena, *Solid State Physics* (Macmillan, Bangalore, 2006)
4. M. Tinkham, *Introduction to Superconductivity* (McGraw Hill, New Jersey, 1996)
5. J.E. Zimmerman et al., Appl. Phys. Lett. **51**, 617 (1987)
6. T.V. Ramakrishnan, C.N.R. Rao, *Superconductivity Today* (Wiley, New Delhi, 1992)
7. N. Khare, A.K. Gupta, A.K. Saxena, K.K. Verma, O.N. Srivastava, Supercond. Sci. Technol. **7**, 402 (1994)
8. S.V. Subramanyam, E.S.R. Gopal, *High Temperature Superconductors* (Wiley, New Delhi, 1989)
9. D. Cohen, E. Polturak, Phys. Rev. B **41**, 11619 (1990)
10. G. Deutscher, R.W. Simon, J. Appl. Phys. **69**, 4137 (1991)
11. V. Duzer, Appl. Phys. Lett. **58**, 753 (1991)
12. Anonymous, Phys. Rev. Lett. **59**, 1745 (1987)

Chapter 7
Theories of Superconductivity

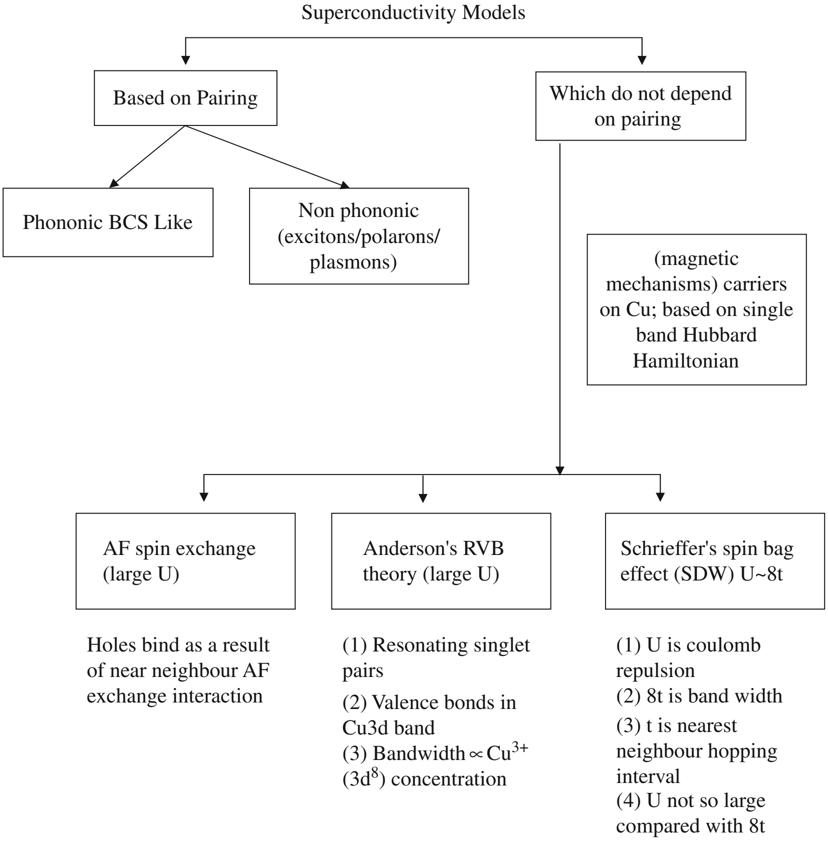

Note: In the limit $U \rightarrow \infty$, charge transfer interaction governs the creation of holes in oxygen band, which is fundamental to the mechanism leading to high T_c.

A. K. Saxena, *High-Temperature Superconductors,* Springer Series in Materials Science 125, DOI: 10.1007/978-3-642-28481-6_7,

7.1 Microscopic Theory of Superconductivity (The BCS Theory)

Theoretical understanding of the phenomenon of superconductivity came more than 50 years after its discovery. A famous comprehensive microscopic theory of superconductivity was developed by Barden, Cooper and Schrieffer in 1957 [1], named as BCS theory. It has also amazingly good quantitative success in explaining several important parameters characterising the superconducting behaviour in materials. Prior to the BCS theory, it had been suggested by several physicists that lattice valuations of the material might play an important part in superconductivity. It becomes evident from the following developments, which took place before the advent of the BCS theory:

(1) The first experimental evidence was due to Maxwell of University of Washington and Reynolds of Rutgers University, New Jersey. They showed that if the atomic weight of mercury is changed by substituting a different isotope, then the critical temperature changed. This seemed to indicate that changing the mass of mercury altered the frequency of lattice vibrations. An ion with a lighter nucleus would vibrate faster than an ion, with a heavier nucleus.
(2) Frohlich (University of Liverpool) predicted that the lattice vibrations could yield an attractive interaction between electrons:

Imagine an electron moving through a lattice of positive ions. It will pull positive ions towards itself. But ions are heavy, moving more slowly than the electron, so they do not relax back to their normal positions as soon as the electron has passed by. Thus, the electron produces a wake, which manifests itself as a tube of enhanced positive charge. This tube may attract a second electron, so that the pair then moves along in convoy. The two electrons need not be near to each other, so they do not feel each other's repulsive electrical interaction.

It was followed by an important concept inferred by experiments of Brian Pippard of Cambridge University in 1953.

(3) Superconducting electrons behave in a rigid way over a length of about a micrometer, called by pippard, the coherence length. The behaviour is rigid in the sense that, if you give the electrons a push at one point, (by applying an external force, say an electric field), they all move in the same direction and at the same speed up to a distance of about a micrometer from where you apply a force.
(4) Blatt and Schaffroth (University of Sidney, Australia) showed that a gas of bosons each with an electric charge, undergoing Bose–Einstein condensation would show the Meissner effect. They postulated electrons bound together in pairs. There was a snag, however, in this for bosons (pairs) to be independent entities (i.e. spatially well separated), the binding energy (inversely related to boson size) would be prohibitively large, producing a large energy gap.
(5) Leon Cooper of University of Urbana, in 1956, suggested the famous superconducting electron pair, incorporating all the above mentioned ideas. He showed that if two electrons interact via lattice vibrations, they tend to stick together to form a bound state with their spins in the opposite direction. The presence

of other electrons does not prevent the formation of pairs, as the long range Coulomb repulsion between two electrons is largely suppressed by screening due to strong correlation effects of the other electrons. The pairing does not require non-overlapping bound state of Blatt and Schaffroth. Cooper thought that coherence length is the same as the size of the pair and energy gap corresponds to the binding energy of the pair.

7.1.1 Qualitative Ideas

Later, in 1957, Bardeen Cooper and Schrieffer put forward their microscopic theory, whose main points are as follows:

(a) The electron–lattice interaction leads to an electron–electron interaction and electrons form bound pairs in the superconducting state.
(b) The electron–electron interaction is mediated by the exchange of virtual phonons between two electrons of a pair.
(c) The pairing is such that an electron with spin-up and momentum $\vec{k}$ is paired with one of spin-down and momentum $-\vec{k}$ and that the angular momentum of the pair is zero.
(d) The coherence length is the same as the size of the pair, and energy gap observed corresponds to binding energy of the pair.

Consider a metal with conduction electrons inside the Fermi sphere. Suppose two electrons (labelled 1 and 2) lie just inside the Fermi surface. If they form a bound pair, their motion is correlated, provided they are close to the Fermi surface. The pair formation leads to the condensation (Bose–Einstein condensation) of all electrons in the vicinity of Fermi surface into a sea of Copper pairs.

Let us now consider how the attraction is brought about in the first place. Since the electron 1 is near the Fermi surface, its speed is great (=Fermi velocity). As it passes by the positive ions, the ions being heavy, respond rather slowly. By the time the ions feel and completely respond to the electron 1, it leaves its initial region, at least partially, stimulating an overcompensation (Fig. 7.1a). In the language of field theory, due to lattice distortion (caused by electron scattering), a virtual phonon is created, i.e. each electron is surrounded by a phonon cloud and the electrons 1 and 2 interact by the exchange of a phonon (Fig. 7.1b).

The phonon of momentum q, emitted by electron 1, is absorbed by the electron 2. As a result, the electrons 1 and 2 acquire momenta $(k_1 - q)$ and $(k_2 + q)$, respectively. This interaction is strongest, when the two electrons 1 and 2 have opposite momenta and opposite spins.

$$\vec{k}_1 = \vec{k}_\uparrow,$$
$$\vec{k}_2 = -\vec{k}_\downarrow.$$

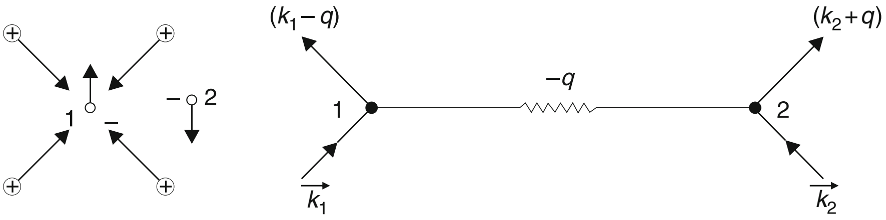

Fig. 7.1 **a**The electron–electron interaction, **b** the phonon-mediated pairing

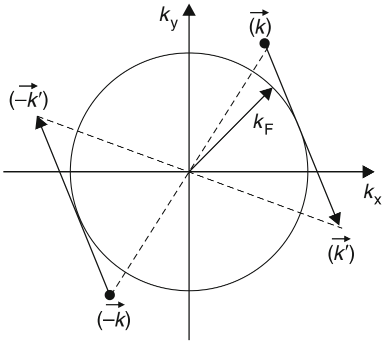

Fig. 7.2 k-space representation of the scattering of an electron pair from $(k, -k)$ to the state $(k', -k')$

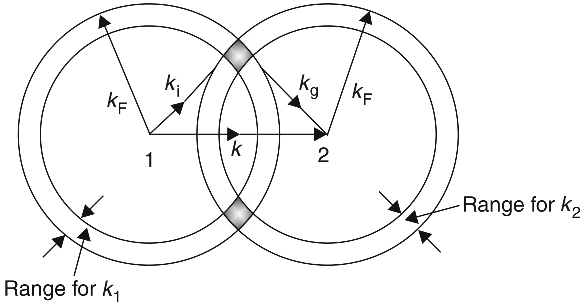

Fig. 7.3 Two shells of radius k_F and thickness Δk. All pairs of momenta $k_i,\ k_j$ satisfy $k_i + k_j = k$

The availability of phonons is restricted to a small energy range $\hbar\omega_D = k_B\theta_D$ (Fig. 7.3), where ω_D is the Debye frequency and θ_D, the Debye temperature. The interaction is attractive if the energy difference is

$$e_{k1} - e_{k2} = \hbar\omega_D.$$

The pair of two electrons is chosen, so that there is a maximum possibility of transition from any one pair state to all other pair states without any change in the total momentum

$$(\vec{k}_1 + \vec{k}_2) = (\vec{k}'_1 + \vec{k}'_2) = \cdots = \vec{k},$$

that is constant momentum for each pair. In the ground state, maximum overlap of phase with largest number of possible transitions is achieved when $\vec{k} = 0$, i.e. when electrons forming a pair have equal and opposite momenta ($\vec{k}$ and $-\vec{k}$) (see Fig. 7.2). A detailed consideration shows that energetically, it is most favourable to restrict the pairing of electrons of opposite spins, i.e. $\left(\vec{k}\uparrow, -\vec{k}\downarrow\right)$.

The energy of pairs is lower than the total energy of free electrons. As a result, a gap is formed near the Fermi energy, which is approximately given by

$$2\Delta = 3.52\, k_{\mathrm{B}} T_{\mathrm{c}},$$

where k_{B} is Boltzmann constant and T_{c} the critical temperature.

Below T_{c}, the energy gap parameter 2Δ rises steeply from zero, accordingly

$$2\Delta(T) \cong 3.52\, k_{\mathrm{B}} T_{\mathrm{c}} (1 - T/T_{\mathrm{c}})^{1/2}.$$

For $0 < T < T_{\mathrm{c}}$, the pairs are continually being scattered by lattice vibrations. But, since the pair assembly involves a high degree of correlation in their motion, the net momentum is always conserved. Therefore, when an electric field is applied, no momentum is transferred from the moving pairs to the lattice and lattice periodicity has no influence on the electron pairs. Therefore, the wave function is not localised, but has infinite extent. The wave function is given by

$$\Psi_{\mathrm{G}} = \Psi\,(r_1,\ r_2)\,\Psi\,(r_3,\ r_4) \cdots\ \Psi(r_{n_{\mathrm{s}-1}},\ r_{n_{\mathrm{s}}}),$$

where n_{s} = number of super electrons and number of pairs = $n_{\mathrm{s}}/2$. All the pairs have the same wavefunction

$$\Psi(r',\ r'') = \sqrt{n_{\mathrm{s}}}\, e^{iS(r)},$$

where the phase function $S(r)$ characterises the coherent state.

The super-electrons (i.e. pairs) provide lossless current, and the superconducting state offers no electrical resistance, as the normal electrons, though present, cannot carry any current as they are shorted out by the super-electrons (pairs).

7.1.2 The BCS Ground State

A weak attractive interaction, resulting from electron–phonon interaction leads to the formation of Cooper pairs. A single pair formation leads to an energy reduction of the Fermi sea. The new ground state of the Fermi sea (after Cooper-pair formation) is achieved through a complicated interaction between the electrons. The total energy reduction is not given by simply summing the contributions of single pairs because the effect of each single pair depends on those already present. Thus, we require the minimum total energy of the whole system for all possible pair configurations taking into account the kinetic one-electron component and the energy reduction due to “pair-collisions”, i.e. the electron–phonon interaction. The kinetic component is given by

$$E_{\text{kin}} = 2\sum_{k'} w_{k'}\xi_{k'},$$

where

$$\xi = \frac{\hbar^2 k^2}{2m} - E_{\text{F}}^0, \tag{7.1}$$

w_k is the probability that the pair state $(\vec{k}\uparrow, -\vec{k}\downarrow)$ is occupied and $E_{\text{F}}^0 = E_{\text{F}}(T = 0°\text{K})$.

The total energy reduction due to the pair collisions $(\vec{k}\uparrow, -\vec{k}\downarrow) \leftrightharpoons (\vec{k'}\uparrow, -\vec{k'}\downarrow)$ can be calculated via the Hamiltonian H, which explicitly takes account of the fact that the annihilation of a pair $(\vec{k}\uparrow, -\vec{k}\downarrow)$ and the simultaneous creation of a pair $(\vec{k'}\uparrow, -\vec{k'}\downarrow)$ leads to an energy reduction of

$$V'_{kk} = \int V(\vec{r})e^{(\vec{k}-\vec{k'})\cdot\vec{r}}d^3\vec{r}\,. \tag{7.2}$$

Since a pair state $\vec{k}$ can be either occupied or unoccupied, we choose a representation of two representative orthogonal states $|\,1\rangle_k$ and $|\,0\rangle_k$ corresponding to occupied and unoccupied states respectively. The most general state of the pair $\left(\vec{k}\uparrow, \vec{k}\downarrow\right)$ is, thus, given by

$$|\,\psi\rangle_k = u_k\,|\,0\rangle_k + v_k\,|\,1\rangle_k. \tag{7.3}$$

Hence, $w_k = v_k^2$ and $1 - w_k = u_k^2$ are the probabilities that the pair state is occupied and unoccupied, respectively. In the representation (7.3), the ground state of the many-body system of all Cooper pairs is given by

$$|\,\psi_{\text{BCS}}\rangle_k = \underset{k}{\pi}(u_k\,|\,0\,\rangle_k + v_k\,|\,1\rangle_k). \tag{7.4}$$

(Note that interactions between the pairs are neglected).

In the two-dimensional representation,

$$|0\rangle_k = \begin{pmatrix}0\\1\end{pmatrix}_k; \qquad |1\rangle_k = \begin{pmatrix}1\\0\end{pmatrix}_k \tag{7.5}$$

we use the Pauli spin matrices

$$\sigma_k^{(1)} = \begin{pmatrix} 0 & 1 \\ 1 & 0 \end{pmatrix}_k ; \quad \sigma_k^{(2)} = \begin{pmatrix} 0 & -i \\ i & 0 \end{pmatrix}_k \tag{7.6}$$

to describe the creation and annihilation of a Cooper pair by operators

$$\sigma_k^{+} = \frac{1}{2}\left(\sigma_k^{(1)} + i\sigma_k^{(2)}\right), \quad \sigma_k^{-} = \frac{1}{2}\left(\sigma_k^{(1)} - i\sigma_k^{(2)}\right) \tag{7.7}$$

respectively. σ_k^{+} transforms the state $\mid 0\rangle_k$ into $\mid 1\rangle_k$ and σ_k^{-} transforms the state $\mid 1\rangle_k$ into $\mid 0\rangle_k$. Further,

$$\begin{aligned} \sigma_k^{+} \mid 1\rangle_k = 0, \quad \sigma_k^{+} \mid 0\rangle_k = \mid 1\rangle_k \\ \sigma_k^{-} \mid 1\rangle_k = \mid 0\rangle_k, \quad \sigma_k^{-} \mid 0\rangle_k = 0. \end{aligned} \tag{7.8}$$

Scattering from $(\vec{k}_{\uparrow}, -\vec{k}_{\downarrow})$ to $(\vec{k}_{\uparrow}, -\vec{k'}_{\downarrow})$ is associated with an energy reduction by $\mathrm{V}_{kk'}$. In the BCS model, this interaction matrix element is assumed to be a constant, which was designated as V_0/L^3 The scattering process in two-dimensions is represented as annihilation of $\vec{k}$ and creation of $\vec{k'}$. The operator that describes the corresponding energy reduction is $-(V_0/L^3)\ \sigma_{k'}^{+}\sigma_k^{-}$. The total energy reduction due to pair collision $\vec{k} \rightarrow \vec{k'}$ and $\vec{k'} \rightarrow \vec{k}$ is expressed by the operator

$$H = -\frac{V_0}{L^3}\sum_{kk'}\frac{1}{2}(\sigma_{k'}^{+}\sigma_k^{-} + \sigma_k^{+}\sigma_{k'}^{-}) = \frac{-V_0}{L^3}\sum_{kk'}\sigma_k^{+}\sigma_{k'}^{-}. \tag{7.9}$$

Since V_0 is restricted to the shell $\pm\hbar\omega_{\mathrm{D}}$ (around E_{F}^0), the sum includes only pair states in this shell (the *rhs* follows by exchanging the indices k and k', since scattering takes place both ways).

From perturbation theory, the energy reduction due to collisions is given by

$$\begin{aligned} &\langle\psi_{\mathrm{BCS}}\,|H|\,\psi_{\mathrm{BCS}}\rangle \\ &= -\frac{V_0}{L^3}\left\{\prod_x \left(u_{xy}\,\langle 0\mid + \nu_{xx}\,\langle 1\mid\right)\sum_{kk'}\sigma_k^{+}\sigma_k^{-}\ \prod_y\ \left(u_y\,|0\ \rangle_y + \nu_y \mid 1\rangle_y\right)\right\} \end{aligned} \tag{7.10}$$

In evaluating this, it is to be noted that the operator $\sigma_k^{+}\ \left(\sigma_k^{-}\right)$ operates only on $\mid 1\rangle_k$ $(\mid 0\rangle_k)$. Further,

$${}_k\langle 1\mid 1\rangle_k\ =\ 1, \quad {}_k\langle 0\mid 0\rangle_k\ =\ 1, \quad {}_k\langle 1\mid 0\rangle_k\ =\ 0.$$

Thus,

$$\langle \psi_{\mathrm{BCS}} \left| H \right| \psi_{\mathrm{BCS}} \rangle = -\frac{V_0}{L^3} \sum_{kk'} \nu_k v_k, u_k u_{k'}. \tag{7.11}$$

Hence, the total energy of the system of Copper pairs is obtained by adding (7.1) and (7.11)

$$W_{\mathrm{BCS}} = 2 \sum_k v_k^2 \xi_k - \frac{V_0}{L^3} \sum_{kk'} v_k u_k v_{k'} u_{k'}. \tag{7.12}$$

The BCS ground state (i.e. at $T = 0\,\mathrm{K}$) is given by minimising W_{BCS} with respect to amplitudes u_k and $v_k (w_k = v_k^2; 1 - w_k = u_k^2)$, as

$$\nu_k = \sqrt{w_k} = \cos\theta_k \tag{7.13}$$

$$\begin{aligned}
u_k &= \sqrt{1 - w_k} = \sin\theta_k \\
&\Rightarrow u_k^2 + \nu_k^2 = 1, \\
&\Rightarrow W_{\mathrm{BCS}} = \sum_k 2\xi_k \cos^2\theta_k - \frac{V_0}{L^3} \sum_{kk'} \cos\theta_k \sin\theta_{k'} \cos\theta_{k'} \sin\theta_k \\
&= \sum_k 2\xi_k \cos^2\theta_k - \frac{1}{4}\frac{V_0}{L^3} \sum_{kk'} \sin 2\theta_k \sin 2\theta_{k'}.
\end{aligned} \tag{7.14}$$

This is to be minimised with respect to θ_k

$$\Rightarrow \frac{\partial W_{\mathrm{BCS}}}{\partial \theta_k} = 0 \tag{7.15}$$

or

$$-2\xi_k \sin 2\theta_k - \frac{V_0}{L^3} \sum_{k'} \cos 2\theta_k \sin 2\theta_{k'} = 0 \Rightarrow \xi_k \tan 2\theta_k = -\frac{1}{2}\frac{V_0}{L^3} \sum_{k'} \sin 2\theta_{k'}. \tag{7.16}$$

We get

$$\Delta = \frac{V_0}{L^3} \sum_{k'} u_{k'} v_{k'} = \frac{V_0}{L^3} \sum_{k'} \sin\theta_{k'} \cos\theta_{k'} \tag{7.17}$$

and

$$E_k = \sqrt{\xi_k^2 + \Delta^2}. \tag{7.18}$$

From trigonometry:

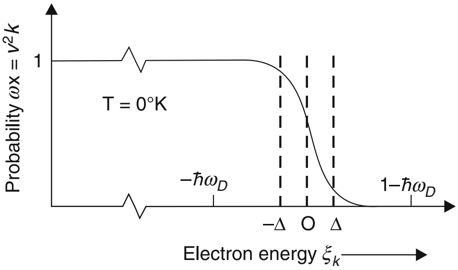

Fig. 7.4 The BCS occupation probability v_k^2 for Cooper pairs in the vicinity of Fermi energy E_F^0, $\left(\xi_k = E(k) - E_F^0\right)$ [2]

$$\frac{\sin 2\theta_k}{\cos 2\theta_k} = \tan 2\theta_k = \frac{-\Delta}{\xi_k}, \tag{7.19}$$

$$2u_k \nu_k = \sin 2\theta_k = \frac{\Delta}{E_k}, \tag{7.20}$$

$$\nu_k^2 - u_k^2 = -\frac{\xi_k}{E_k}. \tag{7.21}$$

Thus, the occupation probability of a pair state $(\vec{k}\uparrow, -\vec{k}\downarrow)$ in the BCS ground state is given by

$$w_k = v_k^2 = \frac{1}{2}\left(1 - \frac{\xi_k}{E_k}\right) = \frac{1}{2}\left(1 - \frac{\xi_k}{\sqrt{\xi_k^2 + \Delta^2}}\right). \tag{7.22}$$

This function is plotted in Fig. 7.4. It has a form similar to the Fermi distribution at the finite critical temperature T_c. Note that Cooper pairs, which contribute to the energy reduction of the ground state, are from a particular k-region, viz. energy shell of $\pm\Delta$ around the Fermi surface.

From (7.12), (7.17) and (7.22), we get

$$W_{\mathrm{BCS}}^0 = \sum_k \xi_k \left(1 - \frac{\xi_k}{E_k}\right) - L^3 \frac{\Delta^2}{V_0} \tag{7.23}$$

as the energy of the superconducting BCS ground state.

It can be proved that

$$\Delta = \left(W_{\mathrm{BCS}}^1 - W_{\mathrm{BCS}}^0\right) = 2E_k' = 2\sqrt{\xi_{k'}^2 + \Delta^2}. \tag{7.24}$$

$\xi_{k'}^2$ describes the kinetic energy of the two electrons scattered out of the Cooper pair. Since $\xi_{k'} = \left(\hbar^2 k'^2/2m\right) - E_F^0$, this will be very small. So, the excitation requires a minimum finite energy 2Δ (i.e. the energy to break up a Cooper pair). We now try to determine Δ. For this, we combine (7.20) with (7.17) and (7.18). From (7.17),

$$\Delta = \frac{V_0}{L^3}\frac{1}{2}\sum_k 2u_k\nu_k.$$

or

$$\Delta = \frac{1}{2}\frac{V_0}{L^3}\sum_k \frac{\Delta}{\mathrm{E}_k} = \frac{1}{2}\frac{V_0}{L^3}\sum_k \frac{\Delta}{\sqrt{\xi_k^2+\Delta^2}}. \tag{7.25}$$

We can replace the sum over k by an integral as

$$L^{-3}\sum_k \rightarrow \frac{1}{(2\pi)^3}\int dk. \tag{7.26}$$

Further, the integral over k-space can be split into an integral over the Fermi sphere and the energy ξ as

$$1 = \frac{V_0}{(2\pi)^3}\iint \frac{\mathrm{d}S_\xi}{\left|\mathrm{grad}_k^\xi(k)\right|}\frac{\mathrm{d}\xi}{\sqrt{\xi^2+\Delta^2}}. \tag{7.27}$$

The first integral (over S_ξ) can be considered as constant and equals density of states. It is to be noted that the pair density of states $Z(E_\mathrm{F}^0+\xi) \equiv \frac{1}{2}D\,(E_\mathrm{F}^0+\xi)$, where D is single-particle density of states; further, ξ lies in the interval $-\hbar\omega_\mathrm{D} \le \xi \le \hbar\omega_\mathrm{D}$.

Hence,

$$1 = \frac{V_0}{2}\int_{-\hbar\omega_\mathrm{D}}^{\hbar\omega_\mathrm{D}} \frac{Z(E_\mathrm{F}^0+\xi)}{\sqrt{\xi^2+\Delta^2}}d\xi. \tag{7.28}$$

In the region $\left(E_\mathrm{F}^0-\hbar\omega_\mathrm{D}\right)$ to $\left(E_\mathrm{F}^0+\hbar\omega_\mathrm{D}\right)$, where V_0 does not vanish, $Z\left(E_\mathrm{F}^0+\xi\right)$ varies only slightly and we can take

$$Z(E_\mathrm{F}^0+\xi) \cong Z(E_\mathrm{F}^0)$$

and due to symmetry

$$\frac{1}{V_0 Z\left(E_\mathrm{F}^0\right)} = \int_0^{\hbar\omega_\mathrm{D}} \frac{d\xi}{\sqrt{\xi^2+\Delta^2}} \tag{7.29}$$

or

$$\frac{1}{V_0 Z(E_\mathrm{F}^0)} = \sin h^{-1}\left(\frac{\hbar\omega_\mathrm{D}}{\Delta}\right)$$

or

$$\Delta = \frac{\hbar\omega_{\mathrm{D}}}{\sin\, h\left[\frac{1}{V_0 Z(E_{\mathrm{F}}^0)}\right]} \approx 2\hbar\omega_{\mathrm{D}} \exp\left[-\frac{1}{V_0 Z(E_{\mathrm{F}}^0)}\right]. \tag{7.30}$$

(Since, in the weak coupling limit, $\left(V_0 Z\left(E_{\mathrm{F}}^0\right) \ll 1\right)$.

7.2 Anderson's Resonating Valence Bond Theory

The very need to formulate a theory different from BCS theory arises from the experimentally observed properties of the cuprate superconductors. In the cuprate superconductors, experimental evidences indicate that the normal state is not a Fermi liquid. This fact invalidates the basis of the standard BCS theory for HTSCs and, as a result, there arises a need for a different formalism.

Hall measurements and flux quantisation experiments confirm the existence of pairs of charge $+2e$ in the superconducting state. The basic hypothesis, which forms the starting point of the R V B pairing theory is that the physics of these materials is the physics of doped Mott insulators. The same repulsive interaction between the electrons, which causes the undoped parent compound to be a Mott insulator, and hence, anti-ferromagnet are also responsible for the unusual normal state, which develops a superconducting instability at low enough temperatures.

7.2.1 Anderson's Valence Bonds

The copper $d_{x^2-y^2}$ level hybridises strongly with four of the oxygen $2p$ orbital pointing towards the copper atom (There are two oxygen $2p$ orbitals and one copper $d_{x^2-y^2}$ orbital per unit cell (Fig. 7.5)).

We have a simple tight bounding model made up of $\mathrm{O}(2p)$ and $\mathrm{Cu}(d_{x^2-y^2})$ orbitals. In the insulator, there are five electrons per unit cell. This tight bonding model, in which the only non-zero hopping matrix element t_{dp} is between the copper orbital (energy $\in_{\mathrm{d}}$) and the neighbouring oxygen orbital (energy $\in_{\mathrm{p}}$), is easily solved to get the dispersion relation

$$\begin{aligned} \in_{k\pm} &= -\left(\frac{\in_{\mathrm{d}} - \in_{\mathrm{p}}}{2}\right) \pm \frac{1}{2}\left[(\in_{\mathrm{d}} - \in_{\mathrm{p}})^2 + 8t^2(1 + \cos k_x a + \cos k_y a)\right]^{\frac{1}{2}}, \\ \in_{k0} &= 0. \end{aligned}$$

The subscripts ± and 0 denote anti-bonding, bonding and non-bonding band respectively. We have three orbitals per unit cell and three bands (Fig. 7.6).

Fig. 7.5 Copper $d_{x^2-y^2}$ orbital hybridising with oxygen 2p orbitals

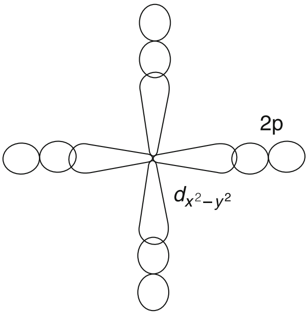

Fig. 7.6 Antibonding, bonding and Non-bonding bands due to tight bonding model

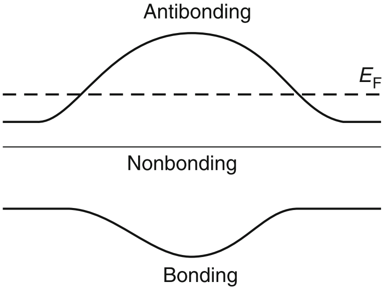

We have five electrons per unit cell. The Fermi level lies in the middle of the anti-bonding band. Anderson argued that the top (viz. anti-bonding) band is sufficient to understand the magnetic, transport and statistical properties of the insulator.

Any excitation involving charge transfer needs an energy $\sim(U - zt)$, where z is coordination number (5 or 6) and t, the hopping integral ($\approx 0.5\,\text{eV}$). This is called Mott Hubbard gap. This gap arises not because of any periodic (self consistent or external) potential, rather it is a genuine many body effect, which escapes explanation even in terms of very sophisticated density functional band theories. The Hamiltonian governing such a system (the planar Hubbard Hamiltonian) is

$$H = -t \sum_{ij} (c_{i\sigma}^{+} c_{j\sigma} + \text{h.c.}) + U \sum n_{i\uparrow} n_{i\downarrow} - \mu \sum n_{i\sigma},$$

where c_i^{+} creates an electron at site i

t is hopping integral
U is onsite Coulomb repulsion between two electrons
μ is chemical potential
(h.c. → hermitian conjugate)

The first term describes hopping of holes between neighbouring sites (ij), the second term is a Coulomb repulsion term between a spin-up and spin-down hole on the same site i, ($n_{i\sigma}$ is number operator of a hole at i with spin σ). The spin configuration with anti-ferromagnetic arrangement can be described by Hamiltonian

Fig. 7.7 A typical configuration of valence bonds at $T = 0$. This corresponds to vacuum state

$$H_{\mathrm{spin}} = \mathrm{J} \sum_{\langle \mathrm{i,j} \rangle} \vec{S}_{\mathrm{i}} \cdot \vec{S}_{\mathrm{j}} \ (J > 0)\,.$$

J is magnetic moment and there is long range order. $\vec{S}$ is vector operator for spin 1/2. The sum runs over nearest neighbour sites i, j of the copper lattice. This long range ordered state of A.F. spins on copper is very close in energy to a spin configuration without long range order but with neighbouring spins (i and j), paired in a singlet state. These singlet "dimer" (a two component object) are called "valence bonds" by Anderson (Fig. 7.7).

In two-dimensions, these singlets (in form of pairs) can be obtained by operating the vacuum state with operator

$$b_{ij}^{+} = \frac{1}{\sqrt{2}} \left(c_{i\uparrow}^{+} c_{j\downarrow}^{+} - c_{i\downarrow}^{+} c_{j\uparrow}^{+} \right).$$

The equation for H_{spin} implies a non-ordered spin configuration for paired states. This is expected to form a triangular lattice. But since, on a triangle, alternating spin arrangement (of single spins) is not possible, i.e. two neighbouring spins will be parallel, if they do form a triangle, which is unfavourable. This leads to situation of frustration.

1. Since copper lattice is a square, frustration is not a necessity
2. Heisenberg model (for H_{spin}) is not an accurate description of localised charges on Cu-sites, a better description is obtained with planar Hubbard Hamiltonian:

$$H_{\mathrm{charge}} = -t \sum_{\langle i,j \rangle \sigma} \left(c_{i\sigma}^{+} c_{j\sigma} \right) + U \sum_{i} n_{i\uparrow} n_{i\downarrow}.$$

For $|t| \ll U$ and near half-filling (Fig. 7.8), the physics described by H_{charge} is same as that by H_{spin}. In fact, a canonical transformation of the form

$$e^{\mathrm{s}} H_{\mathrm{charge}} e^{-\mathrm{s}}$$

produces (along with other terms), H spin with $J = 4t^2/U$.

Next near neighbour frustration terms destroy a possible AF long range order, which can also be caused by lattice distortions (by metal impurities or surplus oxygen corresponding to $x > 0$).

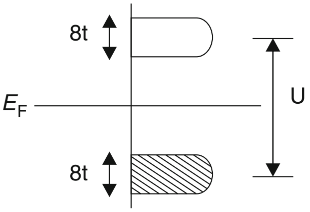

Fig. 7.8 Energy bands of Hubbard model for strong repulsion and half filling

Since an AF square lattice may be subdivided into two sub-lattices (all ↑) and (all ↓), there is an enormous number of configurations in which up and down spins, (not only neighbours) are paired into singlets. For the ground state superconducting, linear combinations of all the singlet configurations may be considered. This leads to *Anderson's resonating valence bonds* (RVBs). This expresses the fact that in a valence bond cycle, one configuration may switch to another, and back again (Fig. 7.9). After having described a ground state, appropriate excitations leading to conduction and superconductivity are necessary for consideration.

According to Anderson, two types of excitations may be generated on top of the R V B ground state:

(1) Neutral (spin 1/2) spinons (Fermions) and
(2) Charged (spinless) holons (Bosons),

i.e.

(1) A broken singlet bond excitation gives rise to two spin 1/2 objects, i.e. zero charge spin half fermions called *spinons* (Fig. 7.10a) (2Δ is the minimum energy to break a singlet pair; this implies a linear term in specific heat of superconducting state).
(2) The second kind of excitation is termed *holons*. A holon represents an unoccupied non-bonded site of charge +*e* and zero spin (Fig. 7.10b). Holons are bosons and are created by extraneous p-type doping. Holons give the Bose condensate at T_c (if is not a Fermi liquid).

A spinon does not require the introduction of additional charges. It is just an isolated unpaired spin σ (up or down), which is essential in a purely ionic approximation and is just a $\mathrm{Cu}_{\sigma}^{2+}$. The single spin may break up a neighbouring valence bond and pair up with one of the former partners of the valence bond, i.e. a spinon can freely move through the copper lattice. A spinon (a spin 1/2 fermion) fills up the lowest energy states defining pseudo Fermi energy.

A holon is a single charge $(+e)$ on a Cu site $\left(\mathrm{Cu}^{+3}\right)$ (Excess charges are introduced into the lattice, either by doping or by having excess oxygen).

In an ionic approximation, a hole reacts with a spinon to give a holon

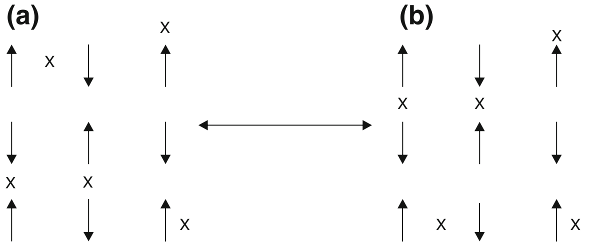

Fig. 7.9 Nearest neighbour valence bonds (marked by *crosses*). A valence bond cycle in one configuration may switch, leading to another configuration and back again

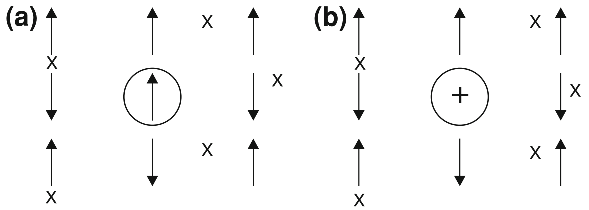

Fig. 7.10 Unpaired spin or "Spinon" Cu^{2+} (**a**), and excess hole or "holon" $\mathrm{Cu}^{3+}_{\uparrow\downarrow}$ (**b**), in a valence bond configuration

$$\begin{array}{ccccc} \mathrm{Cu}^{2+}_{\sigma} & + & \text{hole} & \Longrightarrow & \mathrm{Cu}^{3+} \\ \begin{bmatrix}\text{(Spinon, spin œ)}\\ \text{A copper } d^9 \text{ spin}\end{bmatrix} & & \begin{bmatrix}\text{(fermion,}\\ \text{spin } -\sigma)\end{bmatrix} & & \begin{bmatrix}\text{Holon,}\\ \text{spinless Boson}\end{bmatrix}\end{array}$$

In contradistinction to spinons, holons may pile up in a given state. In particular, at $T = 0$, they may all condense into the zero momentum state (Bose–Einstein condensation).

The above equation shows that a spinon and a holon interact by the exchange of a hole. This relation may be viewed as "supersymmetry", grouping spinon and holon into "superpartners". It is this interaction, which according to Anderson, is responsible for the linear temperature dependence of resistivity ($\rho \propto T$). The argument is as follows:

Scattering among Fermions leads to a T^2- law at low temperatures, but in fermion–boson scattering, the Pauli principle is inoperative, which lower the power of T by one.

Thus, a copper d^9 spin (=1/2) and hole of opposite spin (=1/2) are strongly coupled to form a singlet. This composite-singlet (a holon) may be thought of as a spin-less hole in the Hubbard band. Thus, as first pointed out by Zhang and Rice, the more realistic two band (oxygen-p, Copper d-band) model reduces, in the limit of low doping, to a one band Hubbard model.

Depending on the spin pairing amplitudes and relative phases, there may be various spin liquid possibilities, such as the uniform R V B phase, the spiral, chiral and flux phases. For these various spin liquid possibilities (as proposed by different theoreticians), the common strategy is to look for a possible spin liquid solution, which describes the actual ground state in the presence of holes.

7.3 Spin-Bag Theory

It was introduced by Schrieffer [4]. In this theory, pairing is due to a local reduction of the anti-ferromagnetic order parameter. In the anti-ferromagnetic insulator, with long range spin-order, the spin-bag represents a local decrease in the spin density wave gap $2\Delta_{\mathrm{SDW}}$ over a region of size ξ. In addition, the bag causes a twist of the spin quantisation axis. In the case of large self exchange energy, the spin-bag corresponds to a decrease in the near neighbour spin order $\langle \vec{S}_j \cdot \vec{S}_{j+1} \rangle$ around the hole with S_j^2 being nearly fixed. This region of decreased spin order and spin twist is co-moving with the hole and forms "bag" inside of which, the hole lives. The outward uncertainty principle pressure of the hole is balanced by the inward pressure of anti-ferromagnetism. The combination of spin amplitude (longitudinal) and spin twist (transverse) dynamics leads to bags and their attractive interaction.

7.3.1 Questions Which Remain

1. Existence or not of gaps on the Fermi surface (related to s, p or d type superconductivity)
2. Whether we have k-space pairing or real space pairing (related to short ξ compared with ξ_{BCS})
3. Whether we have strong coupling or a BCS like theory ($T_{\mathrm{c}}/T_{\mathrm{F}} \ll 1$ for weak coupling, but in fact $T_{\mathrm{c}}/T_{\mathrm{F}} \gg 1$).

7.4 Anyonic Theory

In March 1990, Lyons [5] of AT & T Bell Labs proposed that 'anyons' might be responsible for the high $\mathrm{T_c}$ superconductivity. Anyons [6], the strange pseudo-particles that exist only in two dimensions, are best understood with reference to fermions and bosons, the two types of particles that are possible in a three dimensional world. No system can have two fermions occupying exactly the same quantum state. On the other hand, bosons prefer to be in the same quantum state as the rest of their fellows. Anyons lie somewhere in between fermions and bosons. Lyons described his experiments conducted at Bell Labs where he bounced polarized light off Y123 single crystals and Bi2212 single crystals. The polarized light was changed when reflected. This normally can occur only when a material has an internal magnetic field. Since superconductors are normally expected to push away magnetic field, the implication behind the lack of symmetry in the reflected light is that anyons are responsible for high T_c superconductivity. Lyons also checked his findings by heating the Y123 sample to reduce its oxygen content, thereby removing superconducting properties. This time when the polarized laser light was once again shined on the sample, the light did not change upon reflection.

7.5 In High T_c Superconductor, Is the Coupling s-Wave or d-Wave?

Different theories which have tried to explain the mechanism for superconductivity in cuprates may not agree on much, but they all do believe that it involves the coupling of electrons/holes of opposite spin. But paths quickly diverge when it comes to the angular momentum of the pair: is it a BCS like s-wave (with $l = 0$) or a d-wave (or some thing else). (The answer would be linked to the mechanism that couples the electrons). Experiments in past have revealed that the pairing state is at least not isotropic. Now, how does the angular momentum of the paired state manifest itself? For one it determines the wave vector dependence of the energy gap that develops at the Fermi surface when a substance goes superconducting. If the electrons were paired in an ideal s-wave, the energy gap would have the same value at all points on the Fermi surface. But it the electron-pairs have a form of d-wave pairing called d_{x2-y2}, the shape of the gap in k-space resembles a four-leaf clover and is described by the function $\cos(k_x a)$-$\cos(k_y a)$ (or in real space, by x^2-y^2 for points (x, y) on a circle). For d_{x2-y2} wave pairing, the superconducting gap is positive in some directions and negative in others in k-space, and it goes through zeros in between. Consequently, there should be appearance of "nodes in the gap". There may be other forms of anisotropic pairing states, but they do not necessarily have nodes. Evidence of anisotropic pairing come from NMR measurements, angle resolved photo emission and measurements of the microwave penetration depth in a crystal. The NMR experiments have revealed that the behaviour of HTSCs is consistent with the predictions of some d_{x2-y2} pairing models [7].

If electrons pair in a d_{x2-y2} wave, theory predicts that the microwave penetration depth will vary linearly with temperature. When the Vancouver group [8] plotted the changes in penetration depth for four YBCO samples as a function of temperature from 1.3 to 20 K, the points fit a straight line (Fig. 7.11), the dependence expected for a d_{x2-y2}wave-gap. But the scenario was complicated by the measurements made by a group at the University of Maryland [9]. This group studied $Nd_{1.85}$ $Ce_{0.15}$ CuO_4, a material that exhibits a high T_c when doped with electrons rather than with holes, as in YBCO or BSCCO. The temperature dependence of λ for this material is just one would expect for an s-wave BCS superconductor.

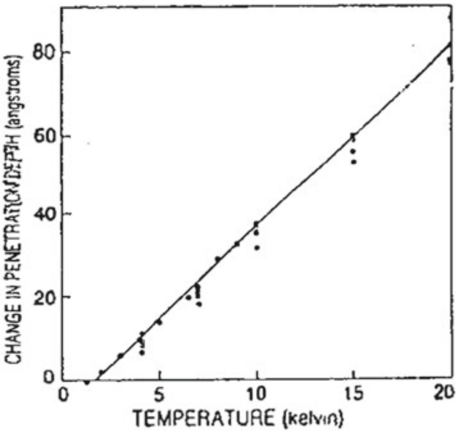

Fig. 7.11 Penetration depth of microwaves in a high T_c crystal, compared to some reference value, is predicted to vary linearly with temperature at low temperatures it the electrons in the superconductor are paired in a particular type of d-wave state [8, 13]

According to Emery [10], the symmetry of the wave function is highly anisotropic. Since then, there have been evidences accumulated for d-wave symmetry. A direct evidence for a sign change of the pair wave function comes from elegant interference experiments by Wollman (Univ Illinois, Urbana); Tsuei (1BM, Yorktown Hights); Wellstood (Univ. Maryland); Brawner (ETH Zurich) which has been explained as follows [11].

In a normal metal, apart from a periodic modulation, the single electron orbitals are plane waves $\psi(r) = \mathrm{e}^{\mathrm{ikr}}$ and have energies which vary continuously with wave vector $\vec{k}$. The order parameter of a superconductor is the 'pair-amplitude'. This is closely related to the wave function $\psi(\vec{r_1} - \vec{r_2})$ of a Cooper pair of electrons at positions $\vec{r_1}$ and $\vec{r_2}$. Specifically, the pair wave function (apart from a periodic modulation) is

$$\psi(r_1 - r_2) = \sum_k g(k) \exp[ik(r_1 - r_2)]$$

where *g(k)*, the Fourier transform of the pair amplitude is proportional to the energy gap Δ_k (the *k*-space energy gap).

The excited states of the superconductor are altered from the normal state. In the normal state, it costs energy $|\in_k - \in_F|$to put an electron into an excited one-electron state, where $\in_k$ is the single particle energy spectrum and $\in_k$ is the Fermi energy.

In the superconducting state, the energy cost is $[(\in_\mathrm{k} - \in_\mathrm{F})^2 + \Delta_\mathrm{k}^2]^{1/2}$. In the normal state, the minimum energy cost is zero, whereas in the superconducting state it is instead the smallest value of $|\Delta_\mathrm{k}|$.

In an s-wave superconductor, Δ_k is approximately a constant Δ_0, independent of *k*, but in a d-wave state, the gap Δ_k has $d(\mathrm{x}^2-\mathrm{y}^2)$ symmetry in k-space : $\Delta_\mathrm{k} \propto k_x^2 - k_y^2$. This function has zeros or 'nodes', when $|\mathrm{k_x}| = |\mathrm{k_y}|$ (at 45° between the $\mathrm{k_x}$ and $\mathrm{k_y}$ axes). The corresponding 'real space' pair wave function $\psi(r_1 - r_2)$ computed from

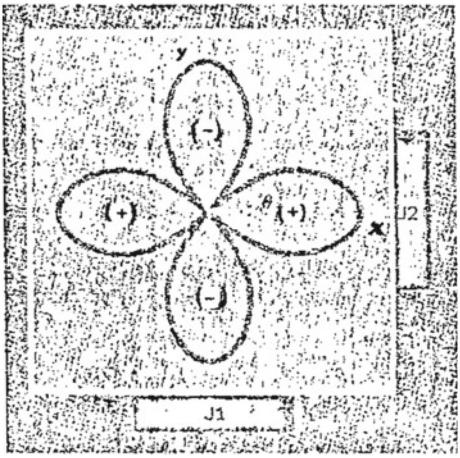

Fig. 7.12 Interference experiment to predict d-wave superconductor [11]

the equation above will then have d-wave ($x^2 - y^2$) spatial symmetry, with nodes and a sign change upon a rotation of 90 °, as indicated in Fig. 7.12

This sign change is directly measurable by doing an interference experiment using Josephson junctions to transfer Cooper pairs into the d-wave superconductor (from a conventional s-wave superconductor) at one angle, and then back out at an angle rotated by 90°, as illustrated (Fig. 7.12). The pairs removed at J_2 have the sign of their wave function changed relative to their sign at the point of insertion J_1. In the conventional superconductor which completes the circuit, there is no sign change, and therefore the wave function violates the requirement of being "single valued" unless the sign change is compensated by a half integral number of magnetic flux quanta through the loop. This unusual magnetic effect has been detected and seems to settle the question of a sign change and nodes in the energy gap[11].

Photoemission Measurements

A Stanford-Los Alamos collaboration led by Zhi-Xun Shen probed the energy gap at different directions on the Fermi surface using angle-resolved photoemission [12]. This group used BSCCO crystals, grown by Aharon Kapitulnik's group at Stanford. By scattering photons off electrons in the crystal, one can sample the energy spectra of the electrons. Because the technique is sensitive to the angle of the emitted electrons, one can determine the spectrum for different wave vectors on the Fermi surface.

Within the resolution of their experiment, the Stanford-Los Alamos group could not tell whether the gap ever goes to zero or just gets very small. Their measurements were sensitive only to the magnitude and not to the sign of the gap, so they could'nt tell if the gap goes negative at some point. They concluded that their results were certainly consistent with d_{x2-y2} pairing but also could fit other forms of anisotropy.

To resolve more specifically whether there are nodes in the gap requires measurement that is sensitive to the sign of the gap. Van Harlingen et al. (Univ. of Illinois) designed such an experiment based on the ideas of Geshkenbein, Larkin (Landau Institute, Moscow) and Barone (Univ. of Naples, Italy) and similar to a proposal of

Sigrist and Rice (ETH, Zurich). Their design consisted of a SQUID in which half of the loop is a single, untwinned crystal of YBCO. (Recall that a SQUID consists of a loop of superconducting material broken at two points by S-I-S junctions). In the Illinois scheme, the superconductor on one half of the loop is lead and on the other half, it is the crystal. The leads are arranged so that one of the junctions is on a face of the crystal perpendicular to the 'a' axis and the other is on a face perpendicular to the 'b' axis. Thus the current in the loop enters in one face and must turn through 90 ° to exit through the other face. If the order parameter is negative in one direction and positive in another, this path introduces an additional phase shift of π that is reflected in a plot of the critical current versus flux.

At the March meeting of 1993, of the American Physical Society in Seattle, Van Harlingen presented the group's preliminary results: They observed a significant phase shift between the phases of the order parameter in the 'a' and 'b' directions, with several samples giving the phase shift of π predicted for the d_{x2-y2} state[13].

7.6 Scenario of Theories Describing Superconductivity in HTSCs

Fig. 7.13 depicts the scenario of various theories given for High T_c superconductors. The left hand side corresponds to Fermi liquid like theories with electron-phonon (top) and electron-electron (bottom) interactions. The right hand side correspond to non Fermi Liquid Theories with electron–phonon (top) and electron-electron (bottom) correlations.

The various proposals for pairing mechanism range from conventional models (i.e. pairing mediated by various type of Bosonic excitations) to exotic models (based on quasi-particles in two dimensions that obey anyonic statistics).

The Bosonic excitations may include (i) ordinary phonons or unusual lattice vibrations associated with the (presumed) polarizability of oxygen. (ii) electronic excitations and (iii) magnetic excitations. Both (ii) and (iii) could be at energies higher than the phonons and therefore, could lead to higher T_c's

In regard to the exotic models, the experimental results are inconclusive so far.

The experimental results such as

(1) increase of phonon-thermal conductivity below T_c,
(2) changes of phonon frequency and life time below T_c,
(3) modification of local atomic coordination near T_c

point to the existence of an interaction between charge carriers and the crystal lattice. Thus electron lattice interaction does exist in HTSCs but no direct measurement of electron-phonon coupling-strength exists so far. Knowing phonon spectra from experiments have led to the conclusion that strong-coupling is required to get the high T_c's A large ($\frac{2\Delta}{k_B T_c}$)value is an indirect evidence of strong coupling (Its value is 5 to 8 for HTSCs whereas 3.5 for the weak BCS coupling). However large $2\Delta/(k_B T_c)$ values are not necessarily indicative of strong coupling but could result from the large pair-breaking effects as measured in $YBa_2Cu_3O_7$.

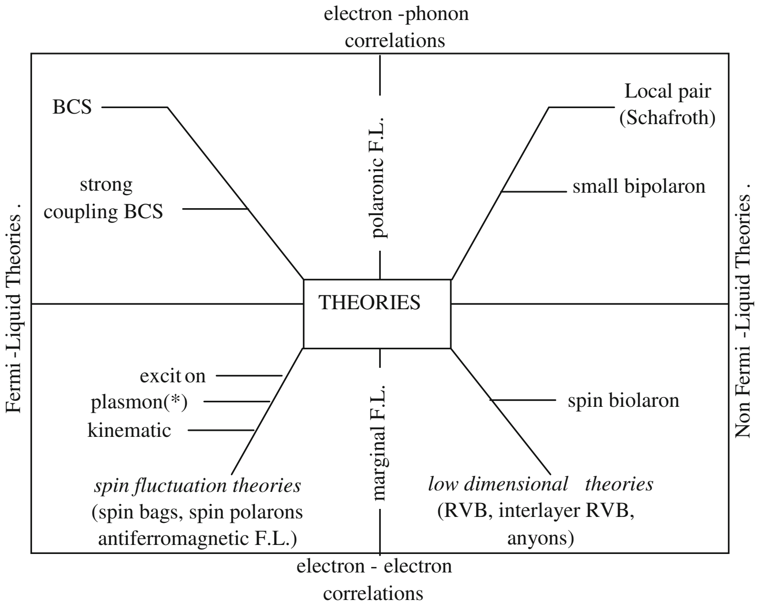

Fig. 7.13 Various theories for High T_c superconductivity. ((*) electron excitons are called plasmons)

It is frequently assumed that the strong coupling variant of the BCS theory can be employed to explain the high temperature superconductivity, because it successfully accounts for the properties of the classic superconductors also. Evidences for this fact stem from a number of observations;

(a) Electron-pairing seen in Shapiro-steps displayed by Josephson tunnel junctions biased with both ac and dc voltages. The steps have voltage spacing $h\upsilon/(2e)$ which implies that the electrons are bound into Cooper pairs.

(b) Electron tunneling and e.m. absorption measurements indicate presence of an energy gap in the distribution of energy levels available to the system. (It is of the same order of magnitude at temperatures $T \ll T_c$ as predicted by BCS theory). Values somewhat larger than $3.53\,k_B T_c$ are known to be associated with either (i) strong electron phonon coupling or (ii) strong electron-other virtual excitation coupling.

By nuclear quadrupole resonance on the copper nuclei of HTSC, two different values of Δ have been observed in the Y123, the larger value is associated with the planes and smaller with the chains.

(c) NMR data on some of ^{17}O nuclei in Y123 show that the relaxation rate $(1/T_1)$ rises to a peak just below T_c and then falls towards zero (as observed in Al by Hebel and Slichter long ago as predicted by the BCS theory).

(d) Temperature dependence of penetration depth (measured by muon spin resonance) has the characteristic as predicted by the BCS theory.

(e) Josephson tunnelling has been observed to occur between a Pb-Sn alloy and $YBa_2Cu_3O_{7-x}$. Such an effect is thought to be impossible between a singlet-paired and a triplet-paired superconductor. Since Pb-Sn alloy is singlet-paired, Y123 is also thought to be singlet paired (as predicted by the BCS theory).

7.7 Arguments Against the Applicability of the Original BCS Theory

(a) Observed values of T_c are probably too high (i.e. some interaction much stronger than electron-phonon interaction is at work).

(b) A linear term in the specific heat versus temperature curve has been observed in La-, Y- and Tl- compounds at low temperatures. The BCS theory predicts an exponentially small electronic specific heat if $T \ll Tc$. (The linear term is present in tetragonal Y123, and absent in non-superconducting $La_{2-x}Ba_xCuO_4$ and BSCCO).

(c) Raman scattering and infra-red absorption measurements imply energy gap (Δ) might various along certain lines or at certain points in momentum space. i.e. for electrons with momentum along certain directions, like heavy fermions superconductors (e.g. UBe_{13}). It may be related to

(i) linear dependence of thermal conductivity of $YBa_2Cu_3O_{7-x}$ observed near 0.1 K.

(ii) linear term in specific heat.

(d) Tunnelling experiments provide evidence against existence of nodes in energy gap (i.e. a reasonably well defined energy gap with very few states (if any) in it). Comparison of tunnelling experiments with the Raman effect experiments may identify states shown up in the Raman effect experiments.

(e) The spectral features associated with Δ barely shift in energy when T_c is approached, as if the gap were nearly constant upto T_c (i.e. no temperature dependence of Δ).

7.8 Identifications of Non-Phononic Mechanism

The isotope effect does not give an unequivocal answer as to whether a non-phonon mechanism is present in high T_c superconductivity. If there is a relationship between T_c and the ion-mass M, then there is definitely a lattice contribution to pairing, but it would be incorrect to try to correlate the value of α (or its deviation from 0.5) with the degree of phonon-participation.

High T_c by itself does not imply the presence of non-phononic mechanism. The high T_c can be produced also by electron-phonon mechanism if the coupling is sufficiently strong. In principle, it is quite realistic that both the mechanisms coexist.

7.8.1 *How to Detect the Presence of Non-Phononic Contribution to Pairing*

This can be done by comparing the results from (a) neutron scattering and (b) tunnelling spectroscopy.

We can obtain $F(\Omega)$, the phonon density of states from an analysis of inelastic neutron scattering (It has nothing to do whether the material is superconducting or not). The function $F(\Omega)$ has a number of sharp peaks which correspond to the dispersion regions where $dq/d\Omega$ is high. (Phonon density of states is proportional to $dq/d\Omega$). Thus the peaks correspond to different branches of the phonon spectrum (e.g. longitudinal and transverse acoustic branches).

Tunnelling spectroscopy determines the quantity

$$g(\Omega) = \Omega^2(\Omega).F(\Omega) \tag{7.31}$$

where $F(\Omega)$ is the density of states and $\alpha^2(\Omega)$ describes the electron-lattice interaction.

If the features, especially location of the peaks of the curves $g(\Omega)$ and $F(\Omega)$ coincide, this means that only the usual phonon-mechanism of superconductivity is active. Additional peaks in $g(\Omega)$ which are absent in $F(\Omega)$ indicate that a non-phonon mechanism is present. (for example, such an analysis can detect the contribution of plasmon modes).

7.9 Other Experimental Evidences for s-Wave/d-Wave Pairing

It was once agreed that the differential conductance dI/dV of the tunneling spectra of high T_c materials possesses a finite value at zero bias ($V = 0$) and a V-linear background extending over 0.1–0.2eV, suggestive of non-s-wave pairing [14]. However the experimental results reported during 1993 [15] were essentially different from earlier ones. The spectrum across an SIS junction on Bi 2212 [16] and the scanning tunnelling spectrum on Y123 laser ablated films [17] showed a square-well like shape in the dI/dV-V characteristics, typical of conventional s-wave superconductivity, with no linear background and a vanishingly small zero-bias conductance. The width of the well, $2\Delta_s/(k_B T_c) \sim 4$–8, is suggestive of strong coupling.

As regards the symmetry of the superconducting gap, ARPES (angle resolved photoemission spectroscopy) of Bi2212 clearly demonstrated a spectral weight transfer from the gap region (from the Fermi level to an energy $\sim\Delta_s$) to the region of higher binding energies, forming pile up peaks at various points in the momentum space.

It was suggested that the width of the gap region is not uniform over the first Brillouin zero. Δ_s was found to be smaller (though not zero) at points where $\Delta(k)$ is expected to have nodes in the case of d-wave pairing.

NMR results were still controversial concerning symmetry of Δ_S. Many features such as the temperature dependence of under relaxation rate T_1^{-1} below T_c, the absence of a coherence peak in T_1^{-1} and its anisotropy, favour d-wave pairing, but the T-dependence of the Knight shift is consistent with an s-wave pairing. The symmetry problem of Δ_s (superconducting gap) is left for future studies. However, improved energy resolution is ARPES and NMR experiments on purer crystals will provide crucial tests.

In the passing, it is worth mentioning that according to Robert Schrieffer:

"I agree that at present no theory can account for all the normal-phase data, including the marginal-Fermi-liquid approach of Varma and his coworkers [18] and the spin fluctuation scheme of Pines group [19]. Deducing a consistent approach to the normal state properties from a first-principles microscopic theory will still require much work, although I believe excellent progress is being made in this direction" [20].

References

1. J. Bardeen, L.N. Cooper, J.R. Schrieffer, Phys. Rev. **108**, 1175 (1957)
2. H. Ibach, H. Luth, *Solid State Physics* (Springer, Heidelberg, 1996)
3. G. Baskaran, in *High Temperature Superconductors*, ed. by S.V. Subramanyam, E.S.R. Gopal (Wiley Eastern Limited, New Delhi, 1989)
4. J.R. Schrieffer, Phys. Rev. Lett. **60**, 944 (1988)
5. K. Lyons, Science **247**, 1410 (1990)
6. G.J. Canright, S.M. Girvin, Science **247**, 1197 (1990)
7. J.A. Martindale, S.E. Barrett, K.E.O. Hara, C.P. Slichter, W.C. Lee, D.M. Ginsberg, Phys. Rev. B **47**, 9155 (1993)
8. W.N. Hardy, D.A. Bonn, D.C. Morgan, R. Liang, K. Zhang, Phys. Rev. Lett. (Submitted 1993)
9. D.H. Wu, J. Mao, S.N. Mao, J.L. Peng, X.X. Xi, T. Venkatesan, R.L. Greene, S.M. Anlage, Phys. Rev. Lett. **70**, 85 (1993)
10. V. J. Emery, Nature **370**, 598–598 (1994)
11. P.B. Allen, Nature **375**, 188–189 (1995)
12. Z.X. Shen, D.S. Dessau, B.O. Wells, D.M. King, W.E. Spicer, A.J. Arko, D. Marshall, L.W. Lombardo, A. Kapitulnik, P. Dickinson, S. Doniach, J. Di-Carlo, T. Loeser, C.H. Park, Phys. Rev. Lett. **70**, 1553 (1993)
13. B.G. Levi, Phys. Today, 17–20 (1993)
14. M. Gurvitch, J.M. Valles (Jr.), A.M. Cucolo, R.C. Dynes, J.P. Garno, L.F. Schneemeyer, J.V. Waszczaki, Phys. Rev. Lett. **63**, 1008 (1989)
15. S. Uchida, Jpn. J. Appl. Phys. **32** (Part. 1, No. 9A) 3784 (1993)
16. J.F. Zasadzinski, N. Tralshawara, P. Romano, Q. Huang, Jun Chen, K.E. Gray. J. Phys. Chem. Solids **53**, 1635 (1992)
17. T. Hasegawa, M. Nantoh, A. Takagi, H-Ikuta, M. Kawasaki, H. Koinuma, K. Kitazawa. J. Phys. Chem. Solids **53**, 1643 (1992)
18. C.M. Varma, P.B. Littlewood, S. Schmitt-Rink, E. Abrahams, A.E. Ruckenstein, Phys. Rev. Lett. **63**, 1996 (1989)
19. A.J. Millis, H. Monien, D. Pines, Phys. Rev. B **42**, 167 (1990)
20. P.W. Anderson, R. Schrieffer, Phys. Today, 55–61 (1991)

Chapter 8
Application of Superconductivity

8.1 Potential Applications

Many possible applications of superconductivity have been explored since the discovery of this phenomenon. Table 8.1 lists major present as well as potential applications under various bases of applications.

8.1.1 Superconducting Magnets

Since $R = 0$, there is no energy dissipation (I^2R loss), a current set up in a closed loop of a superconductor persists forever without decay. Many superconductors can carry (without energy loss) 100–1,000 times larger current densities compared to normal conductors, like copper. These facts have made possible the utilisation of superconductors for building lightweight, high-intensity compact magnets, useful in various applications.

First operational superconductor magnet (developed in 1957) was made with Nb wire, which could produce 0.7 T. In 1962, a superconductor was prepared using NbSn, which could develop 7.0 T. At Present, superconductor magnets are able to produce 17 T of magnetic field.

The superconducting magnets offer the advantage of getting high homogeneity and stability of the field and better reliability as compared to resistive (permanent) magnets. Their use in magnetic resonance imaging ensures a superior image quality. In high energy physics, particles can be accelerated, deflected and focussed by the fields of superconducting magnets. In bubble chambers, high magnetic fields are used to deflect particles, forcing them to follow a curved path. The curvature and direction of their track determines the momentum and charge of the particle.

A. K. Saxena, *High-Temperature Superconductors,* Springer Series
in Materials Science 125, DOI: 10.1007/978-3-642-28481-6_8,

Table 8.1 Applications of superconductivity

Basis for application	Application
$R = 0$ and high J_c	1. Magnets for variety of applications
	2. Passive microwave devices
	3. Interconnects in microelectronics
	4. Electrical energy transport by cables
Josephson tunnelling	1. Microwave detectors and mixers
	2. In physical measurements (SQUIDs etc)
	3. Computers (fast logic and memory circuits)
	4. Plasma and space
	5. In medicine (magnetic encephalography)
High J_c at high H_{c2}	1. Electrical power industry
	2. Plasma confinement (in high energy physics)
	3. In transport (levitation trains, MHD-propelled ships)
	4. Medicine (nuclear magnetic resonance tomography)

Table 8.2 J_c and H_c requirements for various applications in electrical power industry

Application	J_c (Acm^2)	H_c (tesla)
Power transmission	2×10^4	1
Power generation	2×10^4	5–7
Transformer	10^4	1
Power storage	$10^3 - 10^4$	5–10
MRI scanners	10^4	2
Mineral separation	10^4	2–5

8.2 Applications of High-T_c Oxide Superconductors

The SQUIDs are the basis of the most sensitive magnetometers available today. These currently use the conventional superconductors and operate at liquid helium temperature, i.e. 4.2 K. It is expected that SQUIDs made from oxide superconductors and operating at liquid nitrogen temperature (77 K) will be soon available commercially. This will improve the ruggedness and utility of the device and extend its use to major areas, especially military and medical fields.

In VLSI (very large scale integration) technology, the use of HTSC interconnections working at 77 K offers several advantages and it is expected that in high-speed computers and telecommunications, this will be used extensively in near-future.

The use of HTSCs for generation, storage, transmission and transformation of electrical power in electrical industry is being assessed by major industries all over the world. The three parameters, viz. Critical temperature T_c, critical current J_c and critical field H_c are continually being improved to develop the power industry. The current density and magnetic field requirements for different applications are listed in Table 8.2.

Table 8.3 Applications of HTSC films

Basis	Application
Films having zero resistively and high J_c	1. Passive microwave devices
	2. Interconnects (between semiconductor transistors etc.) in micro electronics
Film based junctions Josephson tunnelling, hybrid superconductor/semiconductor junctions	1. SQUIDS
	2. Devices for example microwave detectors and mixers
	3. In medicine
	4. In hybrid technology

Table 8.4 Propagation-delay of several important electronic device technologies

Technology	Lowest propagation delay	
	Observed (ps)	Predicted potential (ps)
Silicon CMOS	75	50
Silicon bipolar	23	15
GaAs bipolar	20	10
GaAs MESFET	10	2
GaAs MOSFET	6	1
JJ devices	3	0.05
GaAs RTD[a]	–	0.1

[a] Resonant tunnelling device

One application of superconductivity that has gained popularity in medical field is magnetic resonance imaging. In this, fairly intense magnetic fields are created, which simulate the resonance of hydrogen atoms in the human body. This helps in the building up of a two-dimensional picture of human organs.

The possibility of applications of HTSCs in magnetically elevated trains and in magnetic mineral separation are also being pursued, though to make cost-effective devices for use in these fields appear to be somewhat remote.

8.3 Applications of High T_c Films

Although the predicted speed potential of Josephson junction devices far exceeds that of all prominent technologies, the high speed electronic devices cannot make use of purely superconductors based Josephson junctions. Because, unfortunately the JJs do not provide a current gain, as do all conventional semiconductor devices and a typical JJ switch has an area, at least an order of magnitude greater than that of the FET structures, which precludes high integration density desired in leading edge applications. However, “hybrid devices” can be made, which combine the desirable attributes of superconducting electronics, viz. lossless interconnects and low power and semiconductor based devices with a current gain and small area, e.g. (1) Hybrid RTT (resonance tunelling transistor), (2) Hybrid MOSFET (Table 8.3).

Hybrid RTT would achieve an order of magnitude improvement over semiconductor technology due (partly) to the fact that tunelling is inherently a faster phenomenon than diffusion (e.g. in BJT) or drift (e.g. FET) and transit distances (which electrons have to travel in transiting the device) are smaller (100 Å versus $\sim 0.1\,\mu\text{m}$). Because of small transit distance, resonant tunnelling structures can achieve low power dissipation and because of less room for inelastic scattering to occur. The second device (hybrid MOSFET) operates using proximity effect.

Both the hybrid devices, would provide a signal gain, as opposed to Josephson junction devices and also, they do not require much device area. These advantages, along with the ability to achieve very low propagation delays, suggest that they are viable alternatives for high speed electronic applications (Table 8.4).

Appendix A
Quasiparticles

A system may be described by single particle excitations or quasiparticle excitations. (The quasiparticle method was formulated by L. D. Landau in his work on superfluidity of liquid helium). Quasiparticles describe weakly excited states of systems with many degrees of freedom, such as crystals, plasmas, electromagnetic fields, liquid He, ferromagnetics, superconductors, etc. Quasiparticles serve to describe the excited state. While the number of quasiparticles is small, which is the case at low temperatures (when the degree of excitation is low), they can be treated as an ideal gas. Thus, a quasiparticle is not a particle in the usual sense of the word but is a convenient representation of an excited state. In this representation, the problem of interaction between systems with many degrees of freedom reduces to that of interacting quasiparticles. This makes it very convenient to utilize the energy and momentum conservation laws, e.g., photons describe excitation of an e.m. field which has a discrete set of energy levels. Similarly, phonons describe a sound wave. Many other quasiparticles have been introduced, such as plasmons, magnons, excitons, and polarons.

A. K. Saxena, *High-Temperature Superconductors*, Springer Series
in Materials Science 125, DOI: 10.1007/978-3-642-28481-6,

Appendix B
Fermiology

In reality, electrons strongly interact with the lattice ions. Many processes (electrical and thermal conduction, superconductivity, etc.) depend strongly on this interaction. The electron–lattice interaction leads to the formation of band structure. An energy band is an interval of allowed values of electron energy. The electron energy spectrum in a solid is given by a function $E(p)$, where p is the crystal momentum (quasimomentum). This function (called the dispersion relation) is generally complicated and strongly depends on the crystal structure.

If a band contains a small number of electrons, the energy near an extremum may be expanded in powers of the crystal momentum. In a cubic crystal $E = p^2/(2m^*)$, where m^* is the electron effective mass, i.e., the effect of the periodic field of the lattice is to alter the electron mass.

Consider the case when the band is almost completely filled. Then, it is more convenient to look at the vacant, rather than filled, states. Instead of a band containing a small number of vacant levels, we are then dealing with an equivalent system made up of a completely filled band and a small number of positive charges, termed holes. The latter occupy levels which were vacant in the original picture. Thus, a nearly filled band is equivalent to a set of holes, i.e., particles whose behavior is described by the same formulas as that of electrons in an almost empty band, but with a positive charge.

The most efficient way to analyze the anisotropy of a metal and to evaluate its normal-state parameters is to describe the system in momentum space; this approach is called *Fermiology*. This is a well-known method in case of metallic systems. The function $E(\vec{p})$ represents the dispersion relation for an electron (or a hole), and the equation $E(\vec{p}) = E_F$ defines the Fermi-surface. For a three-dimensional isotropic system with a simple quadratic dispersion relation $E(\vec{p}) = p^2/(2m^*)$, the Fermi-surface is a sphere. Anisotropy of a system is reflected in the shape of its Fermi-surface.

A. K. Saxena, *High-Temperature Superconductors*, Springer Series in Materials Science 125, DOI: 10.1007/978-3-642-28481-6,

Fermiology encompasses basically two approaches. One is based on band structure calculations: the Fermi-surface parameters are calculated. Another approach looks at certain experimental data which are sensitive to the topology of the Fermi-surface; special theoretical analysis then allows its shape to be reconstructed (e.g. ultrasound attenuation in a magnetic field). The parameters of the FS of many metals and compounds have been established and detailed results have been obtained by this approach. This latter approach to Fermiology is similar in concept to that of tunneling spectroscopy where theoretical analysis allows one to use tunneling data in order to evaluate the major parameters of the electron–phonon interaction.

Finally, we can consider the heat capacity of an electron-gas at low temperatures, which turns out to be directly proportional to the temperature:

$$C_v = \left(\frac{\partial E}{\partial T}\right)_v = \frac{\partial}{\partial T}\left[\frac{(k_B T)^2}{E_F} N\right] = \left(\frac{N k_B^2}{E_F}\right) T$$

This is an important result of quantum theory of metals. For T → 0, the electronic heat capacity decreases linearly.

However, when one takes into account the interaction of the electrons with thermal vibrations of the lattice, this leads to deviations from the linear law (Eliasherg 1963; Kresin and Zaitsev 1976). The degree of this deviation is related to the strength of the electron–phonon coupling.

Appendix C
Pairing in High T_c Cuprates in Relation to Fermi Energy

The small value of the Fermi energy of high T_c cuprates has a strong impact on the superconducting properties. First of all, the ratio $\Delta(0)/E_F$ is an important superconducting parameter. As a result of a superconducting transition and electron pairing, the FS undergoes a reconstruction within a layer of thickness Δ. Therefore, the parameter $\Delta(0)/E_F$ shows what fraction of the electronic states are directly involved in pairing. In conventional superconductors, this ratio is small ($\sim 10^{-4}$), whereas in high T_c oxides, E_F and Δ are comparable $\Delta(0)/E_F = 10^{-1}$. The small value of this ratio in conventional superconductors means that only a small number of states near the FS are involved in pairing. The situation is different in cuprates. The large value of the ratio corresponds to a significant fraction of the carriers being paired up, and this implies a short coherence length. This fact is directly related to the quasi-two-dimensional structure of the cuprates. In conventional superconductors, pairing can occur only near the Fermi-surface. (The states on the FS form a two-dimensional system in momentum space, and this is important because in 2-D, any attraction will lead to the formation of a bound state). But, the layered structure of cuprates makes pairing possible even for states that are distant from the Fermi-surface.

A. K. Saxena, *High-Temperature Superconductors*, Springer Series
in Materials Science 125, DOI: 10.1007/978-3-642-28481-6,

Index

A. K. Saxena, *High-Temperature Superconductors*, Springer Series in Materials Science 125, DOI: 10.1007/978-3-642-28481-6,